UNIVERSITY OF OKLAHOMA

GRADUATE COLLEGE

OBSERVATIONS AND SIMULATIONS OF POLARIMETRIC, X-BAND RADAR SIGNATURES IN SUPERCELLS

A DISSERTATION

SUBMITTED TO THE GRADUATE FACULTY

in partial fulfillment of the requirements for the

Degree of

DOCTOR OF PHILOSOPHY

By

JEFFREY CURTIS SNYDER
Norman, Oklahoma
2013

Downloaded from SHAREOK. Persistent Handle URL: https://hdl.handle.net/11244/6398

OBSERVATIONS AND SIMULATIONS OF POLARIMETRIC, X-BAND RADAR SIGNATURES IN SUPERCELLS

A DISSERTATION APPROVED FOR THE
SCHOOL OF METEOROLOGY

BY

_____
Dr. Howard Bluestein, Chair

_____
Dr. Alexander Ryzhkov

_____
Dr. Jerry Straka

_____
Dr. Guifu Zhang

_____
Dr. S. Lakshmivarahan

© Copyright by JEFFREY CURTIS SNYDER 2013
All Rights Reserved.

To the love of my life, my wonderful wife Kim, who has supported me through the many late nights and through the many years, I owe my greatest debt of gratitude. To my amazing son Jack, who drives me to want to be as great a role model as possible, I hope to do well by you. To my supportive family and friends, you have all shaped me into the person, friend, husband, scientist, brother, and son that I am today. To my advisor, Howie Bluestein, who has provided invaluable guidance and support since I first stepped into his office, I must say that the help and mentorship I have received through the past eight years have been invaluable.

Acknowledgements

This work was supported under NSF grants ATM-0637148, AGS-0821231, and AGS-0934307 awarded to the University of Oklahoma and ATM-0242166 and ATM-0641201 awarded to the University of Massachusetts – Amherst. The computing for this project was performed at the University of Oklahoma Supercomputing Center for Education & Research (OSCER). This work would not have been possible without the insightful discussions I have had with Dan Dawson, Robin Tanamachi, Michael French, Jana Houser, Vivek Mahale, Matthew Kumjian, Vijay Venkatesh, Youngsun Jung, the technical support personnel at OSCER, and many others. Additional guidance and fruitful discussion was provided by the author's Ph.D. committee – Dr. Howard Bluestein, Dr. Alexander Ryzhkov, Dr. Jerry Straka, Dr. Guifu Zhang, and Dr. S. Lakshmivarahan.

Table of Contents

Acknowledgements iv
Table of Contents v
List of Tables vi
List of Figures vii
Abstract xix

Chapter 1: Introduction 1

Chapter 2: Polarimetric Radar Observations 7
a. Radar quantities 7
b. Considerations for Mobile X-Band Radars 11
c. A brief description of commonly-observed polarimetric signatures 16

Chapter 3: Microphysics Relevant to the Numerical Modeling of Supercells 22
a. Bulk Microphysics 22
b. Polarimetric radar emulator 27
1) Fractional water for ice species 27
2) Aspect ratio 31
3) Canting angle 32
4) Dielectric constant 33
5) Radar variables and angular moments 38

Chapter 4: Research Tools and Experiment Design 42
a. Observational Tools 42
b. Numerical Simulation Tools 47

Chapter 5: Observations of Polarimetric Signatures by Two Mobile X-Band Radars 53
a. Low reflectivity ribbon (LRR) 53
b. Reduced mid-level ρ_{hv} to the left of the BWER (LoRB) 61
c. Other polarimetric signatures observed in supercells 66

Chapter 6: Polarimetric Signatures in Numerically-Simulated Supercells 73
a. Polarimetric signature reproducibility 75
b. Structure and evolution of simulated signatures 78
1) Z_{DR} columns and rings 78
2) K_{DP} columns 89
3) ρ_{hv} rings 92
4) Other signatures 96

Chapter 7: Summary and Conclusions 99

References 200

List of Tables

Table 1. Selected characteristics of the UMass XPol (2007–2010) and RaXPol (2011–2013) mobile radars used in this project..... 109

Table 2. Parameters used in the numerical simulations 109

Table 3. A non-exhaustive list of the datasets in which LRRs and LoRBs have been identified in UMass XPol (2007–2010) and RaXPol data (2011–2013). Discontinuities in data collection or deployments likely resulted in these features being missed in other storms in which data were collected. In addition, on many storms, the scanning strategy used precluded the collection of data to an adequate height to observe the LoRB..... 110

Table 4. Estimated 0–3 km storm-relative helicity (SRH) for each simulation based upon a subjectively-analyzed average motion of the cyclonic supercell in each simulation between 4800s and 9000 s. 111

Table 5. A description of the quantities examined and used for correlation statistics. These quantities were calculated for each simulation during the 1800–9000 s period within a subjectively-determined subdomain specific to each simulation. The subdomain was chosen such that primary supercell remained within it during the examined time period while not including other convection. 112

List of Figures

Figure 1. Z_H, Z_{DR}, and K_{DP} (from top to bottom) of monodispersed distributions of rain (left column), dry hail (i.e., f_{wh} = 0%; center column) and hail with fixed f_{wh} = 10% (right column) as a function of equivolume diameter. The solid, dashed, and dotted curves are calculations at S, C, and X bands, respectively. Although similar to the results presented in Snyder et al. (2010), the above quantities have been recalculated consistent with the latest version of the radar emulator (details of which are provided in Chapter 3). 113

Figure 2. Similar to Figure 1 except for A_H, A_{DP}, and δ (from top to bottom) for rain (left) and dry hail (right) at S, C, and X bands. 114

Figure 3. A comparison of Z_H' from S-band WSR88D radars and the X-band UMass XPol. (a) KCYS on the 0.5° elevation angle scan and (b) UMass XPol on the 4.6° elevation angle scan valid around the same time on the evening of 9 June 2010. (c) KAMA at an elevation angle of 0.5° and (d) UMass XPol at an elevation angle of 2.1°. The elevation angles were chosen so that the beam heights from the respective radars were similar. Range ring labels are relative to the respective radars. [From Snyder et al. (2013)] 115

Figure 4. Conceptual models of (a) Low-level polarimetric signatures, (b) mid-level vertical velocity extrema, and (c) mid-level polarimetric signatures. [From Kumjian and Ryzhkov (2008)] 116

Figure 5. Conceptual model of polarimetric supercell structure at (a) 1 km above ground level and (b) "mid-level". [From Romine et al. (2008), adapted from Lemon and Doswell (1979) and Burgess (1993)] 117

Figure 6. Calculated Z_{DR} of a spheroidal hailstone as a function of mass water fraction. The thin solid line represents a soaked hailstone calculated assuming a water matrix and ice inclusion (i.e., $\varepsilon(ws)$), and the dashed line represents a soaked hailstone calculated as a snow matrix with water inclusion (i.e., $\varepsilon(sw)$). The thick solid line is calculated according to the two-layer method (water outer shell with mixed soaked interior). The modeled hailstone has an aspect ratio of 0.8, an ice density of 0.92 g cm^{-3}, and a temperature of 0° C. The calculations were performed at λ = 5.4 cm and use the Rayleigh approximation. (From Ryzhkov et al. 2011) 118

Figure 7. Calculated Z_{DR} at C (λ = 5.4 cm) and S (λ = 11 cm) bands for melting hail. f_{wh} is determined from the critical water fraction described in Rasmussen and Heymsfield (1987) and varies as a function of diameter. Solid lines represent hailstones with ϕ = 0° and σ_h = 0°; dashed lines represent hailstones with a distribution of canting angles (i.e., $\sigma_h \neq 0°$) that depends upon f_{wh}. (From Ryzhkov et al. 2011) 119

Figure 8. Z_H, Z_{DR}, and K_{DP} as a function of equivolume diameter for wet hail (f_w = 10%) at S (solid line), C (long dashed line), and X (short dashed line) bands. Calculations based upon the variable and angular moment equations provided in Jung et al. (2010) and used in this project are marked in black, whereas calculations using the variable and angular moment equations in Ryzhkov et al. (2011) are marked in red. 120

Figure 9. Photographs of the (a) UMass XPol radar collecting data in a tornado in southeastern Wyoming on the afternoon of 5 June 2009 and (b) RaXPol radar collected data in a supercell on 11 June 2011. (Photos courtesy of Jeff Snyder) 121

Figure 10. A skew-T, log-P plot of the idealized sounding used for the eight primary simulations examined in this study. The sounding is based on the analytical sounding presented in Weisman and Klemp (1983)..... 122

Figure 11. The four hodograph shapes examined in this study: (a) half-circle with constant veering between the surface and 10 km AGL (*15r10* and *25r10*), (b) half-circle with decreasing shear and veering between the surface and 10 km AGL (*15r10_057* and *25r10_057*), (c) quarter-circle with 90 degrees of turning from the surface to 3 km AGL with constant, "straight" shear from 3 km to 10 km AGL (*15q10* and *25q10*), and (d) straight-line hodograph with constant shear between the surface and 10 km AGL (*15str* and *25str*). The blue curves represent the "weak" shear cases (mean 0–10 km shear $\approx 4.7 \times 10^{-3}$ s^{-1}); the red curves represent the "strong" shear cases (mean 0–10 km shear $\approx 7.8 \times 10^{-3}$ s^{-1}). All blue hodographs of the same color are the same length. Sounding heights are marked every 1 km by circles along each hodograph. Units are in m s^{-1}. Red and blue stars in each panel represent an estimated storm motion based on peak updraft motion between 4800 s and 8400 s. Winds above 10 km are constant.123

Figure 12. (a) Z_H', (b) Z_{DR}', (c) V_R, and (d) ρ_{hv} from 2209 UTC on 5 June 2009. The local reduction in Z_H' and Z_{DR}' is denoted by the arrows, and the black outline in (b)–(d) mark the approximate periphery of 30 dBZ echo. Here and in all subsequent figures, Z_H and Z_H' are in dBZ$_e$, Z_{DR} and Z_{DR}' are in dB, and V_R is in m s^{-1}. (e) A photograph of the supercell and tornado taken near 2210 UTC has a very similar field of view as the data shown in (a)–(d). (Photo courtesy J. Snyder) [From Snyder et al. (2013)] 124

Figure 13. (a) Z_H', (b) Z_{DR}', (c) V_R, (d) ρ_{hv}, and (e) Φ_{DP} from 0150 UTC on the evening of 10 June 2010 collected at an elevation angle of 4.7°. The black line in (a) marks the radial along which the profile is extracted in Figure 15a. The local reductions in Z_H' and Z_{DR}' are essentially collocated. The approximate location of the 30 dBZ isoecho is shown in black in (b)–(e). (f) A photograph of the supercell as seen to the northwest of the radar deployment location (courtesy J. Snyder). [From Snyder et al. (2013)] 125

Figure 14. (a) Z_H', (b) Z_{DR}', and (c) V_R from 0016:07 UTC on the evening of 18 May 2010. Black arrows in (a) and (b) mark the location of the LRR, and the solid black line in (a) marks the radial from which the data in Figure 15b are shown. A wide-angle photograph of the supercell (d) as it appeared from the deployment location at approximately 0009 UTC looking to the west-northwest (courtesy J. Snyder). [From Snyder et al. (2013)] 126

Figure 15. Radial profiles of (a) Z_H' (solid line), $Z_{DR}' \times 10$ (long dashed line), and ρ_{hv} (short dashed line) from 0150:12 UTC on 11 June 2010 (along black line in Figure 13a) and (b) Z_H' (solid line), $Z_{DR}' \times 10$ (long dashed line), and Φ_{DP} (short dashed line) from 0016:07 UTC on 19 May 2010 (along black line in Figure 14a). To enhance clarity and reduce high-frequency variability, the plotted variables are filtered by centered averaging through either a 500 m (Z_H', Z_{DR}', ρ_{hv}) or 1 km (Φ_{DP}) range. The LRR is centered at ranges of ~17.6 km and ~10.2 km in (a) and (b), respectively. [From Snyder et al. (2013)]..... 127

Figure 16. (a) A photograph, taken near 2331 UTC, of a wall cloud produced by a supercell on 23 May 2008 in extreme northwestern Oklahoma (courtesy H. Bluestein). UMass XPol deployed ahead of the hook echo and strong rear-flank downdraft: (b) K_{DP}, (c) Z_H', (d) Z_{DR}', (e) V_R, and (f) ρ_{hv} valid 2341:42 UTC. The arrows mark the location of the LRR, which is more evident in Z_{DR}' than Z_H'. [From Snyder et al. (2013)] 128

Figure 17. Z_H' (left), Z_{DR}' (center), and V_R (right) valid, top to bottom, at 2239:51, 2241:20, 2342:47, and 2344:29 UTC at ~4.2º elevation angle as a hook echo wraps up over UMass XPol on 23 May 2008. The LRR is clearer in Z_{DR}' than in Z_H'. At this elevation angle, strong radial convergence is associated with the LRR. Peak V_R in the hook echo reaches 45 m s^{-1} by the latest time ~1.3 km W of the radar. Range rings are in 2 km increments. [From Snyder et al. (2013)] ... 129

Figure 18. Z_H' (left), Z_{DR}' (center), and V_R (right) valid at 2343:09 (top), 2343:31 (middle), and 2343:53 (bottom) UTC at 6.1º, 8.0 º, and 10.4º elevation angle. Small-scale vortices (several of which are marked by black circles) stream rapidly southward into the inside part of the wrapping hook echo. Low-level rotation continues to intensify beyond that shown in this figure; by 2344:51 (not shown), V_R increases to 50 m s^{-1} inbound and 45 m s^{-1} outbound, with the extrema separated by 1.0 km in the azimuthal direction. [From Snyder et al. (2013)] 130

Figure 19. UMass XPol (a) Z_H and (b) Z_{DR} from the evening of 7 June 2009 and (c) Z_H and (d) Z_{DR} from the evening of 25 May 2010. The black arrows denote the location of an observed LRR, and the region of ~35 dBZ is outlined in black in (b). [From Snyder et al. (2013)] 131

Figure 20. Polarimetric data from RaXPol collected at an elevation angle of 5° on the afternoon of 23 May 2011: (a) Z_H', (b) Z_{DR}', (c) V_R, and (d) ρ_{hv}. The black

arrows point to the low-reflectivity ribbon, and the black enclosed area marks the probable location of large hail (and possibly non-meteorological scatters associated with strong inflow just south and west of the forward-flank gust front). The black dotted enclosed area marks a three-body scatter spike; the long dash grey line in (a) marks the location of the reconstructed RHI in Figure 21. This supercell produced the largest hailstone ever observed in Oklahoma approximately 25 minutes prior to this scan. A polarimetric three-body scatter spike is also evident and is marked by a black, dotted curve. 132

Figure 21. A reconstructed vertical cross-section (RHI) valid near 2248-2250 UTC on 23 May 2011 through the LRR of a supercell southeast of Gotebo, Oklahoma. (a) Z_H', (b) Z_{DR}', (c) ρ_{hv}, and (d) Φ_{DP} are shown. The cross-section is taken from along the long dashed grey line in Figure 20. The black curves in (a)–(d) mark the approximate location of the 30 dBZ isoecho; the white curve approximates the edge of $\rho_{hv} = 0.4$..... 133

Figure 22. (a) Z_H', (b) Z_{DR}', (c) V_R, and (d) ρ_{hv} valid 2316 UTC on 23 May 2011 along a 2.0° elevation angle; (e) Z_H' and (f) ρ_{hv} valid near the same time along collected at a 14.0° elevation angle. The LRR is marked with black arrows. Range rings are shown every 5 km. The dotted and dashed black lines in (a) denote the azimuths (~350° and ~2°, respectively) of the reconstructed RHIs in Figure 23. 134

Figure 23. Reconstructed RHIs valid 2315-2316 UTC on 23 May 2011(the same volume as Figure 22) at azimuths of (left column) 350° and (right column) 2°. (a)–(b) Z_H, (c)–(d) Z_{DR}, (e)–(f) ρ_{hv}, and (g)–(h) Φ_{DP} are shown. 135

Figure 24. Z_H' (left), Z_{DR}' (center), and ρ_{hv} (right) from near 2329 UTC at elevation angles of, from top to bottom, 3.0°, 8.0°, and 16.0° on 23 May 2011. Range rings are marked every 3 km. 136

Figure 25. (a) Z_H, (b) Z_{DR}, (c) V_R, and (d) ρ_{hv} valid at 2053:46 UTC on 24 May 2011 near El Reno, Oklahoma. The LRR, marked by black arrows, is most apparent in Z_H' and is associated with strong radial convergence observed in V_R. A polarimetric tornado debris signature is marked by the dotted black arrow. The few radially-oriented streaks in (a) and (b) are artifacts of the attenuation correction scheme. 137

Figure 26. (a) Z_H, (b) Z_{DR}, (c) K_{DP}, (d) ρ_{hv}, (e) V_R, and (f) Φ_{DP} valid 2155:21 UTC on 19 May 2013 south of Carney, Oklahoma, at an elevation angle of 1.0°. Solid black arrows mark the LRR; a potential secondary LRR is marked by dashed black arrows in (a). A polarimetric tornado debris signature is evident at the tip of the hook echo at a range of ~12 km and marked by dotted black arrows. Maximum inbound velocities are 90-100 m s^{-1} on the south side of the tornado and were measured during a rightward/eastward "wobble" in the tornado track. 138

Figure 27. (a) Z_H', (b) Z_{DR}', (c) K_{DP}, and (d) ρ_{hv} valid at 2309:45 UTC on 19 May 2013 near Shawnee, Oklahoma. The LRR, marked by solid black arrows, is reflected in all fields. The dotted black arrow in (d) points to the polarimetric tornado debris signature. 139

Figure 28. (a) Z_H, (b) Z_{DR}, (c) K_{DP}, and (d) ρ_{hv} valid 0018:36 UTC 30 May 2013 in southwestern OK at 4.0° elevation angle. A weak tornado develops at the tip of the hook echo. An LRR is marked by black arrows. By 0022:56 UTC, the LRR is no longer evident, but a weak echo hole in (e) Z_H' and couplet in (f) V_R associated with the tornado remain. Peak V_R on the 2° scan (not shown) is ~30 m s^{-1}. 140

Figure 29. Polarimetric data from RaXPol collected on supercell producing a violent tornado on the evening of 31 May 2013: (a) Z_H, (b) Z_{DR}, (c) ρ_{hv}, and (d) V_R. The black arrows point to the LRR. Data are valid at 2313 UTC (i.e., relatively early in the lifecycle of the tornado) at a 3.0° elevation angle. The peak V_R at this time is ~68 m s^{-1}. 141

Figure 30. Polarimetric data from RaXPol collected on the afternoon of 29 May 2012: (a) Z_H', (b) Z_{DR}', (c) K_{DP}, and (d) ρ_{hv}. The black arrows point to the LRR. A hardware problem resulted in reduced data quality and biases in Z_H' and Z_{DR}' that are not accounted for in (a) and (b). 142

Figure 31. (a) Z_H and (b) V_R of a possible LRR (marked by black arrows) observed within a tornadic supercell on 3 April 2012 near the TDAL radar, a C-band Terminal Doppler Weather Radar located near Dallas Love Field Airport. 143

Figure 32. Generalized configurations for the (a) low-reflectivity ribbon (LRR) and (b) area of very low ρ_{hv} on the left side of the BWER (LoRB). Panel (a) is valid within 1 km AGL, and (b) is valid near and within 1 km of the ambient freezing level. As a result of the deployment locations typical of data collection efforts, there often is very high attenuation (sometimes to extinction) along the rear portion (often north and northwest for typical mobile radar deployments) of observed supercells. As such, confidence is low in this region; the double black line at the top of (a) indicates this uncertainty. [From Snyder et al. (2013)] ... 144

Figure 33. A reconstructed vertical cross-section (RHI) valid near 2340 UTC on 29 May 2012 through the BWER of a supercell near Kingfisher, Oklahoma. (a) Z_H', (b) Φ_{DP}, (c) Z_{DR}', and (d) ρ_{hv} are shown. The approximate location of the $\rho_{hv} = 0.85$ isopleth is marked by the black curves in (a)-(c). Hardware problems during the spring of 2012 resulted in a ~2.5 dB bias in Z_{DR}' and an unknown negative bias in Z_H' on this day. 145

Figure 34. (a) Z_H', (b) Z_{DR}', (c) V_R, and (d) ρ_{hv} valid at 18° elevation angle from 17 May 2010 in New Mexico as seen by UMass XPol. The black ellipse marks the large area of very low ρ_{hv} northwest of the BWER where Z_H' values of 30–45 dBZ

reside. The beam height was approximately 5.5 km ARL in the center of the BWER; in the LoRB, the beam was centered approximately 6–8 km ARL. Range rings are marked every 10 km. The black line in (a) marks the azimuth along which the reconstructed vertical cross-sections shown in Figure 35 are created. A near-storm sounding collected during VORTEX2 (not shown) near 2200 UTC measured deep-layer shear oriented southwest to northeast. [From Snyder et al. (2013)] 146

Figure 35. A reconstructed vertical cross-section (RHI) valid near 2218 UTC on 17 May 2010 (representing data along the azimuth marked by the black line in Figure 34a) along the 313° azimuth showing (a) Z_H', (b) Z_{DR}', (c) ρ_{hv}. The black contour in (a) and (b) represents the ρ_{hv} = 0.8 isopleth. 147

Figure 36. (a) Z_H', (b) Z_{DR}', (c) Φ_{DP}, and (d) ρ_{hv} at an elevation angle of 12.3° from a pair of severe storms as UMass XPol collected data in the Texas Panhandle on the evening of 18 May 2010. The black outlines in (b)–(d) approximate the location of the 30 dBZ isopleth. Range rings are shown every 10 km. Anomalously strong attenuation occurs along the left wall of the eastern BWER. Beam heights are ~5.0 km and 3.5 km ARL in the center of the western and eastern BWERs, respectively. NBF may be present as the radially-oriented reduction in ρ_{hv} in those radials that pass through the northwestern section of the eastern BWER (where notable attenuation is present). [From Snyder et al. (2013)] 148

Figure 37. A small sampling of mid-level polarimetric signatures associated with a supercell that occurred on 31 May 2007: (a) Z_H' and (b) ρ_{hv} valid 2336:00 UTC (12.2º elevation), (c) Z_H' and (d) Z_{DR}' valid 2248:55 UTC (13.0º elevation), and (e) Z_H' and (f) ρ_{hv} valid 2349:24 UTC (18.0ºelevation). A LoRB, Z_{DR} half-ring, and ρ_{hv} ring are evident in (b), (d), and (f), respectively. [Adapted from Snyder et al. (2013)] 149

Figure 38. (a) Z_H', (b) Z_{DR}', (c) K_{DP} (in deg. km^{-1}), and (d) ρ_{hv} from a supercell sampled by UMass XPol on 24 May 2008. The black line in (a) marks the radial along which Figure 39 is created, and the approximately area of 30 dBZ is outlined in black. The top of the Z_{DR} and K_{DP} columns is evident in (b) and (c). The black arrow marks the area of reduced ρ_{hv} left of the BWER, though this feature is more evident at slightly lower altitudes. The elevation angle for all panels is 29.4°; the beam height at the range of the BWER is ~5.8 km ARL. The local freezing level is evident in the polarimetric data along the far right side of the image at a range of approximately 14 km. [From Snyder et al. (2013)] 150

Figure 39. Reconstructed RHIs (based upon a series of PPIs) of (a) Z_H, (b) Z_{DR}, and (c) K_{DP} through the center of the BWER (black line) displayed in Figure 38. The reconstruction RHIs are oriented nearly east (left side) to west (right side) across the plots. The largest Z_{DR} observed above ~2 km ARL is observed along at the

bottom of the echo overhang at 8–10 km range and 2–6 km ARL height. [From Snyder et al. (2013)] 151

Figure 40. UMass XPol deployed on a supercell on 22 May 2008, and (a) Z_H', (b) Z_{DR}', and (c) ρ_{hv} at 2301:18 UTC are shown. The 30 dBZ isoecho is shown in black in (b)–(c). A Z_{DR} half-ring is extremely evident, just beyond which is a ρ_{hv} half-ring. The elevation angle is 18.7°, with a beam height of ~3.2 km (at 10 km range) to ~6.4 km (at 20 km range) ARL. (d) A photograph (courtesy H. Bluestein) of the supercell as viewed from the radar deployment location near 2250 UTC. [From Snyder et al. (2013)] 152

Figure 41. (a) Z_H', (b) Z_{DR}', and (c) V_R collected at 0121:08 UTC on 11 June 2010 at an elevation angle of 14.0º. An extremely prominent crescent-shaped BWER is apparent in (a), with a large mesocyclone of diameter O(10 km) (black curved arrows) and a smaller cyclonic-anticyclonic vortex pair of diameter O(1 km) (black circles). The height of the radar beam near the smaller vortex and areas of $Z_{DR}' > 2$ dB is ~7 km ARL. Range rings are shown every 10 km. A (d) photograph of the supercell and tornado was taken near the time these data were collected. (Photo courtesy H. Bluestein) [From Snyder et al. (2013)] 153

Figure 42. (a) Z_H' and (b) Z_{DR}' valid at 2310 UTC on 19 May 2013 as a tornadic supercell moved east of Norman, OK. A Z_{DR} half-ring is readily apparent in (b) and is marked by a black arrow. 154

Figure 43. Z_H', Z_{DR}', ρ_{hv}, and Φ_{DP}, respectively, are shown in first, second, third, and fourth rows from (left column) 0118 UTC on the evening of 9 June 2010, (center column) 0459 UTC on the evening of 9 June 2010, and (right column) 0148 UTC on the evening of 10 June 2010. The black outlines mark areas of local maxima in Φ_{DP} (before and after which Φ_{DP} decreases). These maxima are either the result of local maxima in δ or enhanced resonance effects (and perhaps hydrometeor shapes and orientations) that yield $K_{DP} < 0°$ km^{-1}. [From Snyder et al. (2013)] 155

Figure 44. Polarimetric three-body scatter signatures (highlighted by black arrows in the third row) characterized by (from top to bottom) radially-decreasing Z_H', relatively high and noisy Z_{DR}', very low ρ_{hv}, and relatively weak V_R observed downstream of regions of high Z_H'. These data were collected by RaXPol on (from left to right, respectively) 23 May 2011, 18 March 2012, and 31 March 2013. 156

Figure 45. Z_H', ρ_{hv}, Z_{DR}', and V_R (from left to right, respectively) at 4°, 10°, and 18° elevation angles (top to bottom) on 17 April 203 in southwestern Oklahoma. A well-defined low-level hail signature is evident on the 4 degree scan. The area of low ρ_{hv} at 10° elevation angle is ambiguous in its origins – hail is likely present where ρ_{hv} ~0.6, but the area of $\rho_{hv} < 0.3$ beyond ~20 km range (black curve) may represent either a polarimetric three-body scatter signature or NBF. The close

proximity of the storm precluded the sampling of the BWER even at 18°, but a hint of a BWER is evident as low Z_H' ~5–8 km N of the radar. This being the case, a LoRB appears near 13–16 km range on the 18° scan, with at least two NBF-related streaks evident beyond the LoRB. Hail to 1.75" in diameter was reported with this supercell near this time. 157

Figure 46. Polarimetric tornado debris signature as seen in Z_H', Z_{DR}', V_R, and ρ_{hv} (top to bottom, respectively) from violent tornadoes in central Oklahoma on 19 May 2013 (left) and 31 May 2013 (center and right). The width of the debris cloud as measured by ρ_{hv} is ~1.5 km, ~2.2 km, and ~5 km in the left, center, and right columns, respectively. Southeast of the very large cyclonic tornado (marked by "C") in the right column (2332 UTC) is a debris signature associated with an anticyclonic tornado as well ("A"). 158

Figure 47. Polarimetric fields from the *25r10_057* simulation at (top) S and (bottom) X bands. Z_H (dBZ), Z_{DR} (dB), ρ_{hv}, and K_{DP} (deg. km^{-1}) are shown from left to right. The area of low Z_{DR} and relatively low ρ_{hv} at S band is caused by hail (see D_{mh}, lower left) with relatively high f_{wh}, which, apparently, is masking the low-level hail signature at X band. 159

Figure 48. (a) α_r, (b) f_{wh}, (c) D_{mr} (m) and (d) D_{mh} (m) valid at the same time for the same simulation as Figure 47. 160

Figure 49. (a) ρ_{hv} , (b) Z_{DR} (dB), (c) Z_H (dBZ) and (d) K_{DP} (deg. km^{-1}) at ~5400 m AGL from the *15q10* simulation valid at t = 4800 s at X band. A ρ_{hv} half-ring is evident in (a). In (b), a Z_{DR} half-ring and a part of the Z_{DR} column are apparent. 161

Figure 50. The maximum height (m) of Z_{DR} > 1 dB approximately 5000 s into the (a) *15r10*, (b) *25r10*, (c) *15str*, (d) *25str*, (e) *15q10*, (f) *25q10*, (g) *15r10_057* and (h) *25r10_057* simulations. The horizontal spatial scale is the same in all panels. The hodograph shapes tend to suppress any left-mover / anticyclonic supercell(s), with the exception of the 15str and 25str hodographs. 162

Figure 51. Max height (m) of Z_{DR} > 1 dB at (top) 7200 s and (bottom) 7920 s from the (left) *25q10*, (center) *25str*, and (right) *15r10* simulations. The horizontal scale is equal for all panels and is given as 1x10^4 m. 163

Figure 52. From the *25r10* simulation at t = 4800 s at a height of ~5600 m AGL, (a) Z_{DR} (color; dB) and W (contoured every 5 m s^{-1}), (b) temperature (color; K) and Z_{DR} (contoured starting at 0 dB every 1 dB), (c) q_r (color), D_{mr} (contoured every 0.001 m) and wind vectors, (d) D_{mh} (color; m) and Z_{DR} (contoured; dB), (e) q_h (color) and f_{wh} (contoured every 0.1), and (f) α_h (color) and Z_{DR} (contoured; dB). The red arrow in (a) points out the primary Z_{DR} column; the yellow arrow points out the pseudo- Z_{DR} half-ring. 164

Figure 53. (a) S-band Z_{DR} (dB), (b) X-band Z_{DR} (dB), (c) D_{mh} (m), (d) q_h, (e) D_{mr} (m), and (f) T (K) along a north-south cross-section through the updraft of the supercell from the *25r10* simulation at 7320 s. Black contours in all panels are w (m s^{-1}); contours are plotted every 10 m s^{-1}. 165

Figure 54. Maximum w (m s^{-1}) at ~5500 m AGL from the (a) "weak" shear and (b) "strong" shear simulations. 167

Figure 55. (a) X-band Z_{DR} (color; dB) and w (contoured every 10 m s^{-1}), (b) f_{wh} (color) and q_r (contoured over 0.001), (c) D_{mh} (color; m) and q_h (contoured every 0.002), and (d) D_{mg} (color; m) and q_g (contoured every 0.002) from the *25r10* simulation at 7360 s and heights of ~5500 m (for w) and ~5600 m (for all other variables). 168

Figure 56.The Z_{DR} = 1 dB isosurface valid 7320 s from the 25q10 simulation with the view directed towards the northeast. The black arrow point to the "primary" Z_{DR} column; the blue arrow points to the arcing Z_{DR} half-ring along the eastern edge of the updraft. The horizontal scale is in 10^4 m. 169

Figure 57. Z_{DR} (dB) at (a)–(b) S and (c)–(d) X bands from the *25q10* simulation at a height of ~5600 m. The left column [(a), (c)] is calculated by turning off the fractional water routine in the emulator, which results in all ice being treated as "dry"; the right column [(b), (d)] includes the fractional water routine described in Chapter 2 and in Dawson et al. (2013). 170

Figure 58. From the *25r10* simulation at t = 7320 s – (a) T (color; K) and Z_{DR} (contoured every 1 dB) with wind vectors plotted every 1 km, (b) D_{mh} (color; m) and f_{wh} (contoured every 0.2), and (c) q_r (color) and w (contoured every 10 m s^{-1}; the highest-valued contour is 50 m s^{-1}). The height of the w data is ~6,400 m; height of all other data is ~6,500 m. 171

Figure 59. An east-west vertical cross-section through the updraft of the *25q10* simulation at 6000 s with (a) Z_{DR} (color; dB) and w (contoured every 10 m s^{-1} with dashed contours denoting w $\leq$ 0 m s^{-1}), (b) D_{mr} (color; m) and Z_{DR} (contoured every 1 dB), (c) D_{mh} (color; m) and f_{wh} (contoured every 0.2), and (d) D_{mg} (color; m) and f_{wg} (contoured every 0.2). 172

Figure 60. Vertical cross-sections along an east-west slice of the *25q10* simulation at 6000 s with (a) z_r (color; dBZ) and temperature (countered every 10 K), (b) q_r (color) and Z_{DR} (contoured every 1 dB), (c) q_h (color) and w (contoured every 10 m s^{-1}), (d) z_h (color; dBZ) and Z_{DR} (contoured every 1 dB), (e) α_h (color) and Z_{DR} (contoured every 1 dB), and (f) ρ_{hv} (color) and Z_{DR} (contoured every 1dB). 173

Figure 61. From the *25r10_057* simulation (at t = 9000 s), east-west vertical cross-sections through the updraft showing (a) Z_H (color; dBZ) and w (contoured at 10

m s^{-1}; dotted contours represent $w \leq 0$ m s^{-1}), (b) Z_{DR} (color; dB) and w (contoured at 10 m s^{-1}; dotted contours represent $w \leq 0$ m s^{-1}), (c) q_r (color) and Z_{DR} (contoured every 1 dB with $Z_{DR} \leq 0$ dB dotted), and (d) f_{wh} (color) and D_{mh} (contoured every 0.5 cm). 174

Figure 62. The area of the Z_{DR} column and/or ring ($Z_{DR} > 1$ dB; blue line) and the area of the updraft ($w > 5$ m s^{-1}; green line) at a height of ~3800 m AGL from the *15q10* and *25q10* simulations. The number of gridpoints is used as a proxy for area. 175

Figure 63. Time series of (blue) qr33area and (green) zdr33area from the (a) *15r10* and (b) *25r10* simulations. 176

Figure 64. Scatterplots of (a) the number of gridpoints with $w > 5$ m s^{-1} at ~5,500 m vs. the number of gridpoints with $Z_{DR} > 1$ dB at ~5,600 m AGL and (b) the cross-sectional area of the rain field (defined as the number of gridpoints with $q_r > 0.001$) vs. number of gridpoints with $Z_{DR} > 1$ dB for the "weak" (red) and "strong" (blue) shear hodographs. 177

Figure 65. Scatterplots of (a) dmh33sum5mm vs. zdr33area, (b) wmax33 at ~5520 m AGL vs. zdrmaxheightqrc, and (c) wmax25 vs. zdrmaxheight for (red) "weak" shear and (blue) "strong" shear hodographs. 178

Figure 66. Correlation coefficient between the dmh3area1inch and zdrmaxheight as a function of lag time from the (a) *15q10* and (b) *25r10_057* simulations. 179

Figure 67. Pearson correlation coefficients for all simulations at all times for the set of quantities (defined in Table 5). 180

Figure 68. As in Figure 64 but for the "strong shear" simulations. 181

Figure 69. As in Figure 67 but for the "weak shear" simulations. 182

Figure 70. As in Figure 67 but for the *15r10* and *25r10* simulations. 183

Figure 71. As in Figure 67 but for the *15r10_05757* and *25r10_05757* simulations... 184

Figure 72. As in Figure 67 but for the *15q10* and *25q10* simulations. 185

Figure 73. As in Figure 64 but for the *15str* and *25str* simulations. 186

Figure 74. (a) q_r, (b) q_h, (c) α_h, (d) D_{mh} (m) and f_{wh} (contoured every 0.2), and K_{DP} (deg. km^{-1}) from (e) S and (f) X bands from 6000 s in the *25q10* simulation at ~120 m AGL. 187

Figure 75. East-west vertical cross-sections of (a) Z_{DR} (color; dB) and w (contoured every 10 m s^{-1} with the dotted curves representing $w \leq 0$ m s^{-1}) and (b) K_{DP} (color; deg. km^{-1}) and q_r (contoured every 0.001) valid at 6000 s from the *25r10* simulation across the updraft. The highest occurrence of (c) $Z_{DR} > 1$ dB and (d) $K_{DP} > 1°$ km^{-1} are plotted to show the areal extent of the Z_{DR} and K_{DP} column. 188

Figure 76. A ρ_{hv} half ring in the *25r10* simulation at t = 4800 s and ~5600 m AGL. (a) ρ_{hv} (color) and D_{mh} (contoured every 0.005 m), (b) T (color; K) and ρ_{hv}, (c) q_r (color) and w (contoured every 10 m s^{-1}), (d) f_{wh} (color) and q_h (contoured every 0.002), (e) f_{wg} (color) and q_g (contoured every 0.002), and (f) Z_H (color; dBZ) and Z_{DR} (contoured every 1 dB). 189

Figure 77. Isosurfaces of $\rho_{hv} = 0.8$ (red) and $w = 30$ m s^{-1} (green) valid 7320 s from the *25q10* simulation looking (a) horizontally to the east and (b) downward from the top of the domain. The gridlines in (a) mark the height AGL every 4 km; the gridlines in (b) represent horizontal extent and are marked every 20 km. 190

Figure 78. (a) w (m s^{-1}) and ρ_{hv} at (b) S, (c) C, and (d) X bands from the *25q10* simulation at t = 4220 s and 5600 m AGL. The ρ_{hv} half ring is more prominent and is larger at increasing radar frequency. In all cases, the half ring is located along the eastern edge of the convective updraft. 191

Figure 79. A north-south vertical cross-section of (a) ρ_{hv} (color) at S band and w (contoured every 10 m s^{-1}), (b) ρ_{hv} (color) at X band and Z_{DR} (contoured every 2 dB), (c) ρ_{hv} (color) at S band and D_{mh} (m), and (d) ρ_{hv} (color) at X band with q_r (contoured). Data are from the *25r10* simulation. 192

Figure 80. Time series of the number of gridpoints of $\rho_{hv} < 0.8$ at X band from the (a) "weak" shear and (b) "strong" shear simulations. 193

Figure 81. Time series of the number of gridpoints with $D_{mh} > 0.5$ cm (green line) and the number of gridpoints with low ρ_{hv} (blue line) at (a) S band and (b) X band. All data taken from the vertical grid-level at ~5600 m AGL from the *15r10* simulation. 194

Figure 82. Correlation coefficient between *wmax33* and *rhv33area* as a function of lag time for the (a) "weak" and (b) "strong" shear simulations. 195

Figure 83. (a, c) D_{mr} (m) and (b, d) S-band Z_{DR} (dB) from the *25q10* (a,b) and *15r10* (c,d) simulations valid at 120 m AGL. 196

Figure 84. S-band (a) Z_H (dBZ) and (b) Z_{DR} (dB) at a height of 37.5 m AGL valid 4800 s in the *15q10* simulation. A feature that looks similar to an LRR is evident in (a), but the LRR-like feature is characterized by a local maximum in Z_{DR}. In this case, large hail is occurring on either side of the LRR-like feature, which does

not seem consistent with observations of the LRR presented in this paper. Every fifth wind vector is plotted (i.e., wind vectors are plotted every 1 km). 197

Figure 85. (a) w (m s^{-1}), (b) Z_H (dBZ), (c) q_r, (d) q_h, (e) D_{mh}, and (f) f_{wh} from the *25q10* simulation at 7320 s and ~4600 m AGL. In all panels, ρ_{hv} is contoured every 0.1 decreasing from 0.9. The black line in (a) marks the approximate location of the vertical cross-section shown in Figure 86. 198

Figure 86. An east-west vertical cross-section along the black line in Figure 85a showing (a) Z_H (dBZ), (b) Z_{DR} (dB), (c) D_{mh} (m), (d) q_hx10^3 (e) q_rx10^3, and (f) q_gx10^3 from the *25q10* simulation at 7320 s. In all panels, ρ_{hv} is contoured every 0.1. 199

Abstract

Polarimetric weather radars, with the additional information collected, allow one to infer scatterer and precipitation properties considerably more easily than single-polarization radars. Given the relationship between the thermodynamic, mass, and kinematic fields and the resulting structure of the microphysical quantities within convective storms, examining the polarimetric characteristics of hydrometeors and the polarimetric structure of supercells provides potentially valuable information about processes and storm-relevant variables that are currently unobservable by single-polarization radar. In this study, two previously-undocumented polarimetric signatures – the low-reflectivity ribbon and the area of anomalously low co-polar cross-correlation coefficient to the left of the bounded weak echo region – observed by two mobile, X-band, polarimetric radars are examined. Since there are appreciable differences in scattering properties of some hydrometeors at different radar frequencies and most of the past work on polarimetric signatures in supercells has used S band radar data, examples of other signatures observed by X-band radars are also presented.

Given the recent development of advanced multimoment microphysics schemes and polarimetric radar emulators, examining the polarimetric structure of simulated supercells can help elucidate the microphysical and kinematic structure of simulated polarimetric signatures. To do so, a series of idealized high-resolution simulations are performed using eight different vertical shear profiles in an attempt to investigate the relationships between observed signatures, the structure of microphysical and kinematic fields within the simulated supercells, and potential sensitivities to vertical wind shear

variations. Many of the previously-observed signatures are reproduced in the simulations; results from these simulations are reported.

Chapter 1: Introduction

Weather radars have been used for decades as a remote sensing tool to collect data on across much larger spatial scales than is typically available from in-situ observation platforms. Indeed, radars have been a valuable tool for examining the structure and dynamics of supercells (e.g. Browning and Donaldson 1963; Browning 1964; Lemon and Doswell 1979; Marwitz 1972; Brandes 1978, 1984, 1993), and many of the early studies using radar data primarily focused on power-based (e.g. radar reflectivity factor) and radial velocity measurements. Radars have been used at fixed-land locations, on airborne platforms (e.g. Wakimoto et al. 1996; Bluestein and Gaddy 2001), and on mobile platforms (e.g. Bluestein and Unruh 1989; Bluestein et al. 1995; Wurman et al. 1997; Bluestein and Pazmany 2000; Bluestein et al. 2010; Pazmany et al. 2013). More recently, there has been a significant increase in the number of polarimetric radars; there are now more polarimetric mobile radars (Bluestein et al. 2007a,b; Burgess et al. 2010; Pazmany et al. 2013; Biggerstaff, personal communication) and fixed-site radars (Hubbert et al. 1998; Doviak et al. 2000; Petersen et al. 2005; McLaughlin et al. 2009; Palmer et al. 2011) than ever before. In fact, the nationwide S-band, WSR-88D radar network in the United States is currently near the end of a network-wide upgrade to dual-polarization (Istok et al. 2009).

Polarimetric radars provide many advantages over those radars that transmit and receive only along one polarization plane, and they have been used for many purposes, from detecting hail (e.g. Tuttle et al. 1989; Aydin et al. 1990; Herzegh and Jameson 1992) to locating probable tornado debris (e.g. Ryzhkov et al. 2005b; Bluestein et al. 2007a). The ability to obtain significantly greater amounts of data with polarimetric

radars allows for the retrieval or inference of microphysical structures and processes occurring within deep moist convection.

Since 2002, University of Oklahoma personnel have used polarimetric X-band mobile Doppler weather radars to collect data in close proximity to supercells throughout the Plains of the central United States. These efforts were extended heavily during the second Verification of the Origins of Rotation in Tornadoes 2 (VORTEX 2; Wurman et al. 2012) field experiment during May and June of 2009 and 2010. In addition, since 2007, efforts have focused primarily on collecting volumetric polarimetric data.

Numerical modeling has been an effective tool for simulating supercells and examining the influence of the environment on the evolution of convection. Appreciable knowledge of supercell dynamics was gained by the results of such early numerical simulations as Klemp and Wilhelmson (1978), Rotunno (1981), Klemp et al. (1981), Weisman and Klemp (1982), and Klemp and Rotunno (1983). As computing resources have expanded, higher-resolution simulations of convection and tornadoes have continued in conjunction with the development of more sophisticated modeling schemes (e.g. Wicker and Wilhelmson 1995). Adlerman and Droegemeier (2002, 2005) examined the structure of simulate supercells through a relatively wide parameter, but those works focused on quantities and processes other than emulated polarimetric radar parameters. Similarly, Van Den Broeke et al. (2010) studied the effects of different wind profiles on the evolution and structure of simulated mesocyclones and rear-flank downdrafts (RFDs) primarily from the perspective of microphysical quantities, but

relating the examined variables to polarimetric quantities was outside the scope of their work.

The primary goal of this project is to expand the current breadth of the understanding of polarimetric signatures within supercells by examining such signatures using high-resolution data from a mobile X-band radar and investigating the influence of the vertical wind shear profile on the structure of polarimetric signatures within simulated supercells. This research project has two facets. The first facet pertains to the use and analysis of the polarimetric supercell data thus far collected by the two X-band mobile radars. Much of the current body of research pertaining to polarimetric signatures within supercells has been conducted using data collected by S-band and, perhaps to a more limited extent, C-band polarimetric radars; comparatively little research has been conducted using X-band data (Snyder et al. 2010a,b; Schwarz 2011).

The scattering properties of some hydrometeors have a significant dependence on radar frequency, at least for hydrometeors large enough to fall beyond the Rayleigh regime (Figure 1; Snyder et al. 2010b). Some common polarimetric quantities may be similar at S band and X band, but there are also some very significant differences in some quantities for some hydrometeors. For example, the radar reflectivity factor of water-coated hailstones is significantly different at the different radar frequencies (Figure 1). These differences are very important to recognize for those who may not be familiar with X-band (or C-band) radar data. It is reasonable to suggest that, as a result of the differences in polarimetric quantities for some hydrometeors at different radar frequencies, the polarimetric signatures that have been identified in supercells using S-band radar data (e.g. Kumjian and Ryzhkov 2008a; Romine et al. 2008) may be

presented differently at X band. In addition, there are added complexities that must be accounted for or at least kept in mind when one examines C and X band data, including the much greater attenuation that occurs at the higher frequencies and the possible effects of large gradients in backscatter differential phase (Figure 2) that may complicate the calculation of specific differential phase and attenuation estimation.

The observational radar data used in this project were collected from mobile radars. During many radar deployments, the general strategy was to position the radar very close to the storm or "feature" that was targeted. In doing so, we have been able to collect radar data with significantly greater spatial resolution than most fixed-site radars. With the greater spatial resolution comes the opportunity to see small-scale features that would not be present in coarser-resolution data. Loney et al. (2002) examined data from both in situ aircraft as well as a polarimetric, fixed-site radar at considerable range from a supercell; they conclude that spatial resolutions of no more than a few hundred meters are needed "to resolve significant bulk hydrometeor properties in supercell storms". A new mobile radar also adds the ability to collect rapid-scan data, significantly increasing the temporal resolution capabilities as well. These higher-resolution data can be used to examine the temporal evolution of polarimetric signatures at X band. Van Den Broeke et al. (2008) studied the temporal evolution of the polarimetric fields of several observed supercells using S band data, but little has been studied at X band. This project aims to describe polarimetric signatures within supercells as seen from two mobile, X-band polarimetric radars in resolution typically considerably greater than past studies.

The second facet of the project involves the polarimetric representation of simulated supercells. The continued development of multimoment bulk microphysical schemes (e.g. Milbrandt and Yau 2005a,b) available in numerical models presents a renewed opportunity to examine the microphysical characteristics of simulated thunderstorms in a more accurate manner than has been previously capable. In addition, the recent creation of a polarimetric emulator (Jung et al. 2010) for the Advanced Regional Prediction System (ARPS; Xue et al. 2000, 2001, 2003) allows for the examination of the polarimetric structures of simulated storms. Using a series of idealized simulations, it is possible to investigate how the polarimetric structures associated with thunderstorms (in particular, supercells) change in different environments. It is important to stress from the outset that all current bulk microphysics scheme possess shortcomings that will result in inaccuracies in the model solutions.

The purpose of this undertaking is not to closely scrutinize detailed structures within the simulation supercells. Rather, fully acknowledging the shortcomings that accompany bulk microphysical schemes, the motivation of this study is to extract meaningful information from numerical simulations to provide insight into the microphysical and dynamical processes of simulated polarimetric structures. Jung et al. (2010) demonstrated that high-resolution simulations with multimoment microphysics can indeed capture some well-documented polarimetric signatures. Since operational meteorologists typically use information from weather radars in their critical weather duties, it would be quite beneficial to be able to diagnose (and, if possible, prognosticate) storm structure based upon observed polarimetric data.

Some general background information pertinent to polarimetric radar observations immediately follows this section. Thereafter, a brief overview of numerical modeling (as it relates to supercell simulation) and microphysics schemes is provided in Chapter 3, after which the primary goals of this research are presented. The research tools used for project – some observational (in the form of two mobile radars) and some numerical/computational in nature – are then given in Chapter 4. Chapter 5 examines the observations collected by the mobile radars, focusing primarily on two "new" signatures [the low reflectivity ribbon and the area of low ρ_{hv} on the left (relative to storm motion) side of the bounded weak echo region]. Results from the numerical simulations and more detailed analyses of the results from the polarimetric emulator are discussed in Chapter 6 before a few conclusions are reiterated in Chapter 7.

Chapter 2: Polarimetric Radar Observations

An overview of variables available from polarimetric radars and a brief literature review of polarimetric signatures observed in supercells are presented in this chapter. Portions of this text also appear in Snyder et al. (2013).

a. Radar quantities

Arguably, the most commonly-used radar quantity used by meteorologists is the power-based radar reflectivity factor. The equivalent radar reflectivity factor at horizontal (H) and vertical (V) polarizations can be expressed as

$$Z_{h,v}=\frac{\lambda^4}{\pi^5|K_w|^2}\int_0^\infty \sigma(D)N(D)dD = \frac{4\,\lambda^4}{\pi^4|K_w|^2}\int_0^\infty \left|f_{hh,vv}^{(b)}(D)\right|^2 N(D)dD \qquad (2.1)$$

where $Z_{h,v}$ is calculated in units of $mm^6\ m^{-3}$, λ is the wavelength, $K_w = \frac{m^2-1}{m^2+2}$ is a dielectric factor of water (and m is the complex index of refraction), $\sigma(D)$ is the radar backscattering cross-section, *N(D)* is the drop-size (or particle-size) distribution (DSD), $f_{hh,vv}^{(b)}(D)$ is the backward scattering amplitudes at two orthogonal polarizations [typically horizontal (H) and vertical (V)], and N(D) is the drop-size distribution (DSD). For Rayleigh scatterers, generally approximated in rain as those having a diameter $D < \lambda/16$ where λ is the radar wavelength, $Z_{h,v}$ is proportional to D^6.

Additional power-based products are often produced by radar systems that transmit and receive along two orthogonal polarization planes (e.g., H and V). The utility of a ratio-based quantity, differential reflectivity, was first noted by Seliga and Bringi (1976). Differential reflectivity is defined as

$$Z_{DR} = 10\log\left(\frac{Z_h}{Z_v}\right) = Z_H - Z_V\ (dB) \qquad (2.2)$$

where Z_h and Z_v are given in linear units and Z_H and Z_V are given in logarithmic units.

Since raindrops trend from being nearly spherical at small diameters to being oblate (i.e. an ellipsoid with the major axis aligned in the horizontal and the minor axis aligned in the vertical) at larger diameters (e.g. Pruppacher and Beard 1970; Green 1975), Z_H exceeds Z_V in rain, resulting in $Z_{DR} > 0$ dB. For commonly-used drop size-shape relations (e.g. Brandes et al. 2002), oblateness increases with increasing raindrop diameters; Z_{DR} is larger for larger drop diameters and is always greater than 0 dB; the value of Z_{DR} is related to drop axis ratio (e.g., Jameson 1983). In fact, in most meteorological situations, Z_{DR} will seldom be negative. In hail, Z_{DR} may be less than 0 dB, primarily for two reasons – the orientation of the hail may be prolate or the resonance effects associated with non-Rayleigh scattering may result in greater scattering in V than H. In other situations, a torus of water may form around a water-coated hailstone and yield Z_{DR} significantly greater than 0 dB (Rasmussen et al. 1984; Rasmussen and Heymsfield 1987).

The total differential phase (Φ_{DP}) measured by a polarimetric radar is the sum of two components – backscatter differential phase (δ) and propagation differential phase (ϕ_{DP}):

$$\Phi_{DP} = arg\left\{< n f_{vv}^{(b)} f_{hh}^{(b)*} >\right\} + 2\int_0^r K_{DP}(r')dr' = \delta + \phi_{DP} \qquad (2.3)$$

where n is a proxy for the drop-size distribution (DSD), $f_{vv}^{(b)}$ and $f_{hh}^{(b)}$ are the amplitudes of the copolar (H and V) terms of the backscattering matrix, and K_{DP} is the specific (propagation) differential phase. In many situations, particularly at lower radar

frequencies (e.g. S band), the effects of backscatter differential phase tend to be ignored. At higher frequencies, however, such as at X band, more appreciable δ may be present, indicative of non-Rayleigh scattering. Whereas δ can vary significantly over narrow ranges of particle sizes (Balakrishnan and Zrnic 1990; Figure 2), ϕ_{DP} is a range cumulative effect that is determined by the size and number concentration of the hydrometeors between the radar and the target range.

In many meteorological situations, it is often more desirable to know how ϕ_{DP} changes with range than it is to know the exact values of ϕ_{DP}. Specific propagation differential phase, equal to ½ the range derivative of ϕ_{DP}, can be calculated from the scattering matrix as

$$K_{DP} = \frac{180\,\lambda}{\pi} \int_0^\infty Re\left[f_{hh}^{(f)}(D) - f_{vv}^{(f)}(D)\right] N(D) dD \qquad (2.4)$$

where $f_{hh}^{(f)}(D)$ ($f_{vv}^{(f)}(D)$) is the horizontal (vertical) forward scattering amplitude, and the term in the brackets following Re represents the real part of the difference.

In general, K_{DP} increases with increasing hydrometeor oblateness and increasing dielectric constant. This is because, in a simple sense, the horizontally-polarized waves "intercept" more mass than the vertically-polarized waves as a result of the oblate nature of raindrops, which imposes a slightly larger phase shift on the horizontal plane than the vertical plane. Unlike variables based on the amplitude of the received echo, the phase-based K_{DP} measurement is independent of receiver and transmitter power calibration, and it is unaffected by attenuation and partial beam blockage. It is for this reason that K_{DP}-based precipitation estimates have been shown to perform better, in some cases, than Z_H-based estimates (e.g. Ryzhkov and Zrnic 1995, 1996; Zrnic and

Ryzhkov 1995; Brandes et al. 2001). K_{DP} is less sensitive than Z_H and Z_V to variations in the (DSD), though it does have a dependence on number concentration. The use of K_{DP} is possible as long as the signal-to-noise ratio (SNR) is high enough to provide an accurate phase estimate. K_{DP} may truly be negative in the presence of large hail or in an environment in which ice crystals are preferentially-aligned in the presence of a strong electric field (Bringi and Chandrasekar 2001).

The magnitude of the co-polar cross-correlation coefficient at lag zero, $|\rho_{hv}(0)|$, was first presented by Balakrishnan and Zrnic (1990) and is defined as

$$|\rho_{hv}(0)| = \frac{< n f_{hh}^{(b)} f_{vv}^{(b)*} >}{< n \left|f_{hh}^{(b)}\right|^2 >^{1/2} < n \left|f_{vv}^{(b)}\right|^2 >^{1/2}} \tag{2.5}$$

where the angle brackets represent an ensemble or time average, and * represents the complex conjugate operator. In general, $|\rho_{hv}(0)|$ (or, for simplicity, ρ_{hv}) is a measure of the variability in the horizontal and vertical backscatter cross-sections of scatterers within a radar volume. Alternatively, the cross-correlation coefficient can be written in terms of δ as

$$\rho_{hv} = |\rho_{hv}| e^{j\delta} \tag{2.6}$$

Greater orientation or hydrometeor type diversity tends to reduce ρ_{hv}; the value of ρ_{hv} inside a radar volume that encompasses largely all rain (or all snow) tends to be very near 1.0. Reductions in ρ_{HV} can occur as a result of resonance effects associated with non-Rayleigh scatterers, something that is more likely to occur at higher frequencies and with larger hydrometeors. The parameter ρ_{HV} is often an extremely good discriminator between meteorological and non-meteorological scatterers (e.g. bugs, dirt, tornado debris, etc.).

With the additional information provided by polarimetric radars, it is possible to differentiate objectively those areas within an echo that have polarimetric characteristics consistent with different types of scatterers. Zrnic and Ryzhkov (1999) and Straka et al. (2000) provide extensive discussions on the polarimetric characteristics of different hydrometeors, though the discussions are focused primarily on S-band radar systems. Various hydrometeor classification schemes have been developed using decision trees (e.g. Straka et al. 2000; Holler et al. 1994) and fuzzy logic methods at S band (e.g. Vivekanandan et al. 1999; Liu et al. 2000; Zrnic et al. 2001; Ryzhkov et al. 2005c; Park et al. 2009), C band (e.g. Keenan 2003; Lim et al. 2005; Marzano et al. 2006), and, more recently, X band (Iwanami et al. 2007; Dolan and Rutledge 2009; Snyder et al. 2010b). Polarimetric data have also been used in quantitative precipitation estimation (e.g. Scarchilli et al. 1993; Ryzhkov and Zrnic, 1995, 1996: Matrosov et al. 1999, 2002; Le Bouar et al. 2002; Ryzhkov et al. 2005a; Giangrande and Ryzhkov 2008) and in DSD retrievals (e.g. Zhang et al. 2001; Gorgucci et al. 2002; Bringi et al. 2002; Brandes et al. 2004a,b; Vivekanandan et al. 2004; Cao et al. 2008).

b. Considerations for Mobile X-Band Radars

One of the most significant benefits of operating a mobile radar at X band is that the antenna can be smaller than that which would be required for the same half-power beamwidth for a radar operating at a lower frequency. Unfortunately, there are several points that should be remembered or taken into account when using X-band data collected by a mobile radar. First, X-band radars have a significant disadvantage relative to radars that operate at lower frequency: much more significant attenuation

(Figure 2). To highlight this, Z_H' data from an S-band radar and a mobile X-band radar are shown in Figure 3 – notice the severe attenuation that occurs in the X band data. Second, as a result of resonance effects, the scattering properties of hydrometeors, particularly hail, at X band can differ significantly from those at S band (Figure 1). Considering the apparent rise in popularity of X-band radar systems, it is important to make sure users of such data are aware of the differences. Third, since mobile radars are often positioned within very close proximity to thunderstorms so as to maximize spatial resolution, there are times when very high elevation angles are used. Whereas raindrops typically have a zero mean canting angle relative to horizontal, data collected at high elevation angles (e.g. > 40°) will appear as though the raindrops possess an appreciable canting angle. As such, a geometric adjustment to account for the apparent canting angle (caused by the fact that the H channel is no longer parallel to the local horizontal) should be made, lest the magnitude of Z_{DR} and K_{DP} be smaller than expected.

The results of scattering simulations indicate that attenuation through rain at X band is much greater than that which occurs at C and S bands (Figure 2). Any quantitative use of the attenuated fields (e.g. hydrometeor classification, quantitative precipitation estimation, and drop-size distribution retrieval) requires that attenuation be estimated so that the "true" or unattenuated fields can be estimated.

As electromagnetic energy propagates through the atmosphere, attenuation typically occurs through three types of scatterers – aerosols and atmospheric gasses, cloud water, and hydrometeors. Van Vleck (1974a,b) calculated losses from atmospheric gasses and found A_H and A_{DP} for X band radars to be approximately 0.0095

and 0.003 dB km^{-1}, respectively. As discussed in a later section, many datasets collected by the mobile radars used in this study focus on storms < 45 km from the radar, although < 30 km is often desired. Through these distances, however, attenuation by gasses is often orders of magnitude less than attenuation by hydrometers.

Although water is an attenuating medium, the amount of attenuation that occurs in clouds tends to be small, at least in the data typically collected by X-band mobile radars. From Gunn and East (1954), X-band attenuation by cloud water is approximately 0.02 dB km^{-1} g^{-1} m^3. If the desired target is a significant distance from the radar, and the radar beam propagates through a large area of high cloud water content, it is possible that noticeable attenuation may occur, even if Z_H is very small (which it often is for clouds) at X band.

The measured radar reflectivity factor at horizontal and vertical polarization (Z_H' and Z_V') is equivalent to the following:

$$Z'_{H,V}(r) = Z_{H,V}(r) - 2\int_0^r A_{H,V}(r')dr' = Z_{H,V}(r) - PIA_{H,V} \qquad (2.7)$$

where $Z_{H,V}$ is the intrinsic (i.e. unattenuated) radar reflectivity factor at H and V polarization (in units of dB), $A_{H,V}$ is the specific attenuation at H or V polarization (in units of dB km^{-1}), r is range, r' is the dummy variable of integration, and PIA_H, PIA_V, and PIA_{DP} are two-way path integrated horizontal, vertical, and differential attenuation, respectively. The measured differential reflectivity $Z'_{DR}(r)$ is a combination of the intrinsic given as differential reflectivity ($Z_{DR}(r)$) and losses through differential attenuation:

$$Z'_{DR}(r) = Z_{DR}(r) - 2\int_0^r A_{DR}(s)ds = Z_{DR}(r) - PIA_{DP} \quad (2.8)$$

where $Z_{DR}(r)$ is the intrinsic differential reflectivity in dB and A_{DP} is the specific differential attenuation (in dB km^{-1})

$$A_{DP} = A_H - A_V \quad (2.9)$$

Solving (2.7) and (2.8) for Z_H and Z_{DR} is possible if accurate estimates of attenuation and differential attenuation can be made.

Attenuation within single-polarization data can be estimated using the differential equations in Hitschfeld and Bordan (1954), yielding a formula for A_H that is calculated in an iterative sense from the start of a radial to the end of a radial:

$$A_H = aZ_H{}^b \quad (2.10)$$

where a and b are parameters determined a priori. Park et al. (2005a) calculated a and b to be 1.370x10^{-4} and 0.779, respectively.

The estimation of attenuation is limited when using single-polarization radar data since the use of Z_H to estimate A_H tends to be unstable. Being an amplitude-based measurement, Z_H, and estimates of A_H based upon Z_H, are sensitive to, among other things, errors in system calibration and partial beam blockage. Bringi et al. (1990) found that attenuation estimates based upon ϕ_{DP} are not only more stable than those that use Z_H alone, but they also are immune to calibration errors, noise, and partial beam blockage. The parameterization given in Bringi et al. (1990) estimates attenuation as

$$A_H = \alpha_H K_{DP}{}^{\beta_H} \quad (2.11)$$

$$A_{DP} = \alpha_{DP} K_{DP}{}^{\beta_{DP}} \quad (2.12)$$

where α_H, α_{DP}, β_H, and β_{DP} are the predetermined constants. The exponents β_H and β_{DP} are typically assumed to be near unity [that is, (2.11) and (2.12) are approximately linear], supported by observations at most weather radar frequencies (Bringi et al. 1990; Jameson 1992). Using (2.11) and (2.12) and setting β_H and β_{DP} to unity, A_{DP} can be calculated from A_H as

$$A_{DP} = \frac{\alpha_{DP}}{\alpha_H} A_H = \gamma A_H \tag{2.13}$$

Following Bringi et al. (1990), others have proposed different methods of estimating attenuation using ϕ_{DP} data, including a linear regression method (e.g. Ryzhkov and Zrnic 1995; Carey et al. 2000), the ZPHI rain-profiling algorithm (Testud et al. 2000), and the "self-consistent with constraints" method (Bringi et al. 2001); all of these assume, to varying degrees, that there is a linear relationship between K_{DP} and A_H (and A_{DP}), and they are all primarily focused on attenuation caused by rain. Since hail can be thought of as being statistically isotropic as a result of tumbling (Knight and Knight 1970), the phase lag that accrues along the H and V planes can be very small; K_{DP} tends to be near 0° km^{-1} in hail. Consequently, the constants chosen for (2.11) and (2.12) are likely to be significantly different in hail than in rain. Attempts to account for the effects of attenuation from hail have only recently appeared (e.g. Ryzhkov et al. 2009; Borowska et al. 2011), and the initial results indicate that attenuation through hail, or wet hail at least, may be appreciable.

Further reviews of ϕ_{DP}-based attenuation correction techniques are provided in Park et al. (2005a,b), and Snyder et al. (2010b) examines several techniques using data from a mobile, X-band polarimetric radar. The reader should understand that references to "attenuation correction" herein actually refer to attenuation estimation, since the

"true" state of the atmosphere would need to be known to actually correct for attenuation with complete accuracy given the assumptions and simplifications used in attenuation estimation methods.

Although the effects of attenuation can be estimated, it is important to point out that once the signal is attenuated to the noise floor of the radar system (or at least below some signal to noise ratio), no amount of attenuation correction can recover the signal. In other words, while attenuation correction can recover Z_H and Z_{DR} in some areas, data voids caused by signal extinction will remain. In the case of mobile radar data examined for this project, extinction has been noted over as short as an 8 km two-way path length through heavy precipitation.

c. A brief description of commonly-observed polarimetric signatures

Numerous polarimetric signatures have been identified in radar data of supercells (e.g. Conway and Zrnic 1993). Kumjian and Ryzhkov (2008, hereafter KR08) and Romine et al. (2008, hereafter R08) provide two conceptual models of some often-seen signatures within supercells (Figure 4 and Figure 5). A brief overview of several commonly-observed polarimetric signatures, generally separated by those that occur aloft and those that occur near the surface, is presented in this section.

Analyses of polarimetric radar data have indicated the presence of columns of relatively high Z_{DR} above the "ambient" freezing level in thunderstorms (e.g. Hall et al. 1984; Tuttle et al. 1989; Meischner et al. 1991; Conway and Zrnic 1993; Brandes et al. 1995; Zrnic and Ryzhkov 1999; Loney et al. 2002). The part of a thunderstorm's updraft between the level of free convection and the equilibrium level possesses

positive thermal buoyancy, by definition, and is characterized by a warm temperature perturbation relative to the surrounding environment. As a result, assuming the updraft extends through the environmental freezing level, the local freezing level will be perturbed upward by the updraft (and, as a result of evaporational cooling, perturbed downward by the downdraft). The warm updraft carries liquid water drops to an altitude above that of the environmental freezing level.

Above the perturbed freezing level, there can exist supercooled water drops that provide a source of non-negligible Z_{DR}. Enhanced Z_{DR} was found by Holler et al (1994) to be the result of melted graupel brought back above the freezing level by the updraft. In a dual-Doppler analysis of a Colorado hailstorm, and using trajectory and polarimetric analyses, Conway and Zrnic (1993) noted that the Z_{DR} column was located just west of the updraft and consisted of raindrops and wet hydrometeors. In addition, in the presence of a convective updraft, the smaller drops (which have lower terminal fall speeds) tend to be advected upward much more quickly than the larger drops; the effect of size sorting in an updraft preferentially leaves larger rain drops lower in the updraft as the smaller drops advect more quickly to higher altitudes. Z_{DR} is often largest for large rain drops and near 0 dB for randomly oriented scatterers (e.g. tumbling hail) and, typically, ice and snow. As a result, the region of $Z_{DR} > 0$ dB often extends to a maximum height in an updraft, resulting in what is termed the Z_{DR} tower or column. In situ observations support the notion that the Z_{DR} tower is nearly coincident with the updraft (e.g. Brandes et al. 1995; Bringi et al. 1991).

Similar to the Z_{DR} tower, positive values of K_{DP} have also been observed to extend to a greater height in the relatively warm updraft compared to surrounding areas

(e.g. Hubbert et al. 1998; Zrnic and Ryzhkov 1999; Loney et al. 2002; KR08; R08). The K_{DP} column is a region of locally high K_{DP} that extends well above the ambient freezing level. However, Loney et al. (2002) observed that the K_{DP} and Z_{DR} towers were not co-located in observations of a supercell in Oklahoma, a dislocation noted by Zrnic and Ryzhkov (1999) as well. However, Zrnic et al. (2001) did not observe a misalignment in observations of non-supercell storms. As suggested by KR08, it is possible that environmental vertical shear affects the relative locations of the towers. In cases in which there is an offset, the K_{DP} column is often located on the left (relative to storm motion) flank of the updraft to the west and northwest of the Z_{DR} tower, and it is often, though not always, associated with the maximum in Z_H. In the in situ observations examined by Loney et al. (2002), the highest K_{DP} was located east of the peak in Z_H along the Z_H gradient.

Since K_{DP} is sensitive to the presence of liquid drops and rather insensitive to hail (which tends to be statistically spherical as a result of tumbling), the K_{DP} tower may tend to bias towards areas with maximum liquid water content. In Loney et al. (2002) and Schlatter (2003), the observed K_{DP} tower was composed primarily of a large number of mixed-phase hydrometeors. Hubbert el al. (1998) suggested that the significant liquid water content that comprises the K_{DP} tower may be the result of shed liquid from hail falling at the periphery of the updraft. In addition, the upward advection of rain in the updraft brings these scatterers to heights up to and above the upward-perturbed freezing level. Scatterers located outside the updraft but above the ambient freezing level are likely to be of the frozen variety, which tend to be characterized by $K_{DP} \sim 0°$ km^{-1}.

Observed by polarimetric radars are circular or semi-circular structures in the Z_{DR} and ρ_{hv} data near the freezing level. The features, referred to as Z_{DR} and ρ_{hv} rings by KR08, may be full rings encircling an updraft or only partial rings. In the case of the latter, the Z_{DR} rings are always positioned on the inflow side of the updraft (KR08).

The appearance of the ρ_{hv} ring is quite similar to the structure of ρ_{hv} near the freezing level. Zrnic et al. (1993) observed that there were consistent signals in the radar variables near the freezing level in stratiform precipitation. For example, as a result of the mixture of liquid and ice hydrometeors near the freezing level, ρ_{hv} tends to be markedly reduced and Z_H tends to be markedly enhanced (the so-called bright-band; Zrnic and Ryzhkov 1999; Brandes and Ikeda 2004; Giangrande et al. 2008). A similar reduction in ρ_{hv} is sometimes seen around the presumed convective updraft. It is speculated (e.g. KR08) that the ρ_{hv} ring marks an area where significant mixed phase hydrometeors exist, perhaps the result of frozen particles outside the updraft falling into the relatively warm updraft and partially melting. The melting of previously-frozen hydrometeors can also explain the observed local maxima in Z_{DR} that has also been noted to occur in a similar ring-like structure, although the Z_{DR} ring is not always collocated with the ρ_{hv} ring (KR08).

At lower elevations within supercells and thunderstorms, other distinctive signatures have been identified. Since hail tends to fall in random orientations as a result of tumbling, areas of a storm that contain primarily hail tend to be characterized by relatively low Z_{DR} and perhaps reduced ρ_{hv}. Since hail is often large enough to fall outside the Rayleigh scattering regime, resonance effects lead to frequency sensitivities in Z_H for hail (Figure 1). Where a given distribution of large hail may result in 70 dBZ

at S band, the same distribution may only yield 50 dBZ at X band. As such, although hail tends to be observed in the echo core left (relative to storm motion) and downshear of the updraft (e.g. Conway and Zrnic 1993), the reflection of the forward-flank hail signature (KR08) in the Z_H field likely depends upon radar frequency. In addition, melting hailstones may shed drops that still result in a volume-mean large Z_{DR}. Low ρ_{hv} and Z_{DR} have also been observed along the reflectivity gradient in the rear part of the forward-flank downdraft, and KR08 point out that this is likely the result of the advection of non-meteorological scatterers (e.g. bugs and dust) by strong low-level inflow winds.

A narrow band of high Z_{DR} has been observed along the reflectivity gradient on the right (or inflow) side of the forward-flank downdraft in supercells (e.g. Holler et al. 1994; KR08; Snyder et al. 2010b). This feature is often only 1–2 km in depth, and Z_{DR} can exceed 5 dB along this narrow, shallow band. Z_{DR} of this magnitude implies very large axis ratios and large, oblate raindrops. KR08 and Kumjian and Ryzhkov (2009) propose a mechanism to explain this feature – size sorting. In an environment of large storm-relative helicity (Davies-Jones et al. 1990), the strong low-level vertical wind shear allows only the heaviest and largest drops to fall to the ground, as the smaller and light drops are advected away from this region. The result of this size-sorting process is a narrow zone consisting primarily of large raindrops. Although Z_H scales as D^6 when the Rayleigh approximation is accurate, the low number concentration of large drops may limit Z_H.

In high-resolution X-band observations, a δ arc of sorts may also be evident. As a result of non-Rayleigh scattering (which is much more prevalent at X band than at S

band), backscatter differential phase may be non-negligible (Figure 2), and large heterogeneities in observed DSDs (such as along the Z_{DR} arc) can yield significant gradients in δ that are detected in the measured differential phase data. Since these often occur at the edge of the echo when associated with the Z_{DR} arc, K_{DP} may erroneously be biased negative immediately beyond the maximum δ.

Using data collected by an S-band polarimetric radar during a tornado outbreak on 3 May 1999 in Oklahoma, Ryzhkov et al. (2002) noted an area of very low ρ_{hv} and Z_{DR} ~ 0 dB embedded in the hook echo very near the location of an ongoing tornado. This case, along with data from two other tornadic supercells collected in May 2003, is studied in Ryzhkov et al. (2005b). In all three of these cases, the location of a strong tornado was characterized by $\rho_{hv} < 0.5$, Z_{DR} near 0 dB, and a local maximum in Z_H. Similar characteristics have been observed with strong tornadoes by C band radars (KR08; Palmer et al. 2011; Schultz et al. 2012) and X band radars (e.g. Bluestein et al. 2007a,b, 2012; Snyder et al. 2010b; Burgess, personal communication). This feature, called the polarimetric tornado debris signature, is the result of a large quantity of non-meteorological scatterers (i.e. debris) that is lofted by winds around a strong tornado. The defining characteristics of the debris signature are a local maxima in Z_H, Z_{DR} near 0 dB (but often quite variable if the debris field is well resolved with high-resolution data), ρ_{hv} less than 0.5–0.7, extremely variable ϕ_{DP} (caused by variable δ and low ρ_{hv}), and a strong couplet in V_R.

Chapter 3: Microphysics Relevant to the Numerical Modeling of Supercells

a. Bulk Microphysics

As first suggested by Ulbrich (1983) and supported in subsequent observations (e.g., Mallet and Barthes 2009), hydrometeor size distributions have been observed to fit a gamma distribution in many situations. Following (1) in Milbrandt and Yau (2005a), the gamma distribution can be written as

$$n_x(D) = N_{Tx}\frac{\nu_x}{\Gamma(1+\alpha_x)}\lambda_x{}^{\nu_x(1+\alpha_x)}D^{\nu_x(1+\alpha_x)-1}exp[-(\lambda_x D)^{\nu_x}] \qquad (3.1)$$

where subscript *x* denotes a hydrometeor class (e.g., rain, hail, etc.), D is particle diameter, N_{Tx} is the total number concentration, λ_x is the slope parameter, and ν_x and α_x are shape parameters. This version of the gamma distribution can be simplified (e.g., Ulbrich 1983) by setting ν_x=1 and writing the distribution in terms of a concentration/intercept parameter (N_{0x}) as:

$$n_x(D) = N_{0x}D^{\alpha_x}exp(-\lambda_x D) \qquad (3.2)$$

The number of free variables can be reduced by setting $\alpha_x = 0$, resulting in the (negative) exponential distribution:

$$n(D) = N_{0x}exp(-\lambda_x D) \qquad (3.3)$$

This exponential distribution was first noted in the observations of Marshall and Palmer (1948).

Although there are three parameters that describe a gamma distribution when formulated as in (3.2), they may not be completely independent of one another. Using disdrometer observations and S-band polarimetric data collected during a field project in Florida, Zhang et al. (2001) found that α and λ were highly correlated; Cao et al.

(2008) and Munchak and Tokay (2008) have also established α–λ relations. Using an α–λ relation reduces the number of parameters in (3.2) by one, leading to a so-called constrained gamma distribution.

Useful quantities can be calculated from the gamma distribution. For example, N_T is the 0th moment of the DSD:

$$N_T = M(0) = \int_0^\infty D^0 n(D) dD = \frac{N_0}{\lambda^{\alpha+1}} \Gamma(\alpha + 1) \tag{3.4}$$

In general, the *m*th moment of a gamma distribution is defined as

$$M(m) = \int_0^\infty D^m n(D) dD = \frac{N_0}{\lambda^{\alpha+1+m}} \Gamma(\alpha + 1 + m) \tag{3.5}$$

Hydrometeor mixing ratio (q) is proportional to M(3) as

$$q = \frac{a N_0}{\rho \lambda^{\alpha+b+1}} \Gamma(\alpha + 1 + b) \tag{3.6}$$

where a and b are provided by the mass (m)–diameter (D) power-law relation $m = aD^b$ and ρ is the density of air. For water spheres, $a = \rho_w(\pi/6)$ and $b = 3$, so (3.6) becomes

$$q = \frac{\pi}{6} \frac{\rho_w}{\rho} \frac{N_0}{\lambda^{\alpha+4}} \Gamma(\alpha + 4) \tag{3.7}$$

where ρ_w is the density of water. Reflectivity factor (Z) can be calculated from M(6) as

$$Z = \frac{N_0}{\lambda^{\alpha+7}} \Gamma(\alpha + 7) \tag{3.8}$$

The mean mass diameter (D_{mx}) of a gamma distribution for species *x* is calculated as

$$D_{mx} = \left(\frac{\rho q_x}{a N_{T,x}} \right)^{1/b} \tag{3.9}$$

A full derivation of the moments and other useful quantities (e.g. effective diameter, total surface area, and rainfall rate) for the gamma distribution is provided in Straka (2009).

The ability of a numerical simulation to model realistic distributions depends, in part, on the number of moments predicted by the chosen microphysics scheme. The Kessler (1969) and Lin et al. (1983) microphysics schemes, two examples of single-moment schemes, predict q by fixing N_0 and α in (3.2) and (3.6), only allowing λ to vary. Observations, however, indicate that N_0 can be highly heterogeneous in convective precipitation (e.g. Waldvogel 1974; Ferrier et al. 1995; Testud et al. 2000; Morrison et al. 2005). As a result of the fixed fall speed in single-moment schemes, there is no method by which sedimentation can occur; the fall speed of hydrometeors is independent of size in single-moment schemes. Furthermore, some microphysical processes cannot be accurately modeled as a consequence of only allowing λ to vary. For example, the median diameter of a rain DSD tends to increase through evaporation when precipitation falls through a subsaturated environment; the smaller drops evaporate much more quickly than the larger drops, shifting the mean diameter to the larger sizes. However, in a single-moment scheme, the median drop diameter must decrease through evaporation since a reduction in q can modify only λ. There exists a problem, then, if N_0 is required to be selected *a priori* since the selected value may or may not be accurate for the type of precipitation being modeled. The incorrect selection of N_0 for the hydrometeor classes can significantly affect the storms simulated (e.g. Gilmore et al. 2004; Snook and Xue 2008). In the work of Ferrier et al. (1995), N_0 varied over a few orders of magnitude and λ varied by several factors in simulated

squall lines. Similarly, N_0 for rain varied over two orders of magnitude in raindrop spectra observations in Waldvogel (1974).

As discussed in Dawson et al. (2010), one of the primary consequences of the selection of single-moment schemes for the simulation of moist convection is that cold pools often are too strong. Multimoment schemes, however, predict two or more of the parameters of the modeled DSD (e.g., Ziegler 1995; Meyers et al. 1997; Reisner et al. 1998; Morrison et al. 2005; Milbrandt and Yau 2005a,b). Most of the double-moment schemes predict N_T (i.e., M(0)) in addition to q, fixing α in (3.2) but allowing N_0 and λ to vary. The fall velocities of q and N_t can be different, which allows multimoment schemes to model the effects of sedimentation, among other processes (e.g. Seifert and Beheng 2001; Milbrandt and Yau 2005a; Dawson et al. 2010).

The double-moment schemes traditionally simulate only exponential (3.3) distributions, or at least they require that the shape parameter of the gamma distribution be either determined *a priori* or diagnosed from the other two parameters of the distribution. The shape parameter varies, however, in observations of convective precipitation (e.g., Ulbrich 1983). The triple-moment scheme described in Milbrandt and Yau (2005a,b; hereafter MY3) predicts a third moment – Z. With N_T, q, and Z predicted, all three parameters of the gamma distribution (3.2) can be retrieved. Dawson et al. (2010) examined the evolution of simulated tornadic supercells based on observations from 3 May 1999 using the Milbrandt and Yau (2005a,b) multimoment schemes and the single-moment Lin et al. (1983) scheme and observed that the simulated cold pools appeared to be much more realistic in magnitude and size (compared to available observations) in those simulations that used the multimoment

schemes. The improvement between the triple-moment scheme and the two-moment scheme is much less than that between the double-moment and the single-moment.

The MY3 scheme has five hydrometeor classes – rain water, ice crystals, snow, hail, and graupel. It should be noted that predicting the 0th, 3rd, and 6th moments (noting that the prognostic variable q is not exactly the 3rd moment but, rather, is directly proportional to it) may not necessarily yield the most accurate results; Milbrandt and McTaggart-Cowan (2010) examined sedimentation using different combinations of moments and found that the use of the 1st, 3rd, and 5th moments in a triple-moment scheme yielded the lowest error relative to the results from a spectral bin model. The moments used in the MY3 scheme, however, are linked to quantities that are familiar to the modeling and radar communities (i.e., N_T, q, and Z).

Owing largely to finite computing resources, the majority of past studies using numerical simulations of deep moist convection used bulk microphysics; in many cases, it is not feasible, or possible depending upon the access to explicit or spectral bin microphysics packages, for the particle size distribution for each hydrometeor type to be modified on a bin-by-bin basis at each time step. One such model that can use explicit bin microphysics is the two-dimensional Hebrew University Cloud Model (HUCM); Ryzhkov et al. (2011) examined some polarimetric characteristics of simulated thunderstorms using the HUCM model. The use of explicit bin microphysics in full, 3-dimensional supercell simulations, however, has thus far been limited, although Khain and Lynn (2009) used explicit bin microphysics in a study examining differences between bin microphysics and the Thompson single-moment bulk microphysics (Thompson et al. 2004) in environments of different aerosols types and concentrations.

b. Polarimetric radar emulator

The output from a simulation using, for example, the triple-moment microphysics scheme from Milbrandt and Yau (2005a,b) can be used to calculate the three parameters that describe the gamma distribution (3.2). However, it is difficult to relate the retrieved DSDs to polarimetric variables, just as it is often difficult to relate polarimetric variables directly to modeled DSDs, particularly when multiple hydrometeor species are present. To better allow for the comparison of observed variables with model output, several papers have presented radar simulators (Jung et al. 2008; Pfeifer et al. 2008; Ryzhkov et al. 2011); Jung et al. (2010) presented simulated polarimetric data from modeled supercells using the double-moment Milbrandt and Yau (2005a,b) scheme, and Ryzhkov et al. (2011) discuss the results of polarimetric representations of two-dimensional convection using the explicit bin scheme within HUCM. Utilizing one of these simulators lets one directly examine polarimetric fields from modeled supercells. In this study, the framework for the polarimetric emulator is the derived from Jung et al. (2008; 2010) with modifications explained as necessary. The emulator uses the distributions of rain, snow, graupel, and hail from the microphysics to calculate relevant polarimetric fields.

1) Fractional water for ice species

The proper handling of multi-species hydrometeors such as wet hail and wet graupel is important to be able to represent accurately the polarimetric fields of simulated convective storms. In this regard, perhaps the most important mixed species

to model is "wet" ice (i.e., the combination of water and snow, graupel, or hail). Unfortunately, this is a difficult task and may be limited by the microphysics scheme being used. The MY3 bulk scheme does not explicitly predict melted water fraction and assumes fixed densities for all hydrometeors. As a result, one must employ other methods to diagnose the fractional water on frozen species x (f_{wx}). In addition, even if one can accurately diagnose f_{wx} for a given frozen hydrometeor species, one must still make assumptions about the distribution of water on or in the frozen species (which can affect the angular moments and the effective dielectric constant of the mixed-phase hydrometeor).

The existing emulator modeled "wet" hail, graupel, and snow as explained in Jung et al. (2010). The basic principle was to "reallocate" some of the rainwater mixing ratio (q_r) over to the frozen mass (q_s, q_g, and/or q_h) according to the relative proportion of the mass contents within a grid box. The total fractional water would then be applied equally to all bin sizes for a given species. For example, in a distribution of hail with 10% f_{wh}, all sizes of hailstones within the distribution would be characterized by f_{wh} = 10%. In addition, there was also the option to ignore any interaction between rainwater and the frozen hydrometeors by treating all species separately (i.e., treating all hail, graupel, and snow as "dry").

The recent work of Dawson et al. (2013) added an option to the emulator to diagnose water fraction independently in each size bin according to the critical water fraction described in Rasmussen and Heymsfield (1987). The details of this new method for handling "wet" hail and graupel are described in Dawson et al. (2013) as follows:

The water fraction is diagnosed via an iterative method. As a first guess, liquid water is "borrowed" from the q_r field and added to the q_h field up to a maximum of 90% of the rain (to avoid complete depletion of the existing rain field, which is done only for computational convenience). In the more general case of multiple ice species at a point, the rainwater is distributed among the different species weighted by their fraction of the total ice mass. We denote this "borrowed" or "available" rainwater as $q_{r,a} = 0.9 \times q_r$. Rasmussen and Heymsfield (1987) developed a formula for the maximum or critical water mass $M_{w,crit}$ that can exist on a melting hailstone with ice core of mass M_i (see their equation 6)… Equation (6) of Rasmussen and Heymsfield (1987) is first rewritten as a function of the total mass of the melting hailstone $M_t = M_{w,crit} + M_i$ (where the masses are in kg):

$$M_{w,crit} = 2.35 \times 10^{-4} + 0.122 M_t \qquad (3.10)$$

Then the integration of (3.10) over the entire (discretized) distribution of the melting graupel or hail determines the maximum water fraction allowed for the entire distribution, denoted $f_{w,crit,tot} = M_{w,crit,tot}/M_{t,tot}$, where the subscript *tot* (total) refers to the integral across the entire distribution of the corresponding quantities in (3.10). For the case that the available water from the rain $q_{r,a}$ exceeds $M_{w,crit,tot}$, this computed $M_{w,crit,tot}$ is used as the next guess of rainwater to be added to q_h and the process is iterated until convergence, eventually yielding the final diagnosed water fraction f_w = $f_{w,crit,tot}$. Otherwise, the original first guess qr,a is used to compute f_w =

$q_{r,a}/(q_h + q_{r,a})$. The total number concentrations of both rain and hail are adjusted during this process to preserve their mean mass diameters. The final q_h is simply the sum of the original (dry) q_h and either the original first guess of borrowed rain $q_{r,a}$ or the final iterated $M_{w,crit,tot}$, whichever is less.

After f_w for the hail distribution is determined, this available liquid water is then distributed among the discrete size bins of hail ($M_{w,i}, i = 1, Nbin$ where *Nbin* is the number of discrete bins) in the following manner: 1) the ratio $R_{crit} = \min(1.0, q_{r,a}/M_{w,crit,tot})$ is computed, 2) $M_{w,crit}$ from (3.10) is computed for each bin and multiplied by the ratio R_{crit}. This ensures that the available liquid water is distributed across all (discrete) hail sizes. For each bin, we also compute a local water fraction $f_w = M_{w,i}/M_{t,i}$. If $R_{crit} = 1.0$, corresponding to the case that there is enough rainwater to completely "saturate" the hail distribution, this means that for D < 8 mm, the hail is completely melted. In that case, these bins are simply transferred back to the corresponding bins in the rain distribution; this procedure is done to ensure the emulator treats this portion of the wet graupel and hail spectrum as rain. (Dawson et al. 2013)

The primary benefit of the new fractional water routine is that it models melting hail more accurately by allowing the amount of water on hail to vary as a function of the size of the hail. In this way, small hail may have very high f_{wh} whereas very large hail may have much lower f_{wh}, consistent with the model described by Rasmussen and Heymsfield (1987). The above routine is applied to both the hail and graupel

categories. Wet snow is handled more simply by calculating the mass of water in the wet snow ($fracq_{rs}$):

$$fracq_{rs} = \min(f_{rs} \times q_r, 3f_{rs} \times q_s) \tag{3.11}$$

where f_{rs} is the fraction of snow compared to all frozen categories in the grid box (i.e., $f_{rs} = q_s/(q_s + q_h + q_g)$. The resulting maximum fractional water for snow (f_{ws}) is 75%, and it is assumed that the mass is spread equally among all bins/sizes.

2) Aspect ratio

For all hydrometeor species in this study, it is assumed that the particles are aligned such that the major axis is horizontal and the minor axis is vertical; all hydrometeors are assumed to fall in an oblate fashion (however close to unity the aspect ratio may be). The ratio of the minor to major axes of a spheroidal hydrometeor (i.e., the aspect ratio) is important to specify in a polarimetric radar emulator since the polarimetric variables are often sensitive to scatterer shape. Several drop-shape relations have been developed to describe the aspect ratio of raindrops as a function of drop size [e.g., Green (1975), Pruppacher and Beard (1970), Chandrasekar et al. (1988), and Zhang et al. (2001)]. This study uses the relationship derived from observations and described in Brandes et al. (2002):

$$r_r = 0.9951 + 0.02510D - 0.03644D^2 + 0.005303D^3 - 0.0002492D^4 \tag{3.12}$$

where D is the equivolume drop diameter (in mm).

The original emulator scheme described in Jung et al. (2010) used a fixed (0.75) aspect ratio for snow particles (r_s). As f_{ws} increases, however, the shape of a snow particle is more likely to take on that of a liquid raindrop. As such, consistent with

Ryzhkov et al. (2011), the scheme has been updated to allow the aspect ratio of snow to vary linearly from 0.75 at $f_{ws} = 0$ to that which more closely matches an equivalently-sized raindrop as follows:

$$r_s = 0.75 - f_{ws}(0.75 - r_r) \tag{3.13}$$

where r_r is the aspect ratio of a raindrop with the same mass as a completely melted hailstone or graupel particle.

Similar to snow, the aspect ratio of graupel and hail in the emulator as implemented in Jung et al. (2010) was fixed at 0.75. However, as the relative amount of water on a hailstone or graupel particle increases, the resulting torus of liquid water that encompasses the exterior of the stone decreases the aspect ratio (e.g., Rasmussen et al. 1984). An approach similar to that used by Ryzhkov et al. (2011) is implemented for this project:

$$r_{g,h} = \begin{cases} 0.75 & f_{wg,h} < 0.2 \\ 0.813 - 0.317 f_{wg,h} & 0.2 \leq f_{wg,h} < 0.8 \\ 2.8 - 4.0 r_r + 5.0(r_r - 0.56) f_{wg,h} & f_{wg,h} \geq 0.8 \end{cases} \tag{3.14}$$

More sophisticated aspects ratios should be considered for future use, as the relationship between $f_{wg,h}$ and $r_{g,h}$, as observed by Rasmussen et al. (1984) is a function of the size of the hydrometeor.

3) Canting angle

The effects of uncertainties and possible errors in relationships between the aspect ratio, particle size, and fractional water are mitigated by the observation that many hydrometeors fall with some degree of varying canting angle (e.g., hailstones may tumble, raindrops may vibrate, etc.). From a polarimetric emulator standpoint, the

effect of a distribution of canting angles for all hydrometeors is to reduce the effective/net aspect ratio, which in turn tends to reduce the magnitude of Z_{DR} and K_{DP} (quantities that tend to be affected by the aspect ratio of hydrometeors within a volume).

For all species, it is assumed that the mean canting angle ($\bar{\phi}$) is 0°. The standard deviation of the canting angle for rain (σ_r) is also set to 0°. For ice particles, however, the situation is more complex. At low fractional water, graupel and hail tend to tumble as they fall, whereas the torus of water that tends to coat wet graupel and hail tends to provide a stabilizing influence of the tumbling particles and tends to push the wet ice towards that behavior of rain. Graupel and hail are handled as follows in this study:

$$\sigma_{g,h} = \begin{cases} \frac{\pi}{3}\left(1 - f_{wg,h}\right) & f_{wg,h} \leq 0.5 \\ 0 & f_{wg,h} > 0.5 \end{cases} \tag{3.15}$$

In this manner, $\sigma_{g,h}$ decreases linearly from 60° to 0° as $f_{wg,h}$ increases from 0% to 50%. The handling of snow is carried over from Jung et al. (2010), wherein $\sigma_s = 20°$ independent of f_{ws}.

4) Dielectric constant

The scattering (and absorption) characteristics of hydrometeors are affected by the dielectric properties of the media. In standard use, the relative dielectric constant (ε_r) is a complex number defined as

$$\varepsilon_r = \varepsilon_r' + i * \varepsilon_r'' = \frac{\varepsilon}{\varepsilon_0} \tag{3.16}$$

where ε_r' represents the real part of the complex number, ε_r'' represents the imaginary part, $i = \sqrt{-1}$, ε is the permittivity of the material, and ε_0 is free-space permittivity . Closely related to ε_r is the refractive index (m):

$$m = m' + i * m'' \tag{3.17}$$

where

$$\varepsilon_r = m^2$$

The real part of *m* (i.e., *m*') is proportional to the phase shift of an electromagnetic (EM) wave through a medium, whereas the imaginary part of *m* (i.e., *m*") is proportional to signal attenuation. The dielectric constant factor commonly used in radar meteorology is defined as follows:

$$|K|^2 = \left|\frac{\varepsilon_r - 1}{\varepsilon_r + 2}\right| \tag{3.18}$$

The value of ε_r for a particular scatterer is dependent upon the temperature of the medium, the internal characteristics of the medium (e.g., polarization properties), and the characteristics of the incident EM waves. Given the importance of ε_r to the scattering properties of hydrometeors, it is necessary to calculate ε_r accurately, which may can be quite complex for mixed-phased hydrometeors.

The dielectric constants for hydrometeors used in this study are calculated using the T-matrix code from Vivekanandan et al. (1991). The dielectric constant for rain is calculated according to Cole and Cole (1941) as follows:

$$e_r' = \varepsilon_\infty + \frac{(\varepsilon_s - \varepsilon_\infty)\left[1 + \left(\frac{\lambda_s}{\lambda}\right)^{1-\alpha} \sin\frac{\alpha\pi}{2}\right]}{1 + 2\left(\frac{\lambda_s}{\lambda}\right)^{1-\alpha} \sin\frac{\alpha\pi}{2} + \left(\frac{\lambda_s}{\lambda}\right)^{2(1-\alpha)}} \tag{3.19}$$

$$e_r'' = \frac{(\varepsilon_s - \varepsilon_\infty)\left(\frac{\lambda_s}{\lambda}\right)^{1-\alpha} \cos\frac{\alpha\pi}{2}}{1 + 2\left(\frac{\lambda_s}{\lambda}\right)^{1-\alpha} \sin\frac{\alpha\pi}{2} + \left(\frac{\lambda_s}{\lambda}\right)^{2(1-\alpha)}} + \frac{\sigma\lambda}{1.88496\ x\ 10^{11}} \tag{3.20}$$

where

$$\varepsilon_s = 7.854 \times 10^1 \left[1.0 - 4.579 \times 10^{-3}(T - 25.0) + 1.19 \times 10^{-5}(T - 25.0)^2 - 2.8 \times 10^{-8}(T - 25.0)^3\right]$$

$$\varepsilon_\infty = 5.27137 + 2.16474 \times 10^{-2} T - 1.31198 \times 10^{-3} T^2$$

$$\alpha = \frac{-1.68129 \times 10^1}{T + 273} + 6.09265 \times 10^{-2}$$

$$\lambda_s = 3.3836 \times 10^{-4} e^{\frac{2.51398 \times 10^3}{T + 273}}$$

$$\sigma = 1.25664 \times 10^9$$

All rain calculations are performed at a temperature (T) of 10°C. Sensitivity tests (not shown) reveal that the imaginary component of ε_r for raindrops at common radar frequencies is affected quite substantially by temperature, whereas there is less sensitivity from temperature changes to the real component of ε_r. In this study, the effects of attenuation (which is directly affected by ε_r'') are not considered, so differences in the temperature of the rain in the model and the assumed temperature of rain in the calculation of ε_r is not expected to materially change the interpretation of the results. See Jameson (1992) for more discussion of the effect of temperature on the dielectric constant of rain.

The calculation of ε_r for ice is handled very similar to that for rain (i.e., 3.19–3.20), except that the calculations are carried out assuming a temperature of 0°C and the requisite constants are defined as follows:

$$\varepsilon_s = 2.03168 \times 10^2 + 2.5T + 1.5 \times 10^{-1} T^2$$

$$\varepsilon_\infty = 3.168$$

$$\alpha = 2.88 \times 10^{-1} + 5.2 \times 10^{-3} T + 2.3 \times 10^{-4} T^2$$

$$\lambda_s = 9.990288 \times 10^{-4} e^{\frac{1.3200 \times 10^4}{1.9869(T + 273)}}$$

$$\sigma = 1.26e^{\frac{1.2500\times10^4}{1.9869(T+273)}}$$

The treatment of mixed hydrometeors is more complicated. The T-matrix code available in ARPS, based upon Vivekanandan et al. (1991) and modified by Jung et al. (2008, 2010), assumes mixed-phased hydrometeors are homogeneous mixtures of one species (the inclusion) embedded within a "background" species (the matrix); the Maxwell-Garnett (1904) mixing formula is used for calculating the effective relative dielectric constant as:

$$\varepsilon^{(xy)} = \varepsilon_x \left(\frac{1 + 2f_y \frac{\varepsilon_y - \varepsilon_x}{\varepsilon_y + 2\varepsilon_x}}{1 - f_y \frac{\varepsilon_y - \varepsilon_x}{\varepsilon_y + 2\varepsilon_x}} \right) \tag{3.21}$$

where x is the matrix, y is the inclusion, and f_y is the fraction of y within the mixture.

Dry snow is modeled using air as the matrix and ice as the inclusion (i.e., $\varepsilon_s \approx \varepsilon^{(oi)}$). The density of ice is assumed to be 0.917 g cm^{-3}; the density of snow varies as a function of the fractional water of snow (f_{ws}) as:

$$\rho_{ws} = \rho_s\left(1 - {f_w}^2\right) + \rho_w {f_w}^2 \tag{3.22}$$

where ρ_{ws} is the density of wet snow, ρ_s is the density of dry snow (0.1 g cm^{-3}) and ρ_w is the density of water.

When snow is "wet" (i.e., $f_{ws} > 0\%$), there are at least two primary ways of calculating the relative dielectric constant (ε_{ws}) according to the Maxwell-Garnett mixing formula: wet snow can be modeled as a water matrix with snow inclusion ($\varepsilon^{(ws)}$) or as a snow matrix with water inclusion ($\varepsilon^{(sw)}$). In general, when f_{ws} is low, it is feasible to suggest that $\varepsilon_{ws} \approx \varepsilon^{(sw)}$; when f_{ws} is high, it seems feasible to use $\varepsilon_{ws} \approx \varepsilon^{(ws)}$.

Consistent with Ryzhkov et al. (2011), the relative dielectric constant of wet snow in this project varies as a function of f_{ws} as

$$\varepsilon_{ws} = \frac{1}{2}\left[(1+\tau)\varepsilon^{(ws)} + (1-\tau)\varepsilon^{(sw)}\right] \tag{3.23}$$

where

$$\tau = Erf\left(\frac{2(1-f_{ws})}{f_{ws}} - 1\right)$$

and *Erf( )* represents the error function. In this manner, ε_{ws} varies such that water is a more dominant contributor to ε_{ws} as f_{ws} increases.

Graupel is handled in a manner similar to that of snow. The density of wet graupel (ρ_{wg}) varies as a function of f_{wg} as:

$$\rho_{wg} = \rho_g\left(1 - {f_{wg}}^2\right) + \rho_w {f_{wg}}^2 \tag{3.24}$$

where ρ_g is the density of dry graupel (0.400 g cm^{-3}). It is always assumed that wet graupel has the form $\varepsilon_{wg} \approx \varepsilon^{(ws)} \approx \varepsilon^{(w(oi))}$ (i.e., water matrix with an inclusion snow, which itself is a mixture of air matrix with ice inclusion).

Finally, the density of wet hail (ρ_{wh}) has a similar form as that for wet snow and wet graupel:

$$\rho_{wh} = \rho_h\left(1 - {f_{wh}}^2\right) + \rho_w {f_{wh}}^2 \tag{3.25}$$

where ρ_h is the density of dry hail (0.913 g cm^{-3}). Given the greater density of hail, ε_{wg} is treated as water matrix with ice inclusion ($\varepsilon^{(wi)}$). Calculations for all frozen species are carried out at a temperature of 0° C.

It should be noted that the use of (3.21) is a relatively simple treatment of heterogeneous hydrometeor species compared to the much more complex behavior observed in nature. Other studies treat mixed-phased / mixed-species hydrometeors in a

manner that is more physically realistic. For example, since water often forms a "shell" around hail as hailstones melt, Ryzhkov et al. (2011) modeled melting hail as a two-layer scatterer with water as an outer layer around an inner core of soaked ice characterized by the form $\varepsilon^{(sw)}$). In comparing the two-layer hailstone for melting hail with $\varepsilon^{(ws)}$ and $\varepsilon^{(sw)}$ (Figure 6) assuming Rayleigh approximation is valid, Ryzhkov et al. (2011) showed that using $\varepsilon^{(ws)}$ reasonably approximates the more accurate two-layer scattering model at larger f_{wh}. However, with resonance effects, the differences between the two-layer model and the simpler homogenous mixture model may be significantly different (e.g., Figure 7). This is a limitation of the scattering model used in this study, although the errors may be complex given the non-linearity of resonance and the sensitivity of the differences to f_{wh}.

Scattering amplitudes are calculated for particles with equivolume diameters of 0–8 mm split into 100 bins for rain, 0–50 mm split into 625 bins for graupel, 0–70 mm split into 875 bins for hail, and 0–30 mm split into 112 bins for snow. The resultant bin sizes are 0.08 mm for rain, hail, and graupel and 0.27 mm for snow.

5) Radar variables and angular moments

All hydrometeor species considered in this project are modeled as oblate spheroids with a distribution of canting angles represented by σ_x. Since the polarimetric emulator used in this study is based on the work of Jung et al. (2008, 2010), the calculation of the commonly-used radar variables are detailed in Jung et al. (2010). The equivalent radar reflectivity factors at horizontal and vertical polarizations ($Z_{h,x}$ and $Z_{v,x}$;

$mm^6\ m^{-3}$) for a given species x (r rain, s snow, g graupel, or h hail) are defined as follows:

$$Z_{h,x} = \frac{4\lambda^4}{\pi^4 |K_w|^2} \int_0^{Dmax,x} \left\{ A_x \left| f_{a,x}^{(b)} \right|^2 + B_x \left| f_{b,x}^{(b)} \right|^2 + 2C_x Re\left(f_{ax}^{(b)} f_{bx}^{(b)^*} \right) \right\} N(D) dD \quad (3.26)$$

$$Z_{v,x} = \frac{4\lambda^4}{\pi^4 |K_w|^2} \int_0^{Dmax,x} \left\{ B_x \left| f_{a,x}^{(b)} \right|^2 + A_x \left| f_{b,x}^{(b)} \right|^2 + 2C_x Re\left(f_{a,x}^{(b)} f_{b,x}^{(b)^*} \right) \right\} N(D) dD \quad (3.27)$$

where $f_a^{(b)}$ ($f_b^{(b)}$) is the scattering amplitude in the backward direction (i.e. backscatter amplitude) at horizontal (vertical) polarization, the * operator represents the complex conjugate, Re( ) represents the real part of the quantity included in the parenthesis, $D_{max,x}$ is the maximum size of the particle size distribution,

$$A_x = \langle \cos^4 \phi_x \rangle = \frac{1}{8} (3 + 4\cos(2\bar{\phi}_x) \exp(-2{\sigma_x}^2) + \cos(4\bar{\phi}_x) \exp(-8{\sigma_x}^2)) \quad (3.28)$$

$$B_x = \langle \sin^4 \phi_x \rangle = \frac{1}{8} (3 - 4\cos(2\bar{\phi}_x) \exp(-2{\sigma_x}^2) + \cos(4\bar{\phi}_x) \exp(-8{\sigma_x}^2)) \quad (3.29)$$

$$C_x = \langle \sin^2 \phi_x \cos^2 \phi_x \rangle = \frac{1}{8} (1 - \cos(4\bar{\phi}_x) \exp(-8{\sigma_x}^2)) \quad (3.30)$$

Specific differential phase (in deg. km^{-1}) is calculated as

$$K_{DP} = \frac{180\lambda}{\pi} \int_0^{Dmax} C_{kx} Re\left(f_{a,x}^{(f)} - f_{b,x}^{(f)} \right) N(D) dD \quad (3.31)$$

where $f_{a,x}^{(f)}$ ($f_{b,x}^{(f)}$) is the scattering amplitude in the forward direction at horizontal (vertical) polarization for species x and

$$C_{kx} = \langle \cos(2\phi_x) \rangle = \cos(2\bar{\phi}_x) \exp(-2{\sigma_x}^2) \quad (3.32)$$

The co-polar cross-correlation coefficient is defined as

$$\rho_{hv} = \frac{\left| \sum_{x=r,s,g,h} Z_{hv,x} \right|}{\left[\sum_{x=r,s,g,h} Z_{h,x} \times \sum_{x=r,s,g,h} Z_{v,x} \right]^{1/2}} \quad (3.33)$$

where

$$Z_{hv,x} = \frac{4\lambda^4}{\pi^4 |K_w|^2} \int_0^{Dmax} \left\{ C_x \left(\left| f_{a,x}^{(b)} \right|^2 + \left| f_{b,x}^{(b)} \right|^2 \right) + A_x \left(f_{a,x}^{(b)} f_{b,x}^{(b)*} \right) + B_x \left(f_{b,x}^{(b)} f_{a,x}^{(b)*} \right) \right\} N(D) dD \tag{3.34}$$

For simplicity, in all calculations and plots shown, it is assumed that the elevation angle is 0° and that the earth is flat. In addition, the effects of attenuation are not included.

The angular moments A_x, B_x, C_x, and C_{kx} used in the calculation of the radar variables as defined in Jung et al. (2010) and as used in this project differ from those used in Ryzhkov et al. (2011) and derived from Ryzhkov (2001). In the notation of Ryzhkov et al. (2011), and since $\bar{\phi}_x = 0$ in this study, the moments (3.28–3.30, 3.32) can be written as

$$A = \frac{3}{8} + \frac{1}{2} r + \frac{1}{8} r^4 \tag{3.35}$$

$$B = \frac{3}{8} - \frac{1}{2} r + \frac{1}{8} r^4 \tag{3.36}$$

$$C = \frac{1}{8} - \frac{1}{8} r^4 \tag{3.37}$$

$$C_{kx} = r \tag{3.38}$$

where

$$r = \exp(-2\sigma^2)$$

Different assumptions were used to develop the equations used in the different papers, but modeling calculations using the Jung et al. (2010) equations (3.26–3.30) can vary appreciably from those using the Ryzhkov et al. (2011) equations (e.g., Figure 8). The

differences between the two methods for calculating the radar variables and angular moments are left for future work.

Chapter 4: Research Tools and Experiment Design

The data used in this study are divided into two groups – observational and simulated. The observational data were collected by two mobile, X-band, polarimetric Doppler radars used by graduate students and faculty at the University of Oklahoma. The simulations were conducted at a convection-resolving resolution using a series of different hodograph shapes and lengths.

a. Observational Tools

The observed radar data examined in this project were collected by two mobile, truck-mounted, polarimetric, X-band Doppler radars. In a typical deployment focused on supercell mesocyclones and tornadoes, the field personnel operating the radar attempt to collect data starting 20–25 km downstream (relative to storm motion) of the particular "feature of interest" (often, for the cases examined in this paper, this feature is a tornado, wall-cloud, or mesocyclone) and often to the right of the expected track of the feature. Deployments typically stopped when the feature moved beyond the radar's range or location, though specific deployment strategies varied on a case-by-case basis depending upon the status and expected future evolution of the storm of interest, and the availability of subsequent deployment locations (often affected by the local road network, forward storm motion, time of day, anticipated convective evolution, and other factors).

The UMass X-Pol radar (pictured in Figure 9a) was built and maintained by the Microwave Remote Sensing Laboratory (MIRSL) at the University of Massachusetts – Amherst. Between 2002 and 2010, graduate students and faculty at the University of

Oklahoma, in collaboration with MIRSL personnel, used the UMass X-Pol throughout the central United States to collect data of severe convection. Many of the scanning strategies used before 2007 focused on near-surface observations; the collection of volumetric radar data (i.e. a regular series of elevation angles) did not begin until 2007. The radar transmits simultaneously at H and V at 9.41 GHz and uses a magnetron with peak output power of 12.5–25 kW combined between both channels. The 3-dB beamwidth is 1.25° and the azimuthal rotation rate is 20–25° s^{-1}. The most commonly-used pulse length was 1 μs (yielding a range resolution of 150 m) with a sampling range of 60 m.

More recently, starting in the spring of 2011, a rapid-scan mobile radar has been in use by graduate students, faculty, and engineers at the University of Oklahoma (Figure 9b). This radar, typically referred to as RaXPol (signifying its rapid-scan, X-band, polarimetric characteristics), is unique in that it has the combination of an antenna pedestal can rotate up to approximately 180° s^{-1} and a transceiver chain that can use frequency hopping to sample the atmosphere more rapidly than is possible with nearly all other conventional radars (Pazmany et al. 2013). The rotation rate significantly exceeds that of most other mobile radar systems (e.g. Wurman et al. 1997; Biggerstaff et al. 2005; Bluestein et al. 2007a,b; Melnikov et al. 2009)], greatly increasing the temporal resolution of the data and allowing users of the data to examine in more detail the evolution of processes associated with convective storms (e.g., tornadoes, convective updrafts, etc.).

In normal rapid-scan mode, 11–12 frequencies centered at 9.73 GHz +/- 20 MHz are transmitted on consecutive pulse groups (either using pulse pairs or, when using a

staggered pulse repetition, pulse triples); frequency hopping increases the number of independent samples collected and reduces the dwell time required for averaging the desired number of pulses in the moment calculations. RaXPol's antenna is larger than that on UMass XPol and has a 1° half-power beamwidth. Multiple scanning strategies are used depending upon the goals of the deployment and the nature of the phenomena being targeted:

- Traditional scan: the antenna rotation is set to 40-60° s^{-1}, with a 150 m range resolution oversampled to 75 m. As a result, more than 70 pulse pairs are averaged for the calculation of the moments, resulting in extremely clean data.
- Rapid-scan storm mode: the antenna rotation rate is set to ~180° s^{-1}, with a 75 m range resolution oversampled every 30–75 m. The moments are calculated by averaging 11 pulse groups, and full PPIs are collected every 2 s. With some antenna transition time, a 10 PPI volume can be collected every ~22 s.
- Rapid-scan tornado mode: the antenna rotation rate is 180° s^{-1}, with a 15-30 m range resolution oversampled to 15–30 m. In 2011 and 2012, a single elevation angle was commonly-used to collect data in this mode; in 2013, many "tornado mode" deployments used a shallow volume of, for example, 0° to 5° every 1° to collect data as close to the ground as possible without having to know specific ground clutter clearances. As a result of receiver bandwidth limitation, fewer pulse groups (e.g., < 10)

are used to calculate the moments when range resolution is set to 15 or 30 m.

Selected radar characteristics for the both mobile radars are provided in Table 1. Further technical information on UMass XPol is available in Junyent-Lopez (2003) and Pazmany et al. (2003); additional technical specifications on RaXPol are provided in Pazmany et al. (2013). Products available from the UMass X-Pol and RaXPol radar systems include reflectivity at horizontal polarization (Z_H), differential reflectivity (Z_{DR}), radial velocity (V_R), total differential phase (Φ_{DP}), and the magnitude of the co-polar cross-correlation coefficient at zero lag (ρ_{HV}). A couple of datasets have complete I/Q data available, but the vast majority of the data collected through 2013 were saved as covariances, powers, and complex correlations.

Estimates of A_H from the observed UMass XPol and RaXPol data are retrieved using the ZPHI technique (Testud et al. 2000), and A_{DP} is estimated from (2.13). As noted in Snyder et al. (2010b), the ZPHI technique has some logistical advantages that simplify attenuation correction of X-band convective storm data. Specifically, as a result of resonance effects, UMass XPol has collected datasets for which non-trivial areas of $K_{DP} < 0°$ km^{-1} are present (implying that ϕ_{DP} decreases with range that those areas). In these areas, the parameterization based on Bringi et al. (1990) and (2.11) will produce estimates of $A_H < 0$ dB km^{-1}, which is physically unrealistic. The more advanced self-consistent with constraints method detailed in Bringi et al. (2001) may provide better attenuation estimates for some datasets, but it has severe problems when ϕ_{DP} decreases with range along any length of the ray. The ZPHI method, however, only uses ϕ_{DP} at the start and end of a ray (or radial segment) to determine the

maximum PIA_H; this PIA_H is "distributed" along the radial according to the Z_H profile. As a result, ranges through which ϕ_{DP} may decrease as a result of resonance effects, statistical anomalies, or, less likely, the presence of prolate scatterers, do not detrimentally affect the performance of the attenuation correction scheme.

Based on the previous work of Snyder et al. (2010b), b in (2.10) is 0.8, α_H in (2.11) is 0.313 dB deg^{-1}, and γ in (2.13) is 0.154 [i.e. α_{DP} = 0.0483 dB deg^{-1} in (2.13)], values calculated from disdrometer observations collected in central Oklahoma (Zhang, personal communication). In the near future, it will be worth considering a method such as that used by Gu et al. (2011) that attempts to account for anomalous attenuation that can occur when the signal passes through wet hail. Attenuation that occurs from propagation through cloud water and atmospheric gases is not estimated. Since many of these radars' deployments are from ranges of < 30 km, the total attenuation from these constituents is likely to be dwarfed by attenuation through larger hydrometeors.

The greater influence of resonance effects at X band compared to S band, along with the greater resolution of UMass XPol compared to traditional, fixed-location radar systems, increase the probability that significant gradients in δ will be resolved by the radar. Consequently, the effects of δ should be removed in order to obtain better estimates of ϕ_{DP} from Φ_{DP}. The data from these radars are filtered using a technique similar to that described by Hubbert and Bringi (1995). From the estimated ϕ_{DP}, K_{DP} is then calculated by linear regression over a 1.5 km window.

b. Numerical Simulation Tools

Given the apparent benefits provided by multimoment microphysics in better simulating processes that occur in deep moist convection [e.g. more realistic cold pools (Dawson et al. 2010) and improved modeling of drop size sorting through sedimentation (Milbrandt and Yau 2005a,b)], it is important to use a model that allows for the use of such microphysics. Version 5.3.3 of the Advanced Regional Prediction System (ARPS; Xue et al. 2000, 2001, 2003), maintained and developed by the Center for Analysis and Prediction of Storms (CAPS) at the University of Oklahoma, is used in this study. This version of ARPS includes, among a variety of microphysics options, the three-moment scheme of Milbrandt and Yau (MY3; 2005a,b). Considering the apparent benefits of this scheme compared to other single-moment and double-moment schemes (e.g. Milbrandt and Yau 2005a,b; Dawson et al. 2010), this scheme is used in the current model simulations.

The model is run with a 151 km x 151 km horizontal grid with grid spacing of 200 m. This horizontal grid spacing was chosen as a compromise between computational efficiency for the series of simulations being performed and the desire to resolve as much convective detail as possible. Bryan et al. (2003) examined the evolution of convection in a large eddy simulation (LES) at multiple grid resolutions and concluded that, to properly resolve the inertial subrange, one must use a grid of O(100m). Petch (2006) determined that a grid spacing of no more than 200 m was necessary to produce realistic cloud sizes and structures in sensitivity tests of the effect grid spacing on cloud development and characteristics. Since this project aims to

examine storm-scale polarimetric signatures that have horizontal scale < O(1000 m), the horizontal grid spacing was chosen to be 200 m.

A stretched vertical grid with 83 grid points is used. Vertical grid spacing as low as approximately 85 m near the surface increases to approximately 350 m at top of the model domain (20 km AGL). The initial updraft is developed from the commonly-used ellipsoidal warm bubble (Klemp and Wilhelmson 1978) with a magnitude of 4 K and maximum horizontal and vertical extents of 10 km and 1.5 km, respectively, centered 1.5 km above ground level. The grid for each simulation is translated so as to keep the primary convective cell near the center of the domain; the translation vector was chosen based upon a subjective assessment of the movement of the primary cyclonic supercell produced in each simulation. Model fields are saved every 120 s in HDF4 format, and each simulation is run out to 10800 s (i.e., 3 hours). Several simulations develop unrealistically strong low-level inflow (e.g., > 60 m s^{-1} over a 900+ km^2 area east of the updraft) towards the end of the simulation period, likely caused by boundary condition limitations. In addition, many simulations produce more widespread deep, moist convection near the location of the primary cyclonic supercell after ~9,000–10,000 s, complicating the analyses owing to increased storm collisions and interactions. As such, much of the bulk analysis in this study will exclude the last ~1800 s of the simulations and focus primarily on the 1800–9000 s time period. Fourth-order, monotonic computational mixing (Xue 2000) is utilized to control numerical artifacts. Table 2 contains a summary of the model configuration.

To isolate the influence of the vertical wind profile on the microphysical and polarimetric structure and evolution of simulated convective storms, a single

thermodynamic sounding is used (Figure 10). The thermodynamic sounding was created using a commonly-used analytic sounding (Weisman and Klemp 1982; hereafter WK82) such that sufficient convective available potential energy (CAPE) was present to support intense severe convective storms. The potential temperature (θ) and relative humidity (H) profiles are based upon the analytical model of WK82:

$$\theta(z) = \begin{cases} \theta_0 + (\theta_{tr} - \theta_0)\left(\frac{z}{z_{tr}}\right)^{1.25} & z \le z_{tr} \\ \theta_{tr} \exp\left[\frac{g}{c_p T_{tr}}(z - z_{tr})\right] & z > z_{tr} \end{cases} \quad (4.1)$$

$$H(z) = \begin{cases} 1 - \frac{3}{4}\left(\frac{z}{z_{tr}}\right)^{1.25} & z \le z_{tr} \\ 0.25 & z > z_{tr} \end{cases} \quad (4.2)$$

where θ_0 and θ_{tr} represent the potential temperature (in K) at the surface and tropopause, z_{tr} is the height of the tropopause, and T_{tr} is the temperature (in K) at the tropopause. For this project, z_{tr} has been set to 12 km, θ_0 to 300 K, θ_{tr} to 350 K, and T_{tr} to 220 K. The calculated CAPE, accounting for the virtual temperature correction (Doswell and Rasmussen 1984) but not precipitation loading, for a surface parcel in an environment with this sounding is 2078 j/kg; the convective inhibition (CINH) is -31 j/kg.

Note that the WK82 analytical sounding is characterized by a very moist troposphere. James and Markowski (2010) investigated the role of dry air aloft on the evolution of deep moist convection and found that the reduced precipitation loading associated with dry air aloft tends to counteract the effects of enhancing cooling and negative buoyancy in terms of downdraft intensity and outflow propensity. Interested readers are referred to their study and similar results presented in McCaul and Cohen (2002) for a more thorough discussion of the role of dry air in the structure of

convective storms. One simulation was also carried out using a considerably drier mid- and upper-tropospheric environment by changing the exponent in (4.2) from 1.25 to 0.125 for heights above 3000 m, but the supercell produced in that configuration is considerably more variable in terms of updraft intensity (e.g., it has "pulse-like" qualities). Two other attempts to reduce the depth of the moist layer to match more closely the mixing layer depth (i.e., 1200 m) failed to produce a sustained convective storm. This inability to develop sustained updrafts has been noted by others that have used the warm bubble technique for initiation of convection (e.g., McCaul and Cohen 2004; Wicker et al. 1997) – the updraft nudging technique described by Naylor and Gilmore (2012) appears to be a viable alternative that may allow for the simulation of sustained supercells in environments that have shallower moisture profiles and/or greater convective inhibition.

Supercell organization and intensity and tornado probability tend to be greater in environments of stronger vertical wind shear (as measured by hodograph length, storm-relative helicity, and/or other measures) as noted in previous observational [e.g., Craven and Brooks (2004), Rasmussen and Blanchard (1998), Rasmussen (2003), Thompson et al. (2003), etc.] and numerical modeling studies [e.g., WK82, Weisman and Klemp (1984), Rotunno and Klemp (1982, 1985), etc.]. In order to examine also the role of vertical wind shear on the polarimetric representation of simulated supercells, several vertical wind profiles were created. These profiles have been created by modifying the shape, length, and "distribution" of the hodograph. Eight hodographs are used and are designed as follows (Figure 11):

- Two half-circle hodographs of radius S=15 m s^{-1} and S=25 m s^{-1} with constant veering of winds between the surface and 10 km AGL, above which the wind is constant. These simulations will be referred to as experiments *15r10* and *25r10*.

$$U = \begin{cases} S * cos\left(\pi * \left(1 - \frac{z}{10000}\right)\right) & z < 10000 \\ S & z \geq 10000 \end{cases}$$

$$V = \begin{cases} S * sin\left(\pi * \left(1 - \frac{z}{10000}\right)\right) & z < 10000 \\ 0 & z \geq 10000 \end{cases}$$

- Two half-circle hodographs of radius S=15 and S=25 m s^{-1} wherein wind shear is maximized near the surface and decreases to a height of 10 km, above which the wind is constant. These simulations will be referred to as experiments *15r10_057* and *25r10_057*.

$$U = \begin{cases} S * cos\left(\pi * \left(1 - \left(\frac{z}{10000}\right)^{0.5757}\right)\right) & z < 10000 \\ S & z \geq 10000 \end{cases}$$

$$V = \begin{cases} S * sin\left(\pi * \left(1 - \left(\frac{z}{10000}\right)^{0.5757}\right)\right) & z < 10000 \\ 0 & z \geq 10000 \end{cases}$$

- Two hodographs characterized by a quarter-circle shape with radius S=15 m s^{-1} and S=25 m s^{-1} in the 0 – 3 km AGL layer, with constant shear on a straight-line hodograph from 3 – 10 km AGL. These simulations will be referred to as experiments *15q10* and *25q10*.

$$U = \begin{cases} S * cos\left(\pi * \left(1 - \frac{z}{6000}\right)\right) & z < 3000 \\ (z - 3000) * \left(\frac{S * \pi}{10000}\right) & 3000 \leq z < 1000 \\ \frac{7000 * S * \pi}{10000} & z \geq 10000 \end{cases}$$

$$V = \begin{cases} S * sin\left(\pi * \left(1 - \frac{z}{6000}\right)\right) & z < 3000 \\ S & z \geq 3000 \end{cases}$$

- Two straight-line hodographs with constant shear (along a straight hodograph) between 0 – 10 km. These simulations will be referred to as experiments *15str* and *25str*.

$$U = \begin{cases} \frac{S * \pi * z}{10000} - 23 & z < 10000 \\ S * \pi - 23 & z \geq 10000 \end{cases}$$

$$V = 0$$

The lengths of the "weak" shear hodographs for each hodograph shape (i.e., *15r10*, *15r10_057*, *15q10*, and *15str*) are the same; the length of each of the hodographs in the "strong" shear cases is identical. The 0–10 km mean shear values for the "weak" and "strong" shear hodographs are 4.712 x 10^{-3} s^{-1} and 7.854 x 10^{-3} s^{-1}, respectively. Using these hodographs allows one to examine the effects of the strength of wind shear on polarimetric signatures separately from the effects of different hodograph shapes.

Chapter 5: Observations of Polarimetric Signatures by Two Mobile X-Band Radars

Much of the material in this chapter has been published and can also be seen in Snyder et al. (2013). Additional observations and details are provided for thoroughness without the constraints under which Snyder et al. (2013) was published. In general, cases for each signature will be presented from UMass XPol followed by RaXPol in a semi-chronological order.

a. Low reflectivity ribbon (LRR)

A narrow band of locally-reduced Z_H extending from near where the hook echo "attaches" to the main body of the storm near the rear of the forward-flank downdraft (FFD) has been observed in at least 13 supercells in which UMass XPol and RaXPol have collected data (Table 3). This feature is most evident in Z_H and Z_{DR} data collected in the lower troposphere, typically within 3 km of the ground. Because this feature is essentially a "texture" feature and observed as a local minimum in Z_H and Z_{DR}, and given that attenuation estimation can introduce streakiness and other aesthetic unpleasantries that can complicate analysis (even assuming that the attenuation estimates are accurate), the observed (attenuated) Z_H' and Z_{DR}' tend to highlight the signature well and are used to highlight this feature is most of the UMass XPol cases presented. Attenuation estimates from the RaXPol datasets generally are cleaner on account of the better sensitivity of the system and the observation that many of the observed cases from RaXPol are at relatively close range (and thus are associated with higher signal-to-noise ratio and better quality of polarimetric quantities).

In data collected of a tornadic supercell in southeastern Wyoming on 5 June 2009 (Figure 12), a narrow zone of locally-reduced Z_H' extends northeastward from near the area where the hook echo appears to "attach" to the main body of the storm on the upshear (southwest) side of the FFD. Values of Z_H' within this local minimum are 6–10 dBZ lower than in immediately-adjacent areas, and the reduction in Z_H' is approximately 500–700 m in width. It is most evident from the lowest elevation angle [at a height of approximately 1.25 km above radar location (ARL)] to approximately 3.3 km ARL. At the time of these data, a strong tornado was occurring (Figure 12e), evidence of which is seen in Z_H' (Figure 12a) and as a Doppler velocity couplet (Figure 12c).

Nearly collocated with this narrow, arcing band of reduced Z_H' is an area of Z_{DR}' that is 3–5 dB lower than surrounding areas (Figure 12b); Z_{DR}' near 0 dB in this band is flanked on either side by Z_{DR}' of 3–5 dB. The minimum in Z_{DR}' is located slightly west of the minimum in Z_H'. The east side of the Z_H' reduction is characterized by Z_{DR}' of 4–5 dB; the west side (and for approximately 750 m west of the lowest Z_H') has values of ~0 dB. The low Z_{DR}' band is approximately 700–800 m in width. Little evidence of this signature in ρ_{hv} is noted (Figure 12d), although ρ_{hv} is occasionally reduced in the same area, and only minor radial convergence (~2.5 x 10^{-3} s^{-1}) is observed in V_R. The minima are evident from the time of deployment (2209 UTC) until approximately 2225 UTC, though they are most prominent in the first few minutes after the start of data collection. This signature, hereafter referred to as the low reflectivity ribbon (LRR), is characterized by a narrow, sometimes "winding" band of locally-reduced Z_H , typically nearly collocated with locally-reduced Z_{DR}' , and sometimes associated with reduced ρ_{hv}

and convergence evident in V_R. Considering the method by which K_{DP} is calculated (i.e., linear regression of filtered ϕ_{DP} over a 1.5 km range), the resolution of the K_{DP} data tend to be too coarse to sample the narrow feature.

On the evening of 10 June 2010, a post-tornadic supercell in eastern Colorado exhibited a similar structure – a ribbon of reduced Z_H' that extends from the hook echo and leftward (relative to storm motion) into the FFD (Figure 13). In this case, reductions in Z_H' are approximately 10–15 dBZ and are most evident below ~3 km ARL. As is observed in the previous case, Z_{DR}' near this band is also locally-reduced by as much as 4 dB, spatially dislocated very slightly to the rear side of the observed Z_H' reduction. In addition, a reduction in ρ_{hv} is also apparent. There are no readily-apparent organized patterns in the V_R field near the observed region of locally-reduced Z_H and Z_{DR}. The feature was visible for approximately 10 minutes, and it decayed as the primary mesocyclone occluded and moved rearward.

A tornadic supercell that was scanned intensively by participants of VORTEX 2 on 18 May 2010 in the northern Texas panhandle exhibited similar local reductions in Z_H' and Z_{DR}' (Figure 14). The ribbon of low Z_H' and Z_{DR}' varies between 650 and 1,000 m in width, with magnitudes of reduction of 15–20 dBZ and 2–4 dB in Z_H' and Z_{DR}', respectively. Tornadoes were reported approximately 30 minutes before and after this scan. The ribbon initially is most evident at the highest elevation angles (which, considering the short range of the storm from the radar, results in a beam height of only ~2.5 km ARL), and it is visible for at least 5 minutes before the radar stopped scanning in order to reposition. The feature moved rearward, with time, relative to the position of the hook echo.

Radial profiles of Z_H' and Z_{DR}' (filtered to remove high-frequency variability in the observations) through the LRR clearly show the local minima in Z_H' and Z_{DR}' centered near 17.7 km (Figure 15a) and 10.4 km range (Figure 15b) on scans from the evenings of 10 June 2010 (Figure 13) and 18 May 2010 (Figure 14). In neither case is there substantial spatial dislocation between the Z_H' and Z_{DR}' minima, though the maxima in Z_H' along either side of the LRR in the latter case are shifted slightly farther in range compared to the maxima in Z_{DR}' surrounding the LRR. Note that the decrease in both Z_H' and Z_{DR}' several kilometers beyond the LRR is the result of attenuation. In the 11 June 2010 case, there is a reduction in ρ_{hv} associated with the LRR, though the minimum is slightly up-radial relative to the LRR. In the 19 May 2010 case, there is little reflection of the LRR in ρ_{hv}, but there is also an anomalous local peak in Φ_{DP} within the LRR. It appears more likely that this peak is the result of enhanced δ from the scatterers with appreciable resonance effects within the LRR and less likely that the peak is caused by scatterers that have large K_{DP} along the leading edge of the LRR and $K_{DP} < 0°$ s^{-1} along the rear edge of the LRR.

A supercell observed on 23 May 2008 in extreme northwestern Oklahoma (Figure 16) provides a unique opportunity to examine the LRR owing to the close proximity of the storm to the radar. In fact, the hook echo and extremely strong RFD, which blew over a semi-truck very near the radar deployment location, overtook the radar during data collection. Like most aforementioned LRR examples, the feature is very evident in Z_{DR}' data (Figure 16d), with relatively little spatial association with anomalies in the ρ_{hv} (Figure 16f) and K_{DP} (Figure 16b) fields. Because the radar was so close to the developing hook echo, the radar was able to sample the development of the

hook echo and tornado with particularly high spatial resolution. Data collected very close to the surface (e.g., data in Figure 17 were collected at an elevation angle of 4.2º with a beam height of <500 m for the observed hook echo and LRR) show the LRR best in Z_{DR}' (middle column of Figure 17), though it is evident in Z_H' as well (left column of Figure 17). Between 2339:51 UTC and 2342:47 UTC, the hook echo takes on significant cyclonic curvature. Nearly collocated with the LRR is observed strong radial converge (right column in Figure 17), with 30–35 m s^{-1} inbound V_R; this radial convergence weakens as near-surface cyclonic rotation intensifies through this time period. By 2344:29 UTC (bottom row of Figure 17), there is a broad cyclonic vortex near the surface, with peak V_R of 45 m s^{-1} within 1 km of the radar. During the time spanned in Figure 17, Z_{DR}' within the hook echo is significantly lower than that observed to the north and northwest of the hook echo, indicating the possibility that the mean DSD within this part of the hook echo has relatively small mean diameter [similar to the observations of Kumjian (2011)]. Throughout the deployment, enhanced spectrum width (not shown) was observed within the LRR.

While strong radial convergence is observed, at least initially, near the surface (< 700 m ARL), at higher elevation angles there are indications of small, tightly-spaced vortex signatures along the inside portion of the hook echo. These vortices are apparent in Z_H' and V_R fields with a quasi-regular spacing of 400–600 m, and they stream rapidly southeastward through the inside portion of the hook echo as it wraps up through 2344 UTC. Evidence of these vortices is contained in Z_H', Z_{DR}', and V_R data in a relatively short sequence of scans collected at elevation angles of 6.1º, 8.0º, and 10.0º (Figure 18). The vortices appear to be located within the LRR seen in both Z_H' and Z_{DR}' field; the

LRR that is seen extending into the rear of the FFD (top center of each image in Figure 18) appears to show several vortices in an arc, evident in the Z_H', Z_{DR}', and V_R fields. These vortices move rapidly southward, wrapping cyclonically along the inside part of the hook echo. At times, stronger vortices with a spacing of ~1 km can be seen in the V_R data. The 6.1° elevation angle data subsequent to the times presented in Figure 18 indicate peak V_R is approximately 50 m s^{-1} within 1 km of the radar. The predominance of cyclonic vortices without apparent anticyclonic vortices suggests that shear instability, and not tilting, as a potential causative mechanism. The observation that the vortices become stronger with height may be an indication that vortex stretching is occurring as well.

In data from a supercell on 7 June 2009, a ribbon of low Z_H and Z_{DR} are evident in a similar storm-relative location on data collected at 0120 UTC (Figure 19a-b), but the ribbon is aligned in a more N–S or NW–SE orientation. In this case, separate tornadoes were reported at 0113 UTC and 0127 UTC. In a tornadic supercell that occurred along the Kansas–Colorado border on 25 May 2010 (Figure 19c-d), similar reductions in Z_H and, to a lesser extent, in Z_{DR} are observed in a very similar storm-relative location. A tornado was developing at the time of these data as well.

A visually-spectacular supercell observed by RaXPol on 23 May 2011 (inset picture in Figure 20c) not only produced the largest hailstone in record in Oklahoma at 6" in diameter but also contained an LRR (Figure 20) different than that from previously-observed cases. The LRR is evident at all elevation angles (2°–16°) scanned during two different deployments (2248–2255 UTC and 2310–2339 UTC; Figure 20-Figure 24); at the range from the radar, beam heights were between 400 m and ~3000 m

AGL (Figure 21 and Figure 23). On most scans, the LRR is characterized by a ~500 m wide local minimum in Z_H', Z_{DR}', and, at times, ρ_{hv}. Low perturbations in the latter (Z_{DR}' and ρ_{hv}) are most apparent at heights above ~1000 m AGL. The supercell produced at least one well-defined funnel cloud near the end of the second deployment shortly after 2330 UTC but, apparently, failed to produce a tornado.

To provide a final few examples of the LRR in RaXPol datasets, a tornadic supercell that produced an EF5 tornado with radar-measured maximum V_R of ~124 m s^{-1} on 24 May 2011 possessed an LRR near the genesis of this violent tornado (Figure 25) that was most visible in Z_H. A violent tornado (with RaXPol-measured maximum V_R of 90–100 m s^{-1}) was observed southwest of the town of Carney, Oklahoma, on 19 May 2013 and was also associated with an easily-seen LRR in Z_H, Z_{DR}, and ρ_{hv} (Figure 26). Several hours after this tornado, another violent tornado was observed by RaXPol west of Shawnee, Oklahoma; data collected of the tornadic supercell reveals an LRR apparent in all polarimetric radar fields (Figure 27). A much weaker tornado was observed at close (3–5 km) range on 30 May 2013; the supercell that produced the tornado possessed an LRR evident in Z_H before tornadogenesis (Figure 28). The following day (31 May 2013), an extraordinarily violent tornado (peak V_R > 134 m s^{-1} within 5 km of the radar) was associated with an LRR near the beginning of its life (Figure 29) when maximum V_R was a comparatively weak ~68 m s^{-1}.

Although the LRRs that have been identified in UMass XPol and RaXPol data are more commonly seen in tornadic supercells and often early (or preceding) the lifecycle of a tornado, non-tornadic supercells, such as the one observed on 29 May 2012 near Kingfisher, Oklahoma, have possessed LRRs as well (Figure 30). In the 29

May 2012 case, the supercell produced a tornado 1.75 hours after the data shown in Figure 30 were collected, but it is considered non-tornadic at the time in the figure. All nearly all of the RaXPol cases of the LRR, reduction in ρ_{hv} and Z_{DR} suggest that hail is present within the LRR.

In total, LRRs are evident in at least seven supercell datasets collected by UMass XPol between 2007 and 2010 and in at least six supercells observed by RaXPol in 2011–2013. A possible LRR in a tornadic supercell was observed by a C-band Terminal Doppler Weather Radar (TDWR) located near the Dallas Love Field airport (TDAL) on 3 April 2012 (Figure 31). Unfortunately, the TDWR network is not polarimetric, so analysis is limited to Z_H and V_R. As with the previously-examined LRR cases, a local minimum in Z_H marked the LRR observed by TDAL along a narrow zone between the hook echo and the rear section of the forward-flank echo.

In all cases, the LRR is located near the rear of the convective storm, extending from near the inside edge of the hook echo then "leftward" (typically northward given an easterly storm motion) into the main body of the echo (Figure 32a). In most of the observed cases, the depression in Z_H' is 5–15 dBZ, though a local reduction of greater than 20 dBZ is observed in at least one case. The width of this feature ranges from ~300 m to ~1 km, and it is often most evident below approximately 2.5–3.0 km ARL. Associated with the ribbon of reduced Z_H is almost always an equally-narrow zone of reduced Z_{DR} located either coincident with the Z_H minimum or within approximately one-half the width of the Z_H depression. In a few cases, the LRR is associated with little or no discernible variation in Z_{DR}, and in only one case is the Z_{DR} lowest along the leading (often east) edge of the LRR. In the majority of the remainder of the observed

cases of the LRR, the lowest Z_{DR} is found either centered with the LRR or along the rear edge of the LRR.

In general, the measured Z_{DR} minima are in the 0–2 dB range, yielding local depressions of 2–5 dB relative to the surrounding areas. In most cases, there is little reflection of this signature in K_{DP} or ρ_{hv}, and there is little consistent anomaly in the V_R field (e.g., some cases suggest radial convergence along the LRR, one case shows tightly-spaced cyclonic vortices, and some cases show no distinct heterogeneity near the LRR). However, there are some cases in which it appears that hail is present within or very near the LRR as inferred from the Z_{DR} and ρ_{hv} fields (e.g., Figure 20, Figure 26-29) keeping in mind that hail observed at X band is not necessarily associated with high Z_H (Figure 1) as it often is at S band. The majority of cases in which an LRR was observed were associated with tornadic supercells, though the sample size is too small to infer any possible relationship between the LRR (and processes responsible for the LRR) and tornado occurrence.

b. Reduced mid-level ρ_{hv} to the left of the BWER (LoRB)

A vertical cross-section along a radial through the convective updraft of a supercell observed on 29 May 2012 (Figure 33) reveals a region of very low ρ_{hv} aloft. The values of ρ_{hv} within a sloped layer between 6 and 10 km AGL are primarily in the 0.1–0.3 range, coincident with negatively-biased Z_H' of 10–35 dBZ.

The BWER (Chisholm 1973) typically encloses the updraft of strong convective storms, as very strong vertical velocities quickly loft precipitation upward. Away from the strongest part of the updraft, weaker vertical velocities more slowly evacuate

precipitation from the area, allowing larger particles to fall earthward (e.g., hydrometeors for which the terminal velocity exceeds the updraft's vertical velocity). In at least nine supercells on which UMass XPol and several more on which RaXPol collected data (Table 3), anomalously low ρ_{hv} was found along the left side of the BWER (where "left" is relative to the storm motion vector; Figure 32b). Oftentimes, this area of reduced ρ_{hv} was located adjacent to and rearward from the top of the Z_{DR} column or rearward from the northwest extent of the Z_{DR} ring. For simplicity, this feature will be referred to as the LoRB (**Lo**w $\boldsymbol{\rho}_{hv}$ on the left and rear edge of the **B**WER).

One example of this feature is observed in a supercell that occurred in eastern New Mexico during the afternoon of 17 May 2010 (Figure 34). Rearward and to left of the BWER evident in Z_H' (Figure 34a) is an expansive region of $\rho_{hv} < 0.55$ collocated with the periphery of the BWER (characterized by Z_H' of 30–45 dBZ, enclosed by the black ellipse in Figure 34a). Much of the area that has low ρ_{hv} has Z_{DR}' near 2 dB, although the Z_{DR}' field has high variability in this location (unsurprising given the low ρ_{hv}). It is possible that there are mixed phase hydrometeors with complex shapes residing in the northwest wall of the BWER, which would account for the low ρ_{hv}, and the positive Z_{DR}' suggests the possibility of oblate, water-coated hydrometeors, though resonance effects associated with non-Rayleigh scattering may also yield positive Z_{DR}' even without appreciable oblateness. Tumbling, wet graupel or hail may also help explain the combination of Z_{DR}' near 0–2 dB, Z_H' of 30–45 dBZ, and ρ_{hv} of 0.40–0.55. Two soundings launched east of the supercell by mobile groups associated with VORTEX2 (not shown) measured winds that yield southwest-to-northeast-oriented

shear within the 6–8 km AGL layer. As such, the LoRB in this case is located to the left of the BWER and left of the shear vector near the layer in which the LoRB is most evident.

A reconstructed RHI (Figure 35) created along the 313° azimuth marked by the black line in shows a core of $Z_H' > 35$ dBZ observed to a height of ~8 km AGL at a range of 19–22 km. A minor upward extension of $Z_{DR}' > 2$ dB is observed near the base of this feature up to ~4 km AGL. Above this area of relatively enhanced Z_{DR}', there is a region of ρ_{hv} between 0.4 and 0.8 (marked by the black outline in Figure 35a-b) in the 4–10 km AGL layer. This area of extremely low ρ_{hv} persisted from the start of the deployment at 2215 UTC to approximately 2253 UTC. More than an hour after the data in Figure 34 were collected, we observed fallen hail up to 6.3 cm (2.5 inches) in diameter in an area across which this supercell tracked.

Similar areas of reduced ρ_{hv} are evident leftward and rearward of two BWERs associated with two primary updrafts sampled on the evening of 18 May 2010 (Figure 36). In this case, ρ_{hv} of 0.45–0.60 occurs within the left and rear sections of the BWERs, where Z_H' as high as 50 dBZ is measured. In contrast to the 17 May 2010 case, however, the LoRB is located beyond the area of $Z_{DR}' > 1$ dB. However, the Z_{DR}' is quite variable, almost seemingly "noisy", in the LoRB, unsurprising given the relatively low ρ_{hv}. The effects of particularly strong attenuation in Z_H' are apparent in the northwestern part of the eastern BWER (seen as "shadowing" in the Z_H'), where enhanced increase in Φ_{DP} with range is observed. Significant heterogeneities in particle composition and size distributions can result in large gradients in Φ_{DP} (implying large gradients in attenuation rates), signaling potential complications from nonuniform beam

filling [often seen as significantly reduced ρ_{hv} downrange of the initial Φ_{DP} gradients; Ryzhkov (2007)].

Another example of the LoRB is shown in Figure 37a–b; the observed supercell that occurred on 31 May 2007 is characterized by $\rho_{hv} < 0.7$ (with local minima to ~0.50) in an area Z_H' of 30–45 dBZ. Areas of $\rho_{hv} < 0.7$ extend to the top of the scanned domain in this dataset, so the zone of low ρ_{hv} extends upward to a height of at least 5.5 km ARL. A final and less extreme example of reduced ρ_{hv} along the rear edge of the BWER comes from data collected in northern Oklahoma on 24 May 2008 (Figure 38). Rearward of the BWER is an area of reduced ρ_{hv}, though the magnitude of the reduction is significantly less than that seen in Figure 34.

It is important to mention that nonuniform beam filling (NBF) can bias polarimetric measurements and detrimentally affect the quality of the measurements. Ryzhkov (2007) noted that NBF typically results in radially-oriented "streaks" of reduced ρ_{hv} beyond the area of significant NBF [c.f., Figs. 1–3 in Ryzhkov (2007)] since NBF is, essentially, a range-cumulative effect. Although NBF scales with radar frequency (i.e., stronger NBF at X band than at S band), the convective phenomena scanned by these mobile radars often occur within 30 km of the radar and, in some cases presented in this paper, within 10 km. At a range of 20 km, for example, the radar resolution volume size is 150 m in range with a cross-sectional diameter of approximately 436 m. Undoubtedly, the measurements at and radially-beyond areas in which NBF is present are being biased by the NBF. However, NBF does not appear to be a primary reason for the appearance of the LoRB.

The LoRB described above may be similar to the linear depolarization ratio (LDR) "cap" discussed by Hubbert et al. (1998), wherein increased LDR and reduced ρ_{hv} was observed at the top of the Z_{DR} column in a Colorado supercell. The so-called "LDR cap" was also discussed in Kennedy et al. (2001), in which it was postulated that areas of relatively large LDR located atop the Z_{DR} column in the 0ºC and -20ºC layer of nonsupercell storms were likely associated with regions of hail growth. Jameson et al. (1996) observed a similar structure in Florida thunderstorms and attributed it to the freezing of supercooled raindrops. In UMass XPol and RaXPol cases, the reductions in ρ_{hv} are much greater than those observed in Hubbert et al. (1998). Typically, radar volumes containing meteorological scatterers tend to be characterized by relatively high ρ_{hv}, and the values of ρ_{hv} measured in the observed LoRB cases (e.g., $\rho_{hv} < 0.50$) are typically thought to be in the realm of non-meteorological scatterers (e.g., biological scatterers, ground clutter, etc.). The presence of such low ρ_{hv} collocated with relatively large $Z_{H'}$ likely is the result of very significant resonance effects associated with non-Rayleigh scattering that can occur at X band in the presence of large, mixed-phase hydrometeors with varying shapes and of varying sizes.

Others have observed reduced ρ_{hv} aloft in reference to the ρ_{hv} ring, but note that the LoRB is different than the ρ_{hv} ring highlighted in KR08, Payne et al. (2010), and Palmer et al. (2011). Picca and Ryzhkov (2012) observed low ρ_{hv} above the ambient freezing level in a supercell sampled by polarimetric S- and C-band radars attributed to areas of large hail growth, but that discussion did not address the relationship between the BWER and particularly low ρ_{hv}. KR08 and Kumjian et al. (2010a,b) discussed low ρ_{hv} aloft as a proxy for updraft location. If the BWER is nearly centered on the updraft,

however, then the observations of the LoRB presented in this paper mean that the very low ρ_{hv} within the LoRB is offset, perhaps substantially (at least 5 km in several storms), from the center of the updraft.

c. Other polarimetric signatures observed in supercells

Since 2008, the collection of volumetric data (that is, data from near the surface to 8+ km AGL) has been prioritized, allowing for the examination of structures within the polarimetric fields near and above the freezing level of many of the storms on which data were collected. For the most part, many of the previously-seen polarimetric signatures are evident in various datasets collected by UMass XPol and RaXPol. For example, mid-level Z_{DR} columns, rings, or half-rings are apparent in data from 18 May 2010 (Figure 36), 31 May 2007 (Figure 37), 24 May 2008 (Figure 38 and Figure 39), and 22 May 2008 (Figure 40).

On 18 May 2010, two BWERs associated with the updrafts of two severe thunderstorms were associated with rings of enhanced Z_{DR}' (Figure 36b), with values of 3 dB to nearly 6 dB. Located with the eastern ring is a similarly-shaped ring of enhanced Φ_{DP} (Figure 36c), likely resulting from significant δ from non-Rayleigh scattering. Note that the accumulated increase in Φ_{DP} with range down-radial of the northwestern section of the eastern BWER is co-located with the "shadowing" in Z_H' that is indicative of substantial attenuation in the same area. The radially-oriented reduction in ρ_{hv} in the same area may be the result of both reduced SNR and NBF. Differential attenuation is seen as radially-oriented reductions in Z_{DR}' through and beyond the left rear section of both BWERs.

A supercell in the Oklahoma panhandle on 31 May 2007 exhibited many of the above-mentioned polarimetric signatures. On the 11.7° elevation angle scan, a Z_{DR} half-ring is apparent (Figure 37d), located on the inflow side of the supercell and beyond which differential attenuation is present [an observation similar to that seen in Palmer et al. (2011)], consistent with the observations of KR08. Above the rear-most extent of the Z_{DR} half-ring is a large area of very low ρ_{hv} (Figure 37b). At higher elevations, such as on the 18.0° scan (Figure 37f), a complete ρ_{hv} ring is apparent. Some reduced ρ_{hv} is located to the north of this ring. Again, it is likely that mixed phase hydrometeors reside within the ρ_{hv} ring.

The top extents of Z_{DR} and K_{DP} columns [Figure 38b,c; the latter of which is located rearward of the former, consistent with observations by KR08 and Hubbert et al. (1998), among others] are evident in data from a tornadic supercell that occurred on 24 May 2008 (Figure 38). The radar beam height at the center of the BWER in Figure 38a is ~6.3 km ARL, or more than 2 km above the ambient freezing level (~4.1 km AGL determined from nearby radiosonde data). An attenuation-corrected, reconstructed range-height indicator (RHI) plot through the BWER clearly displays the weak echo hole associated with the updraft (Figure 39a). A significant upward extension of $Z_{DR} > 1$ dB is evident along the edges of the BWER, with the highest Z_{DR} associated with the echo overhang at a range of approximately 7–10 km from the radar; K_{DP} in the echo overhang is quite small. The presence of a K_{DP} column is evident in Figure 39c as $K_{DP} > 5° \text{ km}^{-1}$ nearly collocated with the small BWER and the area of positive Z_{DR}.

Data collected on a northwestern Oklahoma supercell that occurred on 22 May 2008 contain well-defined mid-level Z_{DR} and ρ_{hv} half-rings (Figure 40). The Z_{DR} half-

ring has a diameter of approximately 4.5 km and is characterized by Z_{DR}' of 3–4 dB. Slightly beyond the Z_{DR} half-ring is a ρ_{hv} half-ring (Figure 40c), having a diameter of at least 7 km and minimum ρ_{hv} in the 0.45–0.50 range. The Z_{DR} associated with the ρ_{hv} half-ring is actually 0.5–1 dB lower than farther away from the Z_{DR} half-ring. Little indication of the presence of these polarimetric signatures is found in Z_H, evidence of the significant benefit of the additional data provided by polarimetric radars. *Without such data, it would be significantly more difficult to make any assessments regarding the microphysical characteristics of the radar echoes*. Additionally, the use of polarimetric data can allow one to locate more quickly and easily the location of the updraft and other storm-scale features, an ability that can aid radar interpretation.

To provide two final examples of a mid-tropospheric Z_{DR} features, data collected of tornadic supercells on the evenings of 10 June 2010 and 19 May 2013 are shown in Figure 41 and Figure 42, respectively. In the former case, the supercell possessed a crescent-shaped BWER with astounding visual structure (Figure 41d). The local maximum in Z_H' that is nearly encircled by the crescent-shaped BWER shows very little vertical tilt from the lowest elevation angle (2º) to the highest (16º) at the time the tornado was ongoing and sampled in Figure 41. At the given range from the radar (~30 km), the radar beam height is approximately 7.5 km ARL, yet Z_{DR}' of 3 dB is observed along the inside rear portion of the BWER (Figure 41b). The tornadic supercell on 19 May 2013 possessed a thin horseshoe-shaped Z_{DR} ring denoted by the black arrow in Figure 42.

The Z_{DR} arc described in KR08 has also been observed within supercells observed by X-band mobile radars [cf. Fig. 10 in Snyder et al. (2010)]. In datasets from

UMass XPol and RaXPol, however, there is sometimes a local maximum in Φ_{DP} along or very near the location of the Z_{DR} arc, beyond which Φ_{DP} decreases with range. There seems to be two primary reasons why this occurs. First, according to (1), a gradient in δ such that δ decreases with range more quickly than $2 \times K_{DP}$ results in Φ_{DP} decreasing with range. In some cases, an apparent "δ arc" associated with the Z_{DR} arc is seen. For example, on the center-right side of the first column of Figure 43, to the immediate south of the 30 dBZ isoecho contour, Φ_{DP} is locally maximized in the region of very high Z_{DR}' (> 5 dB) with ρ_{hv} between 0.85 (along the far edge of the echo) and ~0.98. Similarly, in the right column of Figure 43, the area marked along the Z_H' gradient is characterized by $Z_{DR}' > 5$ dB with $\rho_{hv} > 0.96$. This is not completely unexpected considering the likely microphysical composition of hydrometeors within the Z_{DR} arc – namely, DSDs that have significantly large mean drop diameter with a dearth of small drops yielding high Z_{DR}.

A second reason why Φ_{DP} may decrease slightly with range along the far right side of the forward-flank downdraft is that the intrinsic K_{DP} may be less than 0° km^{-1}, which may occur in hail (Figure 1). Outside of the Z_{DR} arc, gradients in δ may be located along the edge of the forward flank downdraft echo nearest the storm inflow region in areas of implied hail fall (typically characterized by relatively low ρ_{hv}); hailstones may also have a particular shape and size such that resonance effects create intrinsic $K_{DP} < 0°$ km^{-1}. Examples of the locally-maximized Φ_{DP} in areas that likely contain appreciable amounts of hail are seen in the two rearward enclosed areas in both the left and center columns of Figure 43; the eastern enclosed areas in both columns appear to be associated with the Z_{DR} arc and are likely primarily rain (because $\rho_{hv} >$

0.95). Regardless of whether the cause for the Φ_{DP} peak is attributable to resonance effects from large drops in the Z_{DR} arc or hailstones along the edge of the primary echo, it is difficult to remove the effect of gradients in δ along the edge of the primary echo when calculating ϕ_{DP} and K_{DP}. As a result, it is not uncommon to have $K_{DP} < 0°$ km^{-1} on the immediate inside edge of the Z_{DR} arc and along the right edge of the precipitation echo, which detrimentally affects attenuation estimates and hydrometeor classification . This is usually not a problem at S band because the change in δ with changing drop diameter is significantly smaller than that which occurs at C and X bands.

Although there seemingly is not always reduction in Z_{DR} and ρ_{hv} associated with hail at X band, there are cases in which a very prominent low-level hail signature is evident. For example, a supercell that occurred in southwestern Oklahoma on 23 May 2011 has a large region of 10–45 dBZ Z_H' collocated with a region of -1.5–1.0 dB Z_{DR}' and 0.5–0.8 ρ_{hv} (area enclosed by the black curve in Figure 20). We observed hailstones exceeding 10 cm in diameter near the town of Gotebo before data collection began. In fact, the largest hailstone ever recorded in Oklahoma was produced by this supercell 25–30 minutes before the data in Figure 20 were collected. Large hail exceeding 2 cm was observed intermittently during the deployments presented in those figures. In addition, a polarimetric three-body scatter signature [PTBSS; Hubbert and Bringi (2000); Picca and Ryzhkov (2012); Mahale et al. (2013)] is evident intermittently throughout the deployments; the spike is characterized by radially-oriented and decreasing "streaks" of Z_H' downstream of high Z_H'. This area is characterized by $\rho_{hv} <$ 0.3, $V_R \pm 5$ m/s, and $Z_{DR}' \sim 2$ dB with relatively high variance in Z_{DR}'. Other examples of

polarimetric three-body scatter signatures within supercells observed by RaXPol on 23 May 2011, 18 March 2012, and 17 April 2013 are presented in Figure 44.

There are times at which it is difficult to ascertain the hydrometeors and/or signatures that characterize a specific area of convective storms. A strong supercell on the afternoon of 17 April 2013 in southwestern Oklahoma contained a prominent low-level hail signature at 4° elevation angle characterized by relatively high Z_H', 0-2 dB Z_{DR}', and ρ_{hv} between ~0.6 and 0.7 (Figure 45). At a higher elevation angle (e.g., 10°) this area of implied hail has similar characterizations, but interpretation is complicated by the emergence of a zone of $\rho_{hv} < 0.3$ downradial from the hail core. Since attenuation within the supercell is severe, the signal reaches extinctions before the rear edge of the cell. As such, it is now known if the area of $\rho_{hv} < 0.3$ represents a polarimetric three-body scatter signature or an area affected by NBF. V_R within this downradial zone is +5 m s^{-1}, which is unusual, at least for S-band observations of the PTBSS (Mahale et al. 2013). The highest elevation angle used during this deployment (18°) is still relatively low in altitude given the range of the storm from the radar. However, there are hints of the lower part of a BWER being sampled as an arc of Z_H' ~ 15 dBZ is seen to the southeast of the notch of the hook echo. This is noted because an area of very low ρ_{hv} is observed along the southern edge of the rear of the forward-flank echo directly north of the radar coincident with relatively high Z_H'; this area is likely a LoRB. There are at least two radially-oriented streaks of low ρ_{hv} at the east and west edges of the LoRB that likely are the result of NBF.

Polarimetric tornado debris signatures have been observed previously by X-band radar (e.g., Bluestein et al. 2007a,b). RaXPol observed this signature at close range (3–

10 km) on 24 May 2011 (Figure 25), 19 May 2013 (Figure 26 and Figure 27), and 31 May 2013 (Figure 29). On 19 May 2013, a violent tornado was sampled at < 4 km range west of Shawnee, Oklahoma; the debris signature (left column of Figure 46) is observed as a compact area of high Z_H' (e.g., >50 dBZ), Z_H' ~ 0 dB, a strong V_R couplet (e.g., 151 m s^{-1} ΔV across the tornado), and a ~1.5–2 km wide area of ρ_{hv} <0.7. An even more intense tornado (i.e., maximum V_R exceeding 130 m s^{-1}) was sampled by RaXPol at 3–5 km range on 31 May 2013 near El Reno, OK. Data collected at 2325 UTC reveal a "star-shaped" pattern in the debris signature as the tornado developed significant multiple vortex structure (center column of Figure 46). The width of the debris signature as measured by low ρ_{hv} at this time was 2–2.3 km. Several minutes later, upon leaving the previous deployment location, the debris signature of the primary cyclonic tornado reached nearly 5 km in diameter (right column of Figure 46). In addition, a strong anticyclonic tornado was observed to the southeast of the very large cyclonic tornado and was also associated with a debris signature. The radar was operated in rapid-scan mode during all times shown in these examples, so there is unprecedented opportunity for future work to examine the evolution of the tornado and tornadic debris signature in great detail.

Chapter 6: Polarimetric Signatures in Numerically-Simulated Supercells

There are three primary questions to be examined in this chapter:

1. Can the model and emulator reproduce some of the commonly-observed polarimetric signatures? Where should differences between the observations and simulations be greatest based on the limitations of the simulation system?
2. What are the microphysical compositions of the hydrometeors associated with the polarimetric signatures? Do these differ in different kinematic environments? How are the signatures affected by radar wavelength?
3. Are there prognostic tools available to indicate changes to the structure or evolution of the supercell based upon the structure or evolution the simulated polarimetric signatures?

The primary focus of this section will be on three signatures that are commonly found near and above the environmental freezing level – the Z_{DR} column and ring, the K_{DP} column, and the ρ_{hv} (half) ring. Comments regarding other signatures – such as the low-level hail signature and the Z_{DR} arc – will be made where appropriate but will be covered in significantly less detail. The latter questions will be taken together for each of the three primary signatures to be examined. Since it is important, the reader is reminded that, using the sounding that acts as the initial base state for all simulations (Figure 10), the environmental freezing level is at ~ 3800 m AGL and the 0° C height of the surface parcel is ~4800 m AGL.

Although all simulations were run to 10,800 s (i.e., 3 hours) and the grids were translated to try to keep the primary supercell near the center of the grid, some of the simulations experienced a boundary condition problem near the end of the simulation window. This problem primarily affects the stronger shear cases after ~9,000 s. The strong easterly low-level winds from the eastern lateral boundary tend to increase as storm inflow intensified on with strengthening storm-scale horizontal pressure gradients. In the *25q10* simulation, for example, a "smeared" zone of extremely strong low-level winds (>60 m s^{-1}) approaches the updraft from the eastern boundary around 10,000 s simulation time. This artificial enhancement of the low-level flow results in a series of intense tornado-like vortices. Since the convective storms do not move at a constant speed and bearing, determining the optimal grid translation speed is often difficult if one wants to keep the primary supercell away from lateral boundaries. In addition, many simulations produced more widespread precipitation towards the end of the simulation window, resulting in more widespread storm interactions and collisions. As a result, the analyses examined in this chapter will primarily use data from the 1,800–9,000 s period before this lateral boundary problem becomes more of an issue for some of the simulations and before more widespread convective interference occurs. An obvious solution to this problem is to expand the grid box in the horizontal, and, although it comes at significant computational expense, future simulation likely will use a larger domain.

Even though eight simulations are run at the highest resolution for this project, this is still a relatively limited sample size. As such, it is not possible to attribute all differences in the polarimetric structures of simulated supercells to differences in the

shear profiles. Supercell evolution is extremely non-linear, and minor changes to a shear profile may result in significant changes to the structure and evolution of the simulated convective storms. As a result, the most substantial portion of this section will focus on aggregating all simulations to assess the relationship between the signatures and the microphysical and/or kinematic characteristics of the simulated supercells. Results from the "weak" vs. "strong" shear simulation, straight vs. half-circle hodograph simulation, and other subsets will be examined as well, but the very limited sample size (i.e., four simulations in each "weak" or "strong" shear group and two simulations in each hodograph "shape" group) limits conclusions that can be drawn.

All discussion about the moments of the hydrometeor size distributions in this chapter refer to the quantities predicted by the microphysics scheme. For example, the q_r, z_r, and N_{tr} are those directly predicted from the model and not the fractional-water-modified values. The polarimetric fields that are shown do include, except where noted, fractional water on the ice species in appropriate areas, which means that the actual rainwater mixing ratio, for example, in a volume of mixed hydrometeors will be less than the q_r shown since some of the rainwater will be transferred to hail and thus will be removed from the actual rain field.

a. Polarimetric signature reproducibility

It is prudent to make sure that the signatures and structures that have been observed in nature are actually captured by the emulator and simulations. After all, if basic structures are not represented well, it would be of little benefit to examine the

microphysical structure of the signatures or the relationship between storm evolution and signature evolution.

Although the radar quantities for monodispersed distributions presented in Figure 1 are, to varying degrees, different when different radar wavelengths are used, it is easier to get a feel for the practical effects of these differences using "real" hydrometeor distributions seen in convective storms (at least insofar as the distributions that are produced by the MY3 used in this study are consistent with "real" observations). In some areas (that is, for some distributions and species), the radar quantities at S and X bands are relatively similar; in areas of all rain with relatively wide distributions, for example, there is little difference in Z_H at S and X bands (see the right 25% of the left-most column in Figure 47). However, as seen in Figure 1, one should expect significant differences in radar variables when resonance effects are more pronounced, such as when there is in large hail.

The so-called low-level hail signature discussed by KR08 and observed in S band radar data is typically characterized by very high Z_H and relatively low Z_{DR} and K_{DP}. The microphysics and emulator simulate the low-level hail signature quite well in the S-band calculations presented in Figure 47, noting that the area of reduced Z_{DR} has significant geospatial association with the D_{mh} field (Figure 48d). However, the appreciable reduction in Z_{DR} in the presence of hail at S band is not seen in the X band calculations. Where Z_{DR} at S band is primarily in the 0.5–2 dB range where $D_{mh} > 1$ cm, the Z_{DR} at X band is > 3 dB. At both wavelengths, ρ_{hv} (third column of Figure 47) drops significantly within the area of larger hail; S band ρ_{hv} is 0.9–0.95 and X band ρ_{hv} decreases from ~0.95 to < 0.50 as D_{mh} increases from 1 cm to 3.5 cm. The K_{DP} field is

less affected by hail, in general, but resonance effects are evident in the K_{DP} data at X band as areas of $K_{DP} < 0°$ km^{-1} are found in some of the areas of large hail. Typically, K_{DP} is relatively immune to hail (which is part of the reason why it is being used for quantitate precipitation estimation) except when resonance effects from hail are more prevalent than the more robust influence from rain.

On the positive side, many of the previously-identified signatures observed in supercells seemingly are reproduced by the model and emulator, at least when the fractional water is handled as it is in this project [i.e., following Dawson et al. (2013)]. The simulations reproduce polarimetric structures that look very similar to the Z_{DR} column and ring, ρ_{hv} (half) ring, and the K_{DP} column; see Figure 49 for an example from 4,800 s into the *15q10* simulation at a height of ~5400 m AGL. In this particular case, the reduction in ρ_{hv} at X band is very significant (minimum < 0.4), and this is reasonable in light of some observations presented in Chapter 5 (e.g., Figure 34–Figure 37).

There is one potential issue that should be addressed. Perhaps frustratingly, few simulations produce semi-circular BWERs as some observations have shown, although some simulations do have a crescent-shaped minimum is Z_H along the eastern side of the updraft. The area near and west of the center of the updraft typically is associated with high Z_H and relatively high q_r in the model. The difficulty (or inability) for (some) bulk microphysical schemes to produce a BWER has been noted by others (e.g., Tripoli and Cotton 1980; Straka and Rasmussen 1997). The culprit appears to be the too-rapid production of rainwater in the updraft through aggressive autoconversion. If rain is produced too quickly, it occurs too low (in altitude) within the updraft, which decreases

the likelihood of seeing a BWER (Tripoli and Cotton 1980). Straka and Rasmussen (1997) present an Eularian-based method to account for Lagrangian information (such as the residence time of parcels within a given environment and/or undergoing a particular microphysical process), but such a method is not included in MY3. The purpose of a Lagrangian or semi-Lagrangian technique is to track the residence time of moisture within the updraft, thereby allowing for a natural time lag/delay between the time a parcel reaches saturation or supersaturation and the time at which appreciable rainwater is produced. The non-obviousness of BWERs in some of these simulations is slightly disconcerting considering how some of the polarimetric signatures seem to be spatially associated with BWERs. Even though only crescent-shaped BWERs are produced in these simulations, common polarimetric signatures still are produced in the simulations, indicating that the mechanisms or processes responsible for more traditional BWERs are not entirely responsible for the observed polarimetric signatures.

b. Structure and evolution of simulated signatures

1) Z_{DR} columns and rings

(i) KINEMATIC AND MICROPHYSICAL COMPOSITION

The maximum heights of $Z_{DR} > 1$ dB in columns above each horizontal gridpoint ($Z_{DR_maxheight}$) for a selected time (t ~ 5,040 s) for each simulation reveal the general shape of the Z_{DR} columns (Figure 50) associated with the cyclonic supercells produced in each simulation, although the structures obviously are not static. In general, the highly-curved hodographs tended to have much more cylindrically-shaped Z_{DR} columns; the straight-line hodographs produced Z_{DR} columns that were oriented

elliptically in the east-west direction. Before ~ 6,000 s, the *15r10* and *15r10_057* simulations produced Z_{DR} columns oriented primarily in the N-S direction, with a distinct narrowing on the north side of the column. In addition, the width of the Z_{DR} column tended to be considerably greater for the "strong" shear hodographs than the "weak" shear hodographs (compare left column of Figure 50 with the right column). As would be expected given the hodographs used in this study, all curved soundings produced a dominant cyclonic supercell, whereas the straight hodographs produced splitting supercells. The Z_{DR} columns in both of the straight hodograph and all of the "weak" shear simulations tended to be relatively unsteady with more "pulse-like" behavior (e.g., center and right columns of Figure 51), whereas the other "strong" shear simulations (particularly the 25q10 simulation – left column of Figure 51) tended to be considerably steadier.

In many simulations, Z_{DR} columns tended to be "shed" from the west side of the updraft, a process in which relatively small areas of $Z_{DR} > 1$ dB at higher altitudes (e.g., > 4,500 m AGL) separated from the primary Z_{DR} column. In the curved hodograph simulations, the "shedding" directed the smaller columns northward with a period of approximately 6 minutes; the straight hodograph simulations produced Z_{DR} columns that, when "shed", advected northeastward to the north of the primary updraft.

Despite differences in the size and shape of the Z_{DR} columns, the microphysics accompanying the simulated Z_{DR} columns were similar in all runs. In general, the Z_{DR} columns were located to the west of the center of the maximum vertical velocity within the updraft. If the BWERs observed in Chapter 5 are a valid proxy for the center of the

updraft, then the locations of the Z_{DR} columns relative to the updrafts in the simulations agree well with observations.

One example, consistent with the presentations of the Z_{DR} column from other simulations, is selected from the *25r10* simulation and shown in Figure 52a (where the contours are W at 5 m s^{-1} intervals). The peak updraft velocity at this height (~5,600 m AGL) is 35–40 m s^{-1}. The Z_{DR} column, which is the area of 3–5 dB Z_{DR}, becomes much less distinct above this level in this particular simulation. The air temperature (T) is ~268 K where the Z_{DR} column is located (Figure 52b), and the Z_{DR} column is spatially associated with relatively high q_r (Figure 52c). D_{mr} within the primary column is 1–1.5 mm with $\alpha_r \sim 0$. The column also contains considerable hail (q_h; Figure 52e) with low D_{mh} and low α_h (e.g., $D_{mh} < 5$ mm and $\alpha_h \sim 0$; Figure 52d). Since both hail and rain are present in significant quantities, the fractional water parameterization apportions some of the rain to the hail; the mean f_{wh} (Figure 52e) within the column is ~30%. There is very little graupel present in the Z_{DR} column.

The above results are quite consistent with expectations. The raindrops within the strong updraft freeze into frozen drops, which the MY3 scheme handles as small hailstones according to the probabilistic freezing scheme of Bigg (1953). As implemented in MY3 [see (38) in Milbrandt and Yau (2005b)], the rate of change of N_{tr} owing to the freezing of rain to hail is

$$\Delta N_{tr}]_{FZrh} = -B[\exp(A \times T_c) - 1]\frac{\rho \times q_r}{\rho_w} \qquad (6.1)$$

where T_c is the air temperature in degrees Celsius, ρ is the density of the air, and ρ_w is the density of water. In the MY3 scheme, the default values of A and B are 0.66 K^{-1} and 100 m^{-3} s^{-1}, respectively.

In most simulations at most times, the maximum height of the Z_{DR} column is quite similar (~5,600 m AGL), although the *25r10_057* simulation is a notable exception (wherein the top of the Z_{DR} column easily surpasses 6,000 m AGL). Although this height is ~2,800 m above the environmental freezing level, it is only ~800 m above the parcel-trajectory-determined freezing level, which is lower than observations and explicit bin simulations have shown (e.g., Kumjian et al. 2012). Sensitivity tests reported in Kumjian et al. (2012) indicate that, in their model, the Z_{DR} column height was inversely proportional to the median drop size. If the autoconversion scheme used in MY3 results in the development of rain too early and too low within an updraft, it is possible that the DSD would have a larger median diameter than found in nature (since the collision and coalescence processes would begin earlier and lower within the updraft), which would result in a Z_{DR} column that is lower than it otherwise would be. Above ~5,600 m AGL, most of the q_r is converted to q_h, resulting in relatively dry hail with relatively low Z_{DR}. The Bigg (1953) parameterization requires two constants to be chosen *a priori* [A and B in (6.1)], and it is possible that these constants may need to be modified to allow Z_{DR} columns to reach heights similar to those observed in nature; the rate of drop freezing can be slowed by choosing different constants in the drop freezing parameterization. At considerably greater heights, $Z_{DR} > 2$ dB is observed within ring-like structures in some of the simulations, and this will be discussed later in this section.

The vertical structure of the simulated Z_{DR} columns can be better illustrated with vertical cross-sections. In the *25r10* simulation (Figure 53), a well-defined upward extension of high Z_{DR} (> 3 dB) can be seen at heights to ~5,600 m AGL, and the column is considerably wider at X band (Figure 53b) than at S band (Figure 53a). The column is

spatially correlated with the updraft. Enhanced Z_{DR} is seen near the top of the column, particularly at X band, likely the result of the fractional water parameterization as water and hail coexist in this area. Immediately adjacent to the inside edge of the Z_{DR} column (located near 80 km along the abscissa) is a downward protrusion of relatively low Z_{DR}. This downward protrusion of Z_{DR} ~ 2.5 dB is associated with q_h ~ 0.004 (Figure 53d). At S band, the Z_{DR} column is considerably narrower than it is at X band, and two areas of reduced Z_{DR} are observed at S band where the X band Z_{DR} column is shown – one along the west side of the column in the 3–5 km layer and one along the eastern side of the column from ~5 km down to the surface. Both of these areas have low q_h (Figure 53d). The former is associated with D_{mh} of 2–3.5 cm, while the latter is associated with D_{mh} of 1–1.5 cm (Figure 53c). The entirety of the Z_{DR} column is associated with D_{mh} between 3 and nearly 4 mm (Figure 53e).

Some of the simulations also show well-defined Z_{DR} half-rings along the eastern periphery of the mid-level convective updraft (e.g., the yellow arrow in Figure 52a). This feature is seen most prominently in the *15q10* and *25q10* simulations, although it is also produced in the *25r10* and *25r10_057* simulations. The supercells in these same simulations also had the highest 0–3 km SRH of the eight simulations (based upon the mean motion of the updraft between 4,800 s and 9,000 s; Table 4). The other simulations generally produce only intermittent and "weak" (i.e., with comparatively limited vertical extent) Z_{DR} rings. The simulations that produced the most prominent Z_{DR} rings also had the strongest mid-level updrafts (Figure 54).This feature appears as a curved band of enhanced Z_{DR} usually emanating from the southeastern periphery of the updraft and arcing around the east side of the updraft. The hydrometeors that make up

the Z_{DR} rings are significantly different, however, than those that produce the traditional Z_{DR} column. In the half-rings, q_r and q_h tend to be small (Figure 52c, e), and the air temperature tends to be considerably colder. Collocated with the Z_{DR} half-ring is a similarly-shaped partial ring of hail with larger D_{mh} (e.g., 1–2 cm in Figure 52d) and larger α_h (~4–6). The magnitudes of the Z_{DR} values within the half-rings are proportional to f_{wh} and D_{mh} of the hail within it. A similar structure is seen at later times in the *25r10* as well (Figure 55).

The pseudo-three-dimensional structure of the Z_{DR} = 1 dB isosurface can be seen in Figure 56, created at 7320 s from the *25q10* simulation. The "primary" Z_{DR} column, highlighted by the black arrow, extends ~2 km above the environmental freezing level. A Z_{DR} half-ring, marked by the blue arrow, wraps around the updraft from southeast through northeast, extending another 1-2 km above the top of the "primary" Z_{DR} column. An echo overhang is implied beneath the blue arrow, where the isosurface slopes to the north with decreasing height (i.e., the isosurface moves northward as one moves to towards the domain bottom).

The appearance of the "traditional" Z_{DR} column and the Z_{DR} half-rings is affected by the frequency of the radar being simulated. As a result of resonance effects within the band of wet hail in the Z_{DR} half-ring, the Z_{DR} values are enhanced at X band compared to S band (Figure 57), as are the values of Z_{DR} within the primary Z_{DR} column. If hail is treated exclusively as being dry, Z_{DR} half-rings are not produced at all, and the Z_{DR} magnitudes within the primary column are reduced by at least a few dB. This sensitivity is a potential source of error given uncertainties about the treatment of mixed-phased hydrometeors in the radar emulator.

The Z_{DR} half-ring at a greater height (e.g., Figure 58) shows similar microphysical compositions albeit with higher q_g. Ground-relative wind vectors at the location of the half-rings are typically directed towards the updraft. One may therefore hypothesize that the Z_{DR} half-ring is associated with the advection of hail into the periphery of the (relatively) warm updraft where it can undergo wet growth (f_{wh} in Figure 58b is 20–35%).

A vertical cross-section through the updraft of the supercell in the *25q10* simulation (Figure 59 and Figure 60) better illustrates the microphysical composition of the Z_{DR} column and half-ring. The primary Z_{DR} column (Figure 59a) is composed of rainwater with high z_r (note the lower-case "z" representing the Rayleigh-assumed rainwater reflectivity factor from the MY3 microphysics in contrast to the emulator-calculated Z_H; Figure 60a), high q_r (Figure 60b), and ~2–3.5 mm D_{mr} (Figure 59b), with a local maximum in Z_{DR} at the top of the column where wet hail and graupel exist (Figure 59c-d). Above the Z_{DR} column, q_h rapidly increases (Figure 60c) presumably as collisional freezing between the depleting rainwater and the hail increases. Near the center and along the eastern periphery of the updraft (i.e., near 80 km on the abscissa), z_r of 10–30 dBZ and $Z_{DR} > 3$ dB extends to considerably greater height than in the primary column. In the Bigg (1953) stochastic freezing relation (6.1), the change in N_{Tr} is proportional to q_r. The reduced q_r (Figure 60b) and greater N_{Tr} within this band results in reduced D_{mr} relative to that found in primary Z_{DR} column (save for the top of the column), which results in a reduction of the number of drops that freeze within the part of the updraft marked by the Z_{DR} half-ring. As a result, rainwater is lofted to considerably greater heights (above 9 km and to temperatures colder than -30° C).

Along the eastern periphery of the updraft, rainwater with D_{mr} near 1–1.5 mm interacts with the western periphery of a core of hail falling outside the updraft (D_{mh} ~ 1–2.5 cm and f_{wh} between 10% and 30%), as well as some wet graupel, resulting in a narrow zone of relatively high Z_{DR}. Relatively large hail (D_{mh} up to ~4 cm) is evident falling from the west side of the updraft above ~ 1 km height. The hail that contributes to the Z_{DR} half-ring is along the earthward-side of a large area of hail aloft; the hail, presumably, is being advected northward (into Figure 59 and Figure 60) on storm-relative southerly mid-tropospheric winds. The variability of α_h along the lower part of the hail zone (right side of Figure 60d above 4,000 m) is very evident, appearing to be the product of sedimentation given the tendency for larger α_h with decreasing altitude. The largest hail in the simulations tends to be found in the lowest 4 km beneath the western side of the updraft (through the inside part of the hook echo is most simulations), but the largest hail above 5,000 m AGL tends to be located within the Z_{DR} half-ring (Figure 59c).

Out of all simulations, the *25r10_057* simulation produced $Z_{DR} > 1$ dB within the primary Z_{DR} column at the highest altitude (e.g., ~6200 m AGL), in this case to nearly the same height as the top of the Z_{DR} ring (Figure 61). Perhaps not coincidentally, that simulation also contained the strongest vertical velocities (at least at ~5500 m AGL; Figure 54b). Much of the eastern part of the Z_{DR} column was associated with relatively low q_r (Figure 61c), which may have allowed rainwater to be advected higher and to colder temperatures before freezing. As with the other simulations, f_{wh} was very high (i.e., > 0.8) and D_{mh} was < 1 mm at the top of the Z_{DR} column. The observed local

maximum in Z_{DR} aloft along the eastern periphery of the updraft (i.e., the Z_{DR} ring) generally was characterized by D_{mh} between 1.0 and 1.5 cm amidst bulk f_{wh} of 0.3–0.4.

KR08 presented several hypotheses for the observed Z_{DR} ring, including the advection of large drops and/or melting ice particles around the midlevel mesocyclone and the entrainment of dry air that preferentially eliminates small drops (thereby raising D_{mr}). In the simulations performed for this study, the former hypothesis appears to be supported by the model results. Since the simulated half-ring is located near the downshear (i.e., easterly hodographs used) edge of the updraft where winds are directed towards the updraft, it is possible that there is some contribution from dry air entrainment. However, the sounding used for the simulations in this study is relatively moist throughout the troposphere, so evaporative potential is rather limited, and therefore the entrainment of dry air is likely to be limited.

Surrounding the Z_{DR} columns to the north through east typically is an arcing band of suppressed Z_{DR} as seen by a local minimum in the maximum height of $Z_{DR} > 1$ dB (Figure 50). This band of reduced Z_{DR} is typically larger and more apparent in the S band data than in the X band data, which is consistent with the notion that hail and/or graupel around the updraft tend to reduce Z_{DR} at S band more than at X band. Statistics regarding the size and/or "intensity" of this "Z_{DR} mote" and storm structure (e.g., hail production, downdraft intensity, microburst frequency, etc.) have not been computed but are valid avenues of inquiry for future work.

(ii) EVOLUTION

A set of quantities was calculated for all simulations and all times between 1,800 s and 9,000 s. Some simulations experienced problems with unrealistically strong near-ground easterly inflow as a result of boundary conditions problem after ~9,000 s, and, in others, additional convective development interfered and/or interacted heavily with the primary cyclonic supercell toward the end of the simulation period. Consequently, analyses generally do not include times beyond 9000 s. See Table 5 for a description of the quantities calculated and the shorthand notation that will be used throughout this section.

Since the Z_{DR} column marks the upward protrusion of rainwater within the updraft above the freezing level, one could posit that the size of the Z_{DR} column should be proportional to the size of the updraft in some manner. Indeed, the simulations bore this out. For example, time series of *zdr33area* and *w33area5* from the *15r10* and *25r10* simulations (Figure 62) indicate a relatively strong relationship between updraft width (in this case, the cross-section of $w > 5$ m s^{-1} at ~3,800 m AGL) and Z_{DR} column width – the Pearson correlation coefficient (hereafter referred to as CC to avoid confusion with the radar variable ρ_{hv}) is 0.85 and 0.55 for the *15r10* and *25r10* simulations, respectively. In some simulations, such as the *15str* and *25q10* simulations, the CC between *w25area5* and *zdr33area* exceeded 0.9. The magnitude of CC between the *qr33area* and *zdr33area* for many of the simulations were also quite high – see, for example, Figure 63 from the *15r10* and *25r10* simulations.

Viewed differently, a scatterplot of *w33area5* and *zdr33area* for all simulations (Figure 64a) reveals a rather strong relationship between updraft size and Z_{DR} column

size (at least in terms of area of Z_{DR} > 1 dB and area of w > 5 m s^{-1} near ~5,600 m AGL). In general, the "strong" shear hodographs were associated with considerably larger updrafts with larger areas of Z_{DR} > 1 dB at ~5,600 m. Similarly, the area of q_r > 0.001 is correlated with the area of Z_{DR} > 1 dB (Figure 64b). The "strong" shear simulations generally produced much larger areas of q_r > 0.001 aloft.

In addition to having wider updrafts and more expansive areas of rainwater aloft, supercells in the "strong" shear simulations generally produced larger areas of D_{mh} > 5 mm at ~5,600 m AGL (Figure 65a), and there was a tendency for greater *zdrmaxheight* with increasing *dmh33sum5mm*. There was not much of a discernible trend in the *zdrmaxheightqrc* with changes in *w33max*, although the "weak" shear cases tended to have weaker updrafts (at least at ~5,500 m AGL) but slightly higher *zdrmaxheightqrc* values. The trend for increasing *maxheightzdr* with increasing *w25max* was apparent but not robust; there was a greater tendency for increasing *zdrmaxheight* with increasing *w25max* in the "weak" shear cases than for the "strong" shear cases.

Some CCs may not be high at zero lag time but increase with different lag periods. One such example is the relationship between *dmh3area1inch* and *zdrmaxheight*. In several of the simulations, there is a distinct peak in CC approximately at a lag time of ~20 minutes. For the *15q10* simulation (Figure 66a), the CC was < 0.10 at lag 0 but increases to >0.45 near a lag of 20 minutes; the local maximum in CC was found such that changes in *zdrmaxheight* preceded *dmh3area1inch* by ~20 minutes. More regular periodicity was seen in the *25r10_057* simulation; there were local peaks in CC near +/- 20 minutes and +/- 55 minutes (Figure 66b). Such occurrences were not observed in all simulations, however.

The magnitude of the CC between all quantities listed in Table 5 for all simulations can be seen in Figure 67. CC > 0.5 was observed between *dmh33sum5mm* and nearly all of the *w*-relevant quantities as well as *zdrmaxheight*, *zdrarea33*, and *zdrarea25*. The maximum value of q_h and the sum of at q_h at ~120 m were positively correlated with the updraft size parameters and with *zdrarea25*. In general, these relatively high CCs are observed for all "strong" (Figure 68) and "weak" (Figure 69) shear simulations, as well as for the half-circle (Figure 70), half-circle with decreasing shear with height (Figure 71), quarter-circle with straight-line shear (Figure 72), and straight-line (Figure 73) simulations. CC > 0.50 was observed between *uh16km_area* and *dmh3max*, *dmh3sum1inch*, *dmh3sum2inch*, *zdr25area*, and *zdr33area* (among several *w*-related quantities).

2) K_{DP} columns

In the Rayleigh regime of drop sizes, K_{DP} scales as $D^{4.24}$, indicating that it is generally a better proxy for q than is Z. In addition, as a result of the reduced ε_r for hail, K_{DP} through ice tends to be very small. Consequently, K_{DP} has been used for rainfall estimates in place of Z_H-only relationships (e.g., Zrnic and Ryzhkov 1996). Consequently, one expects that the spatial orientation of the K_{DP} field will very closely match that of the q_r field. Indeed, this tends to be the case in retrieved K_{DP} from the simulations. For example, from the 25q10 simulation, the area of highest q_r tends to relate well to the field of K_{DP} at S band (Figure 74), particularly where $\alpha_r > 0$. At the time of the analysis in Figure 74, the highest q_h is located at the southwest edge of the echo immediately north of the highest D_{mh}, with generally more limited q_h (~0.001) and

smaller D_{mh} elsewhere. The K_{DP} field is, however, considerably different at X band (Figure 74f); there are significant differences between the q_r and K_{DP} fields. For example, the highest K_{DP} at X band is located at the southern edge of the echo, very near the area of maximum q_r immediately southwest of the highest q_h. North of this area is an area of $K_{DP} < 2°$ km^{-1}. Generally, the local maxima in K_{DP} at X band do not correlate well with the maxima in q_r. Resonance effects from wet hail, in this case, have significantly modified the K_{DP} field, making it much more difficult to interpret K_{DP} from the perspective of q_r. Where hail is absent, K_{DP} at X band tends to be proportional to q_r, particularly where α_r varies little.

The simulations tend to produce K_{DP} columns in similar locations as the "primary" Z_{DR} columns within convective updrafts, although the K_{DP} columns are considerably small in cross-sectional area. One representative example is shown in an east-west vertical cross-section from the *25r10* simulation (Figure 75). The K_{DP} field (colored in Figure 75b) tends to be associated quite well with the q_r field (contoured in Figure 75); maxima in K_{DP} and q_r are located along the western side of the primary Z_{DR} column (Figure 75a) within the updraft. At the height where the most freezing of drops occurs (~5,600 m AGL), there is a significantly-enhanced area of K_{DP}, likely caused by the presence water-coated hail, the scattering properties of which can emulate extremely large raindrops. Since K_{DP} is a better measure of concentration of rainwater than is Z_{DR}, there is no apparent signature in K_{DP} associated with the Z_{DR} ring. This makes sense since the latter is typically associated with relatively low q_r and q_h.

The structure of the K_{DP} columns as viewed by the maximum height of $K_{DP} > 1°$ km^{-1} is similar to that of the Z_{DR} columns (e.g., Figure 75c–d), at least where one

expects to see the primary Z_{DR} column associated with high q_r within the updraft. The primary difference between the two, at least when viewed from this perspective, is the smaller size of $K_{DP} > 1°$ km^{-1} aloft relative to the extent of $Z_{DR} > 1$ dB. The area of enhanced Z_{DR} at high altitudes often observed where lofted q_r interacts with q_h along the eastern periphery of the updraft is not seen in K_{DP}.

The shape of the K_{DP} column at most times during the simulations tends to correspond with the overall shape of the Z_{DR} columns. For example, the straight hodographs (i.e., *15str* and *25str*) are associated with zonally-elongated Z_{DR} and K_{DP} columns, and the more highly-curved hodographs tend to produce more cylindrically-shaped Z_{DR} and K_{DP} columns (neglecting the Z_{DR} half-ring). A similar "shedding" process that is observed in some simulations in the Z_{DR} field is also seen in the K_{DP} field, although the local maxima in K_{DP} tend to disappear more quickly after "shedding" from the primary update. All simulations tend to produce a "mote" of reduced heights of $K_{DP} > 1°$ km^{-1} adjacent to the northern, northeastern, and eastern side of the K_{DP} column. Since this area is along the periphery of the updraft, it is postulated that high q_r is evacuated from these areas (both in the vertical given the location of the strong updrafts and in the horizontal as environment flow tends to advect q_r to the north through northwest of the updraft).

Aggregating all simulations between 1800 s and 9000 s (Figure 67), the area with $K_{DP} > 1$ dB km^{-1} at ~5,600 m AGL was correlated (i.e., CC > 0.5) with *dmh33area1inch*, *qhsum3*, *qhmax3*, *qrarea33*, most of the w-related quantities, *zdrarea25*, *zdrarea33*, and *zdrmaxheight*. In general, the CCs between *kdparea33* and

the aforementioned quantities were higher for the "strong" shear simulations (Figure 68) than for the "weak" shear simulations (Figure 69).

3) ρ_{hv} rings

(i) KINEMATIC AND MICROPHYSICAL COMPOSITION

Observations have identified a band of reduced ρ_{hv} encircling the periphery of a supercell's updraft; this feature is called the ρ_{hv} ring (KR08; Figure 37, Figure 40). Often, it is actually seen as a half ring, like the Z_{DR} (half) ring located along the eastern (downshear) periphery of the updraft. Throughout this section, no distinction will be made between a half ring and a full ring; the feature will be referred to as the "ρ_{hv} ring" throughout, although the appearance of the full ring will be stated when such a structure occurs.

The simulations performed for this study often produce a ρ_{hv} ring. A horizontal cross-section from the *25r10* simulation valid ~5,600 m AGL at X band (Figure 76) shows $\rho_{hv} \leq 0.3$ immediately east of the updraft near the gradient between the updraft and downdraft (Figure 76b–c). As with the Z_{DR} ring, q_h and q_r within the ρ_{hv} ring are relatively low (i.e., < 0.001). The ring is nearly immediately east of an arcing area of locally-minimized Z_H (i.e., the weak echo region) and primarily north of locally-maximized Z_{DR}; the ρ_{hv} ring is considerably more expansive and prominent than the similarly-structured Z_{DR} ring. The area of low ρ_{hv} and the magnitude of the minimum ρ_{hv} are spatially associated with D_{mh} such that, in the case of Figure 76, the lowest ρ_{hv} typically occurs with the larger D_{mh}. The fractional water of hail and graupel affects the Z_{DR} ring more than the ρ_{hv} ring.

A pseudo-volumetric perspective of the ρ_{hv} ring from the 25q10 simulation details the structure of the ρ_{hv} ring (Figure 77). As viewed from the west of the updraft looking to the east, two areas of $\rho_{hv} < 0.8$ can be seen – a horizontally-limited area ~4 km tall near the ground and one taking the form of an arcing band of low ρ_{hv} that is ~4 km in vertical extent centered between 7 and 9 km AGL. The latter is the ρ_{hv} ring, and the height of the ring decreases with northward (leftward) extent around the updraft (left side of Figure 77a). Viewed from above looking downward (Figure 77b), the area of $\rho_{hv} < 0.8$ near the ground is located west and southwest of the primary curved ρ_{hv} ring and to the southwest of the 30 m s^{-1} *w* isosurface. The inner part of the ρ_{hv} ring is within the $w = 30$ m s^{-1} isosurface, and it generally traces the eastern periphery of the updraft.

From mobile X-band radars presented in Chapter 5, the magnitude of ρ_{hv} above the freezing level within these rings typically is less than that associated with previously-published ρ_{hv} rings in S-band radar data. The ρ_{hv} rings produced in these simulations support these observations in terms of the extremely low values of ρ_{hv} that can occur above the freezing level at X band. For example, from the *25q10* simulation, the minimum value of ρ_{hv} along the eastern periphery of the updraft at 4,220 s and ~5,600 m AGL is 0.92, 0.88, and 0.55 at S, C, and X bands, respectively (Figure 78). In addition, the ρ_{hv} ring at X band is considerably larger than that at S band and larger than that at C band, with a "double ring" structure evident at times. Again, this is, seemingly, consistent with observations that reveal extremely low ρ_{hv} within these rings in some supercell datasets from X band mobile radars. The inference from this is that ρ_{hv} at X band may be more sensitive to hail than it is at lower radar frequencies (which can also be inferred from Figure 47).

Significant differences in ρ_{hv} at X and S bands are evident in an east-west vertical cross-section through the updraft in the *25r10* simulation at 7,320 s (Figure 79). At S band, ρ_{hv} is generally greater than 0.9 at all heights within the cross-section, showing little deviation below ~0.98 above 6,000 m AGL. The reduction in S-band ρ_{hv} below that level is associated with increased D_{mh} (contoured in Figure 79a). In contrast, there are very significant reductions in ρ_{hv} above 6,000 m AGL at X band; ρ_{hv} is as low as ~0.3 between 3,000 and 4,000 m, with $\rho_{hv} < 0.85$ extending to a height of nearly 8,000 m AGL. The melting layer immediately below 6,000 m within the updraft and near ~3,000 m east of the updraft is evident as local reductions in ρ_{hv} as well. At this particular time, ρ_{hv} reductions occur on both the east and west sides of the updraft, where $D_{mh} > 1.5$ cm.

(ii) EVOLUTION

The ρ_{hv} rings observed in the "weak" shear simulations tend to be much less steady state than those observed in the "strong" shear simulations. In general, the "weak" shear simulations tended to produce ρ_{hv} rings that were considerably smaller in horizontal extent and had weaker minima than those produced in the "strong" shear simulations (Figure 80). The *15str*, *15r10*, and *15r10_057* simulations all had ρ_{hv} rings generally averaging ~200 gridpoints in horizontal extent at ~5,600 m AGL (as defined by $\rho_{hv} < 0.8$ at X band), whereas the ρ_{hv} rings in the *25q10*, *25r10*, and *25r10_057* simulations averaged ~800-900 gridpoints in horizontal extent. There were two exceptions to this observation – the *25str* simulation only produced very intermittent, ill-defined, and "weak" ρ_{hv} rings (or ρ_{hv} "blobs" since they were not often "ring-like" in

structure) east of the updraft through much of the first ~7,000 s of the simulation, and the *15q10* simulation produced comparatively robust and large (in horizontal extent) ρ_{hv} rings. The absolute maximum ρ_{hv} ring sizes at ~5,600 m AGL were produced by the *15q10* and *25q10* simulations with horizontal extents of ~1,300 and ~1,750 grid cells, respectively. The smallest ρ_{hv} rings occurred in the *15str* and *25str* simulations.

The areal extent of the ρ_{hv} rings at a given altitude where they were observed were, in general, very well correlated with the areal extent of hail at that altitude. For example, the trends between the number of gridpoints with $\rho_{hv} < 0.98$ (S band) or $\rho_{hv} < 0.8$ (X band) and the number of gridpoints with $D_{mh} > 5$ mm at ~5,600 m AGL in the *15r10* are very similar (Figure 81); CCs are 0.78 and 0.91 at S and X bands, respectively. The minimum value of ρ_{hv} at ~5,600 m from all simulations (Figure 67) was strongly negatively correlated with the maximum value of D_{mh} at 5,600 m (*dmh3max*), the area of $D_{mh} > 5$ mm at 5,600 m (*dmh33area5mm*), the areal extent of the ρ_{hv} ring at 5,600 m (*rhvarea33*), and the intensity of the updraft (e.g., *w25max* and *w33max*). Conversely, the size of the ρ_{hv} ring at 5,600 m (i.e., gridpoints with $\rho_{hv} < 0.8$) was strongly positively correlated with updraft intensity (*w25max* and *w33max*), *dmh3area5mm*, and *dmh33max*.

In most simulations, the highest correlation coefficient between the maximum updraft velocity at ~5,600 m AGL (*wmax33*) and the area of $\rho_{hv} < 0.8$ (*rhv33area*) occurred at a lag time of -5 to -10 minutes (Figure 82); the CC was highest for the *25r10* (~0.8), *25r10_057* (~0.6), and *15r10_057* (~0.6) simulations. Both the *15q10* and *25q10* simulations were associated with positive lag times for maximum CC; CCs were low (generally < 0.4) for all other simulations.

4) Other signatures

As noted previously, the low-level hail signature is typically much more apparent in the S-band quantities than in the X-band quantities. In nearly all of the simulations, X-band Z_{DR} in hail in the lower troposphere is not reduced nearly as greatly as is S-band Z_{DR}. Anecdotally, there is observational evidence supporting the notion that, at least at frequencies above S band (e.g., C and X bands), hail, particularly if it is "wet", may be associated with relatively high Z_{DR}. The difficulty in accurately correcting for attenuation and differential attenuation in observed X-band data, however, makes this assessment more complicated. Scattering simulations (e.g., Figure 1) support this as well, although the relationship is highly non-linear. The correct handling of Z_{DR} in areas with hail in the model are heavily dependent upon the accuracy of the scattering matrices (themselves affected by such assumptions as the canting angle distribution, the temperature used in the calculation of the dielectric constant, the angular moments, etc.) as well as the proper modeling of the interaction between water and ice (i.e., the fractional water routine).

All simulations produce a rain field with the largest D_{mr} along the southern part of the forward-flank downdraft (FFD) and with generally decreasing D_{mr} to the north. For example, Figure 83 shows D_{mr} and Z_{DR} for a selected time in the *25q10* and *15r10* simulations, although the general observations were seen in most of the simulations at most of the times during which a mature supercell occurred. In both D_{mr} images, D_{mr} ~ 3–3.5 mm is seen along the south flank of the FFD near the edge of the FFD echo. In several simulations, there is a secondary peak in D_{mr} within the hook echo and a relative

minimum between the two peaks in D_{mr} (e.g., Figure 83a); in others, the band of high D_{mr} extends rearward into the FFD without any significant change (e.g., Figure 83b). Relatively high D_{mr} located along the southern edge of the FFD appears to be consistent with the observations and modeling work reported by KR08.

Although there are UMass XPol and RaXPol observations of the Z_{DR} arc extending along the south edge of the forward-flank echo to the inside part of the hook echo, the simulations typically have the highest Z_{DR} along the south side of the forward-flank echo but ahead of the hook echo (e.g., Figure 83b). At S band, many simulations do show a narrow band of relatively high Z_{DR} extending along the inside edge of the rear part of the FFD echo into the hook echo, but this area of enhanced Z_{DR} appears to be the primary result of hail reducing Z_{DR} along the rear part of the FFD echo and into the hook echo (resulting in a local maximum along the edge of the echo). At X band, however, significant reductions in Z_{DR} in the presence of hail are not seen as often and certainly not to the degree than are observed at S band, which makes the Z_{DR} arc much more subtle in the X-band products.

Aside from intrinsic scattering differences, there may be other causes for the differences in Z_{DR} in hail at S and X bands that pertain to the initial environmental sounding and a limitation of the current MY3 scheme. In nearly all of the simulations, low Z_H is seen in the near-surface inflow of the simulated supercells. This area of light rain is characterized by α_r of 3–7 (Figure 48a); the DSD of this "inflow band" is narrow and dominated by very small raindrops. Since the MY3 scheme has only one rain category and allows for only unimodal distributions, when precipitation characterized by this narrow-but-low-D_{mr} DSD advects into the south edge of the FFD characterized

by higher D_{mr} and much smaller α_r, the former DSD mixes with the latter and results in a significant reduction in D_{mr} along the south edge of the FFD. The reduction in D_{mr}, in turn, potentially reduces Z_{DR}; this is attributable to the requirement that all rain be described by a single gamma distribution (with one mode). This effect may be exacerbated by the sounding used in these simulations, which is very moist and has very high relative humidity in the lower troposphere. As a result, rather limited lifting is required for the parcels to reach their lifted condensation level. It is possible that using a sounding with a drier lower troposphere or, perhaps, greater convective inhibition may result in a more typical Z_{DR} arc.

Although the mid-level ρ_{hv} field in many of the simulations contained a ρ_{hv} ring, no simulations produced the expansive areas of very low ρ_{hv} aloft observed as the so-called LoRB, a signature observed by UMass XPol and RaXPol mobile radars and addressed in Chapter 5. There was a general inability to simulate more cylindrically-shaped BWERs, and there generally were no particularly large areas of very low ρ_{hv} along the northern (i.e., left) periphery of the crescent-shaped BWERs observed in some of the simulations.

Chapter 7: Summary and Conclusions

Much of the past work examining polarimetric signatures associated with supercells in the United States has involved the use of S-band and, in a more limited fashion, C-band radar data (e.g., Ryzhkov et al. 2005b,c; KR08; R08). In this dissertation, examples of many of these commonly-identified polarimetric signatures from two X-band mobile radars were presented. One previously undocumented signature (the LRR) and one signature that has seen little documentation at X band (the LoRB) have been observed in UMass XPol and RaXPol data. The LRR is characterized by a narrow zone of reduced Z_H and Z_{DR} that is located near the location where the hook echo or appendage along the upshear side of a supercell interacts with the rear part of the FFD (Figure 32a). The Z_H and Z_{DR} depressions are typically 5–20 dBZ and 2–5 dB, respectively, lower than the surroundings, and these quasi-linearly-oriented minima are ~300–1000 m wide. In addition, a reduction in ρ_{hv} is observed in several of the cases, but any appreciable reduction in ρ_{hv} is absent in others. There is typically little evidence of the LRRs in K_{DP}, although the spatial resolution of K_{DP} tends to be more than an order of magnitude less than the spatial resolution of the other polarimetric variables owing to the method by which K_{DP} is calculated.

Although it is not known exactly what the LRR signature represents, it is hypothesized, based upon the polarimetric characteristics of the signature, that this area may be characterized by either DSDs with an appreciably smaller mean drop diameter compared to the surroundings or by hail of unknown size and number distribution. The former explains the observed reduction in Z_H and Z_{DR} (both of which are sensitive to drop size) and the sometimes-observed unaffected ρ_{hv} field. In those cases in which the

Z_H and Z_{DR} depressions are offset, it is possible that size sorting mechanisms act along at least a part of the LRR. There are cases for which ρ_{hv} is depressed within the LRR (i.e., 0.8–0.9), suggesting that hail may be present (e.g., Balakrishnan and Zrnić 1990; Straka et al. 2000). Unfortunately, extremely limited disdrometer data are available near these features (Dawson and Romine 2010), and the author knows of no datasets that have associated "ground truth" data of sufficient resolution to examine the detailed structure of the LRR.

There are likely at least a couple of plausible reasons why the LRR has thus far gone undocumented in formal literature. Since the observed LRR are typically quite narrow, the observing radar system must have sufficient spatial resolution to sample these LRRs thoroughly. Spatial resolution increases when the distance between the supercell and the radar is minimized, and reducing this distance is much easier with a mobile radar than with a fixed radar. In addition, resonance effects, which are much more prominent at X band than at S band, may make the signature more readily identifiable at X band.

The relationship between the LRR and the structure of the kinematic and/or thermodynamic fields within supercells is unknown. The large gradients in the polarimetric variables across the LRR suggest that there may also be significant gradients in buoyancy and other thermodynamic and/or kinematic quantities across the LRR given the impact of relevant microphysical processes implied by the heterogeneities in hydrometeor concentration and/or type. It is also possible that the LRR is the result of other storm-scale processes and is the byproduct of microphysical processes occurring with undiagnosed dynamical processes.

In addition to the LRR, another signature – the LoRB – has been identified in X-band mobile radar data as a region of very low ρ_{hv} located along the left side of the BWER (Figure 32b). In the cases in which the LoRB is evident, $\rho_{hv} < 0.6$ is juxtaposed with Z_H' of 25–50 dBZ. Typically, ρ_{hv} this low is observed with non-meteorological scatterers (e.g., biological scatterers, tornado debris, etc.). Given the location of the observations, however, it seems likely that the radar is detecting the presence of significant mixed phase hydrometeors with the reduction in ρ_{hv} exacerbated by resonance effects at X band; the LoRB, possibly analogous to the "LDR cap" or updraft signature observed by others at C and S bands, may also represent areas of very large hail aloft. Considering the apparent sensitivity of wet hail to ρ_{hv} observed in the numerical simulations performed for this project, it seems plausible to suggest that the expansive areas of $\rho_{hv} < 0.6$ several kilometers above the freezing level observed with the LoRB represent regions of wet hail growth aloft.

If the LoRB represents areas of wet hail growth, the presence, structure, and evolution of LoRBs may be a useful prognostic tool for identifying supercells capable of producing very large hail (Picca and Ryzhkov 2012). The relationships between the LoRB and other radar and environmental parameters (e.g., the height at which a LoRB is observed relative to the ambient freezing level, the area-averaged ρ_{hv} collocated with relatively high Z_H', etc.) are unknown; the areal extent and structure of the LoRB seem likely to be affected by hail size, hail concentration, and fractional water content. Although one can infer hydrometeor type based upon the polarimetric quantities, it would be extremely beneficial to have in-situ observations – such as those from a

penetrating aircraft – to provide the in situ verification for what is actually responsible for this signature.

In an effort to study the microphysical structure of some commonly-observed polarimetric signatures within supercell, high-resolution simulations using the MY3 three-moment bulk microphysics scheme alongside a polarimetric emulator were performed. The emulator used in this study was based upon that described in Jung et al. (2010) with additional modifications and updates to bring it more in line with Ryzhkov et al. (2011). To increase the sample size and better established relationships between the signatures and the microphysical and kinematic structure of simulated supercells, eight simulations were carried out using eight hodographs of four "shapes" and two lengths. This was still a relatively small sample size, but the decision to modify only the vertical shear profile while keeping everything else constant (e.g., thermodynamic profile) was made to limit the parameter space and degrees of freedom.

Some past research has focused on the structure of microphysical parameters within simulated supercells through a larger parameter space, but there has been comparatively little examination of simulated polarimetric signatures in three-dimensional, high-resolution supercell simulations. The primary focus of this numerical simulation facet of this project was on polarimetric signatures, which can be used directly to compare with "real-world" signatures and structures found in nature without requiring one to make a series of assumptions to estimate or qualitatively assess polarimetric quantities from model microphysics (which is made more complex when resonance effects must be included). The appearance of the signatures examined in this project – specifically, Z_{DR} columns and rings, K_{DP} columns, ρ_{hv} rings, and low-level hail

signatures – was also examined at different radar wavelengths to assess basic sensitivities of the signatures to radar wavelength.

In general, the "strong" shear hodographs (i.e., the long hodographs) were associated with supercells with larger and stronger updrafts. In addition, these supercells tended to produce the widest and tallest Z_{DR} columns and rings. In most simulations, there were two distinct regions of and processes responsible for $Z_{DR} > 1$ dB above the freezing level. First, the so-called primary Z_{DR} column was typically associated with high q_r lofted within and immediately west of the center of the updraft. This rainwater typically froze near 5,600 m AGL (~1,800 m above the environmental freezing level and ~1,000 m above the parcel freezing level), where Z_{DR} was locally maximized in a regime of rainwater and wet hail. This height corresponded to temperatures of approximately -5° to -7° C; observations and numerical modeling results using more sophisticated explicit bin schemes have shown Z_{DR} columns to higher heights and colder temperatures. In the future, it may be worth modifying the two constants that are used in the Bigg (1953) drop freezing parameterization to better simulate the depth of the Z_{DR} column. In at least one simulation (*25r10_057*), an intense updraft and relatively low q_r combined to yield a particularly high Z_{DR} column (with a top near ~6,300 m AGL). At most times in most simulations, the Z_{DR} columns were centered west of the maximum vertical velocities with the updrafts.

The second region of enhanced Z_{DR} aloft appeared to be very similar to observed Z_{DR} rings. In nearly all cases, the Z_{DR} rings were actually half-rings along the eastern side of the updraft immediately adjacent to the maximum vertical velocities within the updraft. These Z_{DR} rings typically extended to considerably higher heights than did the

primary Z_{DR} columns. In terms of the microphysics of these rings, the rings were position where relatively low q_r was superimposed on low q_h, and the rings were nearly collocated with a local maximum in D_{mh}. The fractional water method reapportioned the q_r predicted by the microphysics scheme and, essentially, placed it on the hail, creating wet hail that produced relatively high Z_{DR}. The importance of allowing the water to be added to the hail (thereby creating "wet" hail) was shown when the Z_{DR} rings were unable to be reproduced when rainwater was treated independent of hail (i.e., hail was treated as dry). In general, the stronger shear simulations produced more prominent Z_{DR} rings; the most prominent Z_{DR} rings were associated with supercells in the *25q10*, *15q10*, *25r10_057*, and *25r10* simulations, which happen to be the simulations with the highest 0–3 SRH. The Z_{DR} rings were more apparent at X band than at S band.

Combining all simulations, the number of gridpoints with $Z_{DR} > 1$ dB at a given height tended to be proportional to the width of the updraft (or at least the area with $w >$ 5 m s^{-1}), and the maximum height of $Z_{DR} > 1$ dB tended to increase with increasing w. *This suggests that monitoring the evolution of the Z_{DR} column may be an effective way by which one can assess the evolution of the updraft as well* (which is typically quite difficult to observe in real-time in nature). The extent of the rain and hail fields aloft was also found to be positively correlated with the extent of the Z_{DR} columns and rings. In most of the simulations, there was a relative maximum in the correlation between the number of gridpoints with $D_{mh} > 2.54$ cm at 120 m AGL and the maximum height of $Z_{DR} > 1$ dB at lag time ~20 minutes, although the value of the CC was < 0.5.

Similar to the sizes of Z_{DR} columns, the sizes of K_{DP} columns were proportional the sizes of the updrafts within the simulated supercells. K_{DP} column sizes were best correlated (with CCs > 0.75) with Z_{DR} column sizes, the amount of rainwater aloft, and 1–6 km AGL updraft helicity. In terms of the maximum height of $K_{DP} > 1°$ km^{-1}, the highest CC occurred when it was paired with the area of 1–6 km AGL updraft helicity above 250 m^2 s^{-2}. Given the stronger theoretical relationship between q_r and K_{DP} than that between q_r and Z_{DR}, the K_{DP} columns tended to track the q_r field very well; most K_{DP} columns were located west of the center of the updrafts. At X band, resonance effects resulted in anomalously high K_{DP} near the top of the K_{DP} columns, where there was wet hail. Wet hail affected K_{DP} at X band considerably more than that at S band, which made it difficult to interpret low-level K_{DP} if one wanted to use it as a proxy for q_r or rain-rate.

Many of the simulations produced structures that looked like ρ_{hv} rings; these rings were larger in size and had lower ρ_{hv} minima at X band than they did at S band. Particularly evident in the *15q10*, *25q10*, *25r10_057*, and *25r10* simulations, the rings occurred to the east of the strongest part of the convective storm updraft. In these areas, q_r, q_h, and q_g typically were quite small, and the available q_r was reapportioned to create wet hail and wet graupel. Whereas the Z_{DR} ring was strongly correlated with f_{wh}, the ρ_{hv} rings are strong correlated with, among other quantities, both the area of $D_{mh} > 5$ mm aloft and the largest D_{mh} with the ring. Given temperatures of -5° to -20° C, this likely represents an area of hail growth, and sedimentation along the periphery of the updraft may be resulting in relatively large D_{mh} on account of significant size sorting.

Although the model and emulator were able to capture rings and columns, any LoRB-like features are ambiguous and difficult to label. There were areas of anomalously low ρ_{hv} located in similar storm-relative position as the observed LoRB cases; the microphysical composition of these areas of ρ_{hv} reductions does not match the hypothesized mechanism responsible for the LoRBs, however. The *25q10* simulation, for example, produced a separate area of $\rho_{hv} < 0.7$ north of and below (in height) the primary ρ_{hv} ring (Figure 85). This area of reduced ρ_{hv} wrapped around the northern side of the updraft (Figure 85a) approximately 5–7 km N of the northern edge of a crescent-shaped BWER (Figure 85b); hydrometeors in this area were characterized by $q_h \sim 0.004$ and minimal q_r and q_g. The lack of appreciable q_r resulted in $f_{wh} \sim 0$. At the height shown in Figure 85, the area of $\rho_{hv} < 0.6$ is the only area where $D_{mh} > 0.75$ cm and $D_{mh} >$ 0.004 overlapped (i.e., there was a relatively large quantity of moderately-large hail). A vertical cross-section through this area of reduced ρ_{hv} (Figure 86) supports the notion that this feature is associated directly with a streak of hail of diameter O(1 cm) in non-trivial quantities. This does not appear exactly like the observed LoRB cases, but this area of low ρ_{hv} is not far removed from the northern edge of the BWER, and it is separate from the ρ_{hv} ring.

LRR-like features were captured in the Z_H field in some simulations (e.g., Figure 84a), but a closer examination of Z_{DR} (Figure 84b) and the hydrometeor fields reveals that these LRR-like features are created by local maxima in Z_{DR} in the presence of large hail that are separated by 1–5 km. The result is an LRR-like feature in Z_H, but Z_{DR} tends to be much different than has been observed. Instead of hail being inferred within the LRR as is done with at least a few observed cases, these simulations tend to

produce hail *around* the LRR-like feature. Since it is possible that the LRR marks a zone along which the kinematic properties of the surrounding air change, the potential errors associated with the emulator may result in scattering heterogeneities that mask the kinematic feature.

It is important to remember that all simulations performed in this study used the same thermodynamic sounding, and each of the eight simulations used one of eight different hodographs that certainly do not cover the entirety of the hodograph parameter space. As such, it is possible that simulating other environments (e.g., different thermodynamic soundings, different shear profiles, etc.) may yield simulated supercells that feature more LoRB-like and/or LRR-like structures. Of course, it is also possible that it is difficult or not possible to simulate such structures within the constraints of the MY3 bulk scheme (e.g., one rain category, fixed densities for all hydrometeors, etc.).

Although the modeling results in this paper indicate that some polarimetric signatures are captured by the model, more accurate representations of the signatures appear to require a more sophisticated microphysics scheme. Bulk microphysics schemes, although more computationally efficient than explicit / spectral bin schemes, tend to be prone to error where a multi-modal distribution would naturally occur, such as can occur when different microphysical processes produce rainwater with different mean sizes (e.g., water shed from melting graupel and hail, vertical advection of large raindrops into regions of a more diverse spectrum, etc.). The MY3 scheme only predicts a single rain category, and the densities for all hydrometeors are fixed; both of these are limitations that affect the "real-world" representativeness of the simulated supercells. In addition, further development of the radar emulator to handle more

sophisticated scattering models is warranted (e.g., allow wet hail to be modeled both as a water shell around a water/ice mixture as well as homogeneous mixture of ice and rain to account for different water distributions within and around hailstones as they accrete water, melt, shed, or undergo other processes that result in the exchange of water between the hailstones and the rain category). Despite the limitations and potential sources of errors in the MY3 and in the emulator, it is encouraging that some of the most common polarimetric signatures observed with supercells are able to be simulated with this model.

Table 1. Selected characteristics of the UMass XPol (2007–2010) and RaXPol (2011–2013) mobile radars used in this project.

	UMass XPol	**RaXPol**
Operating Frequency	9.41 GHz	9.73 GHz +/- 20 MHz
Antenna Diameter	1.8 m	2.4 m
Antenna 3 dB Beamwidth	1.25°	1.0°
Azimuthal Rotation Rate	Up to 24° s^{-1}	Up to 180° s^{-1}
Peak Power (H+V)	25 kW	20 kW
Pulse Width	Typically 1 μs	0.5 – 40 μs
Range Resolution	Typically 150 m	15 – 150 m
PRF	1.6 kHz & 2.0 kHz	User-definable
Sampling Resolution	60 m	7.5 – 75 m

Table 2. Parameters used in the numerical simulations

Model Configuration	
Model	ARPS v5.3.3
Horizontal Grid Spacing	200 m
Vertical Grid Spacing	Stretched - 75 m near surface, ~800 m near model top
Domain Size	753 x 753 x 83 (150 km x 150 km x 20 km)
Time Steps	Large: 1.0 s Small: 0.2 s
Computational Mixing	4th order in horizontal and vertical
Microphysics	Three moments (NT, Q, Z), five species (Milbrandt and Yau 2005a,b)
Turbulence Parameter.	Anisotropic 1.5 order TKE
Boundary Conditions	Lateral: radiation Bottom: Rigid, free-slip Top: Rigid, Rayleigh damping
Initial Perturbation	Magnitude: 4 K Shape: 10 km x 10 km x 1.5 km centered 1.5 km AGL

Table 3. A non-exhaustive list of the datasets in which LRRs and LoRBs have been identified in UMass XPol (2007–2010) and RaXPol data (2011–2013). Discontinuities in data collection or deployments likely resulted in these features being missed in other storms in which data were collected. In addition, on many storms, the scanning strategy used precluded the collection of data to an adequate height to observe the LoRB.

Feature	Date	Description
Low Reflectivity Ribbon (LRR)	5/23/2008	Tornadic supercell (NW OK)
	6/5/2009	Tornadic supercell (E WY)
	6/7/2009	Tornadic supercell (NW MO)
	6/9/2009	Non-tornadic supercell (SW KS)
	5/18/2010	Tornadic supercell (NW TX)
	5/25/2010	Tornadic supercell (W KS)
	6/10/2010	Tornadic supercell (E CO)
	5/23/2011	Non-tornadic supercell (SW OK)
	5/24/2011	Tornadic supercell (C OK)
	5/29/2012	Non-tornadic supercell (C OK)
	5/19/2013	Tornadic supercell (C OK)
	5/30/2013	Tornadic supercell (SW OK)
	5/31/2013	Tornadic supercell (C OK)
Low ρ_{hv} left of BWER (LoRB)	5/31/2007	Tornadic supercell (NW OK)
	5/24/2008	Tornadic supercell (N OK)
	6/5/2009	Tornadic supercell (E WY)
	6/6/2009	Non-tornadic supercell (C NE)
	6/7/2009	Tornadic supercell (NW MO)
	5/17/2010	Non-tornadic supercell (E NM)
	5/26/2010	Non-tornadic supercell (NE CO)
	6/11/2010	Tornadic supercell (E CO)
	6/13/2010	Nontornadic supercell (NW OK)
	5/19/2013	Tornadic supercell (C OK)

Table 4. Estimated 0–3 km storm-relative helicity (SRH) for each simulation based upon a subjectively-analyzed average motion of the cyclonic supercell in each simulation between 4800s and 9000 s.

Simulation Name	**0-3 km SRH (m^2 s^{-2})**
15r10	106
25r10	362
15r10_057	261
25r10_057	808
15q10	336
25q10	996
15str	91
25str	110

Table 5. A description of the quantities examined and used for correlation statistics. These quantities were calculated for each simulation during the 1800–9000 s period within a subjectively-determined subdomain specific to each simulation. The subdomain was chosen such that primary supercell remained within it during the examined time period while not including other convection.

Shorthand Notation	Description
dmh33area1inch	Number of gridpoints with Dmh > 2.54 cm at ~5600 m
dmh33max	Maximum value of Dmh at ~5600 m
dmh33sum5mm	Sum of Dmh values greater than 5 mm at ~5600 m
dmh3area1inch	Number of gridpoints with Dmh > 2.54 cm at ~120 m
dmh3max	Maximum value of Dmh at ~120 m
dmh3sum1inch	Sum of Dmh values greater than 2.54 cm at ~120 m
dmh3sum2inch	Sum of Dmh values greater than 5.08 cm at ~120 m
kdparea25	Number of gridpoints with K_{DP} > 2.54 cm at ~5600 m
kdparea33	Number of gridpoints with K_{DP} > 2.54 cm at ~5600 m
kdpmaxheight	Maximum height of K_{DP} > 1° km^{-1}
qhmax3	Maximum value of q_h at z ~120 m
qhsum3	Sum of q_h at z ~ 120 m
qrarea33	Number of gridpoints with q_r > 2.54 cm at ~5600 m
rhvarea33	Number of gridpoints with ρ_{hv} > 2.54 cm at ~5600 m
rhvmin33	Minimum value of ρ_{hv} at ~5600 m
uh16km_area	Number of gridpoints with 1–6 km updraft helicity > 250 m^2 s^{-2}
uh16km_max	Maximum value of 1–6 km updraft helicity >250 m^2 s^{-2}
uh50_500m_area	Number of gridpoints with 50–500 m updraft helicity > 500 m^2 s^{-2}
uh50_500m_max	Maximum value of 50–500 m updraft helicity > 500 m^2 s^{-2}
vvortmax3	Maximum value of vertical vorticity at ~120 m
vvortmax33	Maximum value of vertical vorticity at ~5600 m
w25area5	Number of gridpoints with w > 5 m s^{-1} at ~3830 m
w25max	Maximum value of w at ~3830 m
w33area5	Number of gridpoints with w > 5 m s^{-1} at ~5500 m
wmax33	Maximum value of w at ~5500 m
zdrarea25	Number of gridpoints with Z_{DR} > 2.54 cm at ~5600 m
zdrarea33	Number of gridpoints with Z_{DR} > 2.54 cm at ~5600 m
zdrmaxheight	Maximum height Z_{DR} > 1 dB
zdrmaxheightqrc	Maximum height Z_{DR} > 1 dB where q_r > 0.001

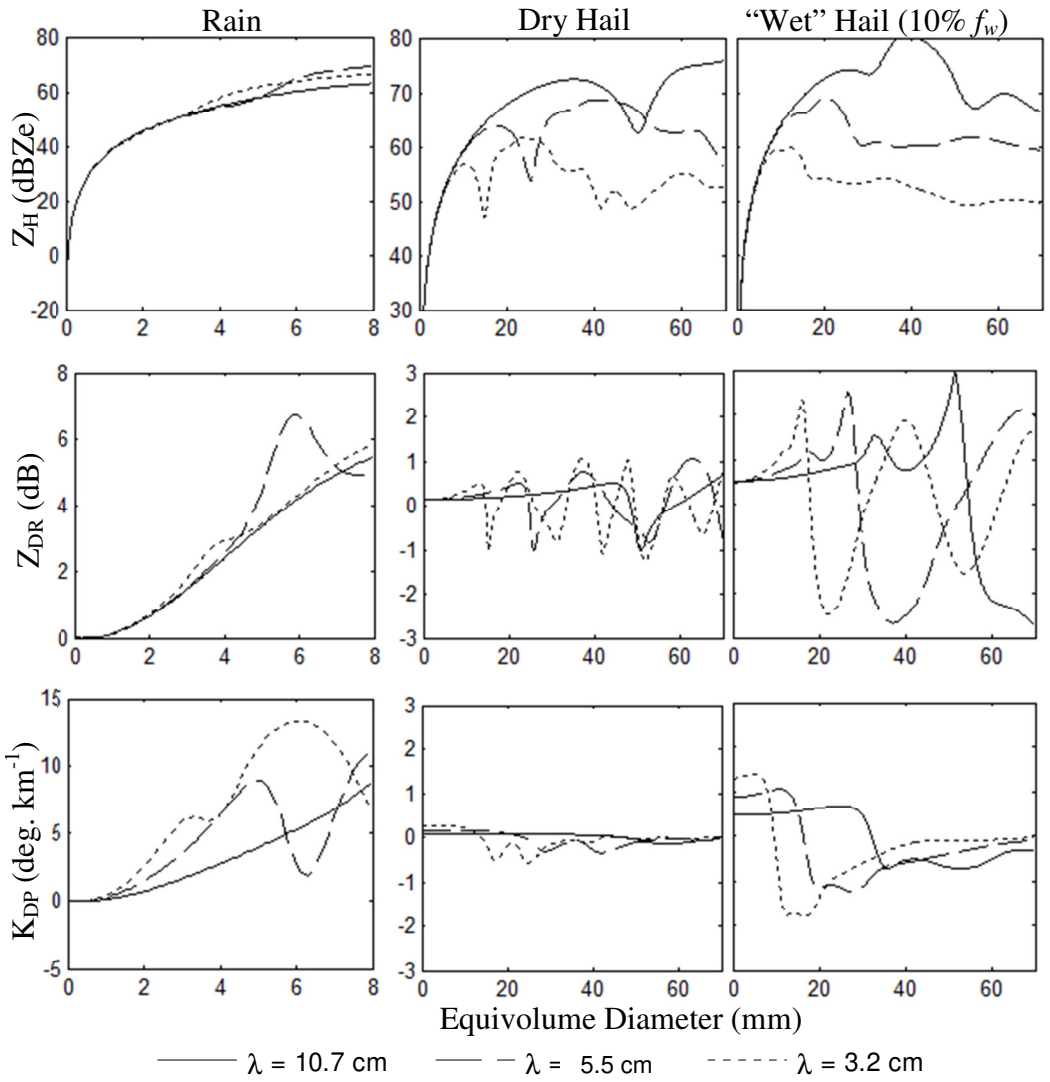

Figure 1. Z_H, Z_{DR}, and K_{DP} (from top to bottom) of monodispersed distributions of rain (left column), dry hail (i.e., f_{wh} = 0%; center column) and hail with fixed f_{wh} = 10% (right column) as a function of equivolume diameter. The solid, dashed, and dotted curves are calculations at S, C, and X bands, respectively. Although similar to the results presented in Snyder et al. (2010), the above quantities have been recalculated consistent with the latest version of the radar emulator (details of which are provided in Chapter 3).

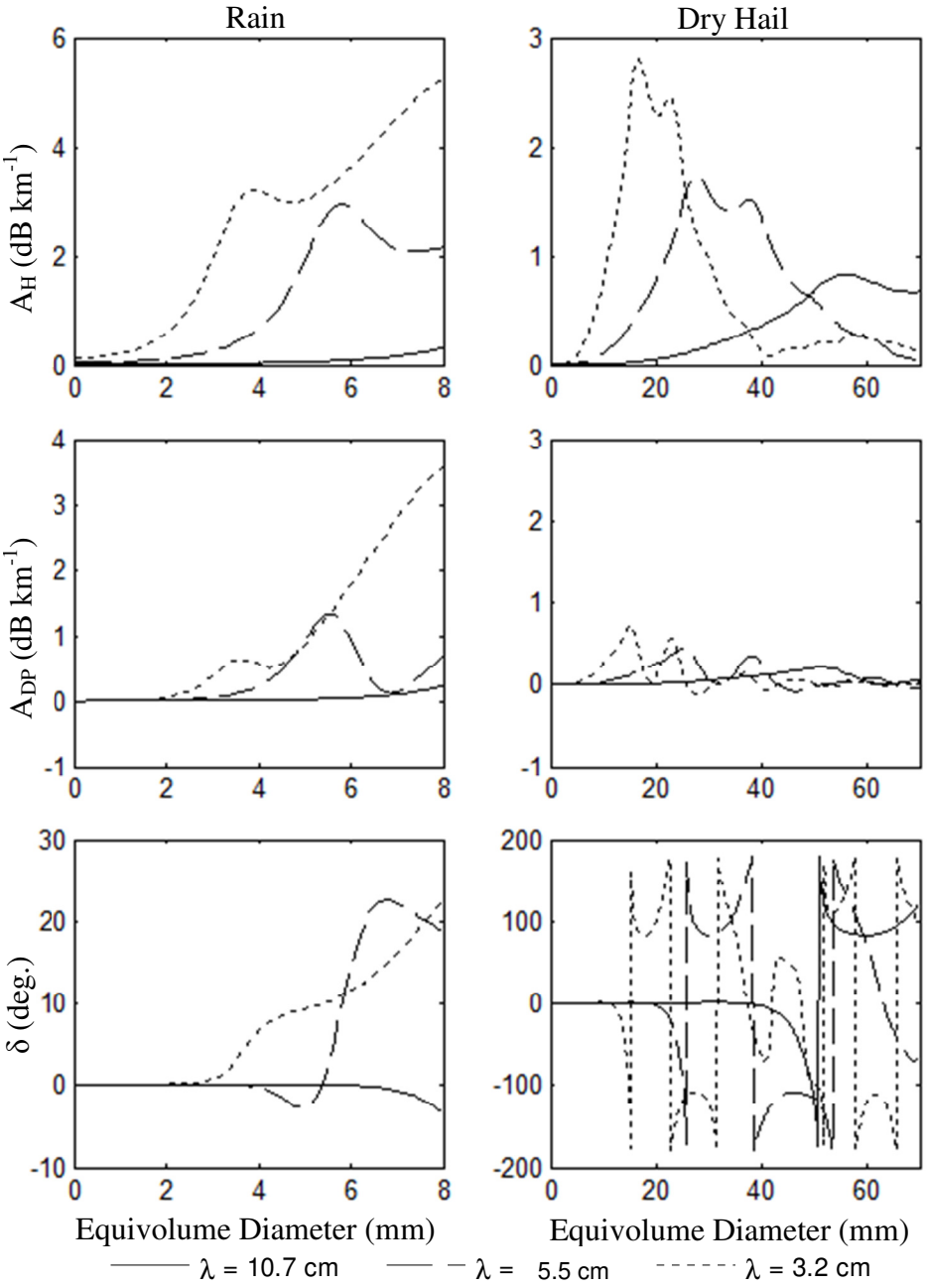

Figure 2. Similar to Figure 1 except for A_H, A_{DP}, and δ (from top to bottom) for rain (left) and dry hail (right) at S, C, and X bands.

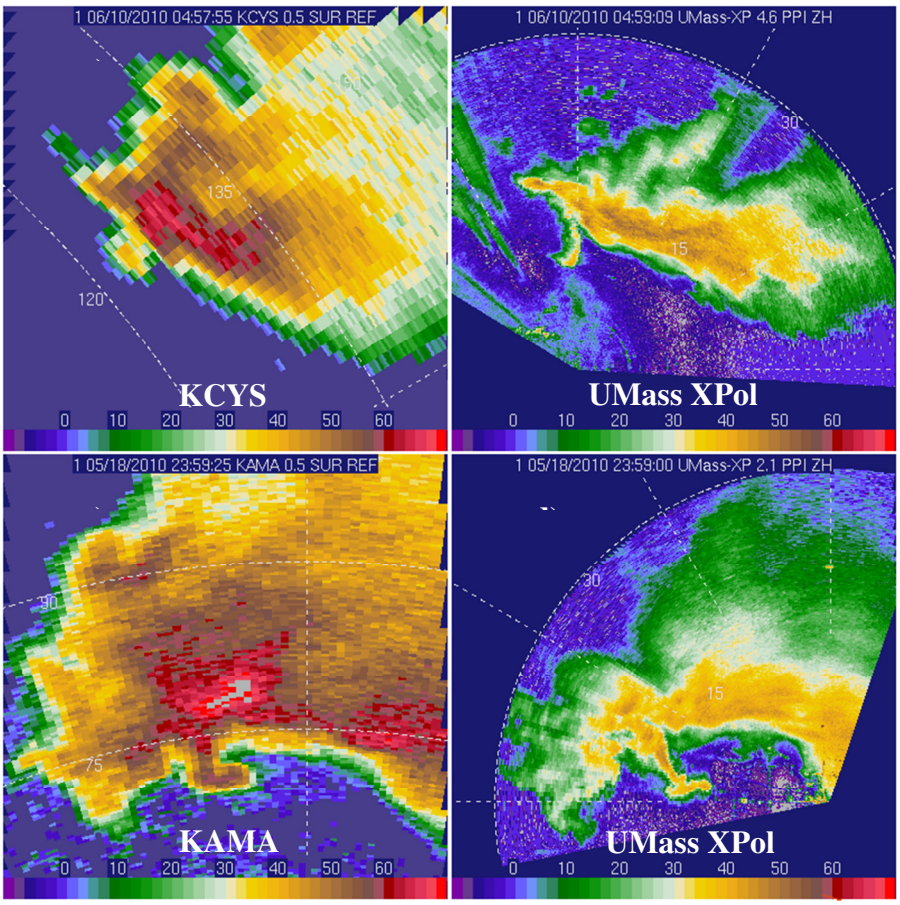

Figure 3. A comparison of Z_H' from S-band WSR88D radars and the X-band UMass XPol. (a) KCYS on the 0.5° elevation angle scan and (b) UMass XPol on the 4.6° elevation angle scan valid around the same time on the evening of 9 June 2010. (c) KAMA at an elevation angle of 0.5° and (d) UMass XPol at an elevation angle of 2.1°. The elevation angles were chosen so that the beam heights from the respective radars were similar. Range ring labels are relative to the respective radars. [From Snyder et al. (2013)]

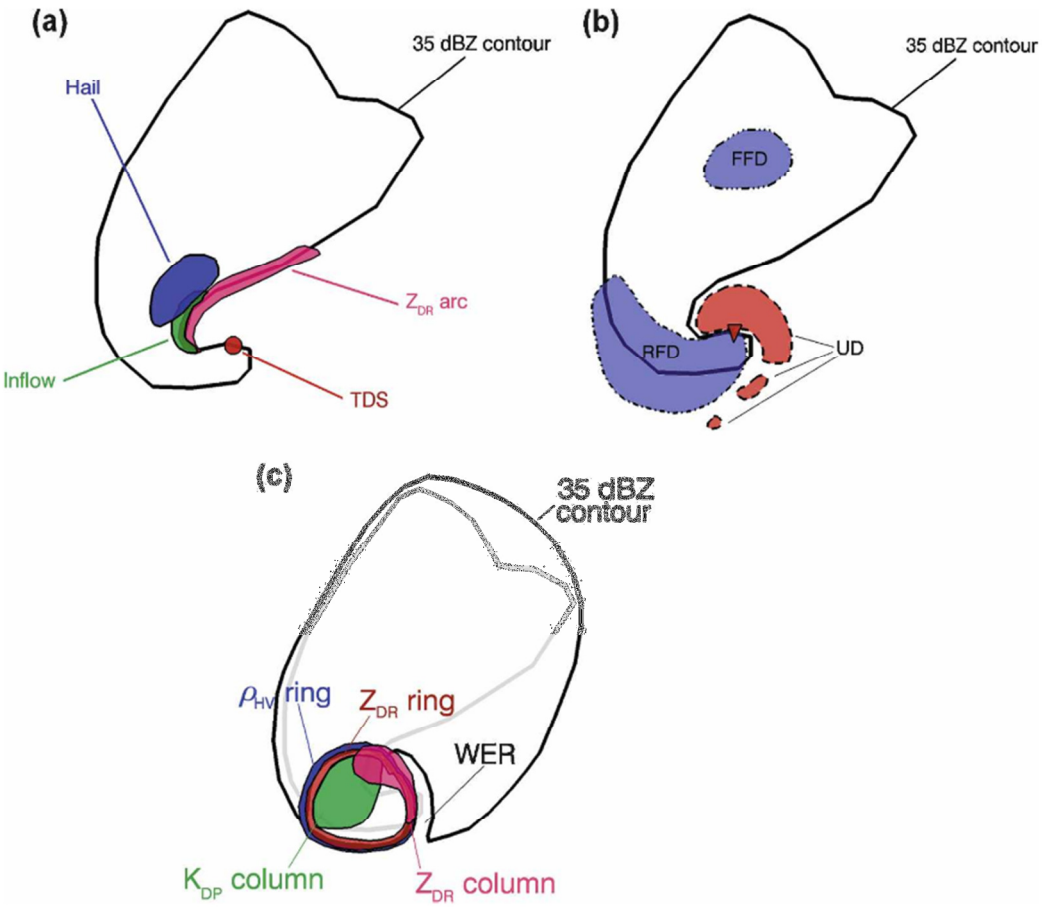

Figure 4. Conceptual models of (a) Low-level polarimetric signatures, (b) mid-level vertical velocity extrema, and (c) mid-level polarimetric signatures. [From Kumjian and Ryzhkov (2008)]

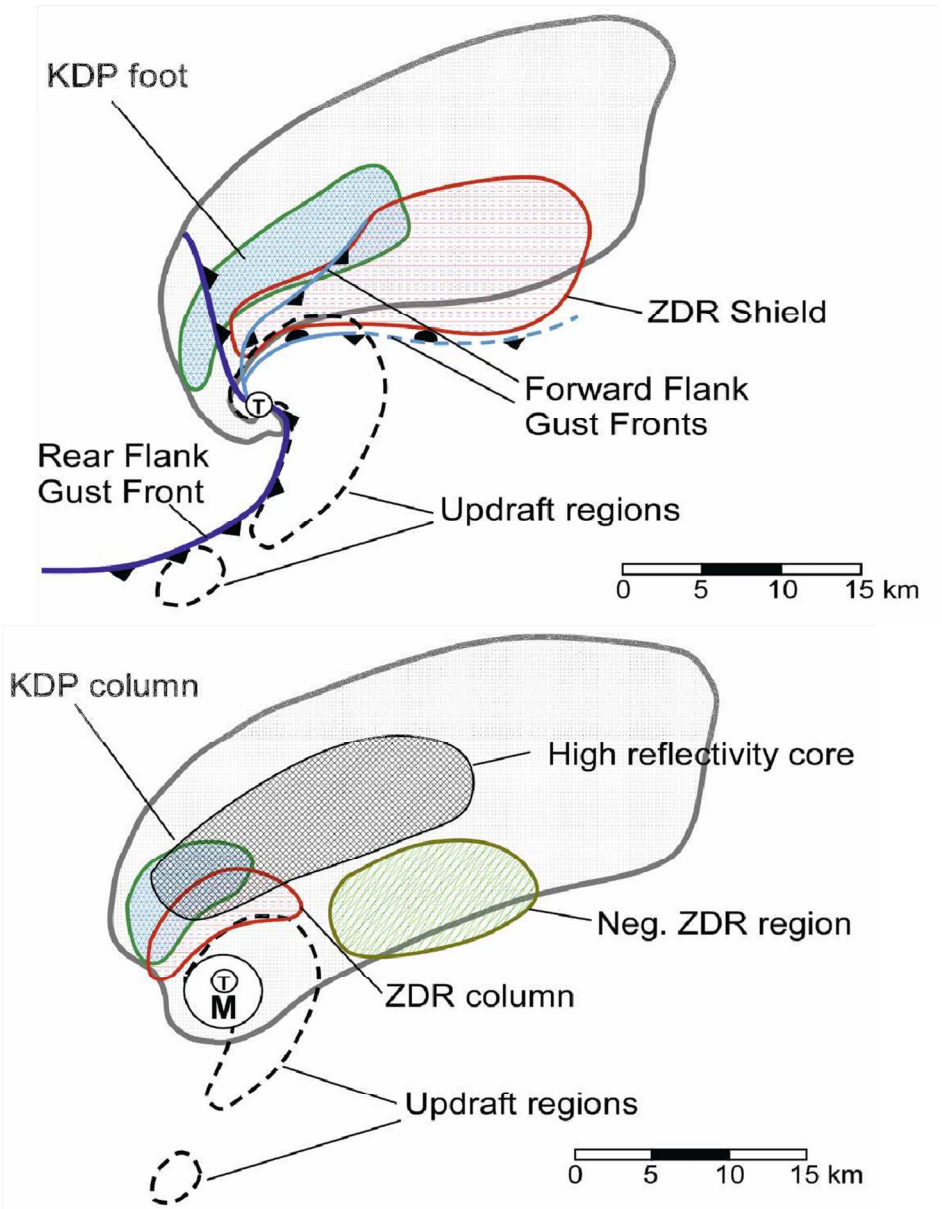

Figure 5. Conceptual model of polarimetric supercell structure at (a) 1 km above ground level and (b) "mid-level". [From Romine et al. (2008), adapted from Lemon and Doswell (1979) and Burgess (1993)]

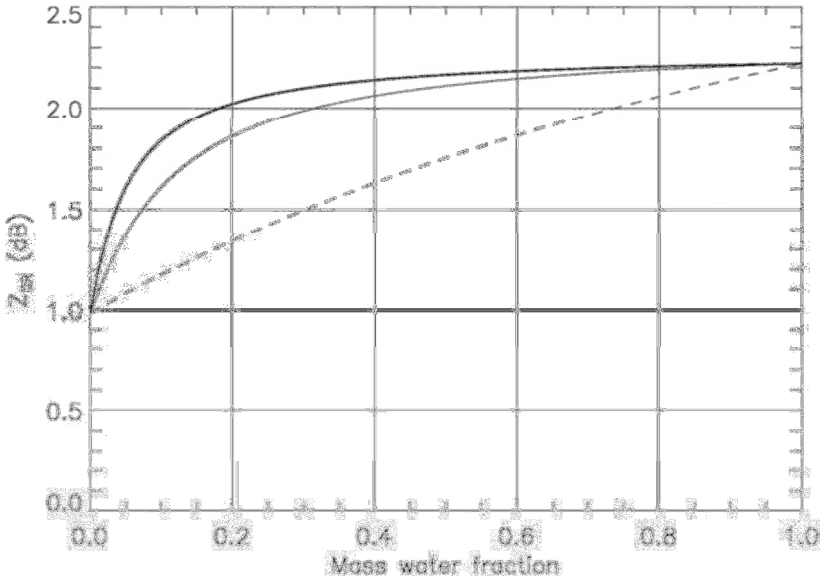

Figure 6. Calculated Z_{DR} of a spheroidal hailstone as a function of mass water fraction. The thin solid line represents a soaked hailstone calculated assuming a water matrix and ice inclusion (i.e., $\varepsilon^{(ws)}$), and the dashed line represents a soaked hailstone calculated as a snow matrix with water inclusion (i.e., $\varepsilon^{(sw)}$). The thick solid line is calculated according to the two-layer method (water outer shell with mixed soaked interior). The modeled hailstone has an aspect ratio of 0.8, an ice density of 0.92 g cm^{-3}, and a temperature of 0° C. The calculations were performed at λ = 5.4 cm and use the Rayleigh approximation. (From Ryzhkov et al. 2011)

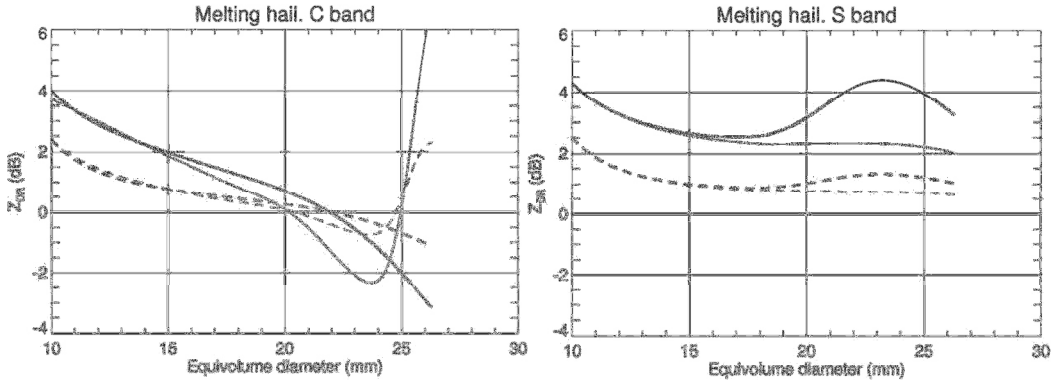

Figure 7. Calculated Z_{DR} at C ($\lambda = 5.4$ cm) and S ($\lambda = 11$ cm) bands for melting hail. f_{wh} is determined from the critical water fraction described in Rasmussen and Heymsfield (1987) and varies as a function of diameter. Solid lines represent hailstones with $\bar{\phi} = 0°$ and $\sigma_h = 0°$; dashed lines represent hailstones with a distribution of canting angles (i.e., $\sigma_h \neq 0°$) that depends upon f_{wh}. (From Ryzhkov et al. 2011)

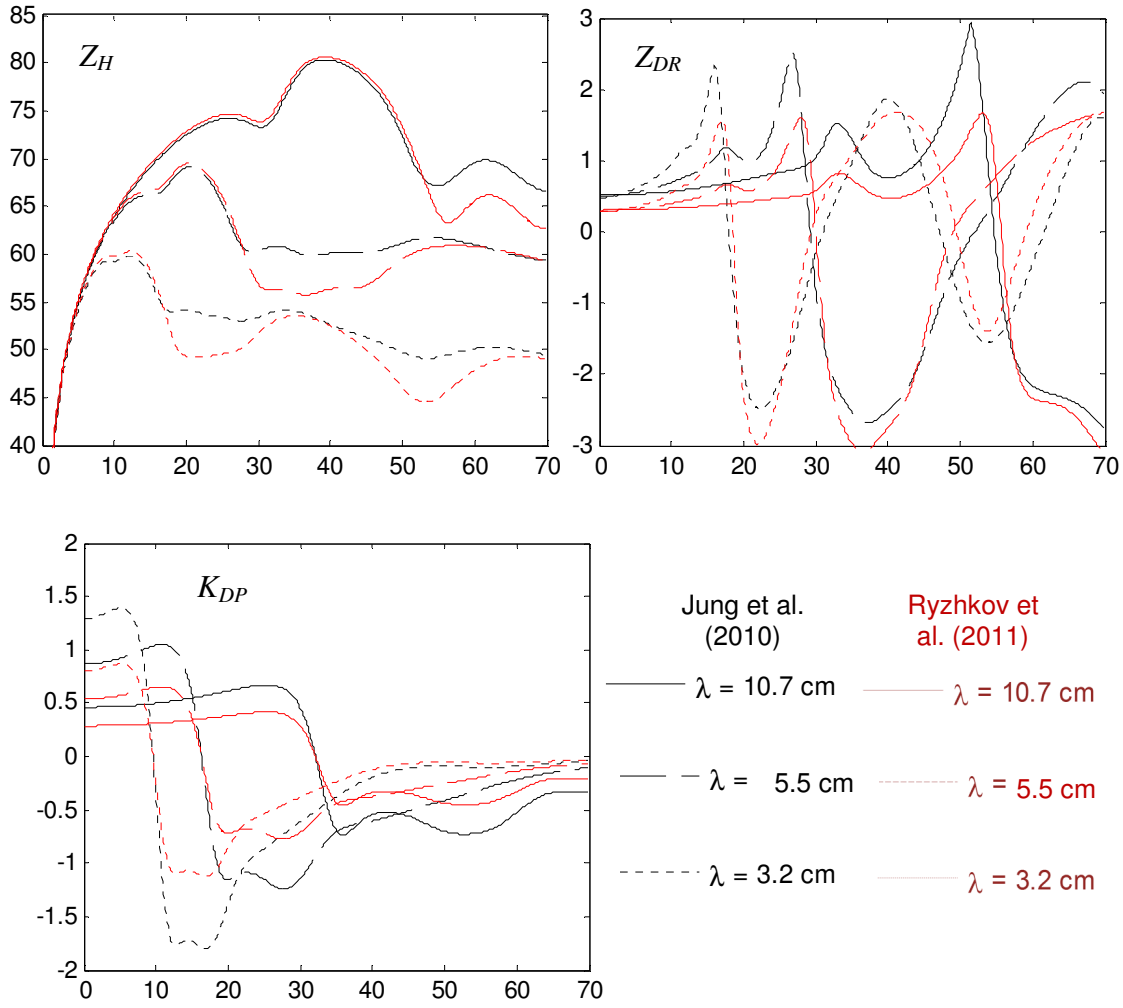

Figure 8. Z_H, Z_{DR}, and K_{DP} as a function of equivolume diameter for wet hail (f_{wh} = 10%) at S (solid line), C (long dashed line), and X (short dashed line) bands. Calculations based upon the variable and angular moment equations provided in Jung et al. (2010) and used in this project are marked in black, whereas calculations using the variable and angular moment equations in Ryzhkov et al. (2011) are marked in red.



Figure 9. Photographs of the (a) UMass XPol radar collecting data in a tornado in southeastern Wyoming on the afternoon of 5 June 2009 and (b) RaXPol radar collected data in a supercell on 11 June 2011. (Photos courtesy of Jeff Snyder)

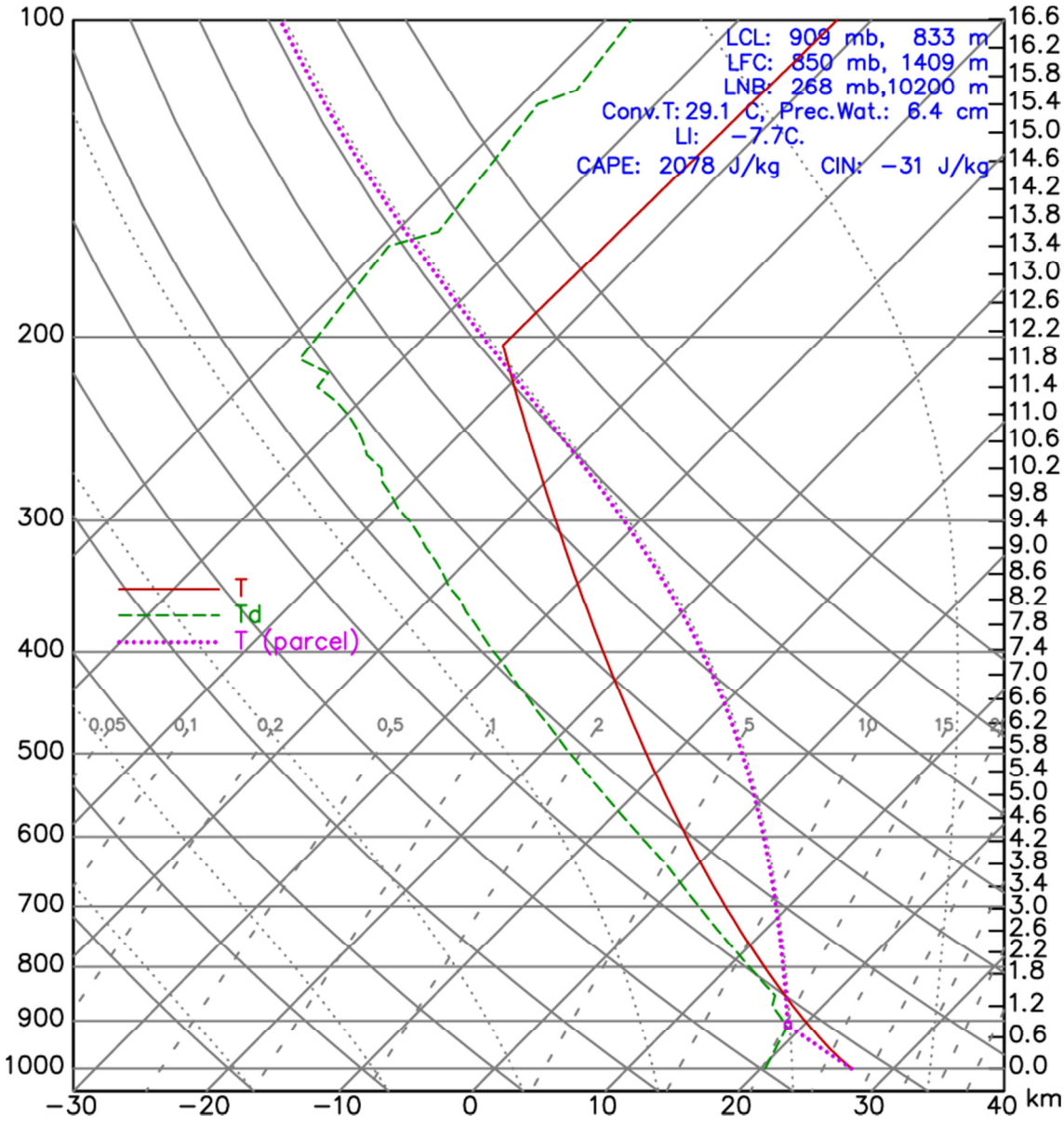

Figure 10. A skew-T, log-P plot of the idealized sounding used for the eight primary simulations examined in this study. The sounding is based on the analytical sounding presented in Weisman and Klemp (1983).

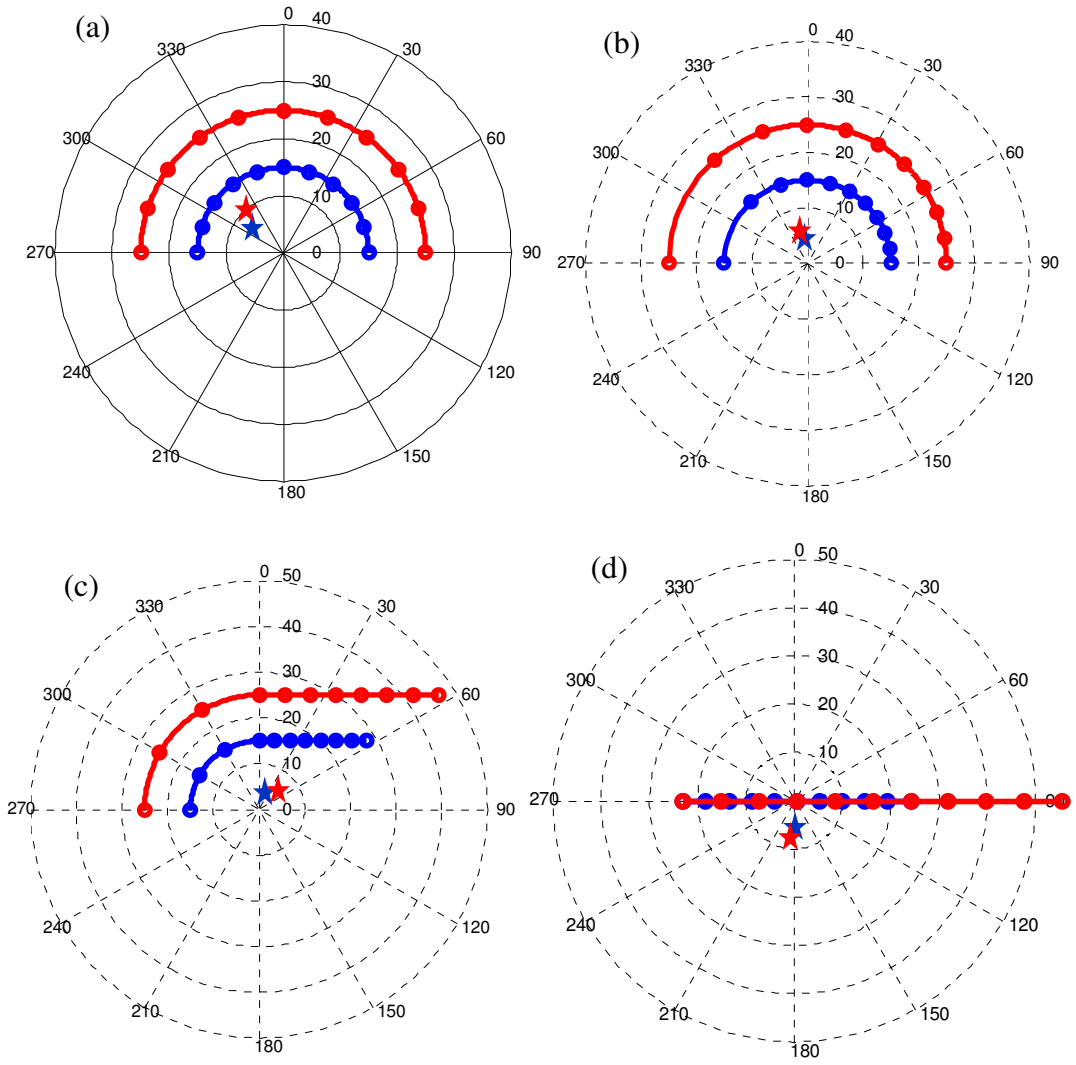

Figure 11. The four hodograph shapes examined in this study: (a) half-circle with constant veering between the surface and 10 km AGL (*15r10* and *25r10*), (b) half-circle with decreasing shear and veering between the surface and 10 km AGL (*15r10_057* and *25r10_057*), (c) quarter-circle with 90 degrees of turning from the surface to 3 km AGL with constant, "straight" shear from 3 km to 10 km AGL (*15q10* and *25q10*), and (d) straight-line hodograph with constant shear between the surface and 10 km AGL (*15str* and *25str*). The blue curves represent the "weak" shear cases (mean 0–10 km shear $\approx 4.7 \times 10^{-3}\ s^{-1}$); the red curves represent the "strong" shear cases (mean 0–10 km shear $\approx 7.8 \times 10^{-3}\ s^{-1}$). All blue hodographs of the same color are the same length. Sounding heights are marked every 1 km by circles along each hodograph. Units are in m s^{-1}. Red and blue stars in each panel represent an estimated storm motion based on peak updraft motion between 4800 s and 8400 s. Winds above 10 km are constant.

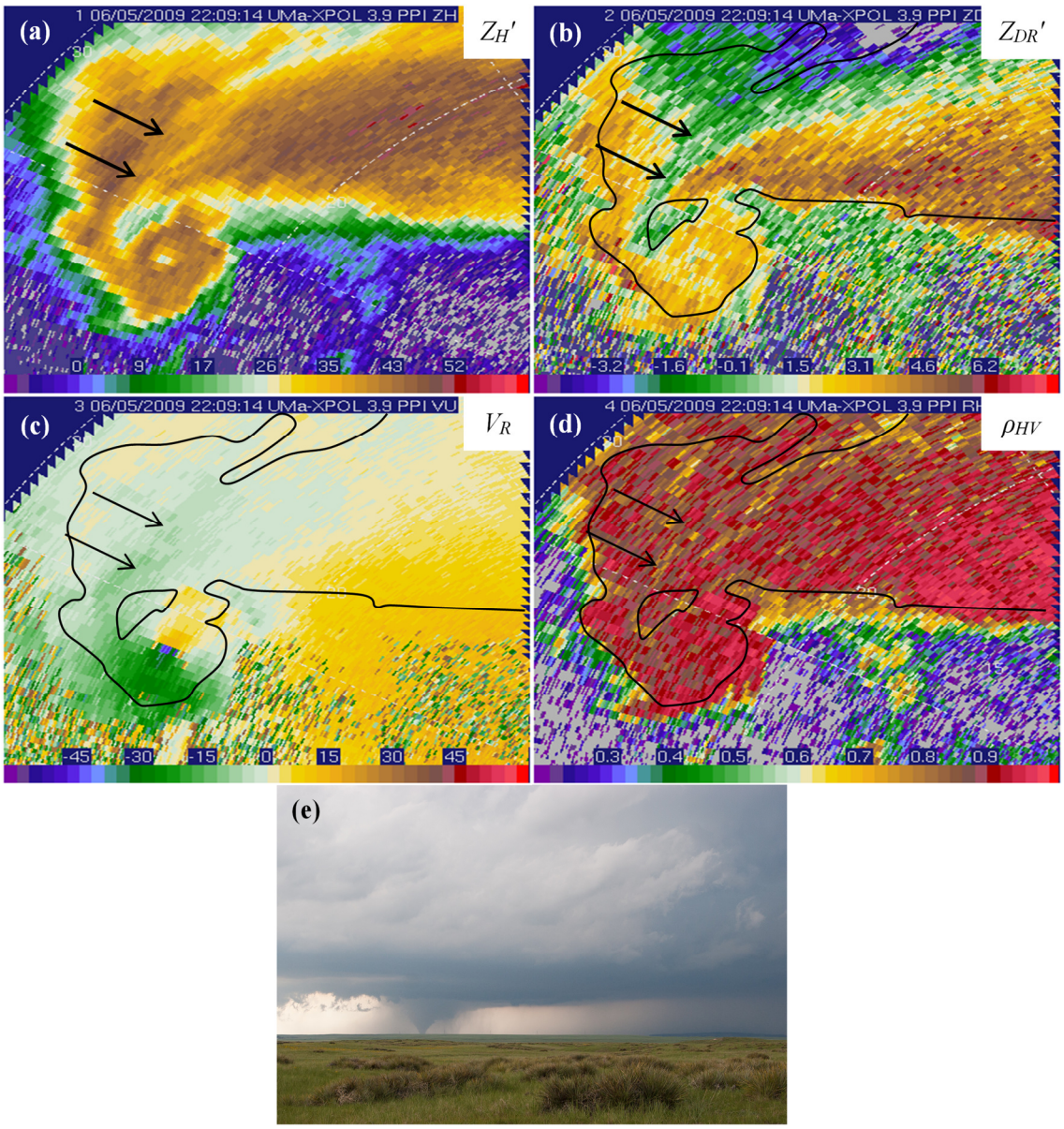

Figure 12. (a) Z_H', (b) Z_{DR}', (c) V_R, and (d) ρ_{hv} from 2209 UTC on 5 June 2009. The local reduction in Z_H' and Z_{DR}' is denoted by the arrows, and the black outline in (b)–(d) mark the approximate periphery of 30 dBZ echo. Here and in all subsequent figures, Z_H and Z_H' are in dBZ_e, Z_{DR} and Z_{DR}' are in dB, and V_R is in m s^{-1}. (e) A photograph of the supercell and tornado taken near 2210 UTC has a very similar field of view as the data shown in (a)–(d). (Photo courtesy J. Snyder) [From Snyder et al. (2013)]

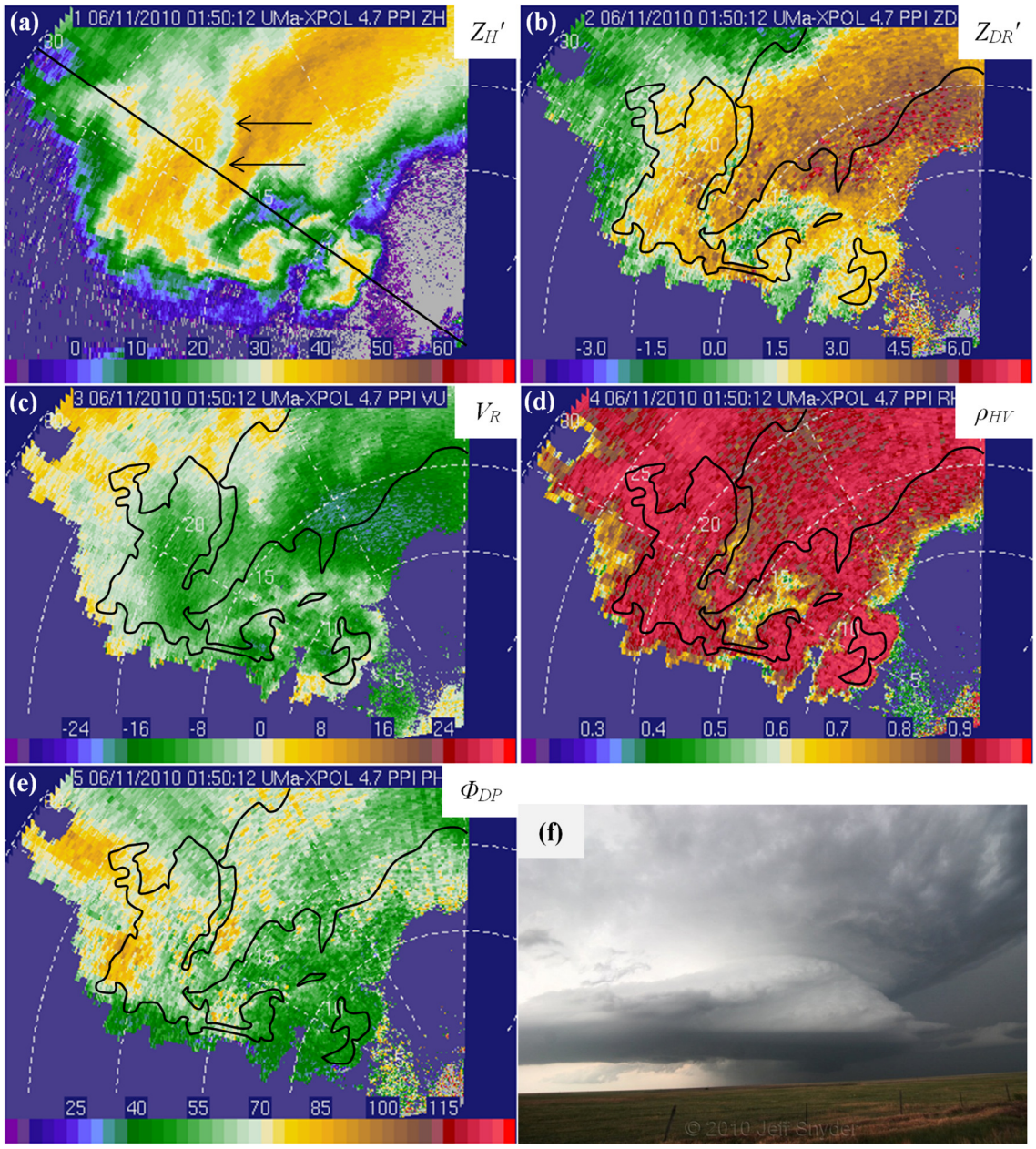

Figure 13. (a) Z_H', (b) Z_{DR}', (c) V_R, (d) ρ_{hv}, and (e) Φ_{DP} from 0150 UTC on the evening of 10 June 2010 collected at an elevation angle of 4.7°. The black line in (a) marks the radial along which the profile is extracted in Figure 15a. The local reductions in Z_H' and Z_{DR}' are essentially collocated. The approximate location of the 30 dBZ isoecho is shown in black in (b)–(e). (f) A photograph of the supercell as seen to the northwest of the radar deployment location (courtesy J. Snyder). [From Snyder et al. (2013)]

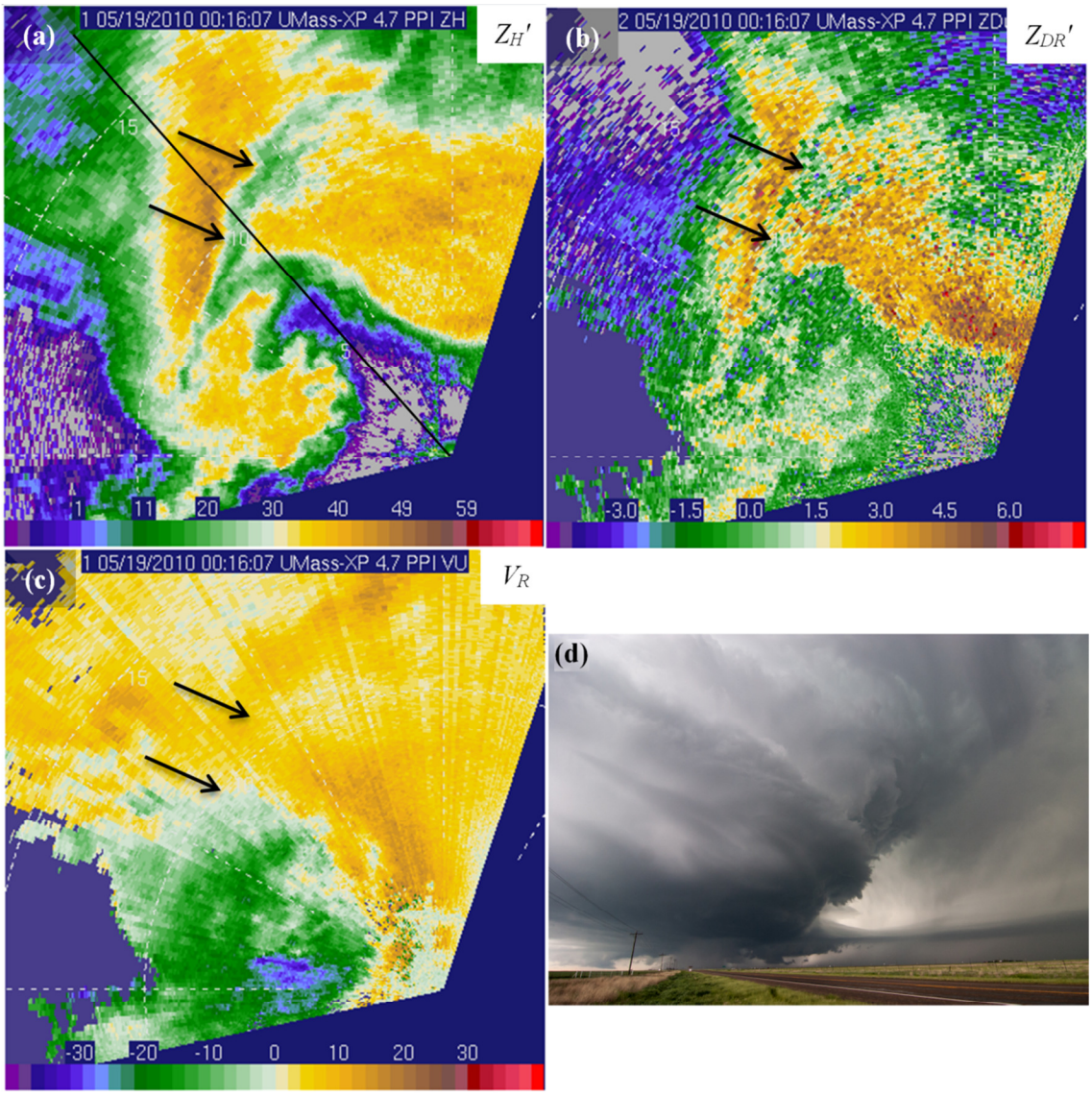

Figure 14. (a) Z_H', (b) Z_{DR}', and (c) V_R from 0016:07 UTC on the evening of 18 May 2010. Black arrows in (a) and (b) mark the location of the LRR, and the solid black line in (a) marks the radial from which the data in Figure 15b are shown. A wide-angle photograph of the supercell (d) as it appeared from the deployment location at approximately 0009 UTC looking to the west-northwest (courtesy J. Snyder). [From Snyder et al. (2013)]

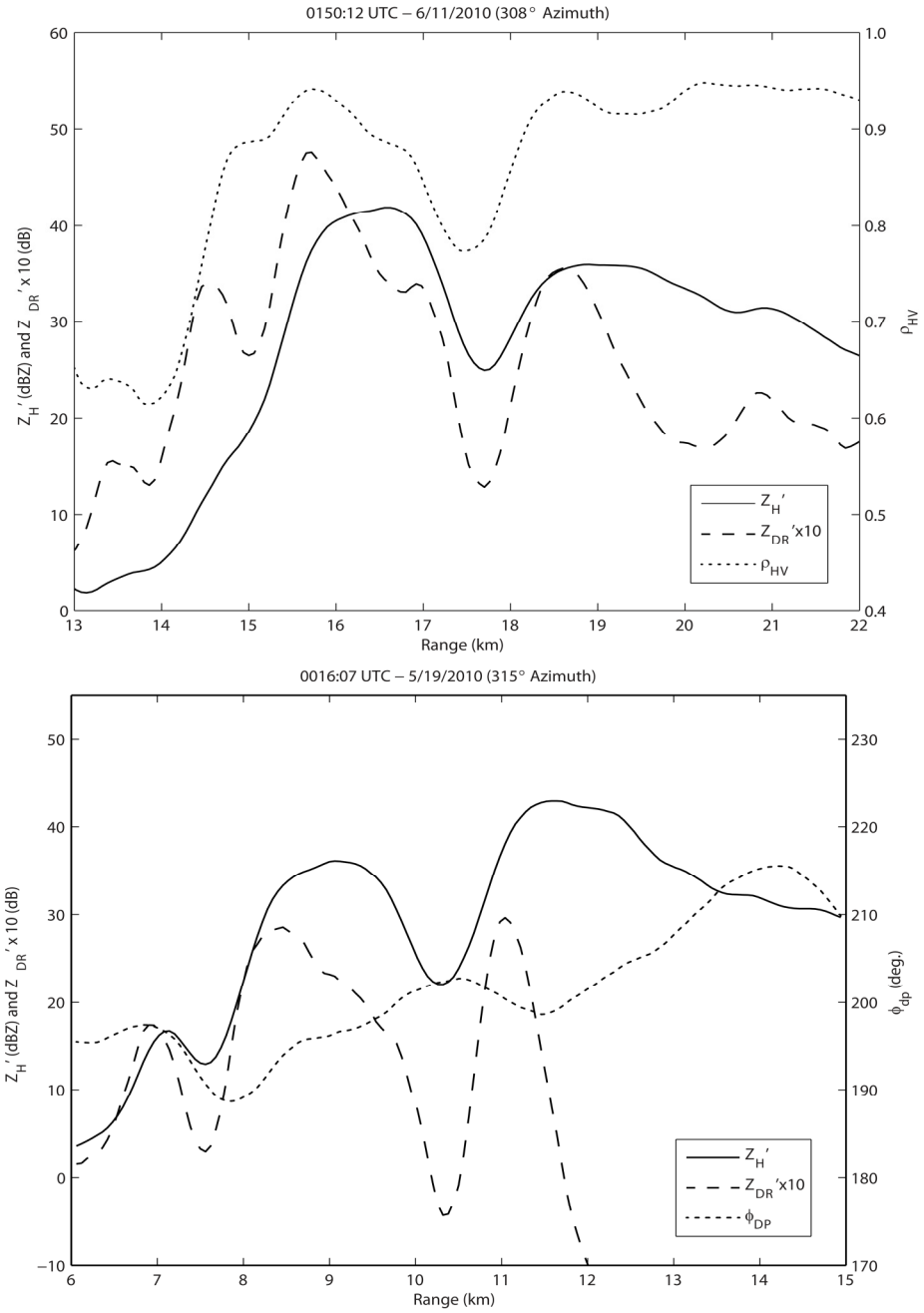

Figure 15. Radial profiles of (a) Z_H' (solid line), $Z_{DR}' \times 10$ (long dashed line), and ρ_{hv} (short dashed line) from 0150:12 UTC on 11 June 2010 (along black line in Figure 13a) and (b) Z_H' (solid line), $Z_{DR}' \times 10$ (long dashed line), and Φ_{DP} (short dashed line) from 0016:07 UTC on 19 May 2010 (along black line in Figure 14a). To enhance clarity and reduce high-frequency variability, the plotted variables are filtered by centered averaging through either a 500 m (Z_H', Z_{DR}', ρ_{hv}) or 1 km (Φ_{DP}) range. The LRR is centered at ranges of ~17.6 km and ~10.2 km in (a) and (b), respectively. [From Snyder et al. (2013)]

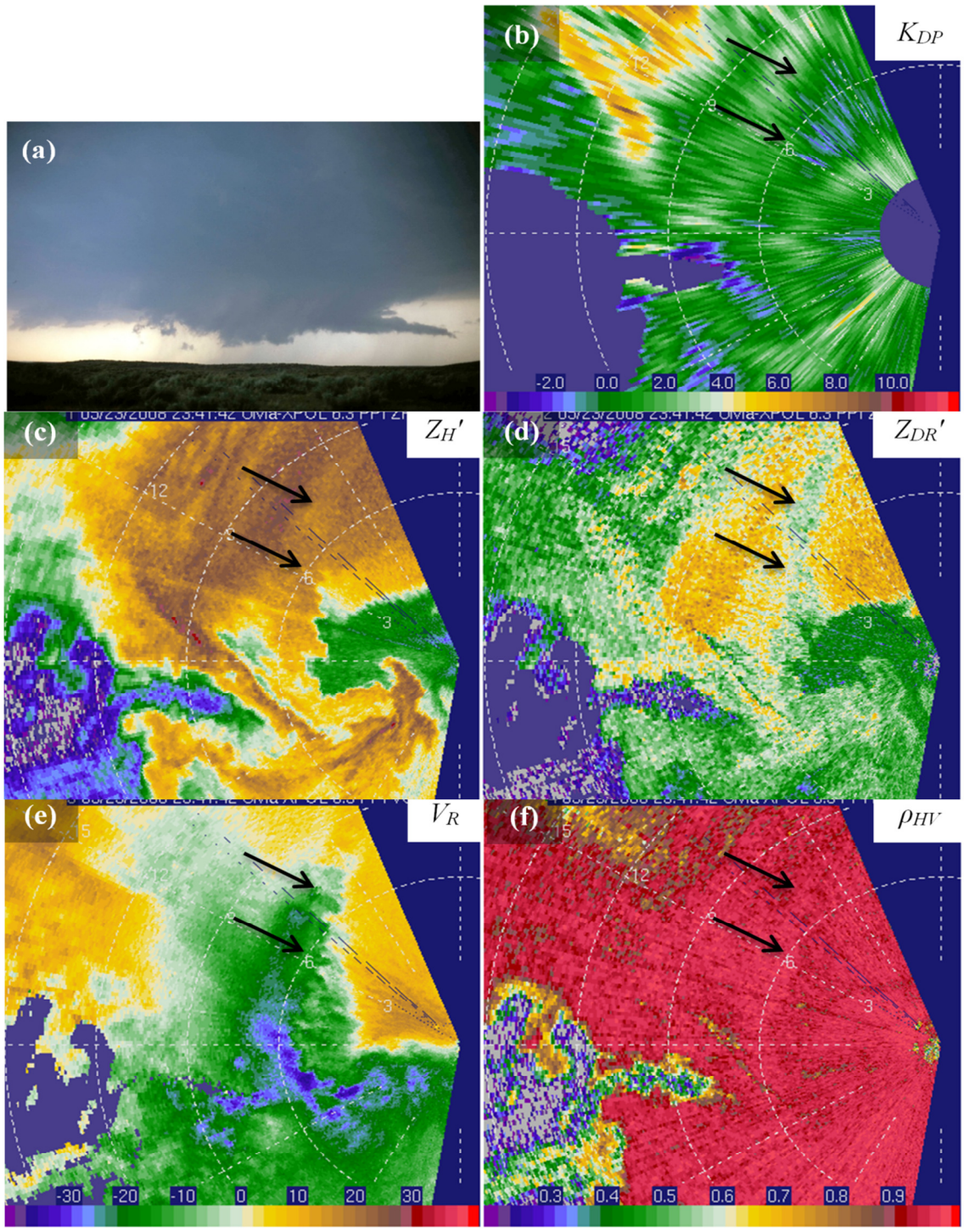

Figure 16. (a) A photograph, taken near 2331 UTC, of a wall cloud produced by a supercell on 23 May 2008 in extreme northwestern Oklahoma (courtesy H. Bluestein). UMass XPol deployed ahead of the hook echo and strong rear-flank downdraft: (b) K_{DP}, (c) Z_H', (d) Z_{DR}', (e) V_R, and (f) ρ_{hv} valid 2341:42 UTC. The arrows mark the location of the LRR, which is more evident in Z_{DR}' than Z_H'. [From Snyder et al. (2013)]

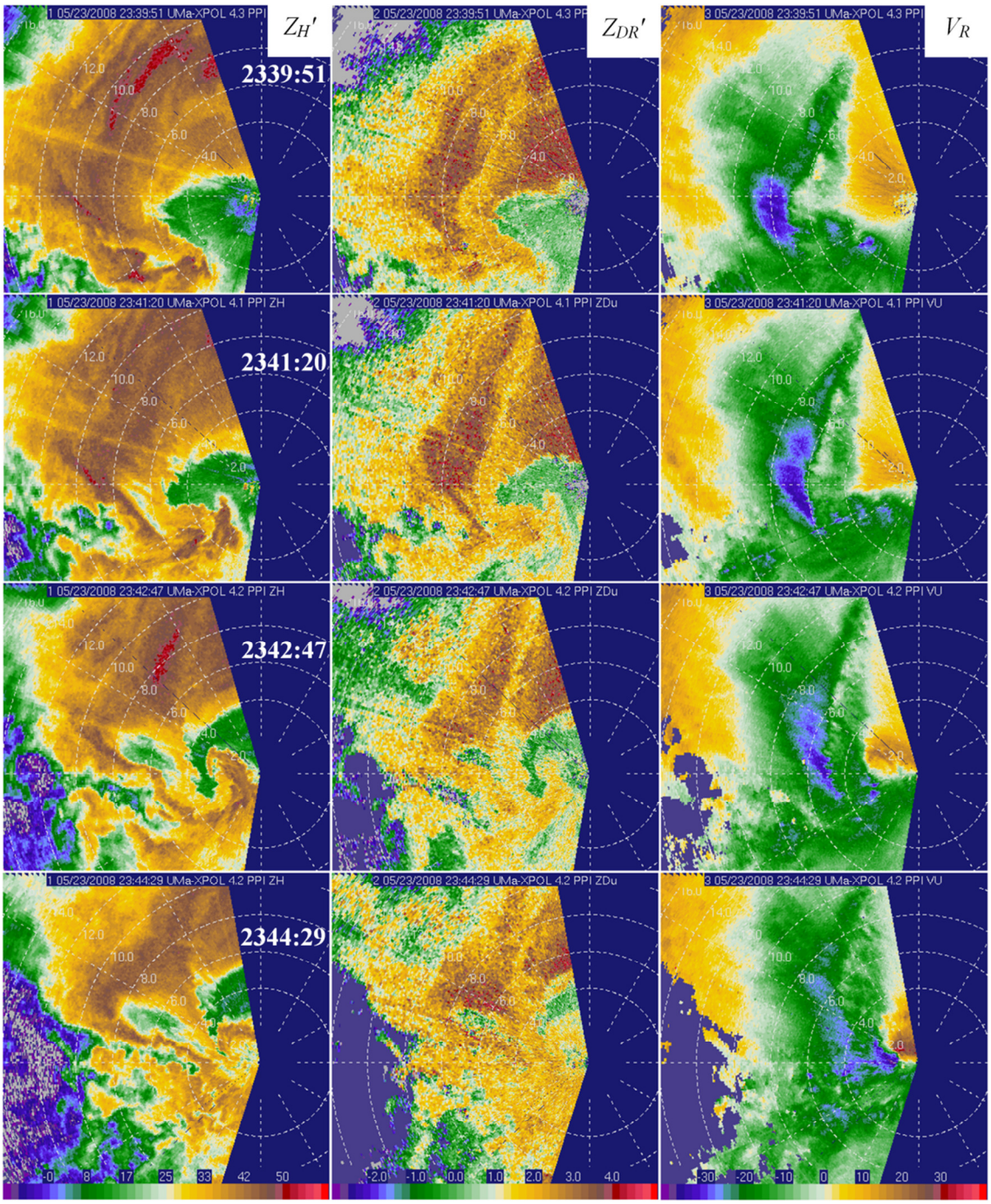

Figure 17. Z_H' (left), Z_{DR}' (center), and V_R (right) valid, top to bottom, at 2239:51, 2241:20, 2342:47, and 2344:29 UTC at ~4.2º elevation angle as a hook echo wraps up over UMass XPol on 23 May 2008. The LRR is clearer in Z_{DR}' than in Z_H'. At this elevation angle, strong radial convergence is associated with the LRR. Peak V_R in the hook echo reaches 45 m s^{-1} by the latest time ~1.3 km W of the radar. Range rings are in 2 km increments. [From Snyder et al. (2013)]

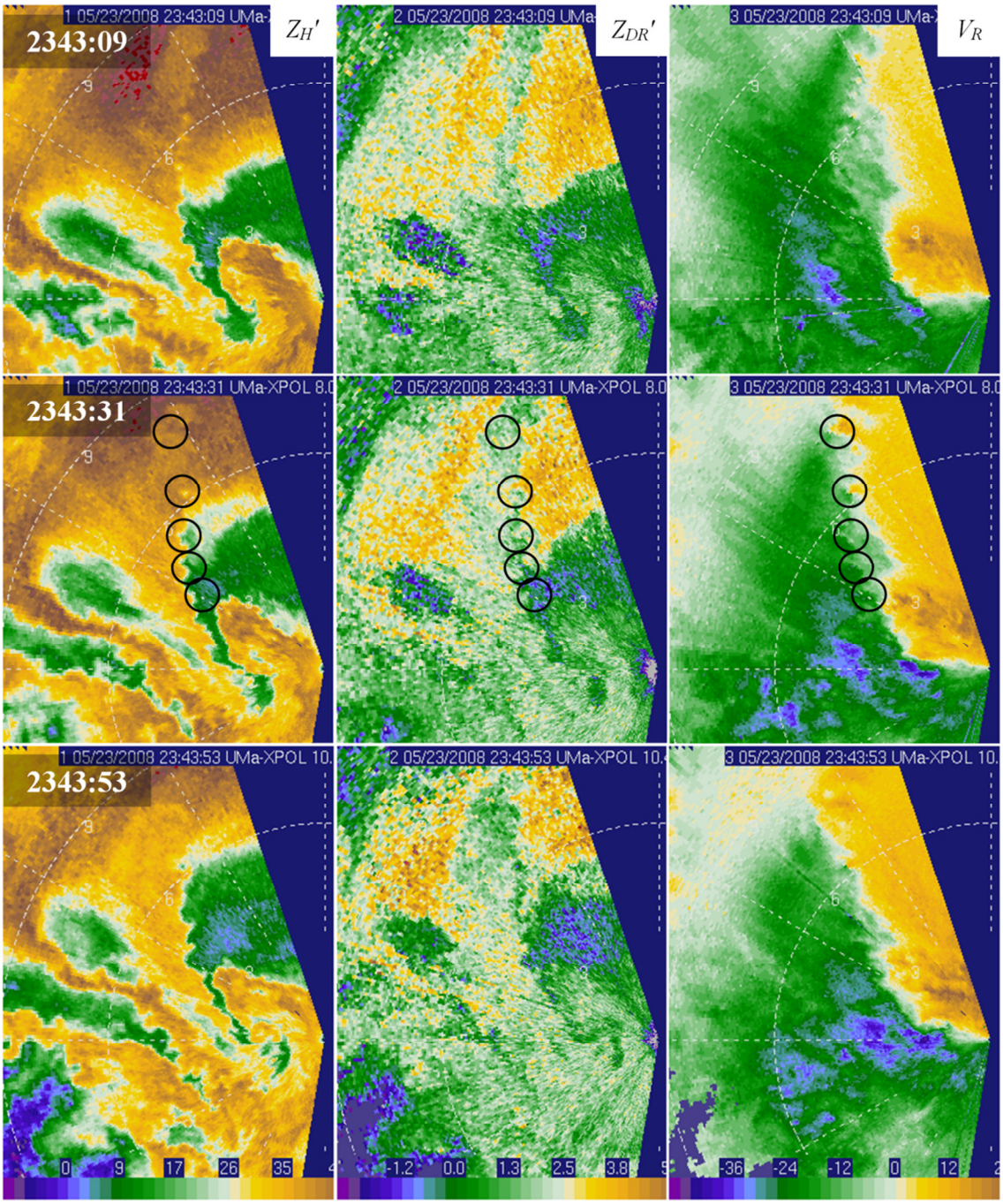

Figure 18. Z_H' (left), Z_{DR}' (center), and V_R (right) valid at 2343:09 (top), 2343:31 (middle), and 2343:53 (bottom) UTC at 6.1°, 8.0 °, and 10.4° elevation angle. Small-scale vortices (several of which are marked by black circles) stream rapidly southward into the inside part of the wrapping hook echo. Low-level rotation continues to intensify beyond that shown in this figure; by 2344:51 (not shown), V_R increases to 50 m s^{-1} inbound and 45 m s^{-1} outbound, with the extrema separated by 1.0 km in the azimuthal direction. [From Snyder et al. (2013)]

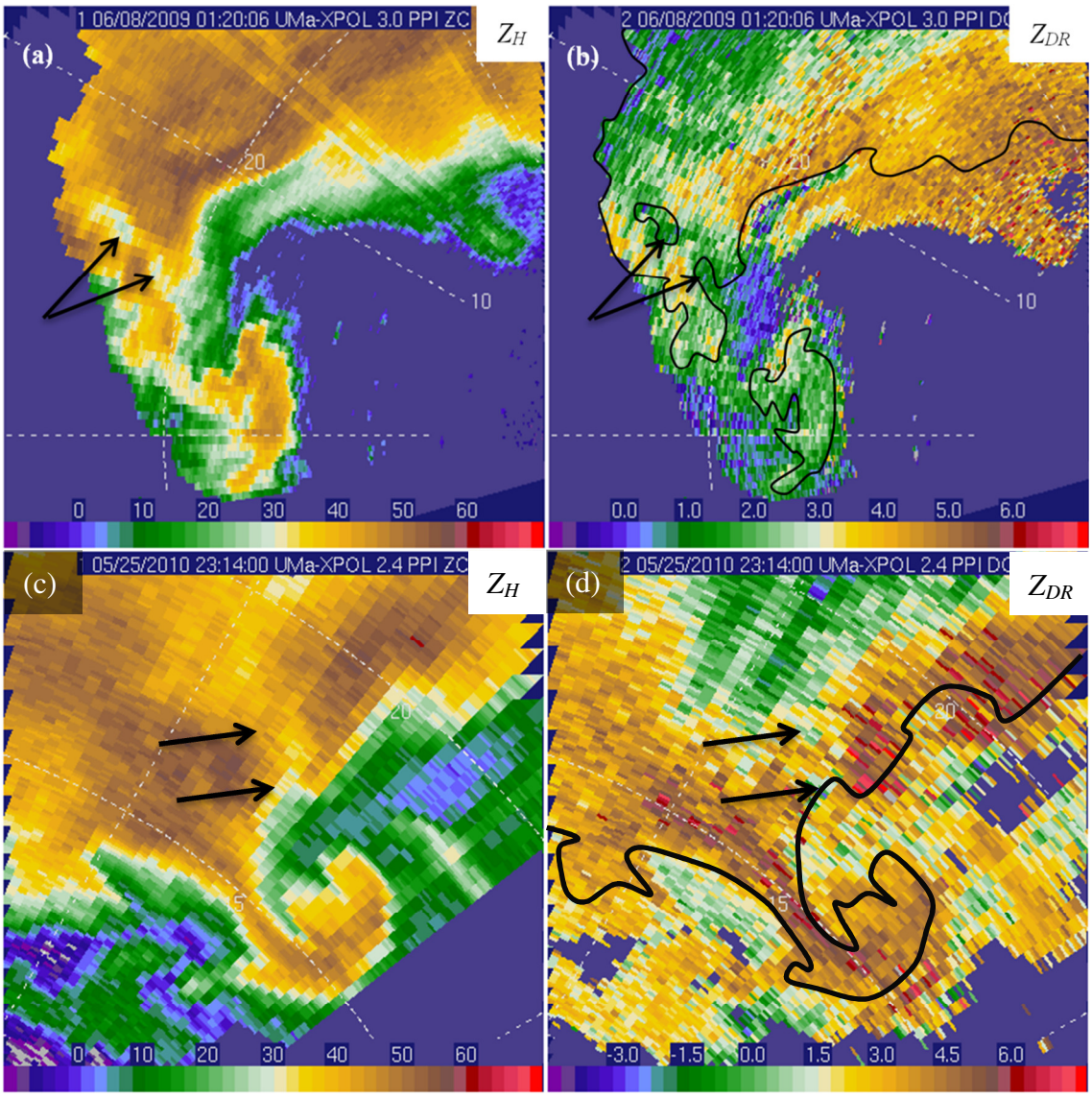

Figure 19. UMass XPol (a) Z_H and (b) Z_{DR} from the evening of 7 June 2009 and (c) Z_H and (d) Z_{DR} from the evening of 25 May 2010. The black arrows denote the location of an observed LRR, and the region of ~35 dBZ is outlined in black in (b). [From Snyder et al. (2013)]

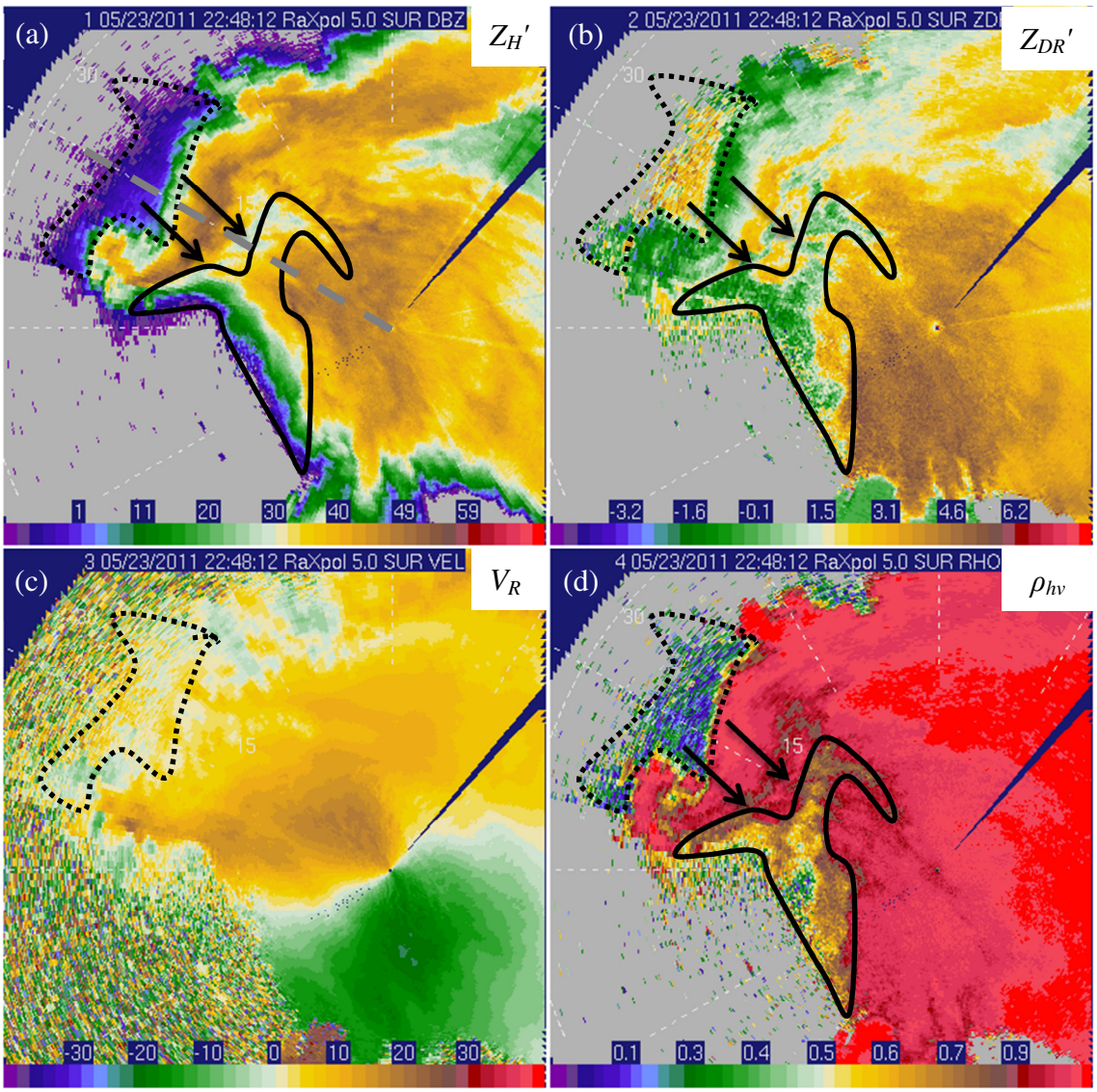

Figure 20. Polarimetric data from RaXPol collected at an elevation angle of 5° on the afternoon of 23 May 2011: (a) Z_H', (b) Z_{DR}', (c) V_R, and (d) ρ_{hv}. The black arrows point to the low-reflectivity ribbon, and the black enclosed area marks the probable location of large hail (and possibly non-meteorological scatters associated with strong inflow just south and west of the forward-flank gust front). The black dotted enclosed area marks a three-body scatter spike; the long dash grey line in (a) marks the location of the reconstructed RHI in Figure 21. This supercell produced the largest hailstone ever observed in Oklahoma approximately 25 minutes prior to this scan. A polarimetric three-body scatter spike is also evident and is marked by a black, dotted curve.

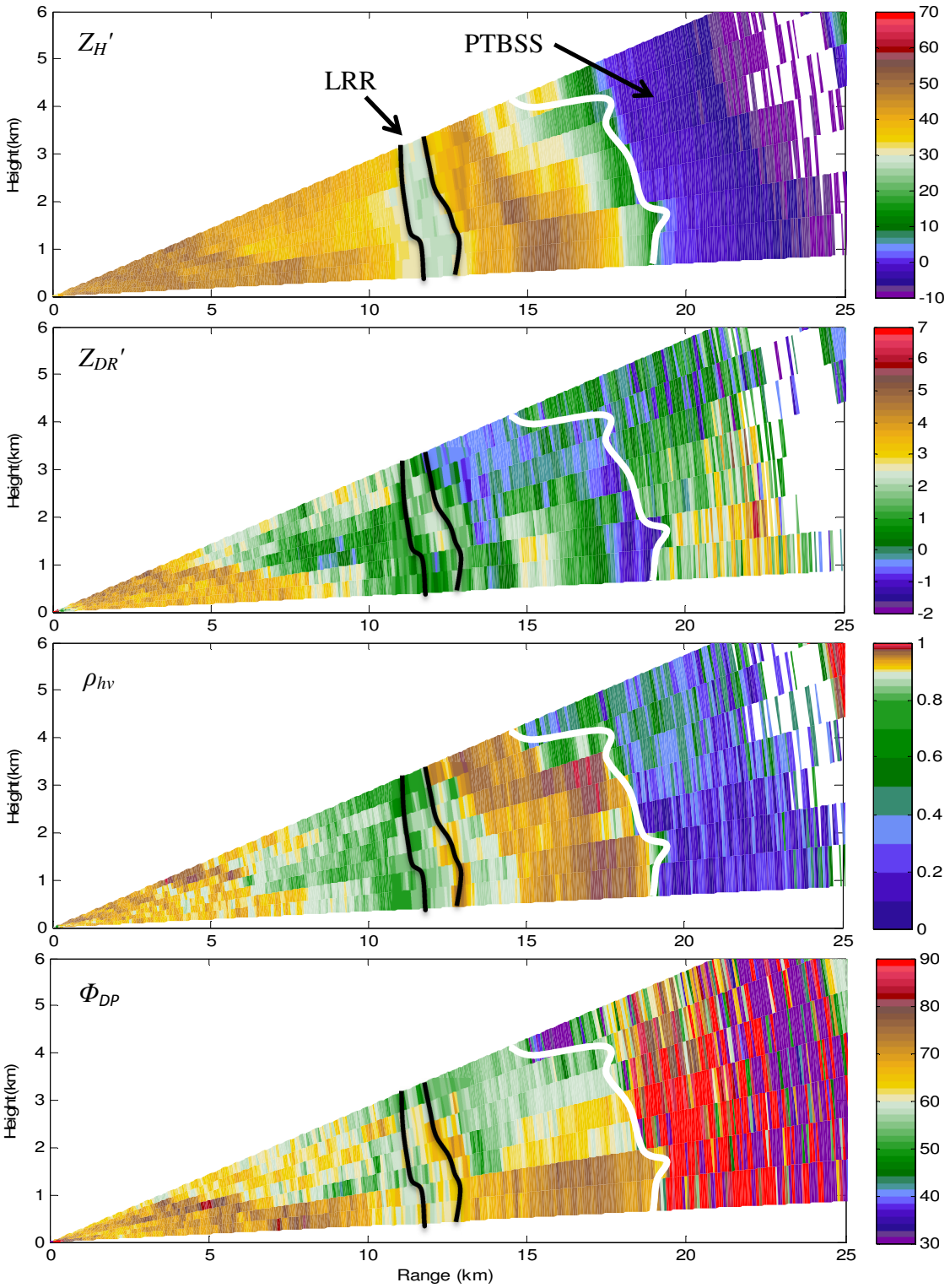

Figure 21. A reconstructed vertical cross-section (RHI) valid near 2248-2250 UTC on 23 May 2011 through the LRR of a supercell southeast of Gotebo, Oklahoma. (a) Z_H', (b) Z_{DR}', (c) ρ_{hv}, and (d) Φ_{DP} are shown. The cross-section is taken from along the long dashed grey line in Figure 20. The black curves in (a)–(d) mark the approximate location of the 30 dBZ isoecho; the white curve approximates the edge of ρ_{hv} = 0.4.

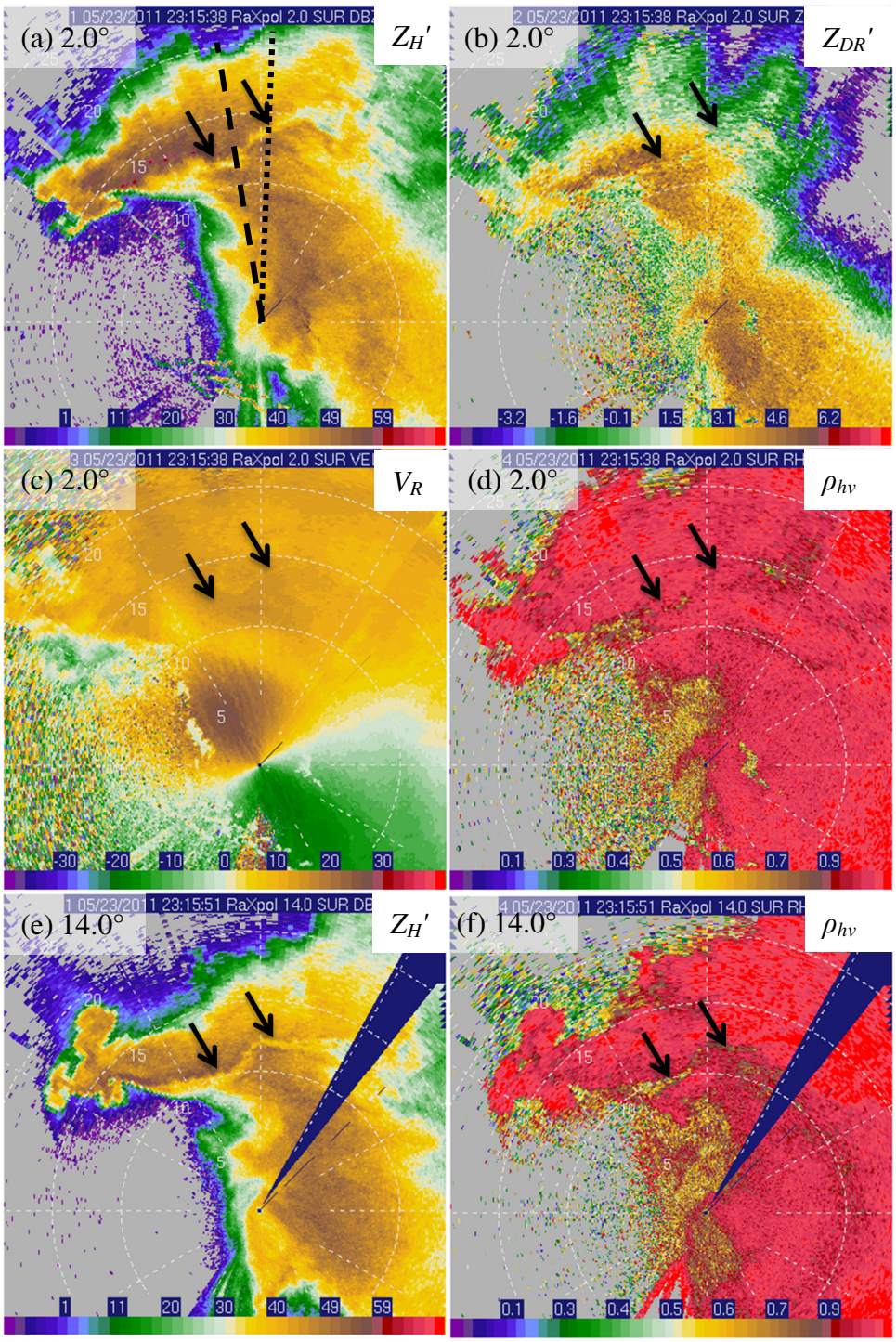

Figure 22. (a) Z_H', (b) Z_{DR}', (c) V_R, and (d) ρ_{hv} valid 2316 UTC on 23 May 2011 along a 2.0° elevation angle; (e) Z_H' and (f) ρ_{hv} valid near the same time along collected at a 14.0° elevation angle. The LRR is marked with black arrows. Range rings are shown every 5 km. The dotted and dashed black lines in (a) denote the azimuths (~350° and ~2°, respectively) of the reconstructed RHIs in Figure 23.

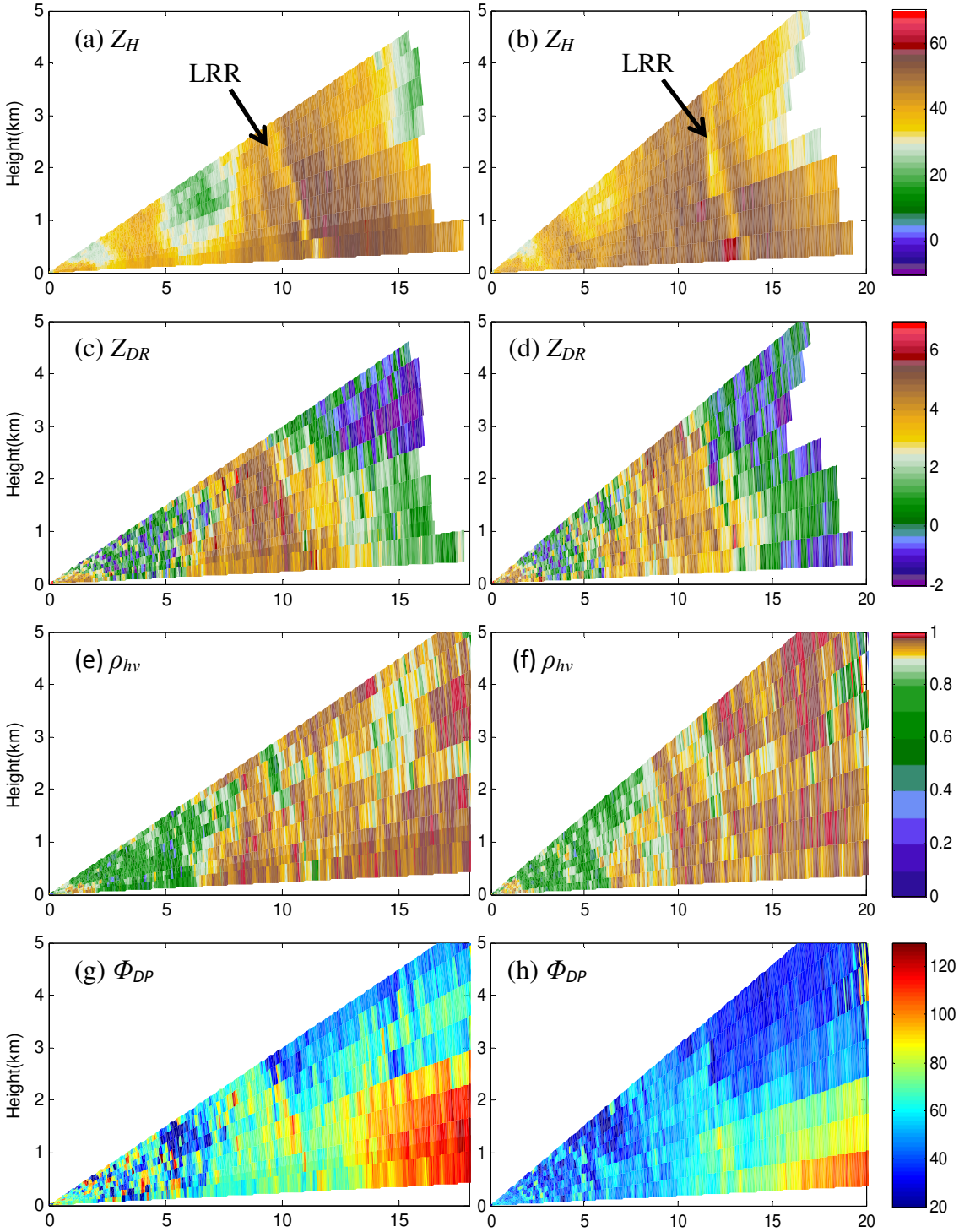

Figure 23. Reconstructed RHIs valid 2315-2316 UTC on 23 May 2011(the same volume as Figure 22) at azimuths of (left column) 350° and (right column) 2°. (a)–(b) Z_H, (c)–(d) Z_{DR}, (e)–(f) ρ_{hv}, and (g)–(h) Φ_{DP} are shown.

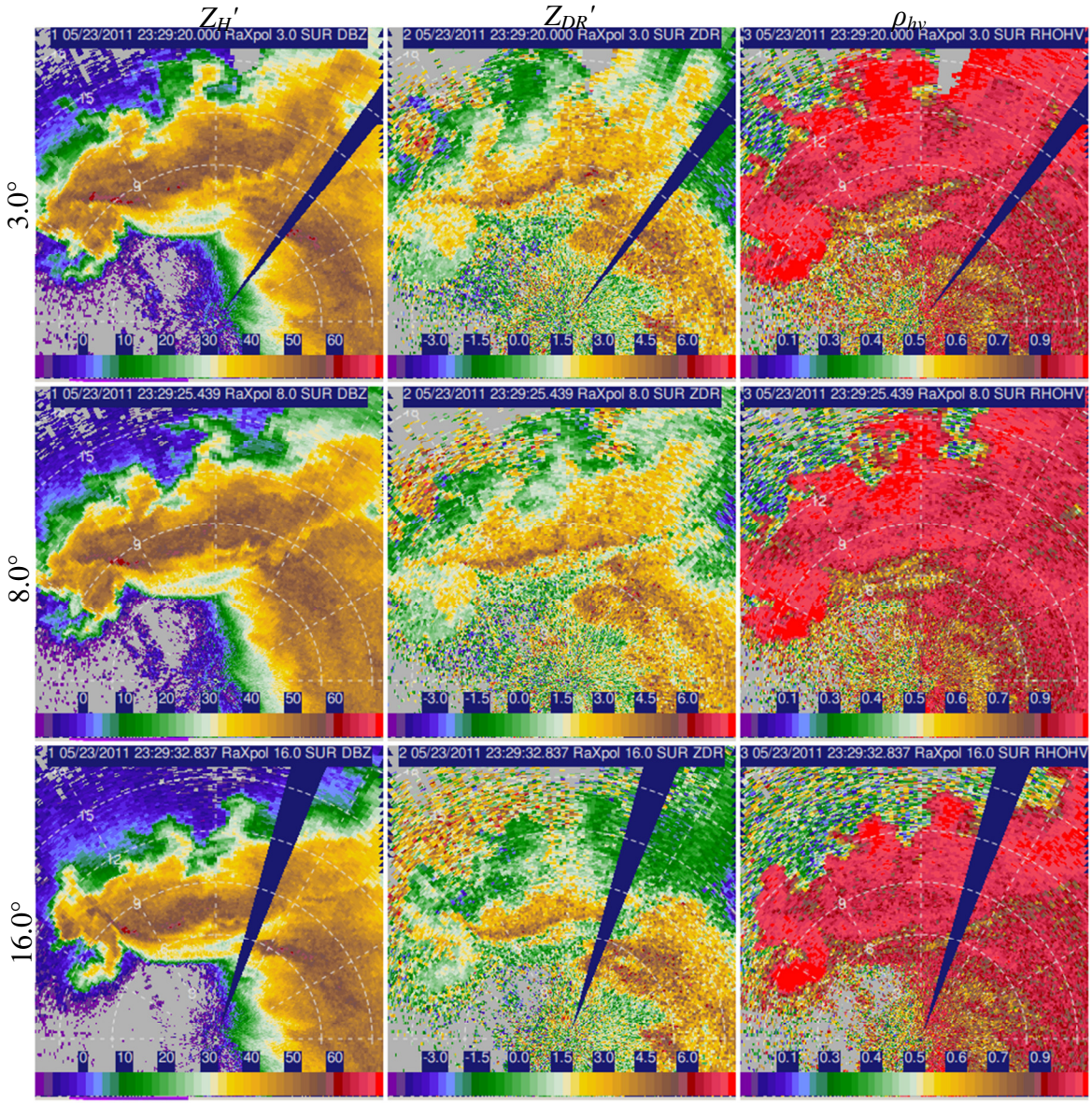

Figure 24. Z_H' (left), Z_{DR}' (center), and ρ_{hv} (right) from near 2329 UTC at elevation angles of, from top to bottom, 3.0°, 8.0°, and 16.0° on 23 May 2011. Range rings are marked every 3 km.

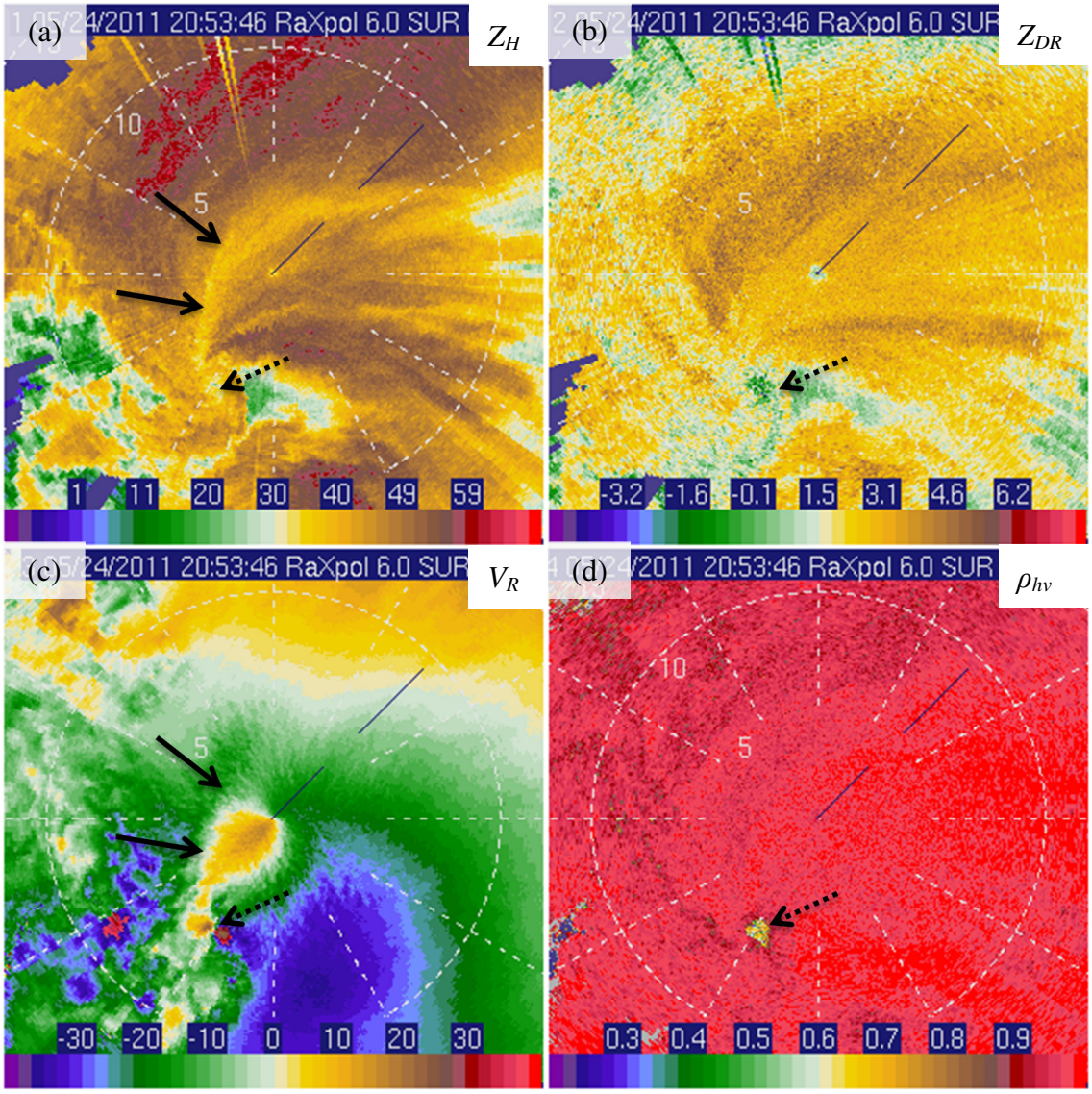

Figure 25. (a) Z_H, (b) Z_{DR}, (c) V_R, and (d) ρ_{hv} valid at 2053:46 UTC on 24 May 2011 near El Reno, Oklahoma. The LRR, marked by black arrows, is most apparent in Z_H' and is associated with strong radial convergence observed in V_R. A polarimetric tornado debris signature is marked by the dotted black arrow. The few radially-oriented streaks in (a) and (b) are artifacts of the attenuation correction scheme.

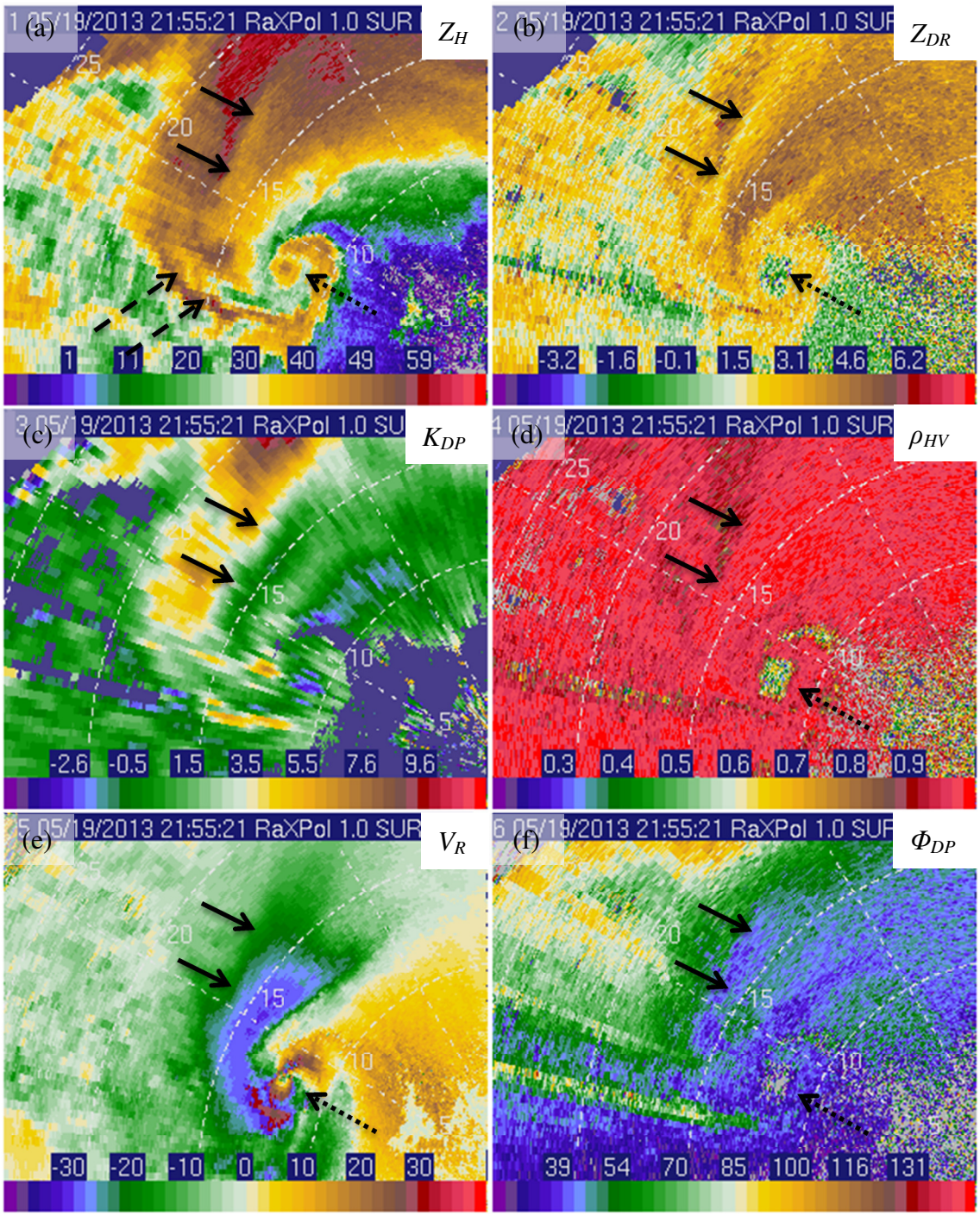

Figure 26. (a) Z_H, (b) Z_{DR}, (c) K_{DP}, (d) ρ_{hv}, (e) V_R, and (f) Φ_{DP} valid 2155:21 UTC on 19 May 2013 south of Carney, Oklahoma, at an elevation angle of 1.0°. Solid black arrows mark the LRR; a potential secondary LRR is marked by dashed black arrows in (a). A polarimetric tornado debris signature is evident at the tip of the hook echo at a range of ~12 km and marked by dotted black arrows. Maximum inbound velocities are 90-100 m s^{-1} on the south side of the tornado and were measured during a rightward/eastward "wobble" in the tornado track.

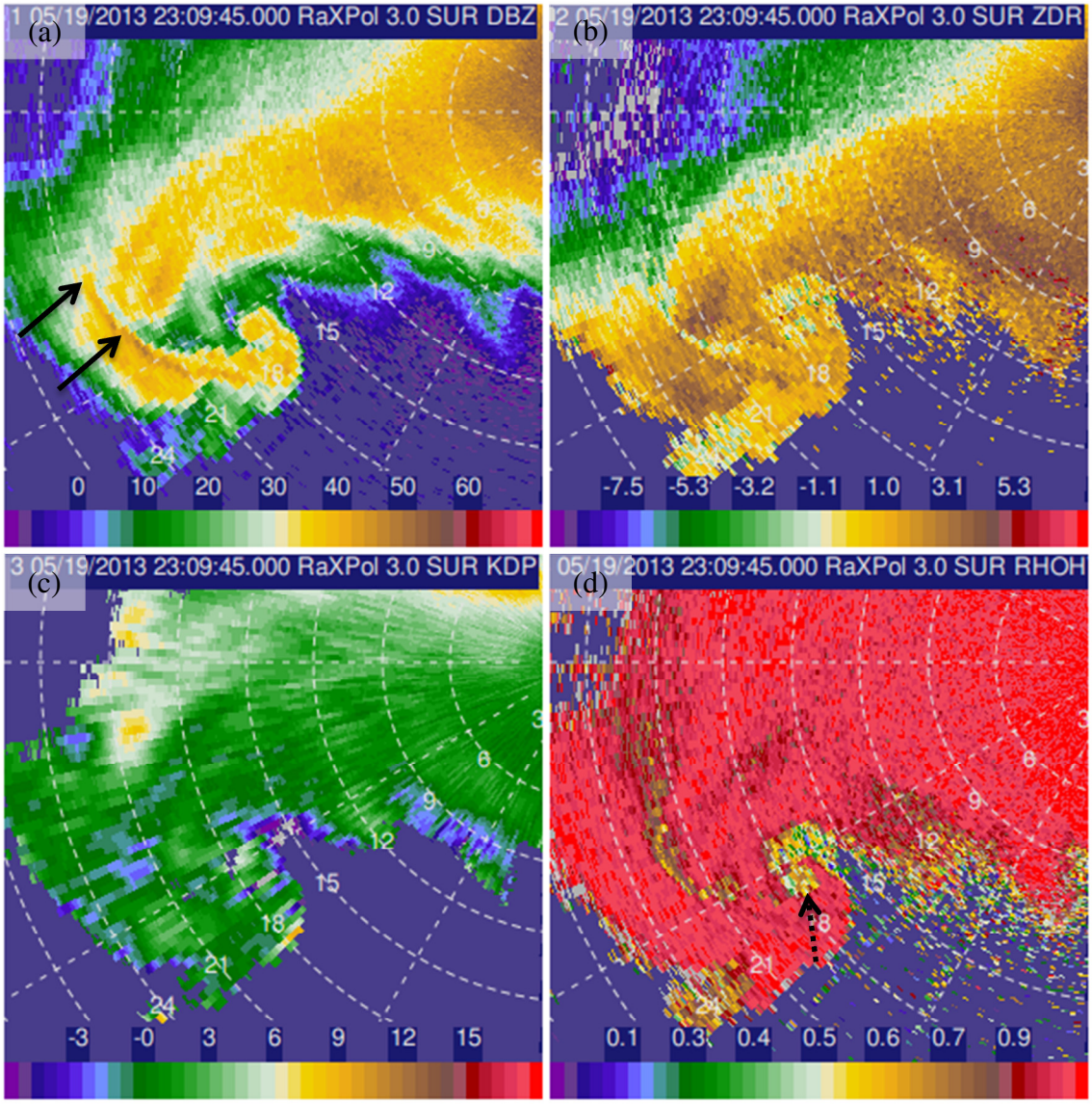

Figure 27. (a) Z_H', (b) Z_{DR}', (c) K_{DP}, and (d) ρ_{hv} valid at 2309:45 UTC on 19 May 2013 near Shawnee, Oklahoma. The LRR, marked by solid black arrows, is reflected in all fields. The dotted black arrow in (d) points to the polarimetric tornado debris signature.

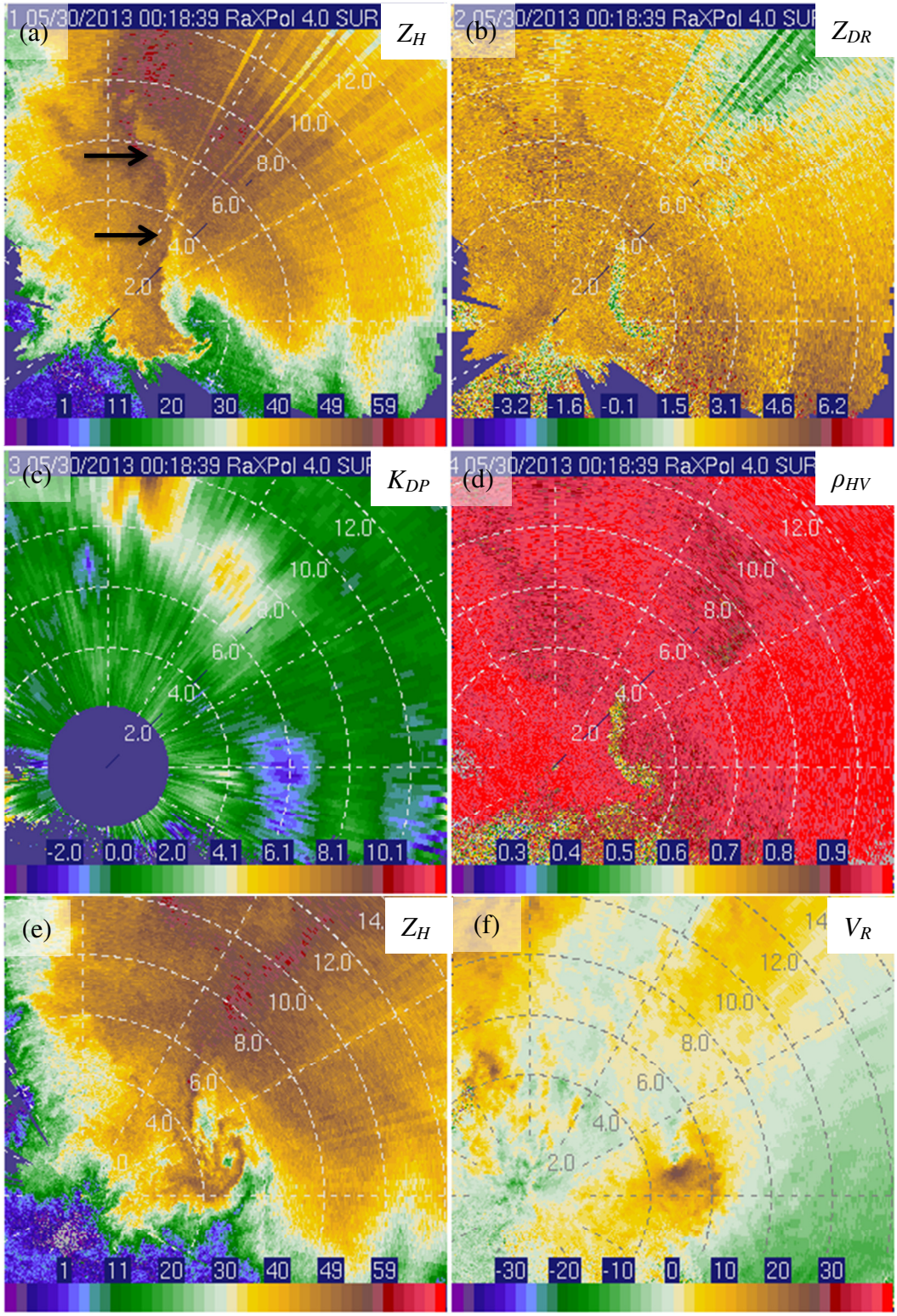

Figure 28. (a) Z_H, (b) Z_{DR}, (c) K_{DP}, and (d) ρ_{hv} valid 0018:36 UTC 30 May 2013 in southwestern OK at 4.0° elevation angle. A weak tornado develops at the tip of the hook echo. An LRR is marked by black arrows. By 0022:56 UTC, the LRR is no longer evident, but a weak echo hole in (e) Z_H' and couplet in (f) V_R associated with the tornado remain. Peak V_R on the 2° scan (not shown) is ~30 m s^{-1}.

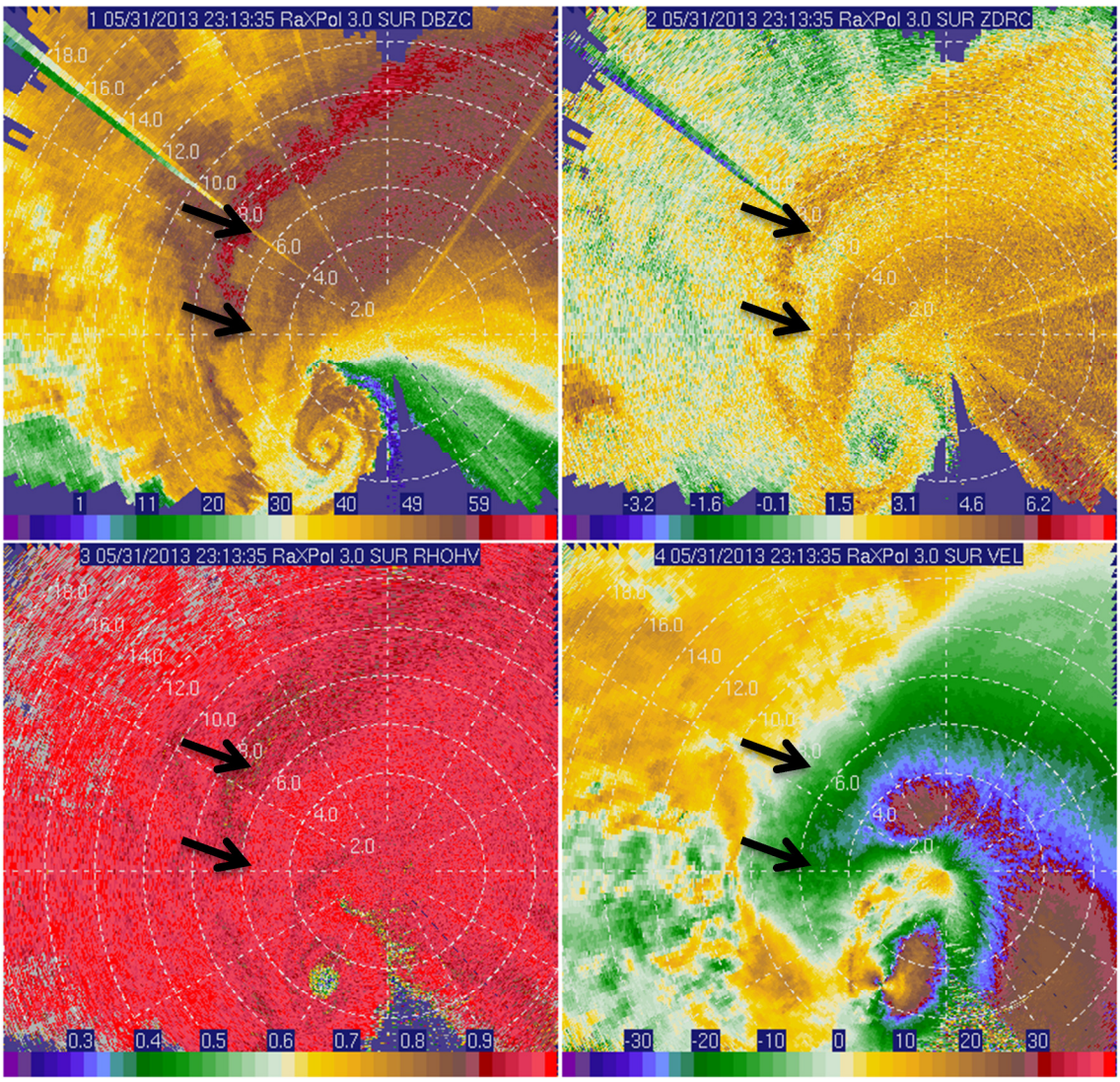

Figure 29. Polarimetric data from RaXPol collected on supercell producing a violent tornado on the evening of 31 May 2013: (a) Z_H, (b) Z_{DR}, (c) ρ_{hv}, and (d) V_R. The black arrows point to the LRR. Data are valid at 2313 UTC (i.e., relatively early in the lifecycle of the tornado) at a 3.0° elevation angle. The peak V_R at this time is ~68 m s^{-1}.

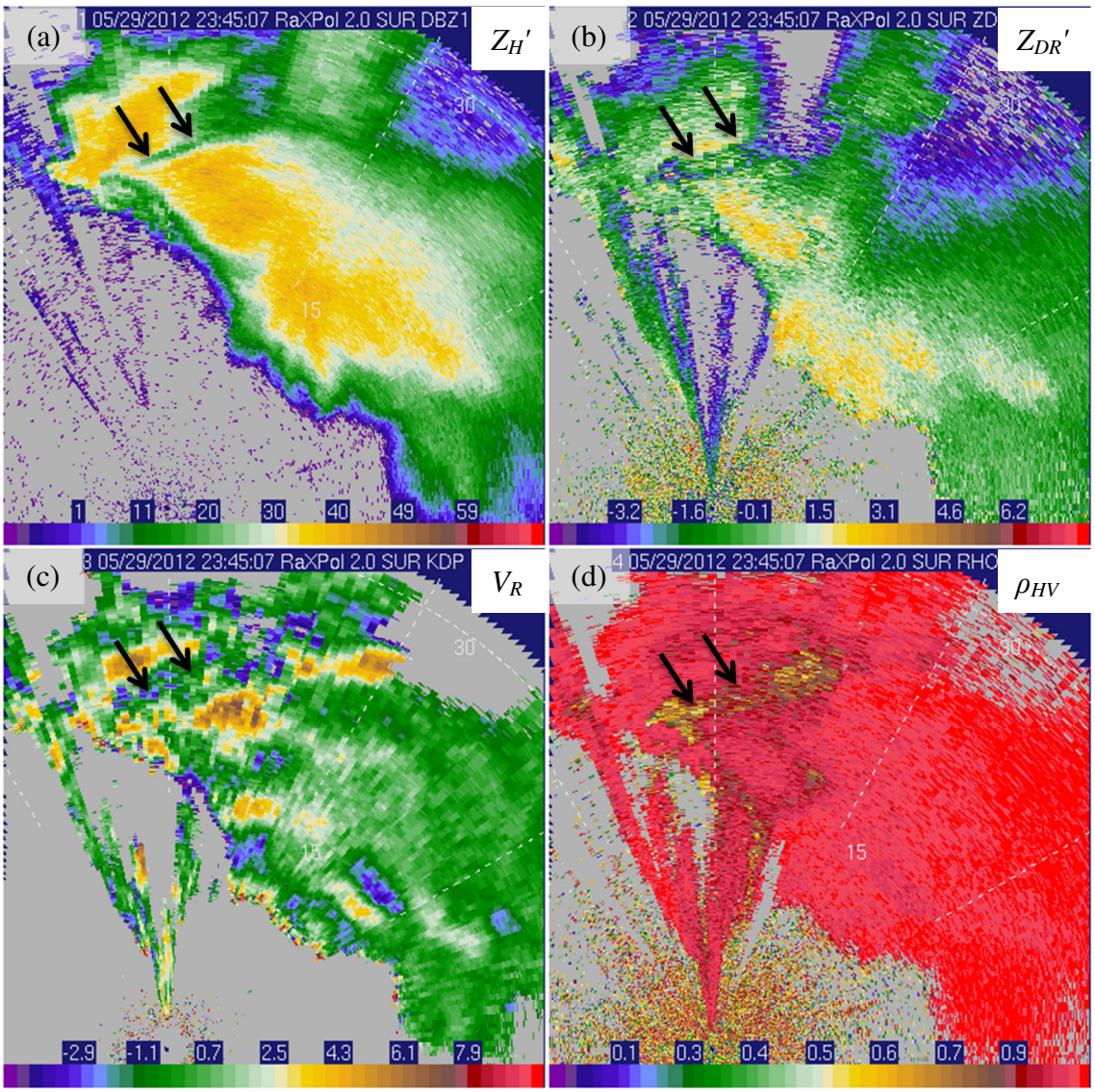

Figure 30. Polarimetric data from RaXPol collected on the afternoon of 29 May 2012: (a) Z_H', (b) Z_{DR}', (c) K_{DP}, and (d) ρ_{hv}. The black arrows point to the LRR. A hardware problem resulted in reduced data quality and biases in Z_H' and Z_{DR}' that are not accounted for in (a) and (b).

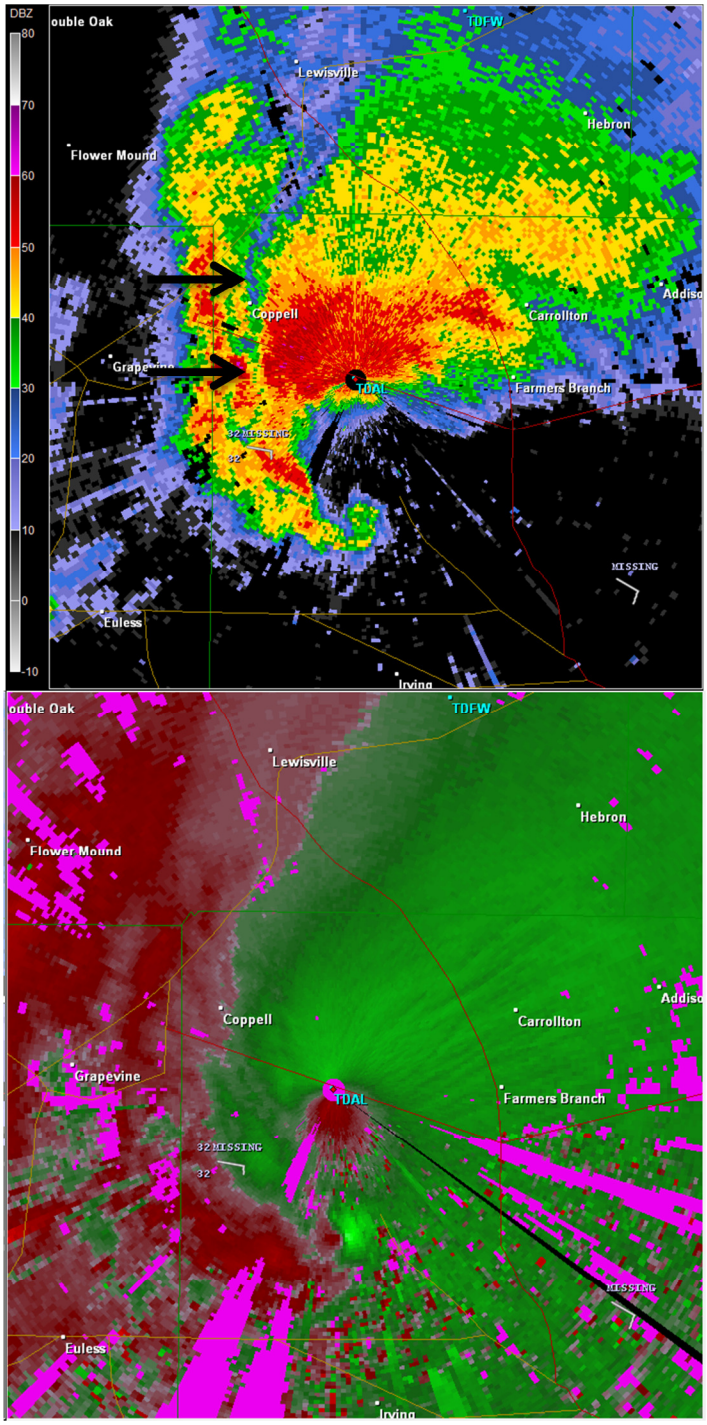

Figure 31. (a) Z_H and (b) V_R of a possible LRR (marked by black arrows) observed within a tornadic supercell on 3 April 2012 near the TDAL radar, a C-band Terminal Doppler Weather Radar located near Dallas Love Field Airport.

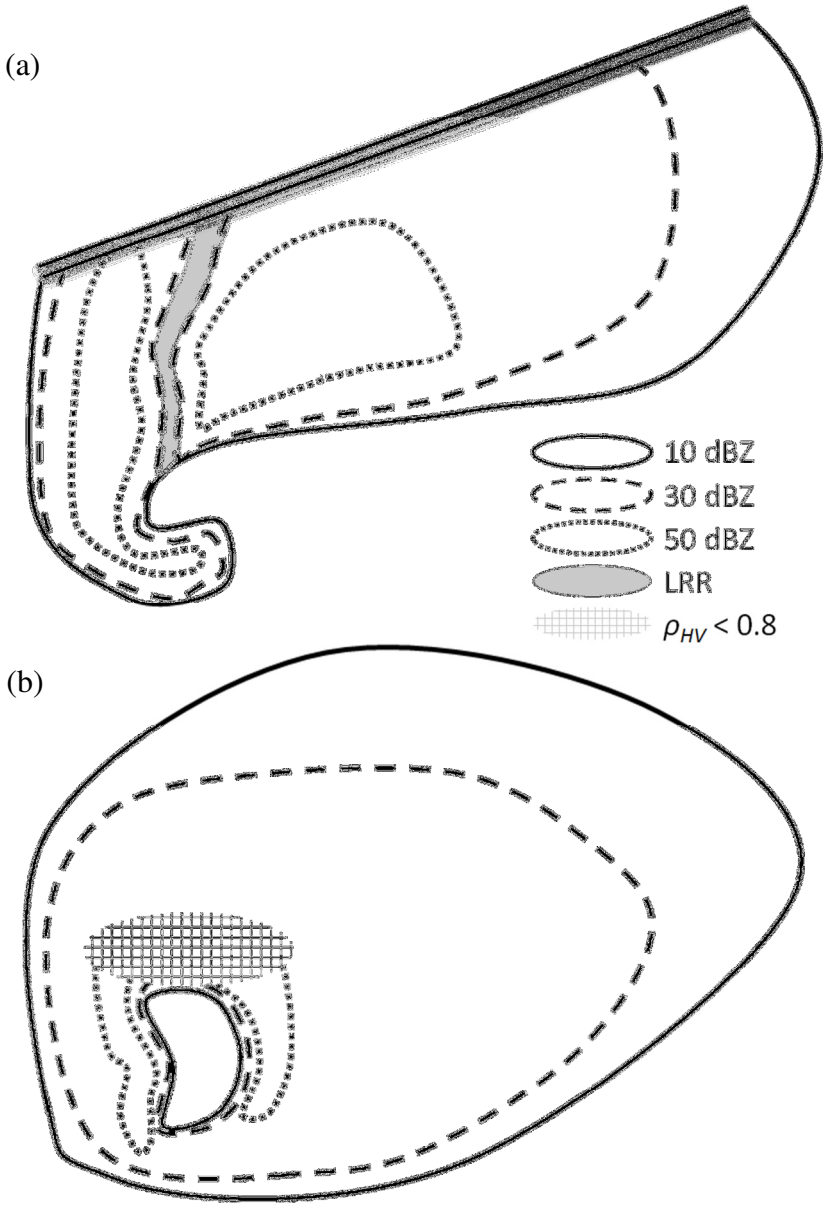

Figure 32. Generalized configurations for the (a) low-reflectivity ribbon (LRR) and (b) area of very low ρ_{hv} on the left side of the BWER (LoRB). Panel (a) is valid within 1 km AGL, and (b) is valid near and within 1 km of the ambient freezing level. As a result of the deployment locations typical of data collection efforts, there often is very high attenuation (sometimes to extinction) along the rear portion (often north and northwest for typical mobile radar deployments) of observed supercells. As such, confidence is low in this region; the double black line at the top of (a) indicates this uncertainty. [From Snyder et al. (2013)]

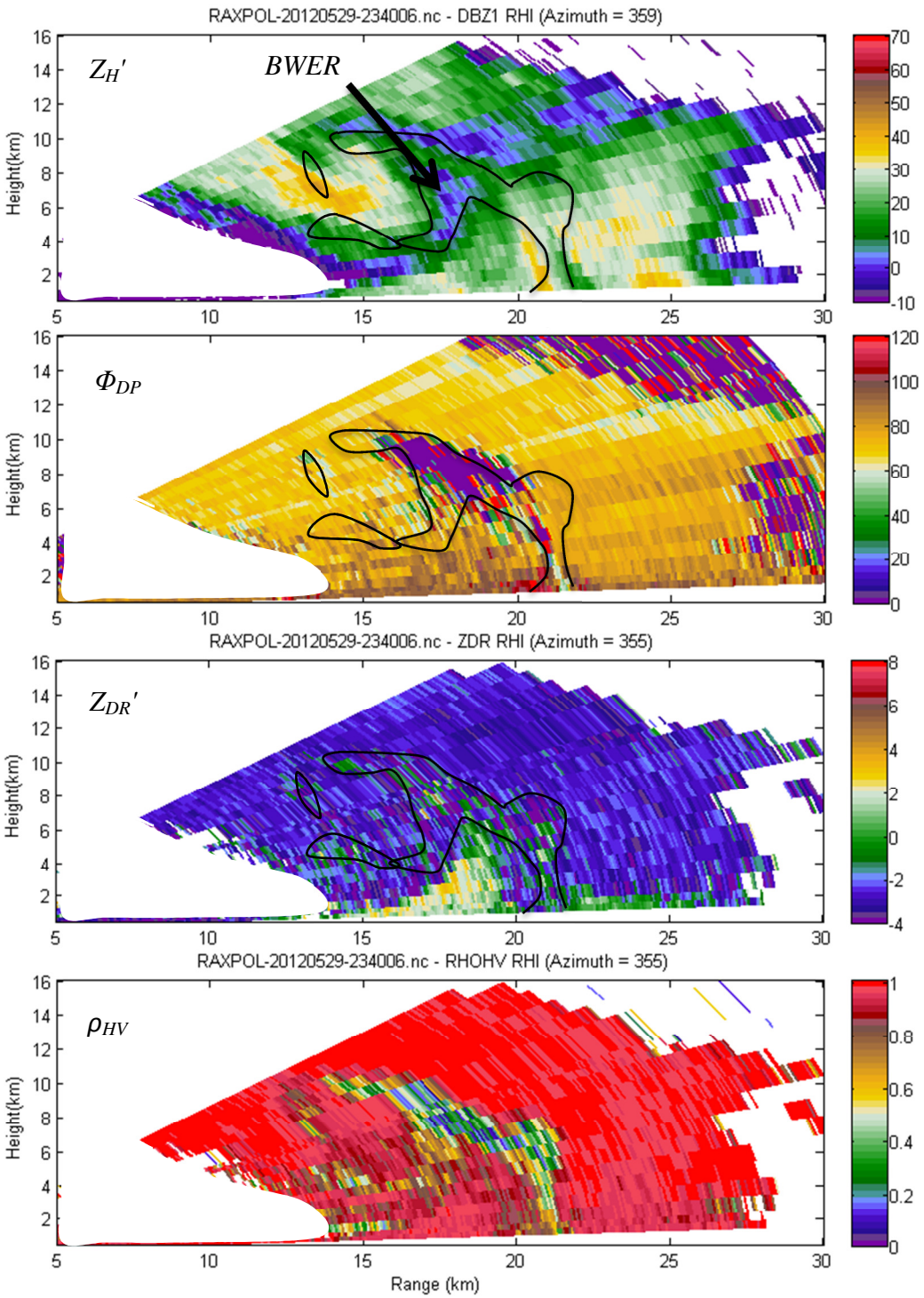

Figure 33. A reconstructed vertical cross-section (RHI) valid near 2340 UTC on 29 May 2012 through the BWER of a supercell near Kingfisher, Oklahoma. (a) Z_H', (b) Φ_{DP}, (c) Z_{DR}', and (d) ρ_{hv} are shown. The approximate location of the $\rho_{hv} = 0.85$ isopleth is marked by the black curves in (a)–(c). Hardware problems during the spring of 2012 resulted in a ~2.5 dB bias in Z_{DR}' and an unknown negative bias in Z_H' on this day.

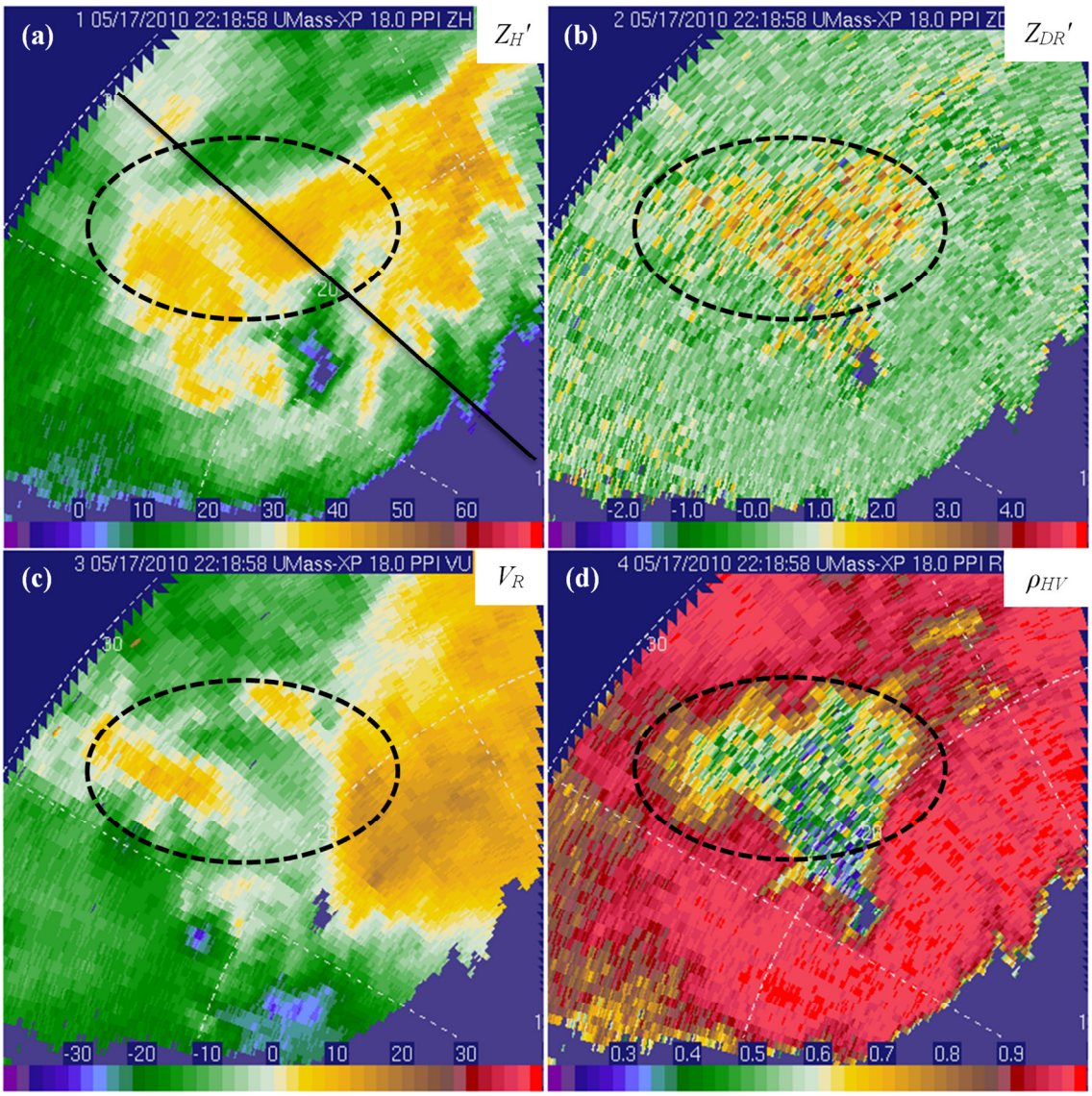

Figure 34. (a) Z_H', (b) Z_{DR}', (c) V_R, and (d) ρ_{hv} valid at 18° elevation angle from 17 May 2010 in New Mexico as seen by UMass XPol. The black ellipse marks the large area of very low ρ_{hv} northwest of the BWER where Z_H' values of 30–45 dBZ reside. The beam height was approximately 5.5 km ARL in the center of the BWER; in the LoRB, the beam was centered approximately 6–8 km ARL. Range rings are marked every 10 km. The black line in (a) marks the azimuth along which the reconstructed vertical cross-sections shown in Figure 35 are created. A near-storm sounding collected during VORTEX2 (not shown) near 2200 UTC measured deep-layer shear oriented southwest to northeast. [From Snyder et al. (2013)]

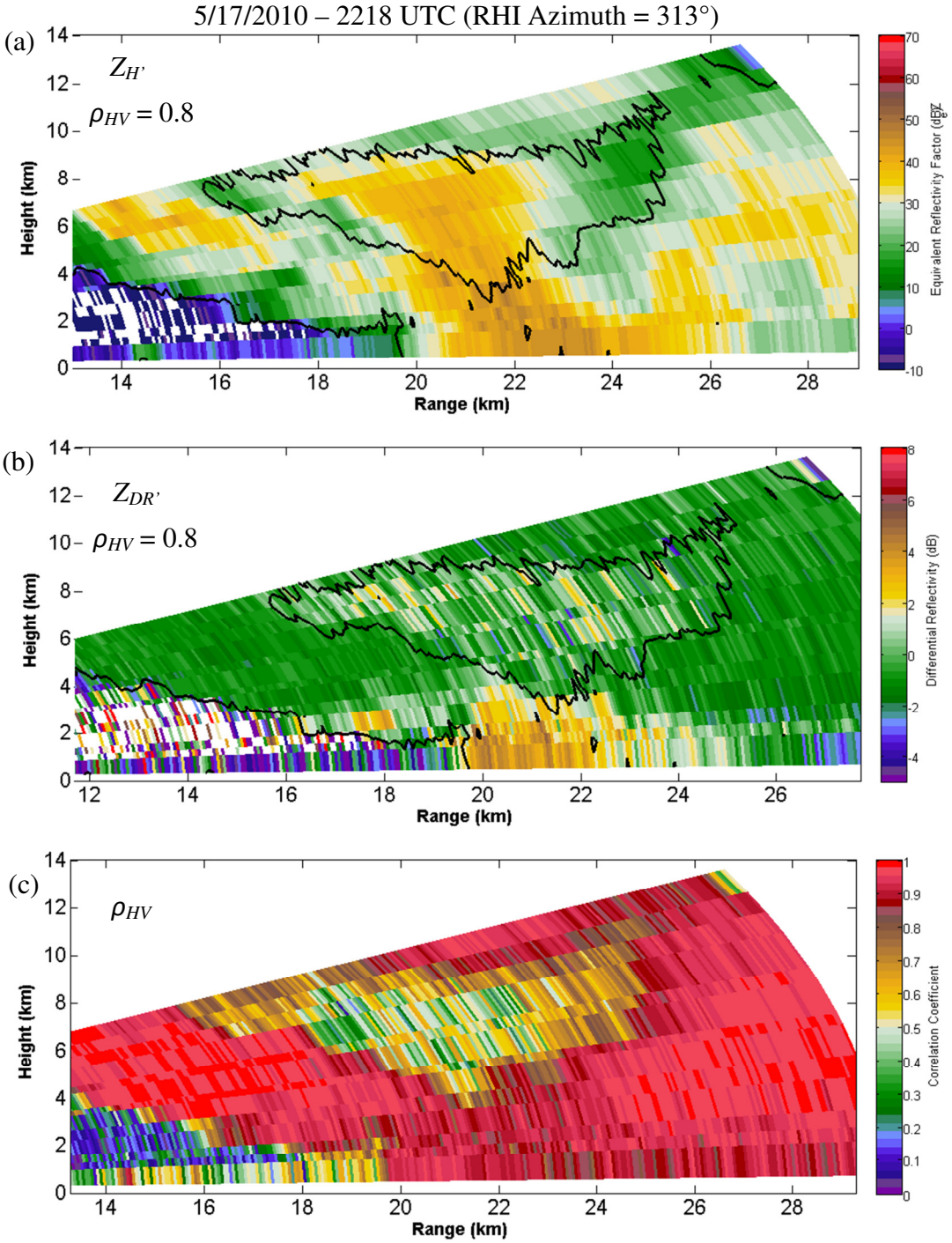

Figure 35. A reconstructed vertical cross-section (RHI) valid near 2218 UTC on 17 May 2010 (representing data along the azimuth marked by the black line in Figure 34a) along the 313° azimuth showing (a) Z_H', (b) Z_{DR}', (c) ρ_{hv}. The black contours in (a) and (b) represents the $\rho_{hv} = 0.8$ isopleth.

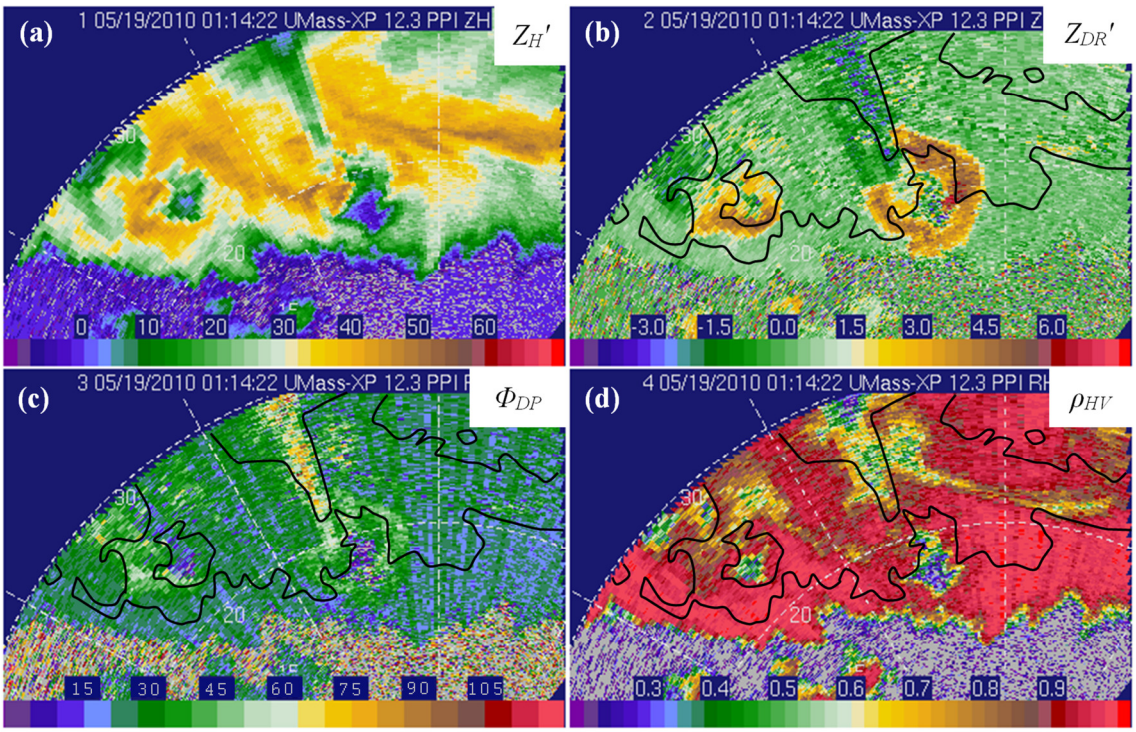

Figure 36. (a) Z_H', (b) Z_{DR}', (c) Φ_{DP}, and (d) ρ_{hv} at an elevation angle of 12.3° from a pair of severe storms as UMass XPol collected data in the Texas Panhandle on the evening of 18 May 2010. The black outlines in (b)–(d) approximate the location of the 30 dBZ isopleth. Range rings are shown every 10 km. Anomalously strong attenuation occurs along the left wall of the eastern BWER. Beam heights are ~5.0 km and 3.5 km ARL in the center of the western and eastern BWERs, respectively. NBF may be present as the radially-oriented reduction in ρ_{hv} in those radials that pass through the northwestern section of the eastern BWER (where notable attenuation is present). [From Snyder et al. (2013)]

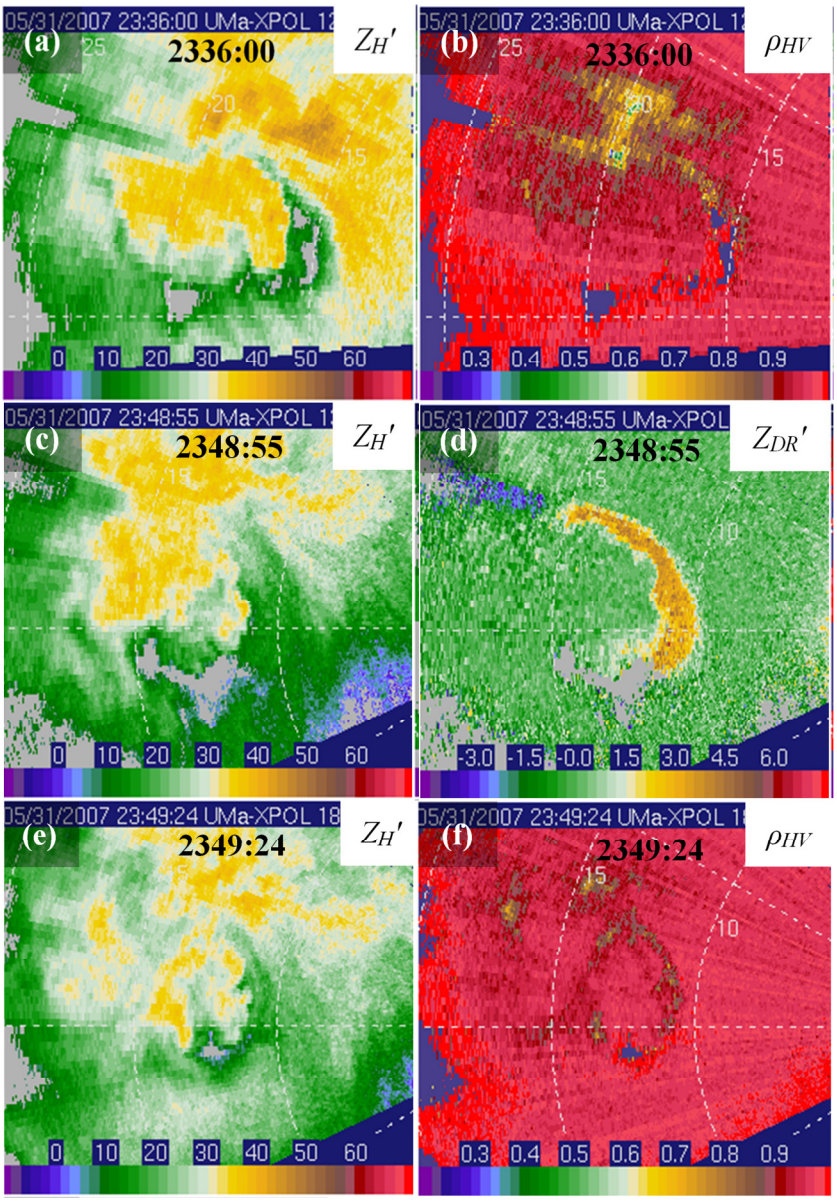

Figure 37. A small sampling of mid-level polarimetric signatures associated with a supercell that occurred on 31 May 2007: (a) Z_H' and (b) ρ_{hv} valid 2336:00 UTC (12.2º elevation), (c) Z_H' and (d) Z_{DR}' valid 2248:55 UTC (13.0º elevation), and (e) Z_H' and (f) ρ_{hv} valid 2349:24 UTC (18.0ºelevation). A LoRB, Z_{DR} half-ring, and ρ_{hv} ring are evident in (b), (d), and (f), respectively. [Adapted from Snyder et al. (2013)]

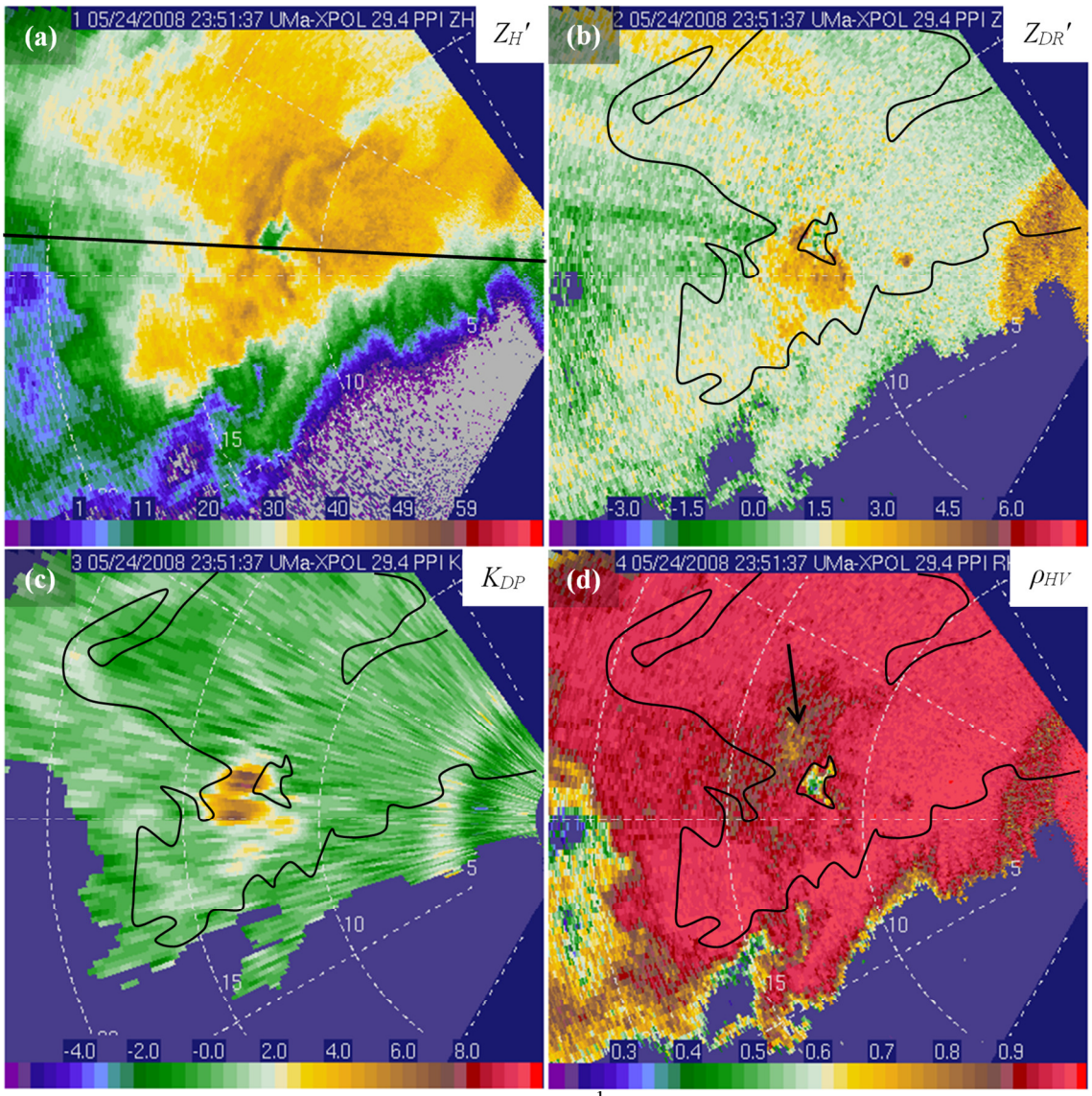

Figure 38. (a) Z_H', (b) Z_{DR}', (c) K_{DP} (in deg. km^{-1}), and (d) ρ_{hv} from a supercell sampled by UMass XPol on 24 May 2008. The black line in (a) marks the radial along which Figure 39 is created, and the approximately area of 30 dBZ is outlined in black. The top of the Z_{DR} and K_{DP} columns is evident in (b) and (c). The black arrow marks the area of reduced ρ_{hv} left of the BWER, though this feature is more evident at slightly lower altitudes. The elevation angle for all panels is 29.4°; the beam height at the range of the BWER is ~5.8 km ARL. The local freezing level is evident in the polarimetric data along the far right side of the image at a range of approximately 14 km. [From Snyder et al. (2013)]

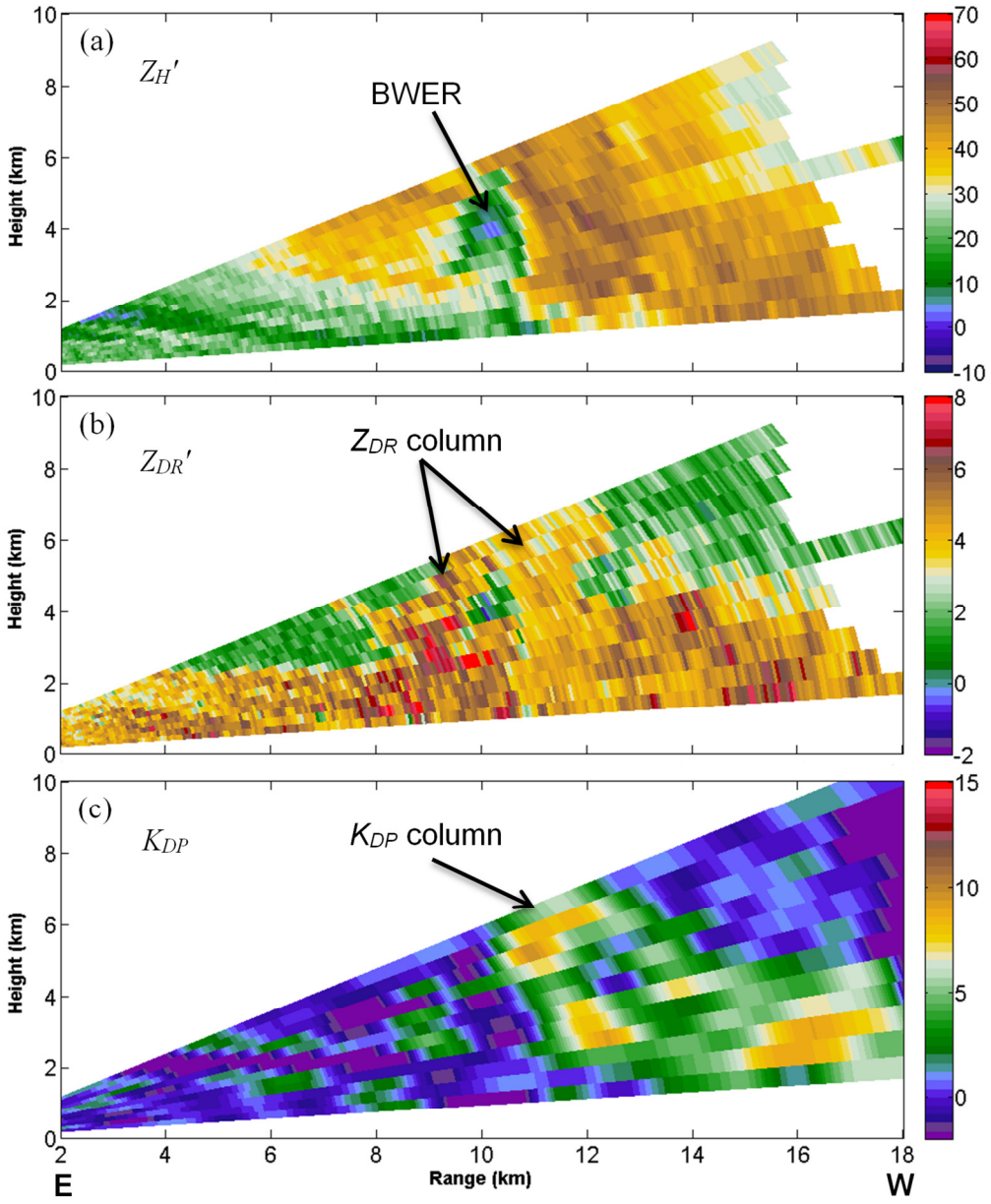

Figure 39. Reconstructed RHIs (based upon a series of PPIs) of (a) Z_H, (b) Z_{DR}, and (c) K_{DP} through the center of the BWER (black line) displayed in Figure 38. The reconstruction RHIs are oriented nearly east (left side) to west (right side) across the plots. The largest Z_{DR} observed above ~2 km ARL is observed along at the bottom of the echo overhang at 8–10 km range and 2–6 km ARL height. [From Snyder et al. (2013)]

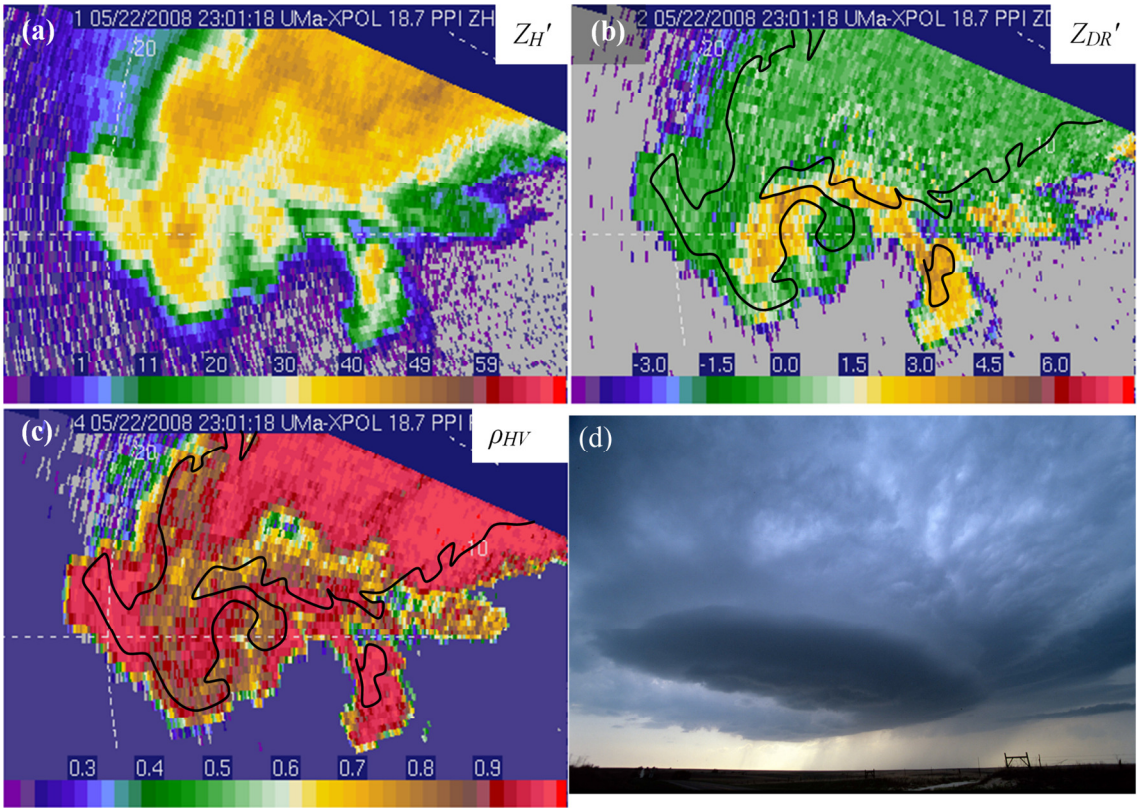

Figure 40. UMass XPol deployed on a supercell on 22 May 2008, and (a) Z_H', (b) Z_{DR}', and (c) ρ_{hv} at 2301:18 UTC are shown. The 30 dBZ isoecho is shown in black in (b)–(c). A Z_{DR} half-ring is extremely evident, just beyond which is a ρ_{hv} half-ring. The elevation angle is 18.7°, with a beam height of ~3.2 km (at 10 km range) to ~6.4 km (at 20 km range) ARL. (d) A photograph (courtesy H. Bluestein) of the supercell as viewed from the radar deployment location near 2250 UTC. [From Snyder et al. (2013)]

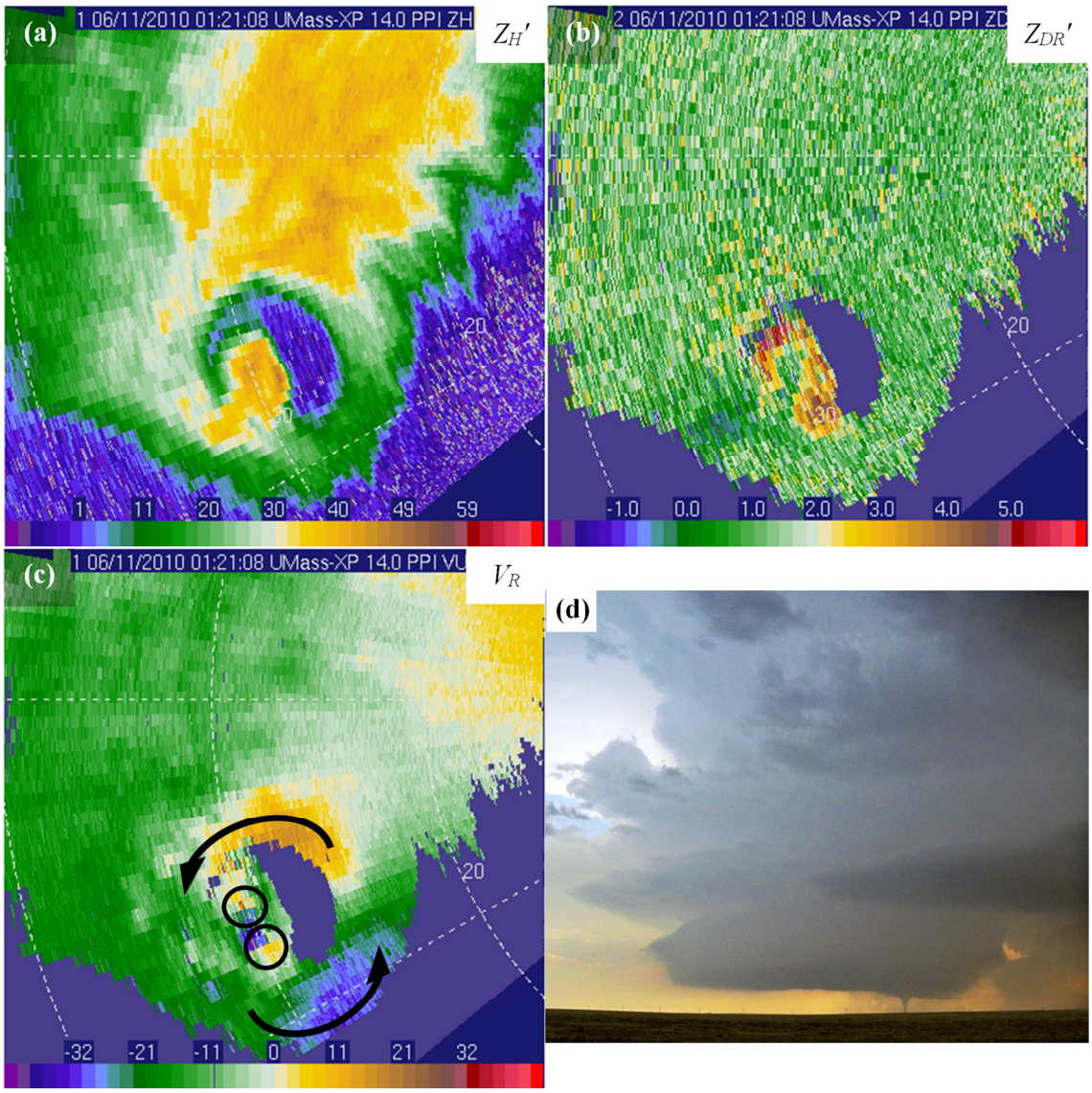

Figure 41. (a) Z_H', (b) Z_{DR}', and (c) V_R collected at 0121:08 UTC on 11 June 2010 at an elevation angle of 14.0º. An extremely prominent crescent-shaped BWER is apparent in (a), with a large mesocyclone of diameter O(10 km) (black curved arrows) and a smaller cyclonic-anticyclonic vortex pair of diameter O(1 km) (black circles). The height of the radar beam near the smaller vortex and areas of $Z_{DR}' > 2$ dB is ~7 km ARL. Range rings are shown every 10 km. A (d) photograph of the supercell and tornado was taken near the time these data were collected. (Photo courtesy H. Bluestein) [From Snyder et al. (2013)]

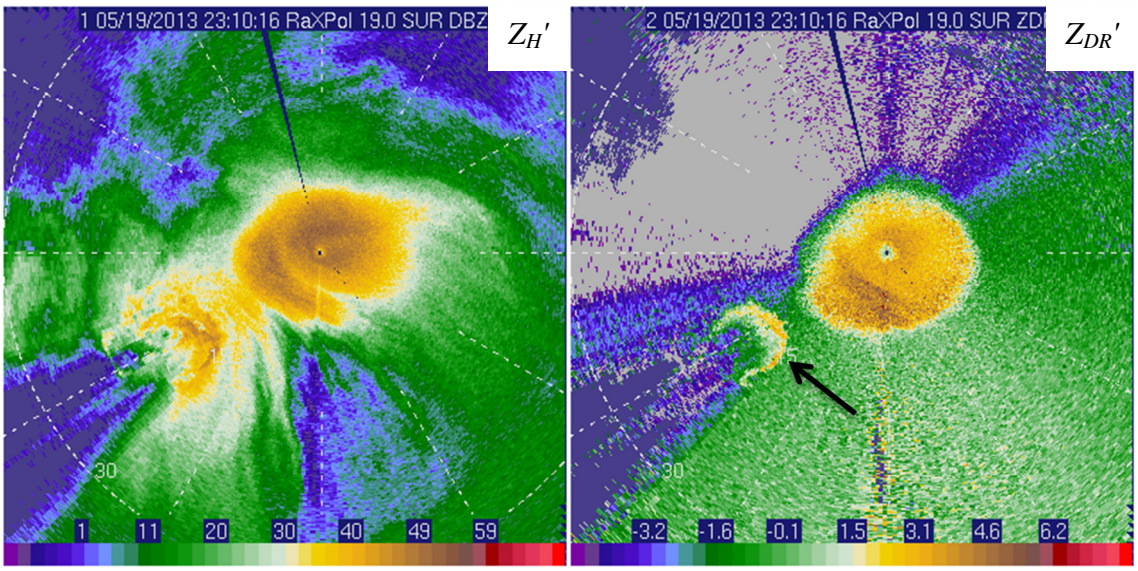

Figure 42. (a) Z_H' and (b) Z_{DR}' valid at 2310 UTC on 19 May 2013 as a tornadic supercell moved east of Norman, OK. A Z_{DR} half-ring is readily apparent in (b) and is marked by a black arrow.

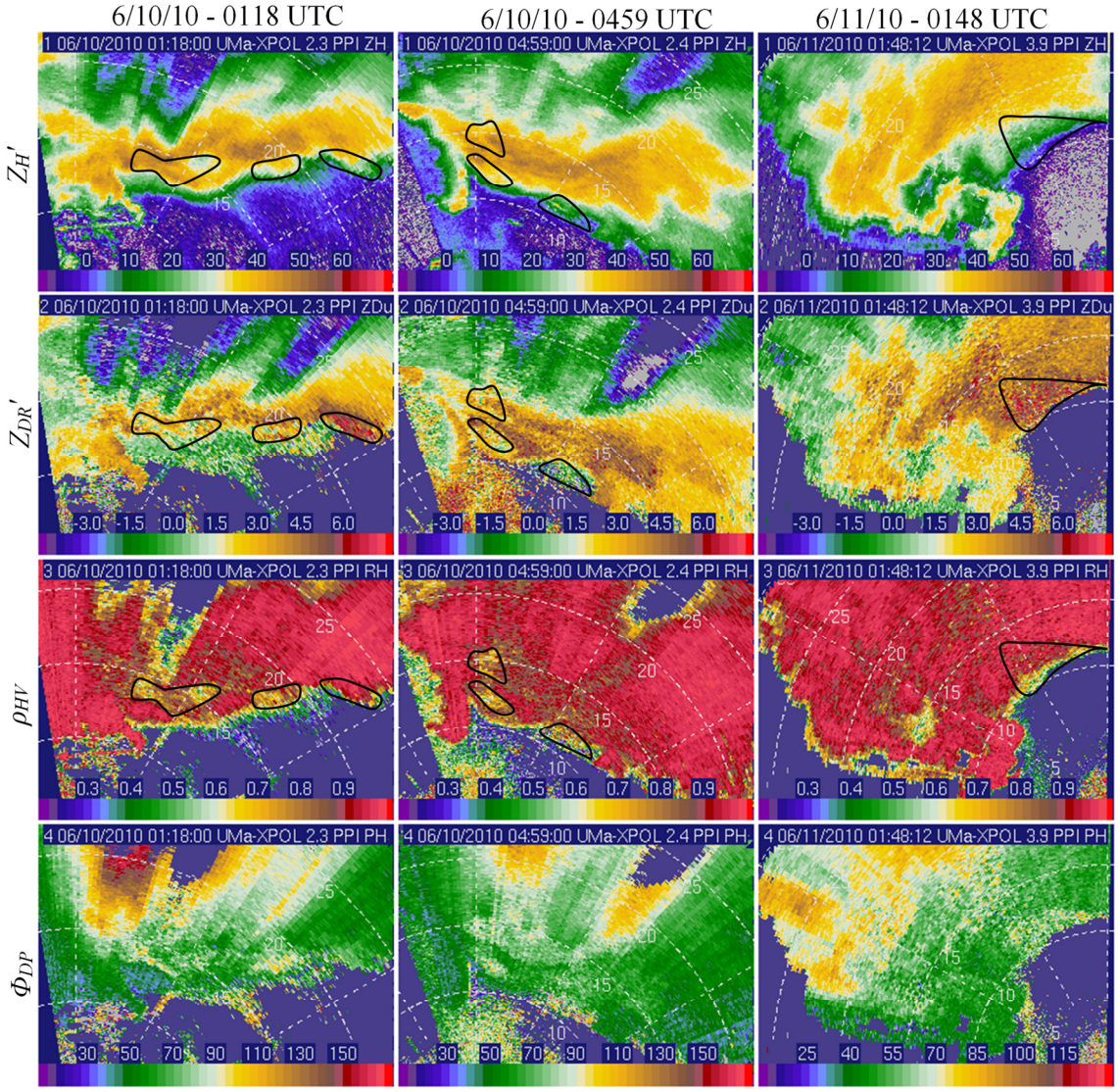

Figure 43. Z_H', Z_{DR}', ρ_{hv}, and Φ_{DP}, respectively, are shown in first, second, third, and fourth rows from (left column) 0118 UTC on the evening of 9 June 2010, (center column) 0459 UTC on the evening of 9 June 2010, and (right column) 0148 UTC on the evening of 10 June 2010. The black outlines mark areas of local maxima in Φ_{DP} (before and after which Φ_{DP} decreases). These maxima are either the result of local maxima in δ or enhanced resonance effects (and perhaps hydrometeor shapes and orientations) that yield $K_{DP} < 0°$ km^{-1}. [From Snyder et al. (2013)]

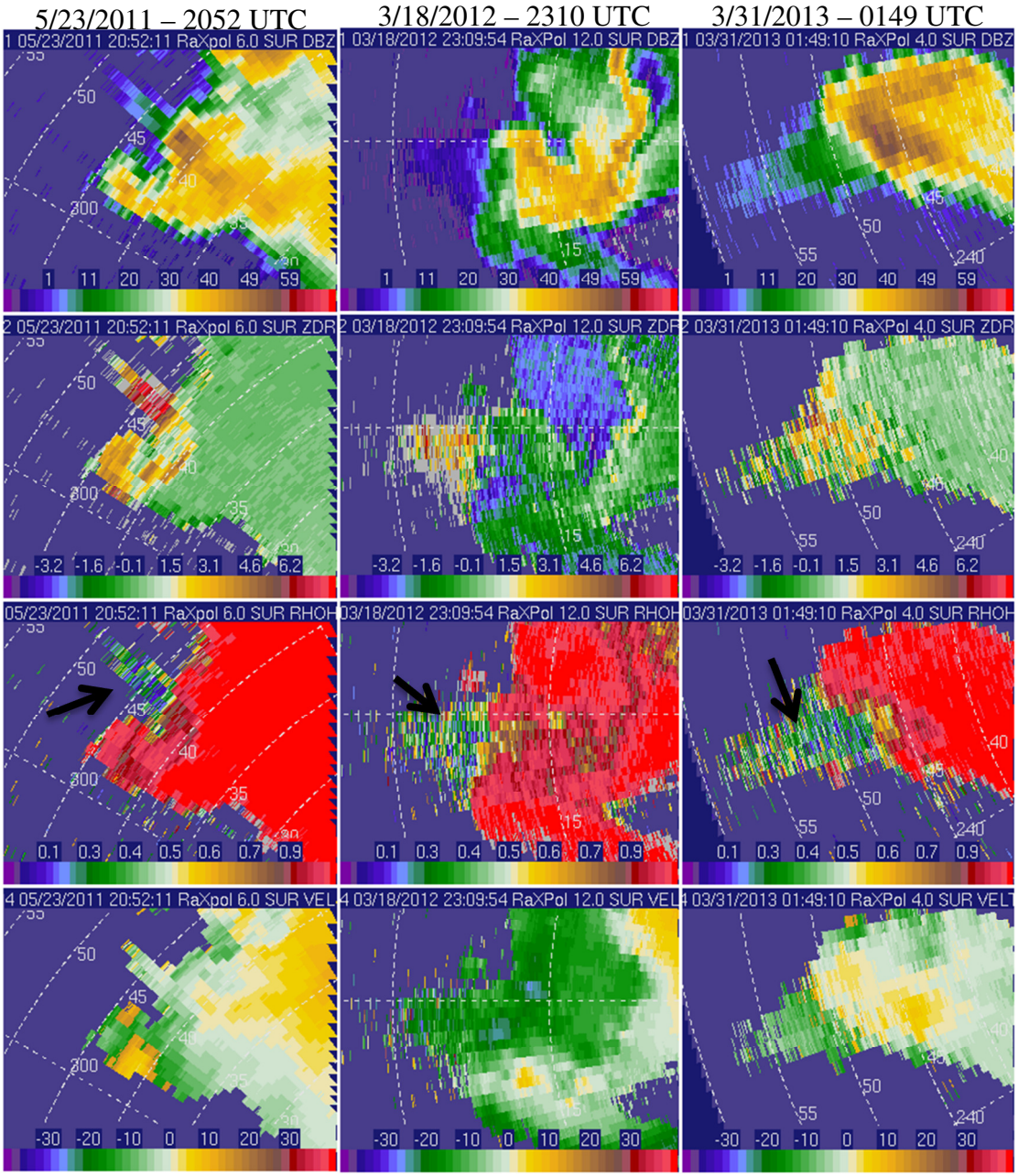

Figure 44. Polarimetric three-body scatter signatures (highlighted by black arrows in the third row) characterized by (from top to bottom) radially-decreasing Z_H', relatively high and noisy Z_{DR}', very low ρ_{hv}, and relatively weak V_R observed downstream of regions of high Z_H'. These data were collected by RaXPol on (from left to right, respectively) 23 May 2011, 18 March 2012, and 31 March 2013.

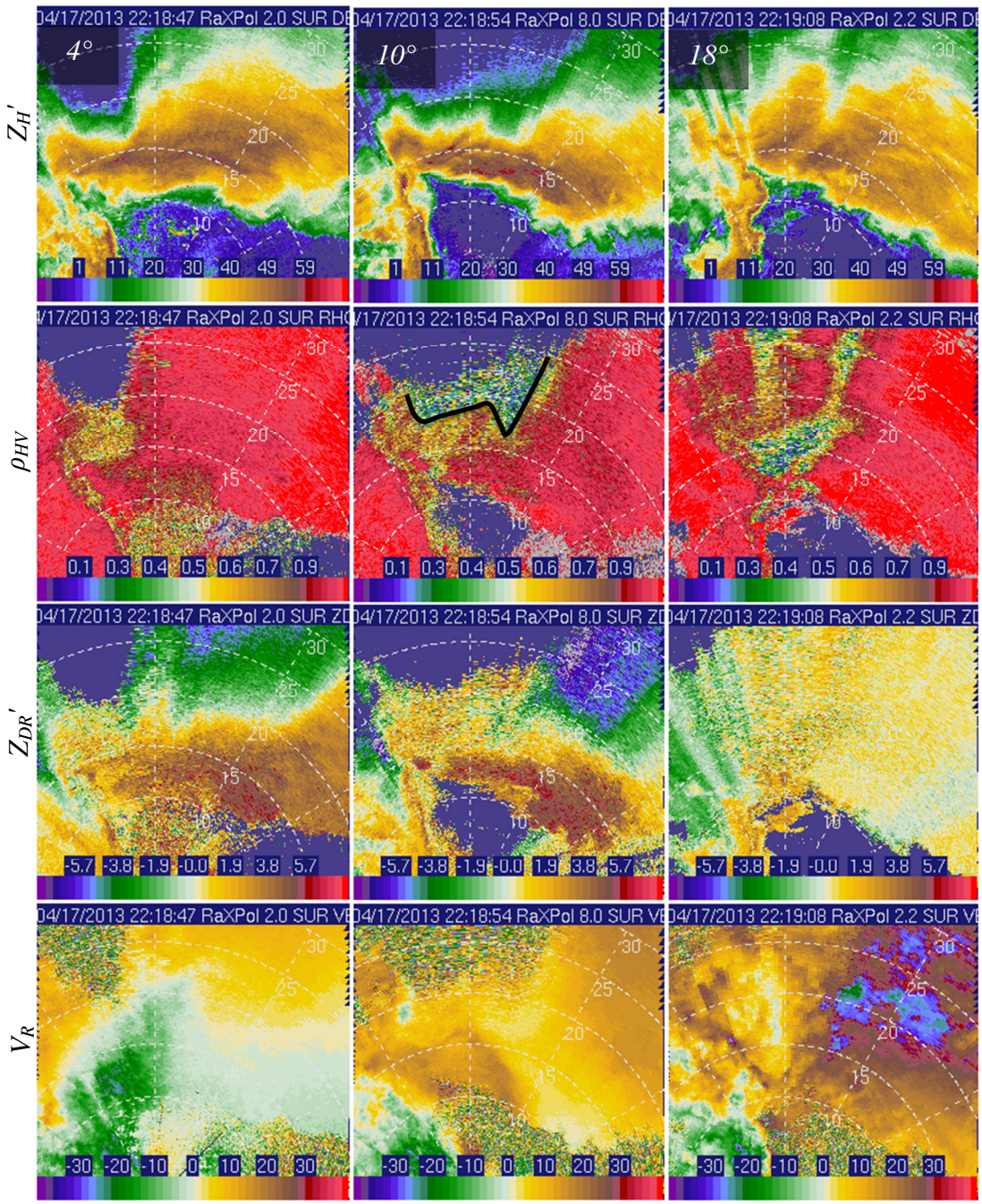

Figure 45. Z_H', ρ_{hv}, Z_{DR}', and V_R (from left to right, respectively) at 4°, 10°, and 18° elevation angles (top to bottom) on 17 April 203 in southwestern Oklahoma. A well-defined low-level hail signature is evident on the 4 degree scan. The area of low ρ_{hv} at 10° elevation angle is ambiguous in its origins – hail is likely present where ρ_{hv} ~0.6, but the area of $\rho_{hv} < 0.3$ beyond ~20 km range (black curve) may represent either a polarimetric three-body scatter signature or NBF. The close proximity of the storm precluded the sampling of the BWER even at 18°, but a hint of a BWER is evident as low Z_H' ~5–8 km N of the radar. This being the case, a LoRB appears near 13–16 km range on the 18° scan, with at least two NBF-related streaks evident beyond the LoRB. Hail to 1.75" in diameter was reported with this supercell near this time.

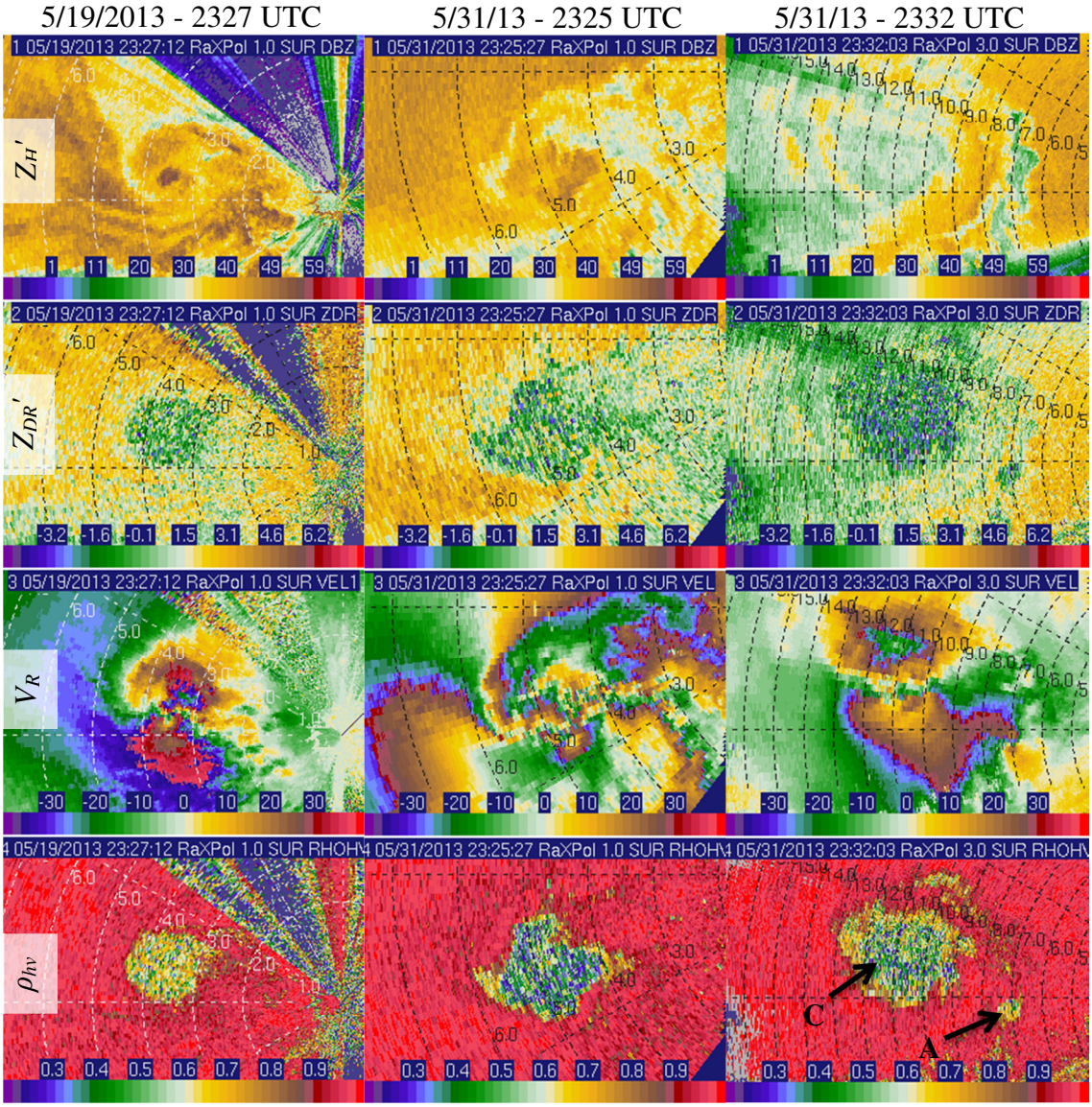

Figure 46. Polarimetric tornado debris signature as seen in Z_H', Z_{DR}', V_R, and ρ_{hv} (top to bottom, respectively) from violent tornadoes in central Oklahoma on 19 May 2013 (left) and 31 May 2013 (center and right). The width of the debris cloud as measured by ρ_{hv} is ~1.5 km, ~2.2 km, and ~5 km in the left, center, and right columns, respectively. Southeast of the very large cyclonic tornado (marked by "C") in the right column (2332 UTC) is a debris signature associated with an anticyclonic tornado as well ("A").

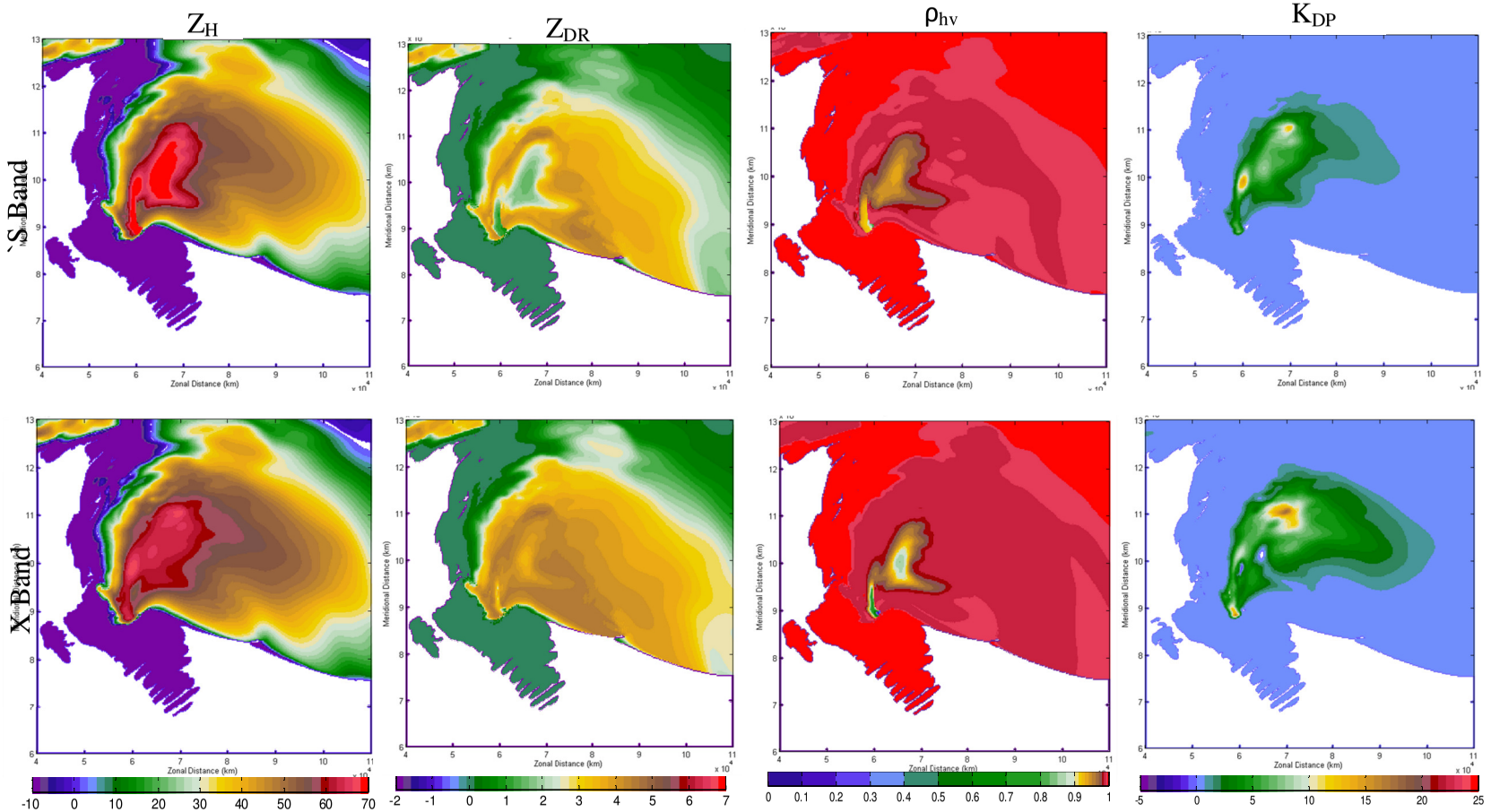

Figure 47. Polarimetric fields from the *25r10_057* simulation at (top) S and (bottom) X bands. Z_H (dBZ), Z_{DR} (dB), ρ_{hv}, and K_{DP} (deg. km^{-1}) are shown from left to right. The area of low Z_{DR} and relatively low ρ_{hv} at S band is caused by hail (see D_{mh}, lower left) with relatively high f_{wh}, which, apparently, is masking the low-level hail signature at X band.

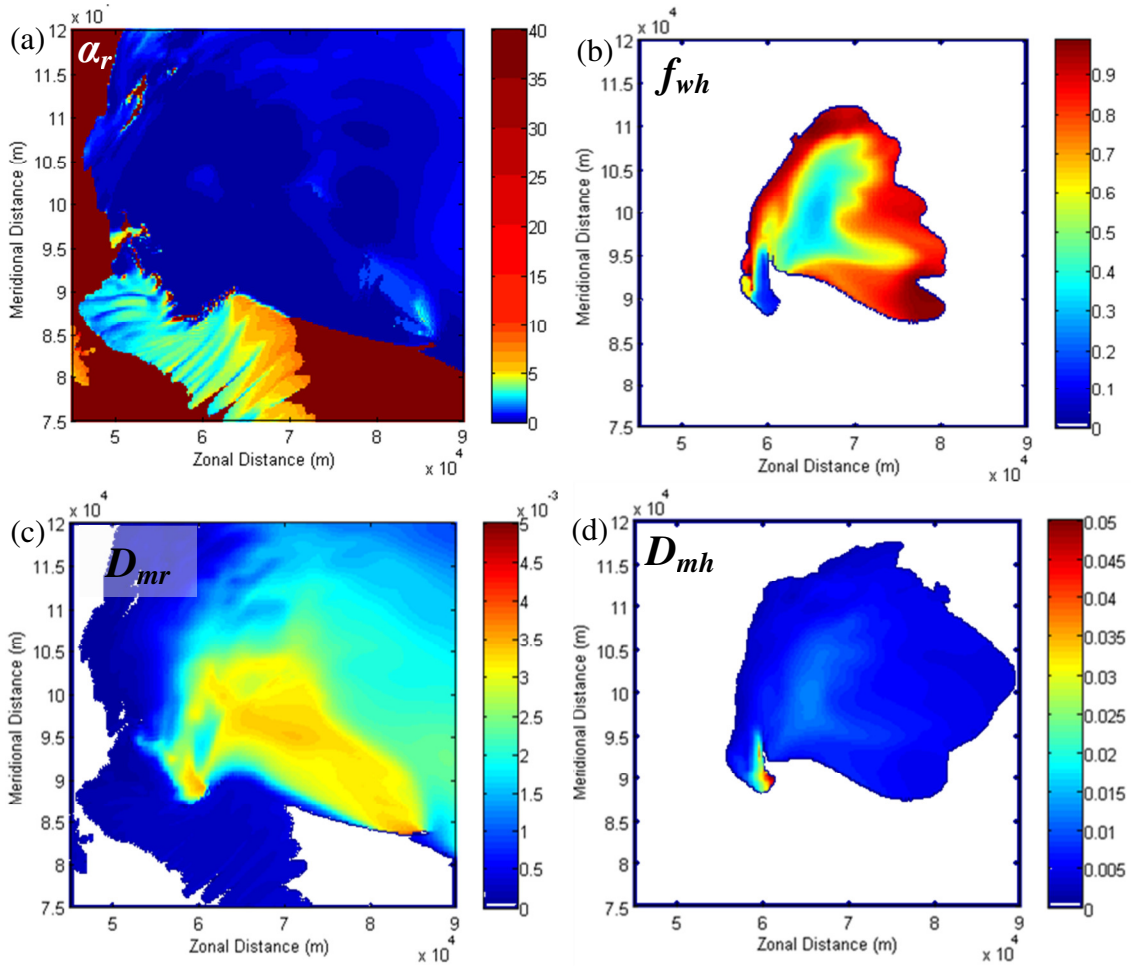

Figure 48. (a) α_r, (b) f_{wh}, (c) D_{mr} (m) and (d) D_{mh} (m) valid at the same time for the same simulation as Figure 47.

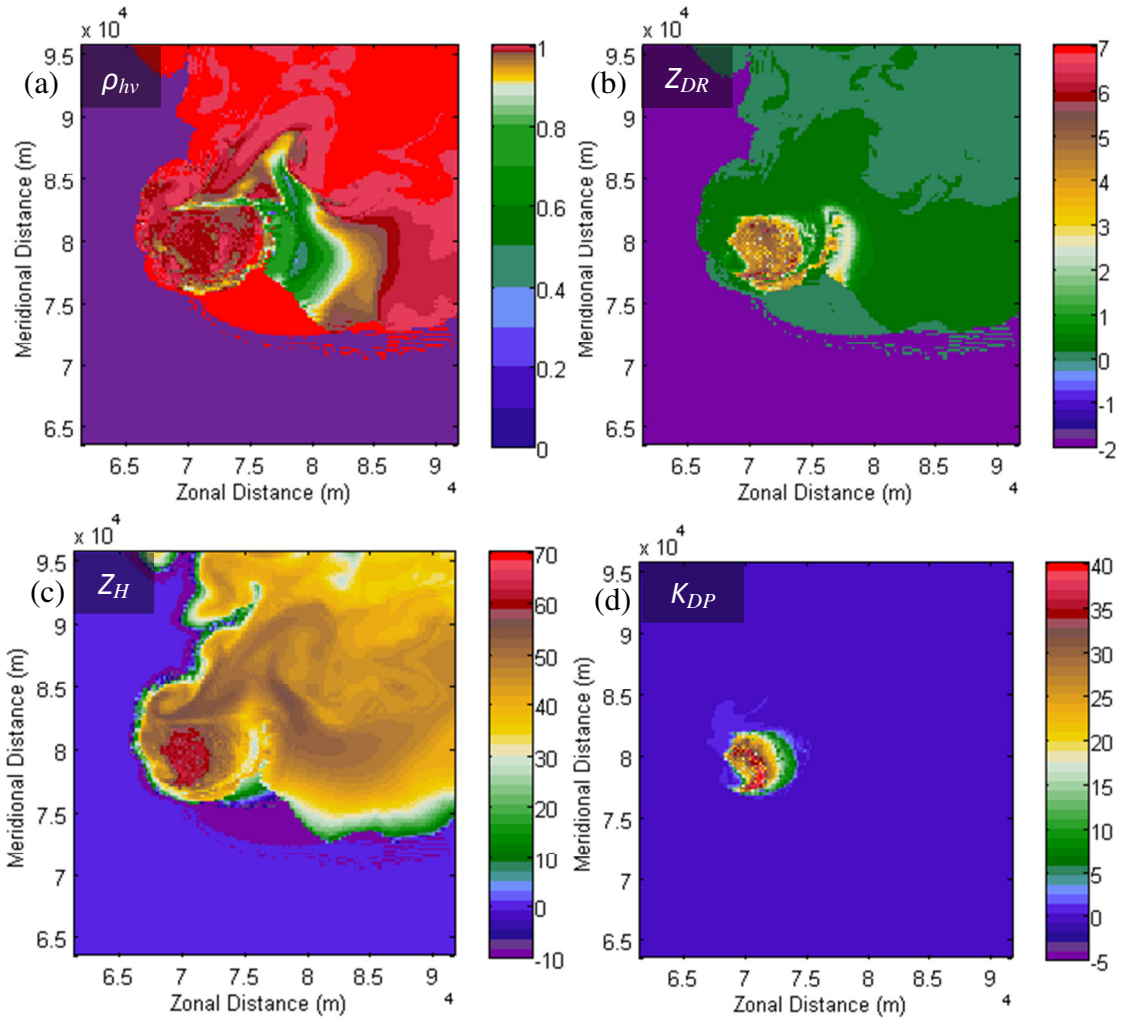

Figure 49. (a) ρ_{hv} , (b) Z_{DR} (dB), (c) Z_H (dBZ) and (d) K_{DP} (deg. km^{-1}) at ~5400 m AGL from the *15q10* simulation valid at t = 4800 s at X band. A ρ_{hv} half-ring is evident in (a). In (b), a Z_{DR} half-ring and a part of the Z_{DR} column are apparent.

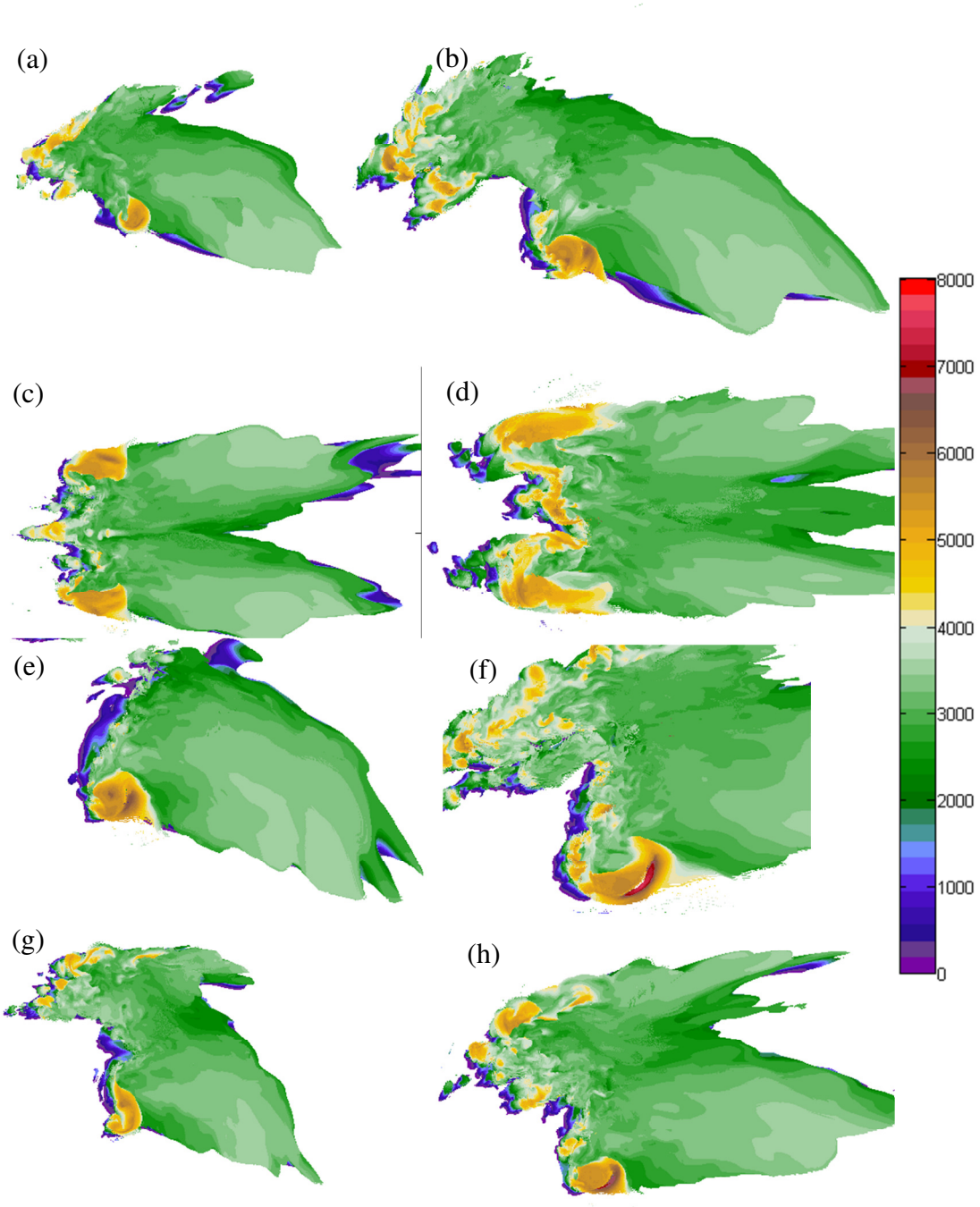

Figure 50. The maximum height (m) of $Z_{DR} > 1$ dB approximately 5000 s into the (a) *15r10*, (b) *25r10*, (c) *15str*, (d) *25str*, (e) *15q10*, (f) *25q10*, (g) *15r10_057* and (h) *25r10_057* simulations. The horizontal spatial scale is the same in all panels. The hodograph shapes tend to suppress any left-mover / anticyclonic supercell(s), with the exception of the 15str and 25str hodographs.

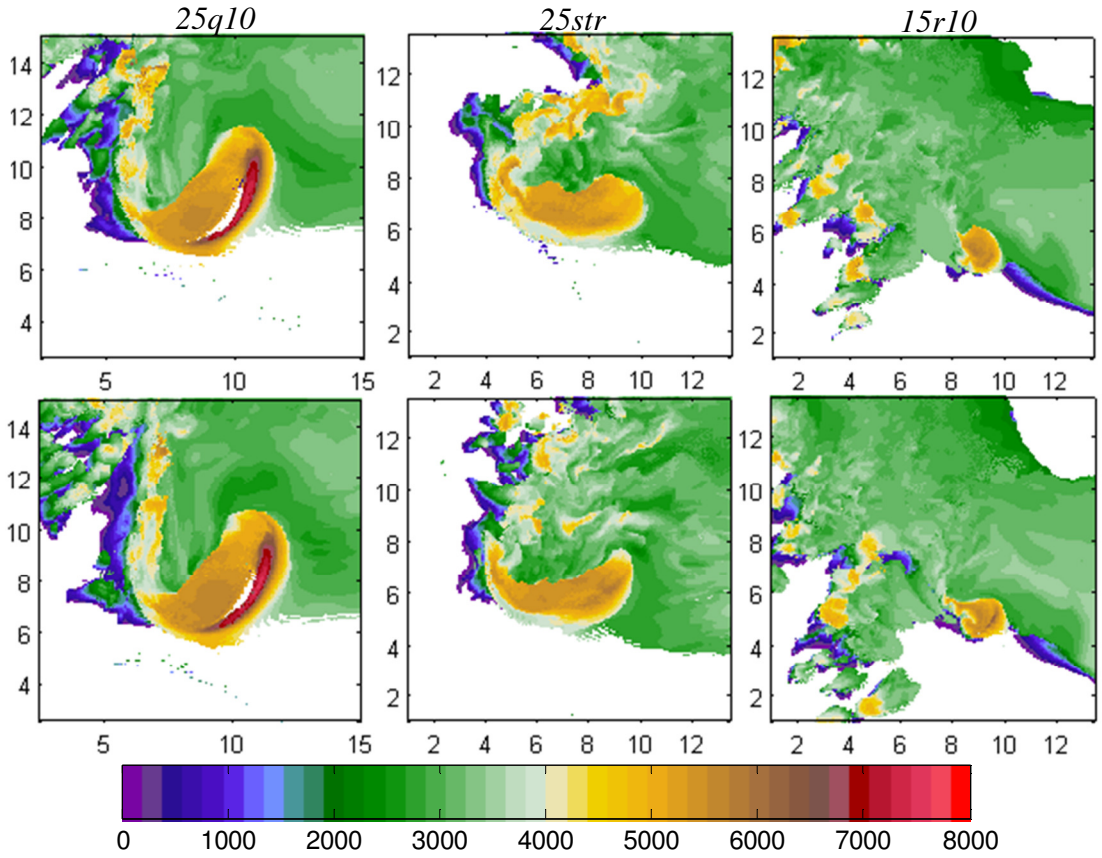

Figure 51. Max height (m) of $Z_{DR} > 1$ dB at (top) 7200 s and (bottom) 7920 s from the (left) *25q10*, (center) *25str*, and (right) *15r10* simulations. The horizontal scale is equal for all panels and is given as 1×10^4 m.

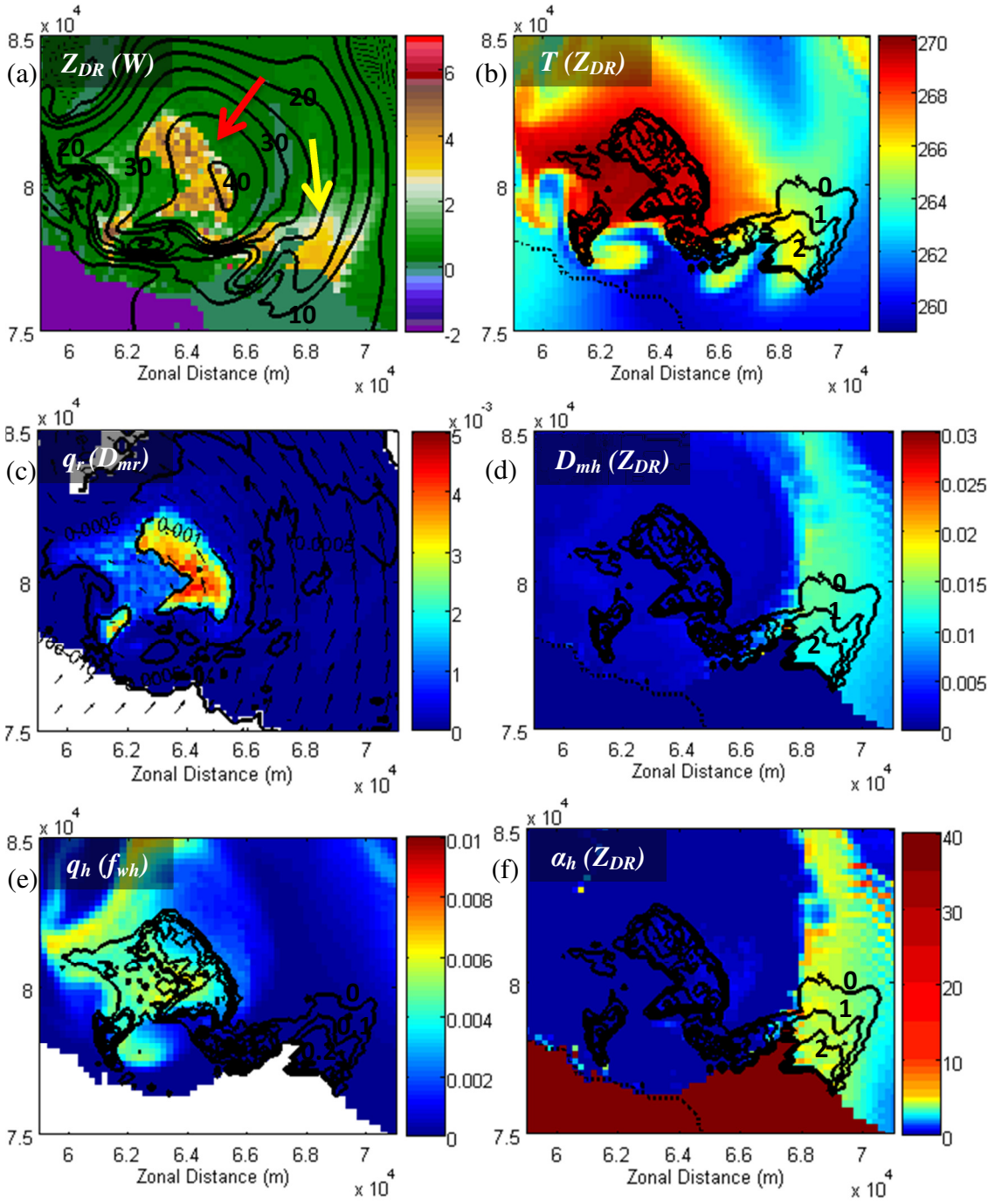

Figure 52. From the *25r10* simulation at t = 4800 s at a height of ~5600 m AGL, (a) Z_{DR} (color; dB) and W (contoured every 5 m s^{-1}), (b) temperature (color; K) and Z_{DR} (contoured starting at 0 dB every 1 dB), (c) q_r (color), D_{mr} (contoured every 0.001 m) and wind vectors, (d) D_{mh} (color; m) and Z_{DR} (contoured; dB), (e) q_h (color) and f_{wh} (contoured every 0.1), and (f) α_h (color) and Z_{DR} (contoured; dB). The red arrow in (a) points out the primary Z_{DR} column; the yellow arrow points out the pseudo- Z_{DR} half-ring.

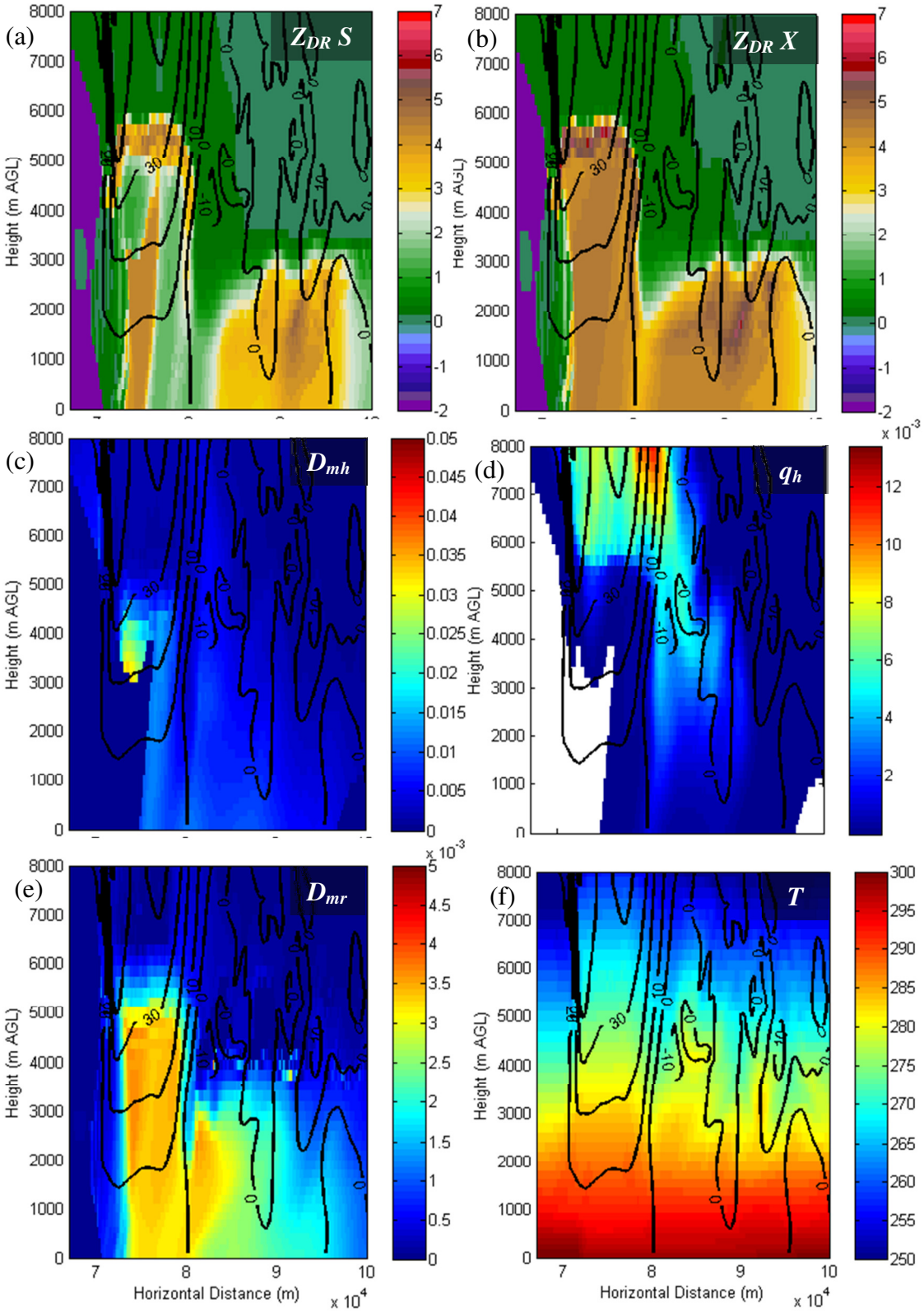

Figure 53. (a) S-band Z_{DR} (dB), (b) X-band Z_{DR} (dB), (c) D_{mh} (m), (d) q_h, (e) D_{mr} (m), and (f) T (K) along a north-south cross-section through the updraft of the supercell from

the *25r10* simulation at 7320 s. Black contours in all panels are w (m s^{-1}); contours are plotted every 10 m s^{-1}.

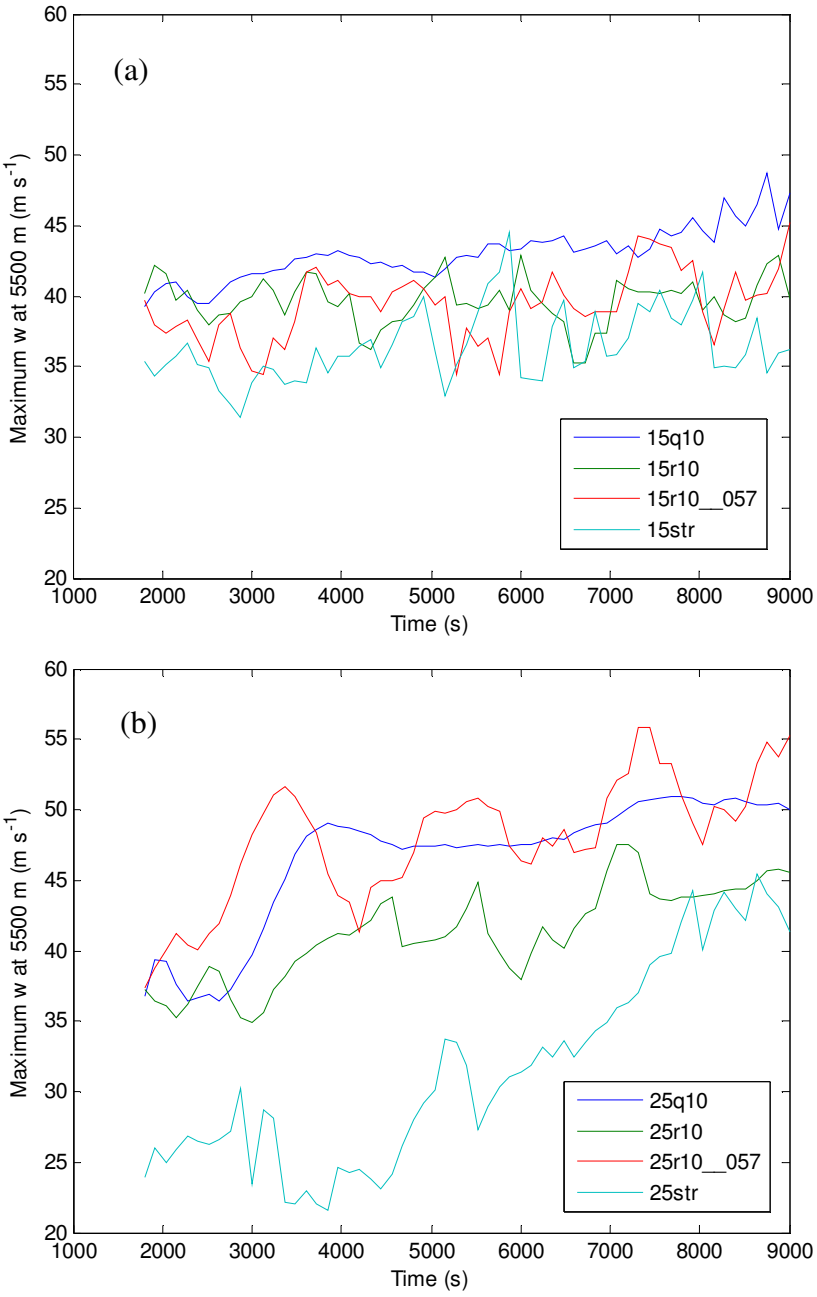

Figure 54. Maximum *w* (m s^{-1}) at ~5500 m AGL from the (a) "weak" shear and (b) "strong" shear simulations.

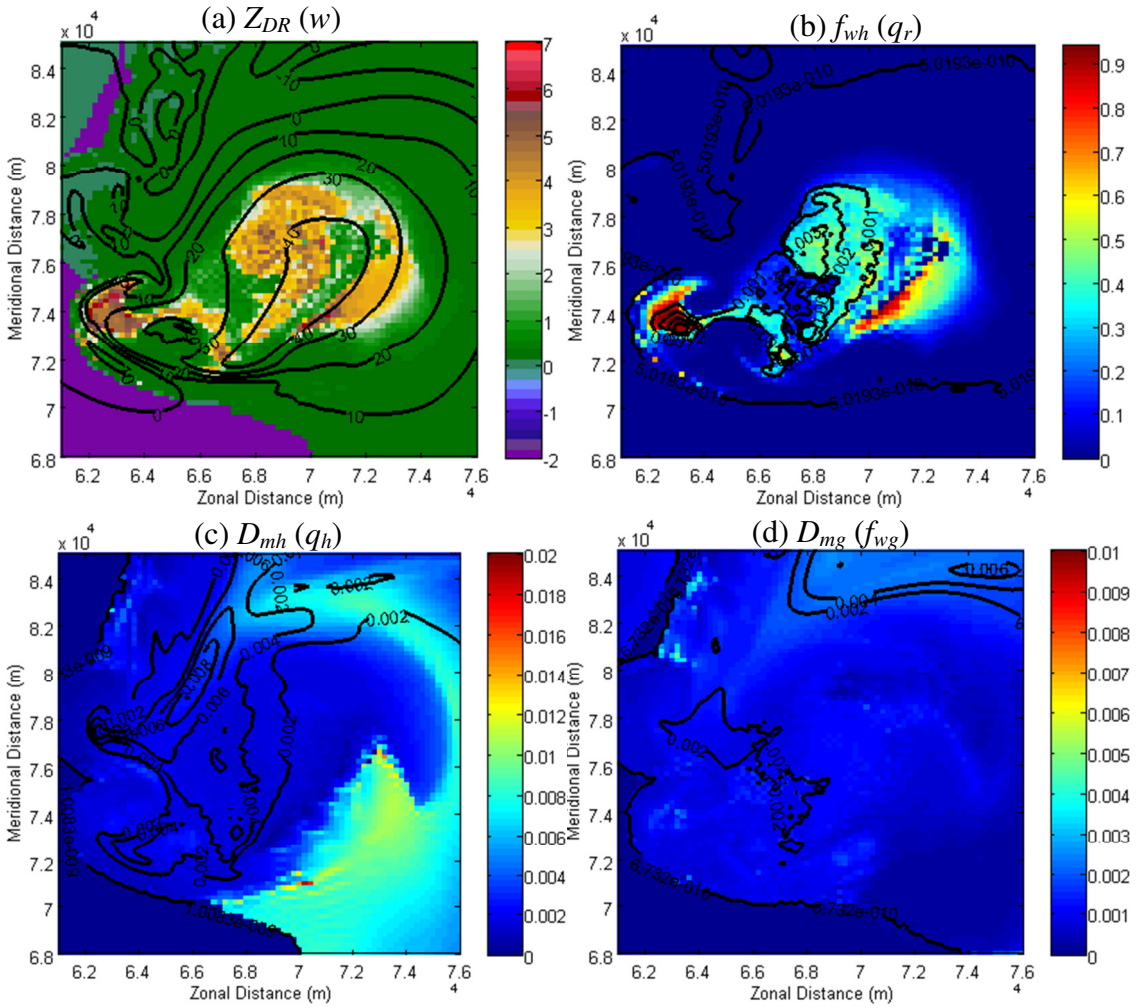

Figure 55. (a) X-band Z_{DR} (color; dB) and w (contoured every 10 m s^{-1}), (b) f_{wh} (color) and q_r (contoured over 0.001), (c) D_{mh} (color; m) and q_h (contoured every 0.002), and (d) D_{mg} (color; m) and q_g (contoured every 0.002) from the *25r10* simulation at 7360 s and heights of ~5500 m (for w) and ~5600 m (for all other variables).

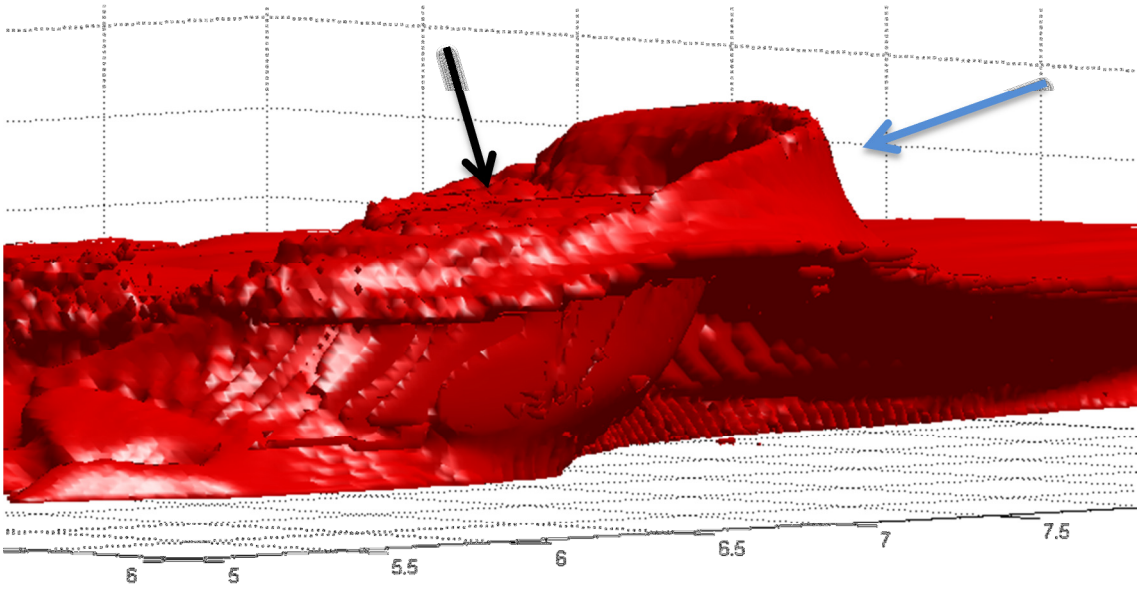

Figure 56.The Z_{DR} = 1 dB isosurface valid 7320 s from the 25q10 simulation with the view directed towards the northeast. The black arrow point to the "primary" Z_{DR} column; the blue arrow points to the arcing Z_{DR} half-ring along the eastern edge of the updraft. The horizontal scale is in 10^4 m.

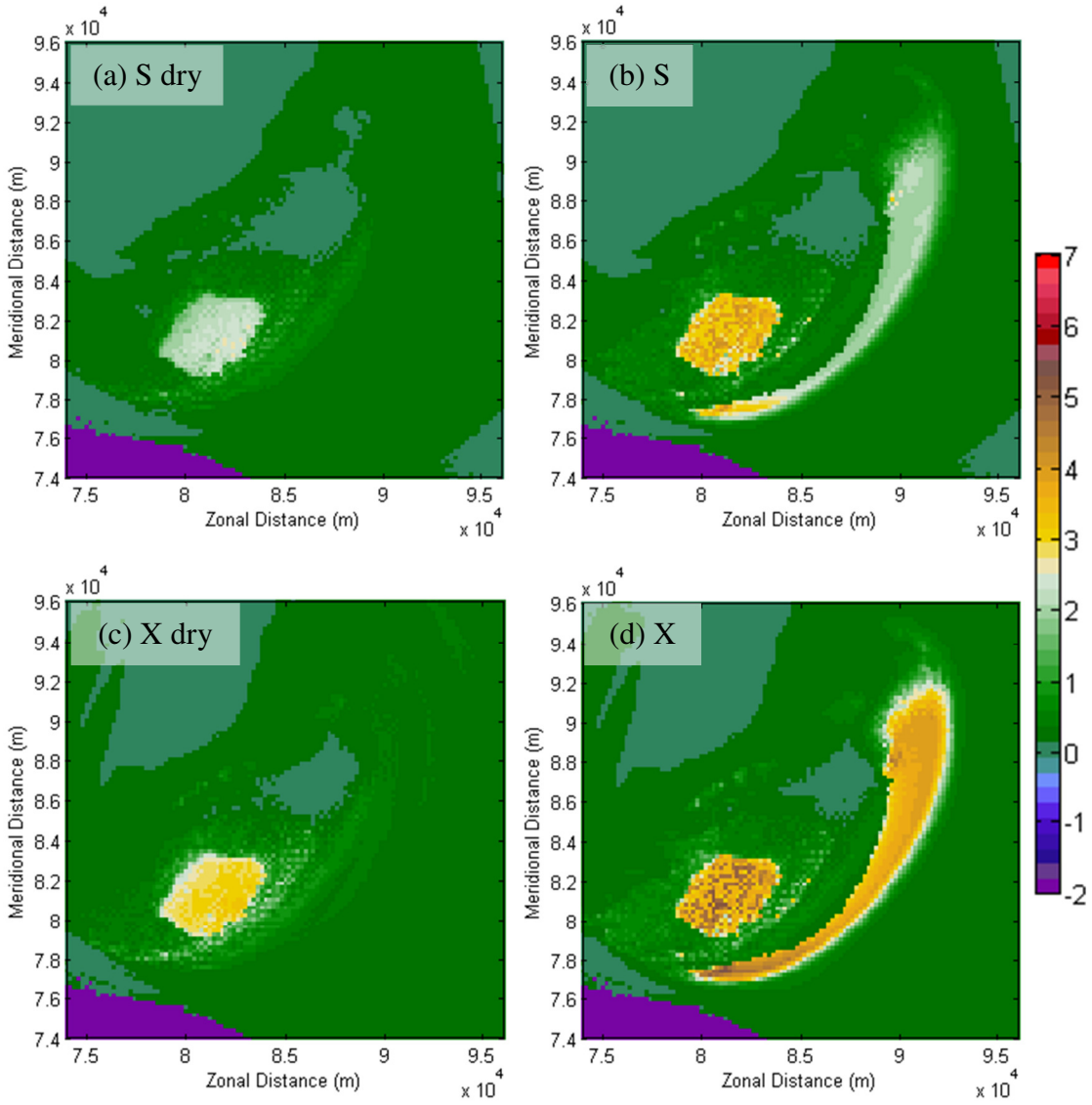

Figure 57. Z_{DR} (dB) at (a)–(b) S and (c)–(d) X bands from the *25q10* simulation at a height of ~5600 m. The left column [(a), (c)] is calculated by turning off the fractional water routine in the emulator, which results in all ice being treated as "dry"; the right column [(b), (d)] includes the fractional water routine described in Chapter 2 and in Dawson et al. (2013).

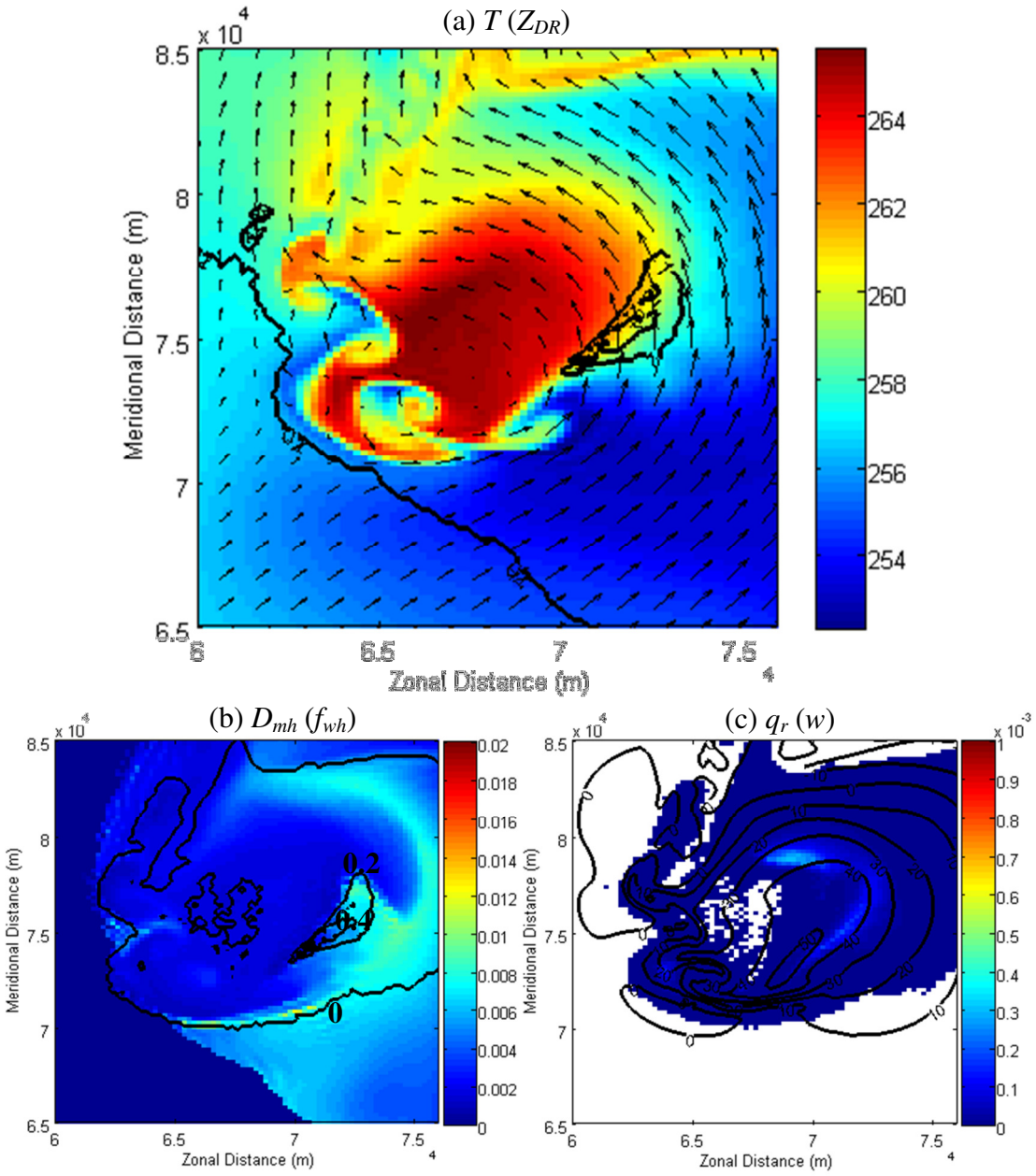

Figure 58. From the *25r10* simulation at t = 7320 s – (a) T (color; K) and Z_{DR} (contoured every 1 dB) with wind vectors plotted every 1 km, (b) D_{mh} (color; m) and f_{wh} (contoured every 0.2), and (c) q_r (color) and w (contoured every 10 m s^{-1}; the highest-valued contour is 50 m s^{-1}). The height of the w data is ~6,400 m; height of all other data is ~6,500 m.

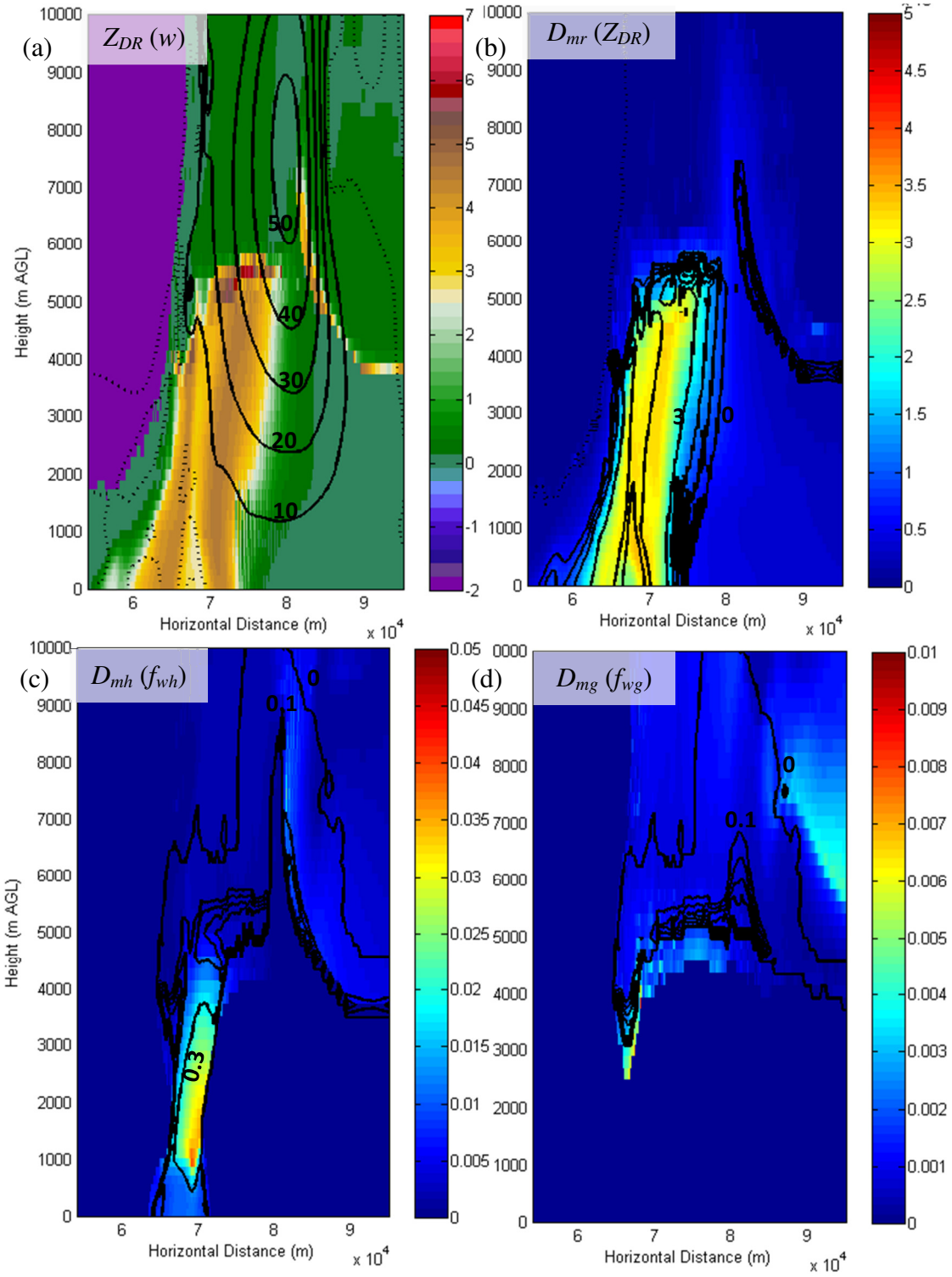

Figure 59. An east-west vertical cross-section through the updraft of the *25q10* simulation at 6000 s with (a) Z_{DR} (color; dB) and w (contoured every 10 m s^{-1} with dashed contours denoting w $\leq$ 0 m s^{-1}), (b) D_{mr} (color; m) and Z_{DR} (contoured every 1 dB), (c) D_{mh} (color; m) and f_{wh} (contoured every 0.2), and (d) D_{mg} (color; m) and f_{wg} (contoured every 0.2).

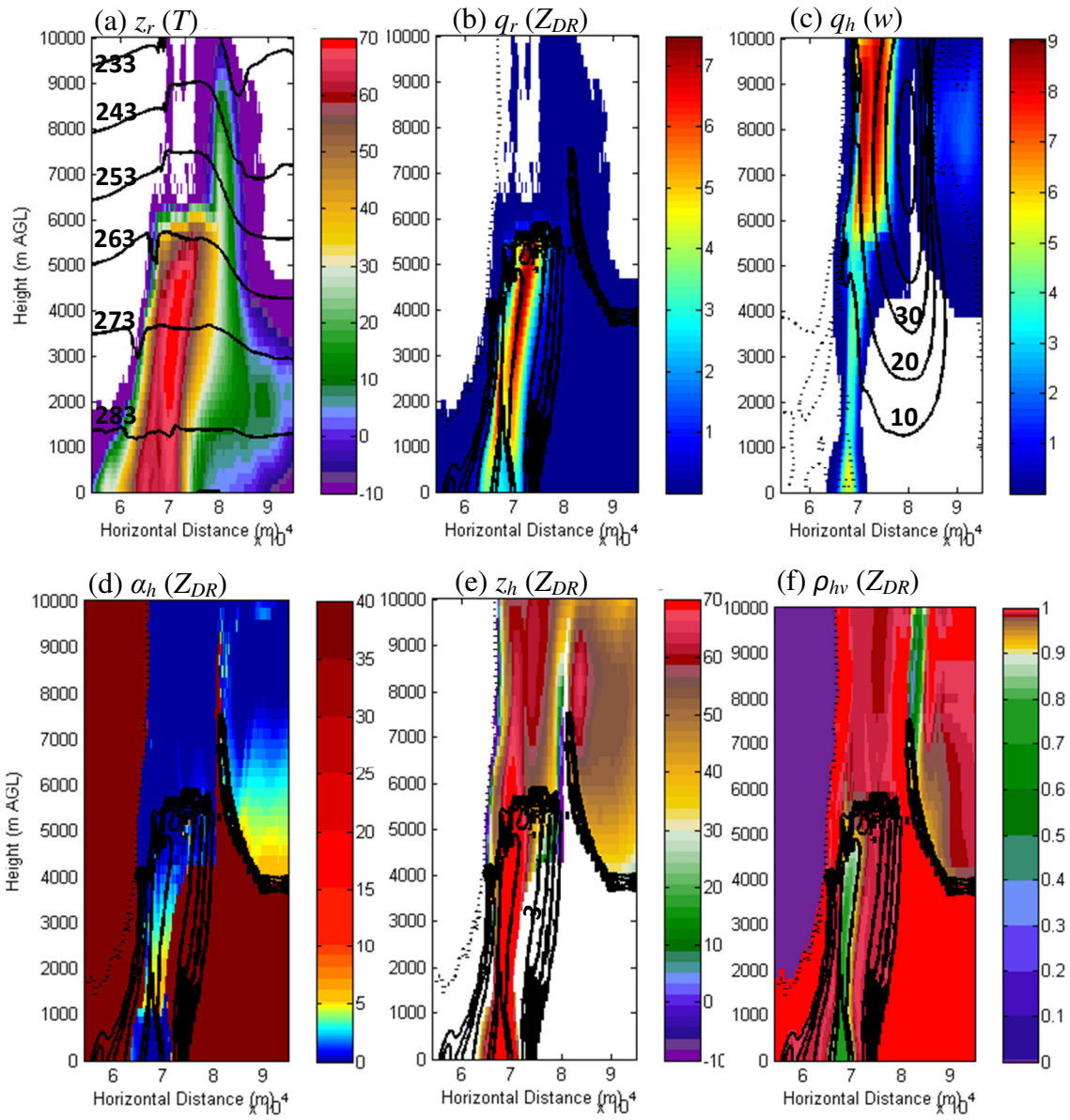

Figure 60. Vertical cross-sections along an east-west slice of the *25q10* simulation at 6000 s with (a) z_r (color; dBZ) and temperature (countered every 10 K), (b) q_r (color) and Z_{DR} (contoured every 1 dB), (c) q_h (color) and w (contoured every 10 m s^{-1}), (d) z_h (color; dBZ) and Z_{DR} (contoured every 1 dB), (e) α_h (color) and Z_{DR} (contoured every 1 dB), and (f) ρ_{hv} (color) and Z_{DR} (contoured every 1dB).

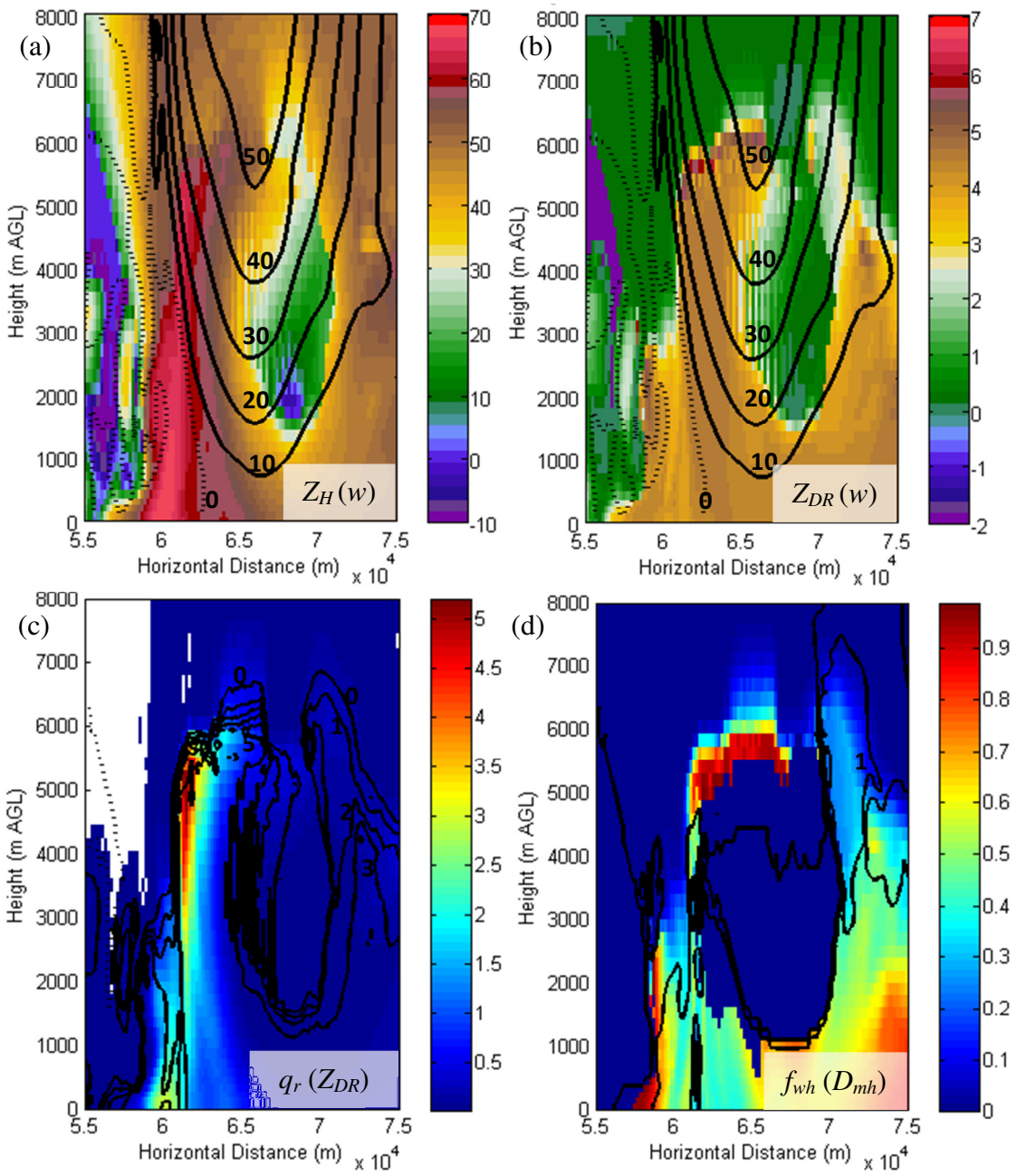

Figure 61. From the *25r10_057* simulation (at t = 9000 s), east-west vertical cross-sections through the updraft showing (a) Z_H (color; dBZ) and w (contoured at 10 m s^{-1}; dotted contours represent $w \leq 0$ m s^{-1}), (b) Z_{DR} (color; dB) and w (contoured at 10 m s^{-1}; dotted contours represent $w \leq 0$ m s^{-1}), (c) q_r (color) and Z_{DR} (contoured every 1 dB with $Z_{DR} \leq 0$ dB dotted), and (d) f_{wh} (color) and D_{mh} (contoured every 0.5 cm).

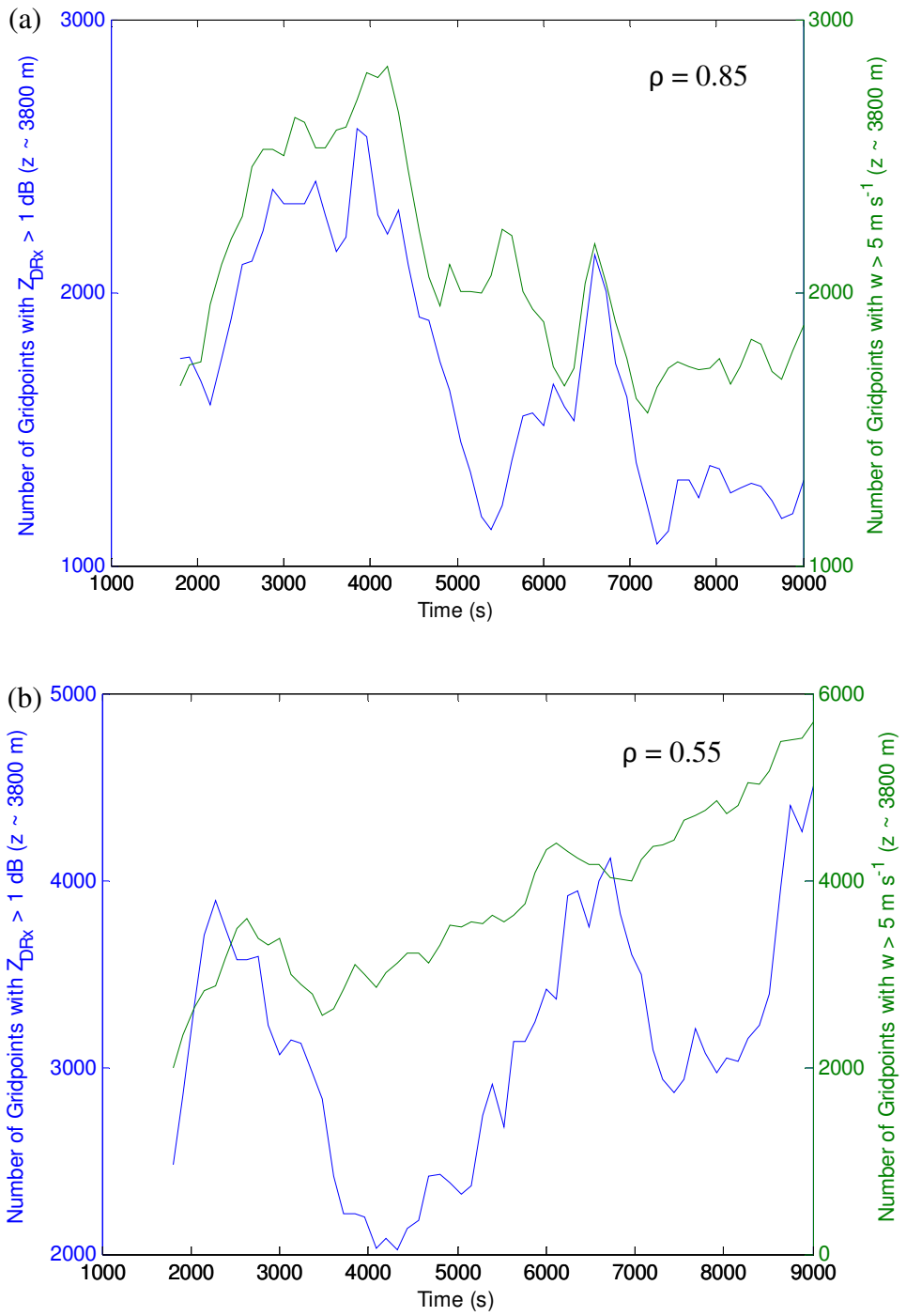

Figure 62. The area of the Z_{DR} column and/or ring (Z_{DR} > 1 dB; blue line) and the area of the updraft (w > 5 m s^{-1}; green line) at a height of ~3800 m AGL from the *15q10* and *25q10* simulations. The number of gridpoints is used as a proxy for area.

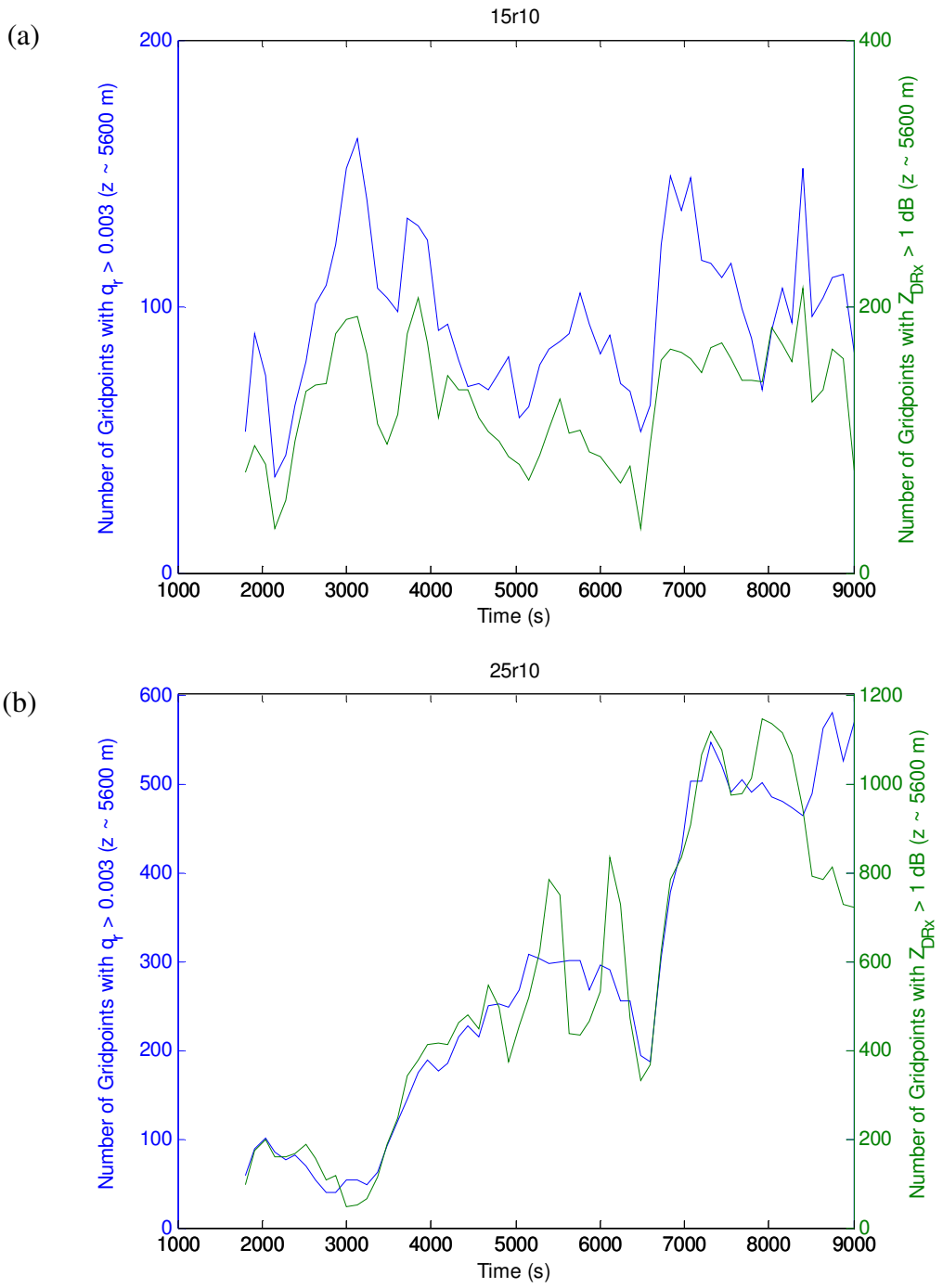

Figure 63. Time series of (blue) qr33area and (green) zdr33area from the (a) *15r10* and (b) *25r10* simulations.

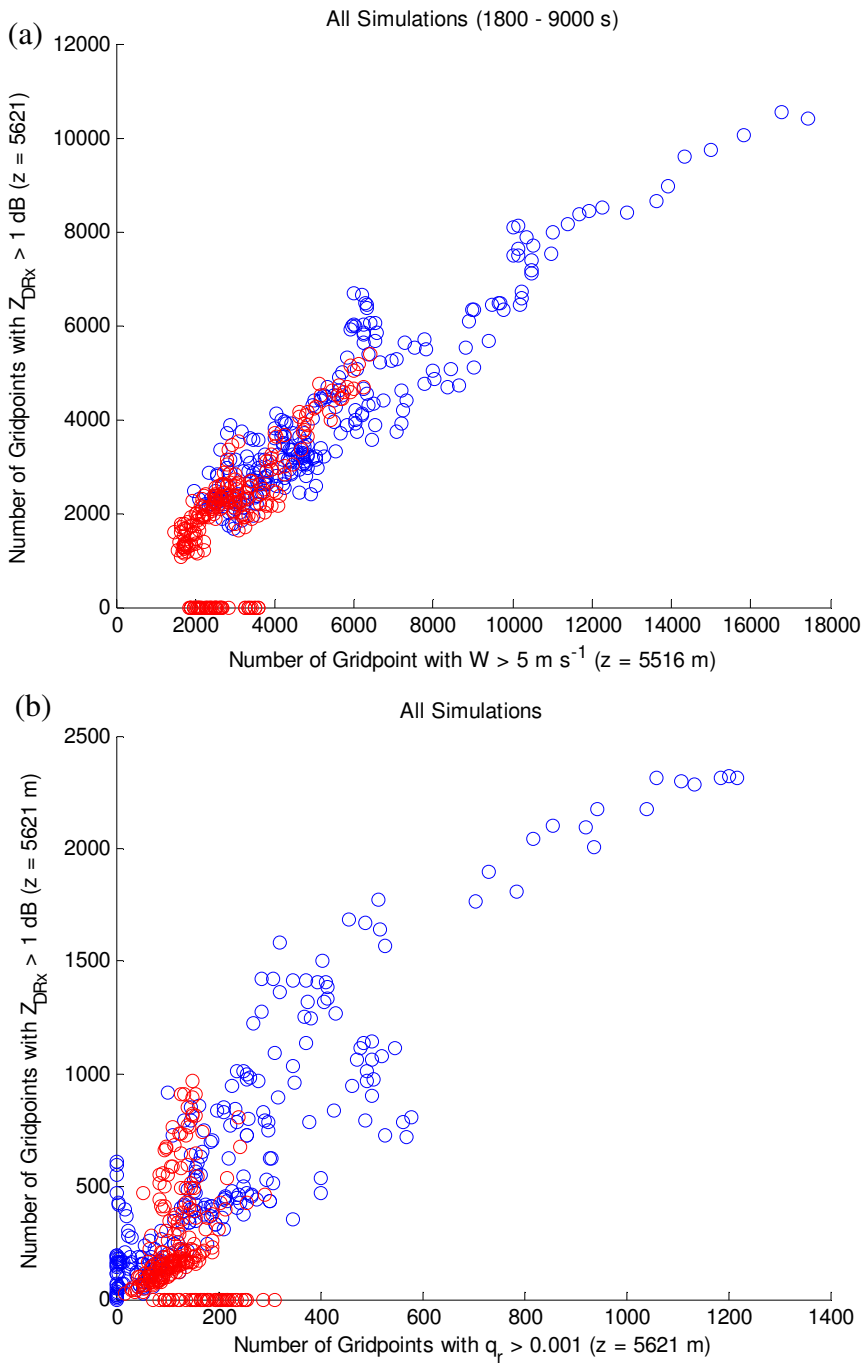

Figure 64. Scatterplots of (a) the number of gridpoints with $w > 5$ m s^{-1} at ~5,500 m vs. the number of gridpoints with $Z_{DR} > 1$ dB at ~5,600 m AGL and (b) the cross-sectional area of the rain field (defined as the number of gridpoints with $q_r > 0.001$) vs. number of gridpoints with $Z_{DR} > 1$ dB for the "weak" (red) and "strong" (blue) shear hodographs.

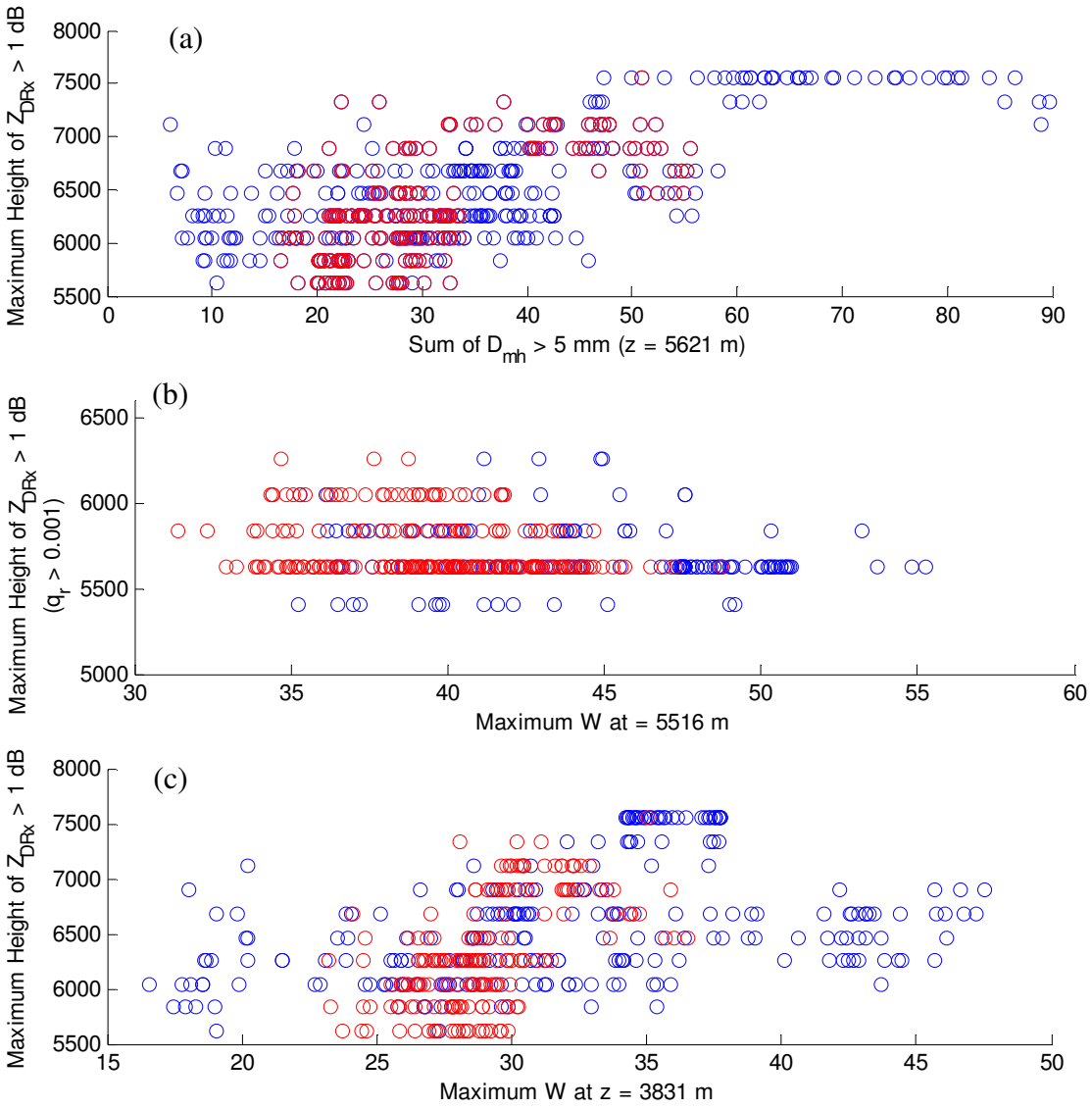

Figure 65. Scatterplots of (a) dmh33sum5mm vs. zdr33area, (b) wmax33 at ~5520 m AGL vs. zdrmaxheightqrc, and (c) wmax25 vs. zdrmaxheight for (red) "weak" shear and (blue) "strong" shear hodographs.

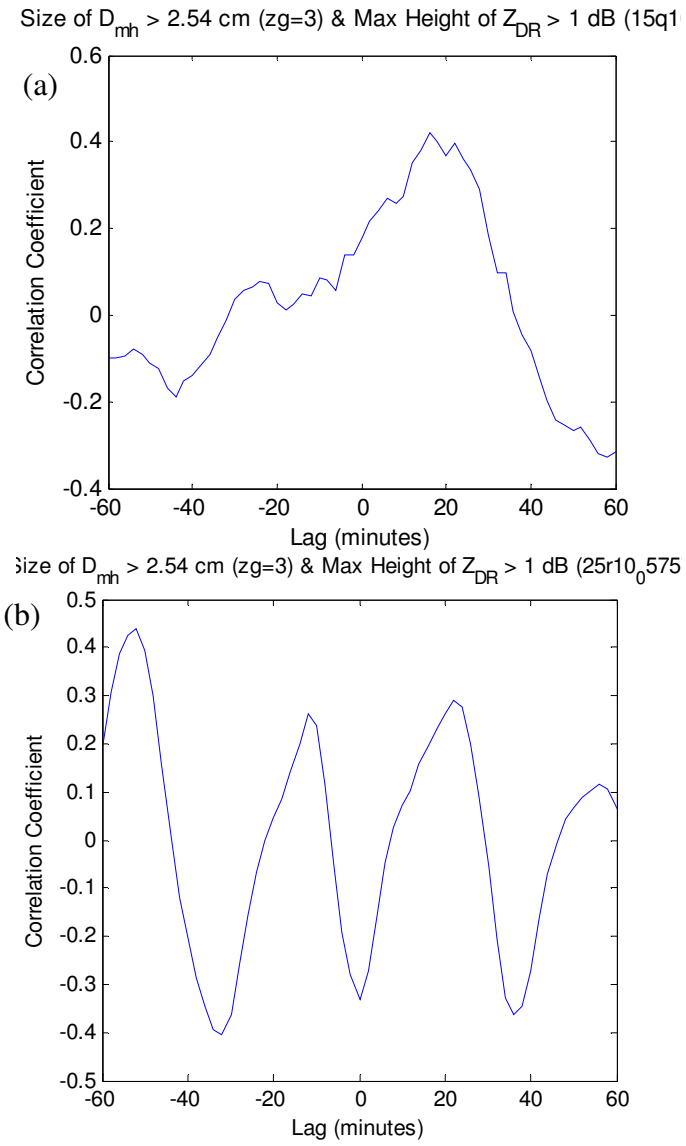

Figure 66. Correlation coefficient between the dmh3area1inch and zdrmaxheight as a function of lag time from the (a) *15q10* and (b) *25r10_057* simulations.

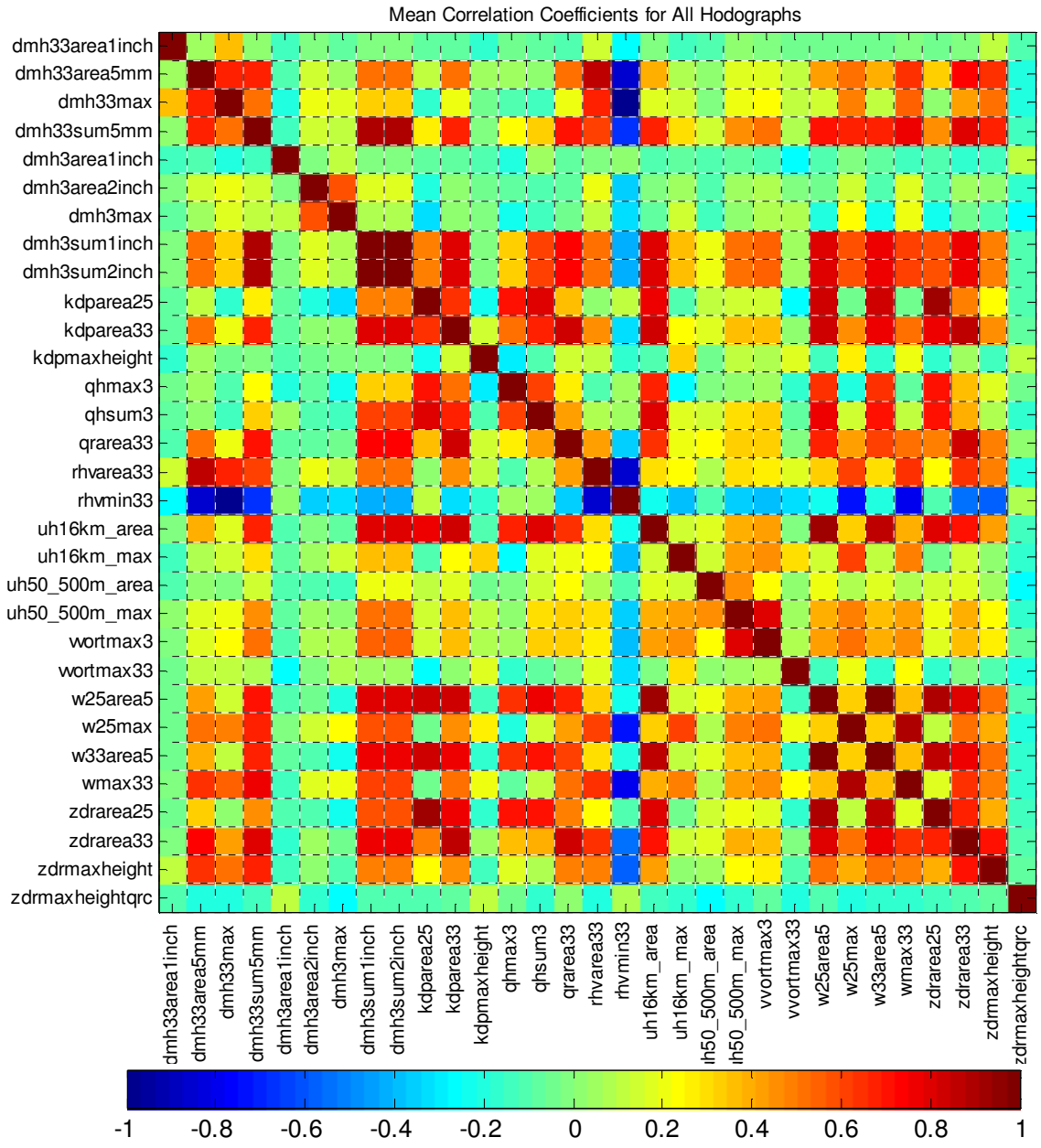

Figure 67. Pearson correlation coefficients for all simulations at all times for the set of quantities (defined in Table 5).

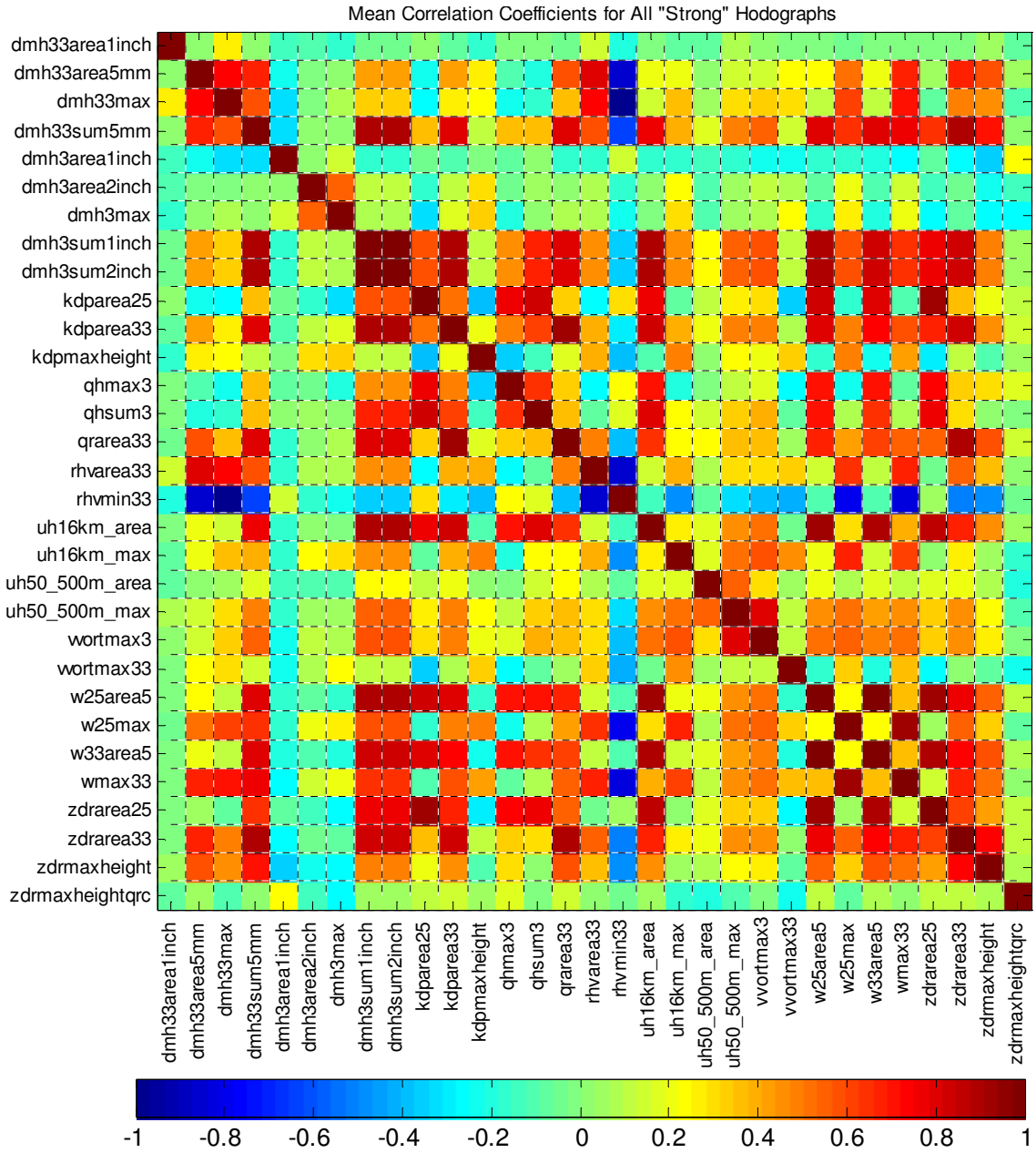

Figure 68. As in Figure 64 but for the "strong shear" simulations.

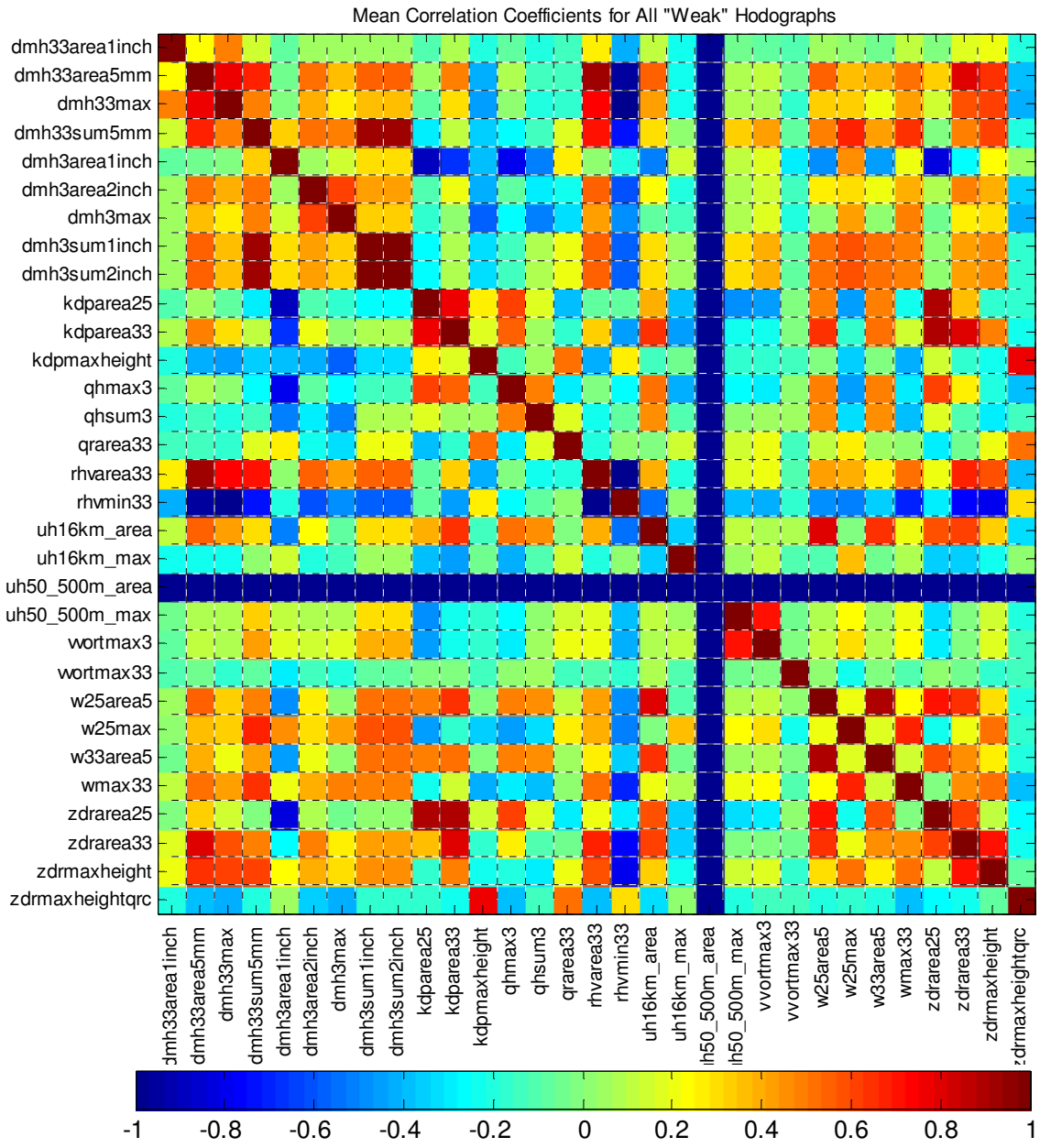

Figure 69. As in Figure 67 but for the "weak shear" simulations.

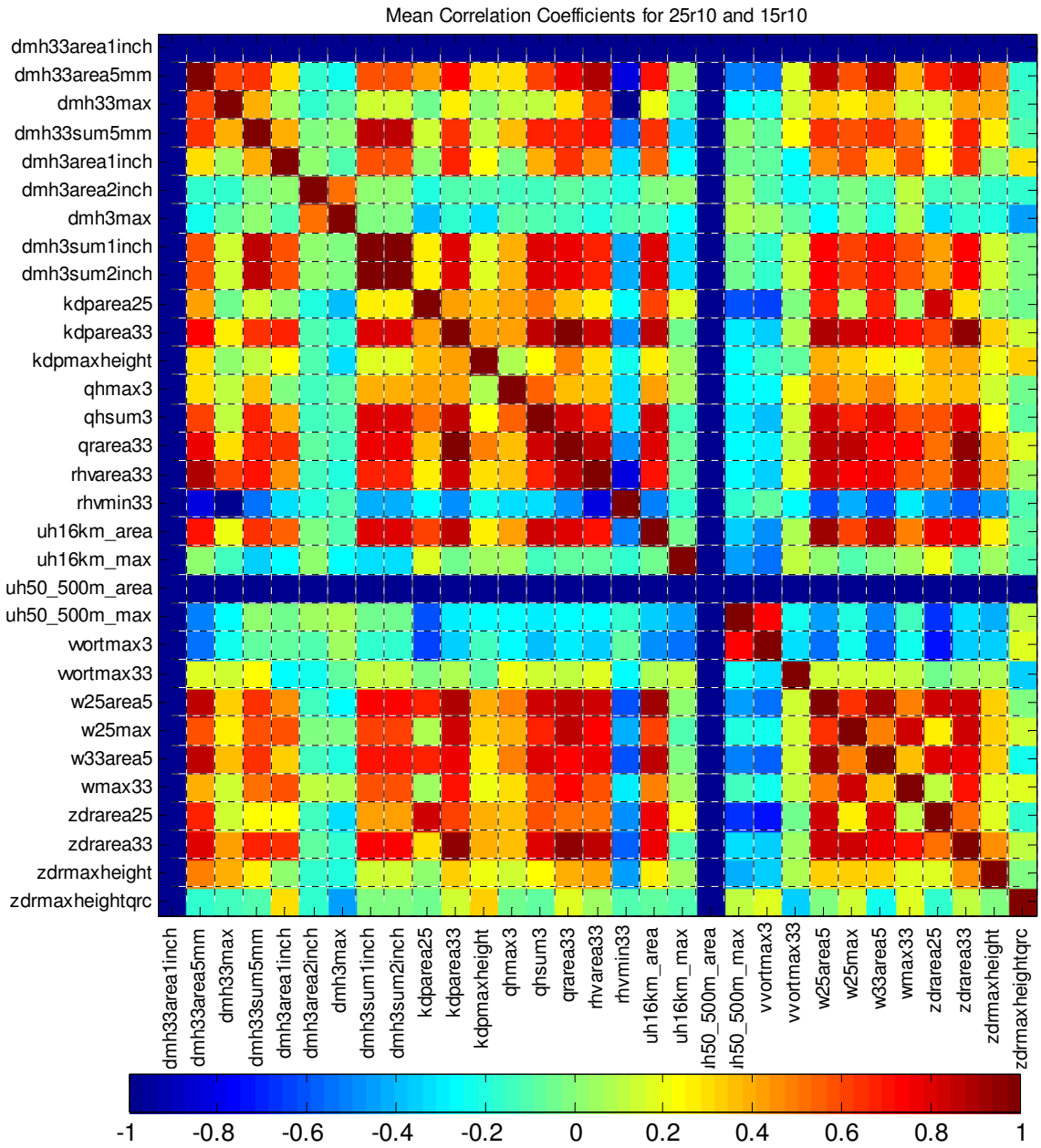

Figure 70. As in Figure 67 but for the *15r10* and *25r10* simulations.

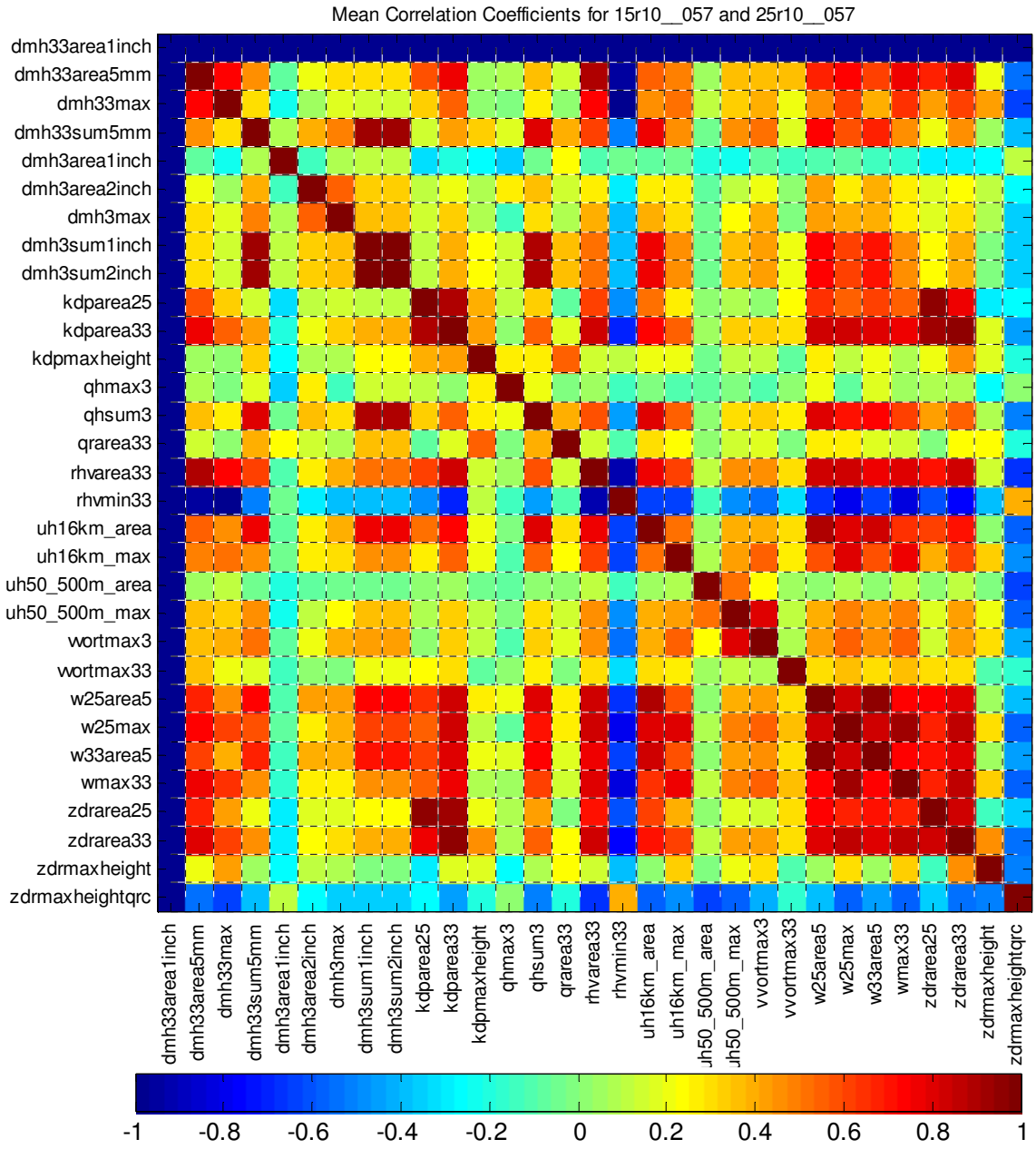

Figure 71. As in Figure 67 but for the *15r10_05757* and *25r10_05757* simulations.

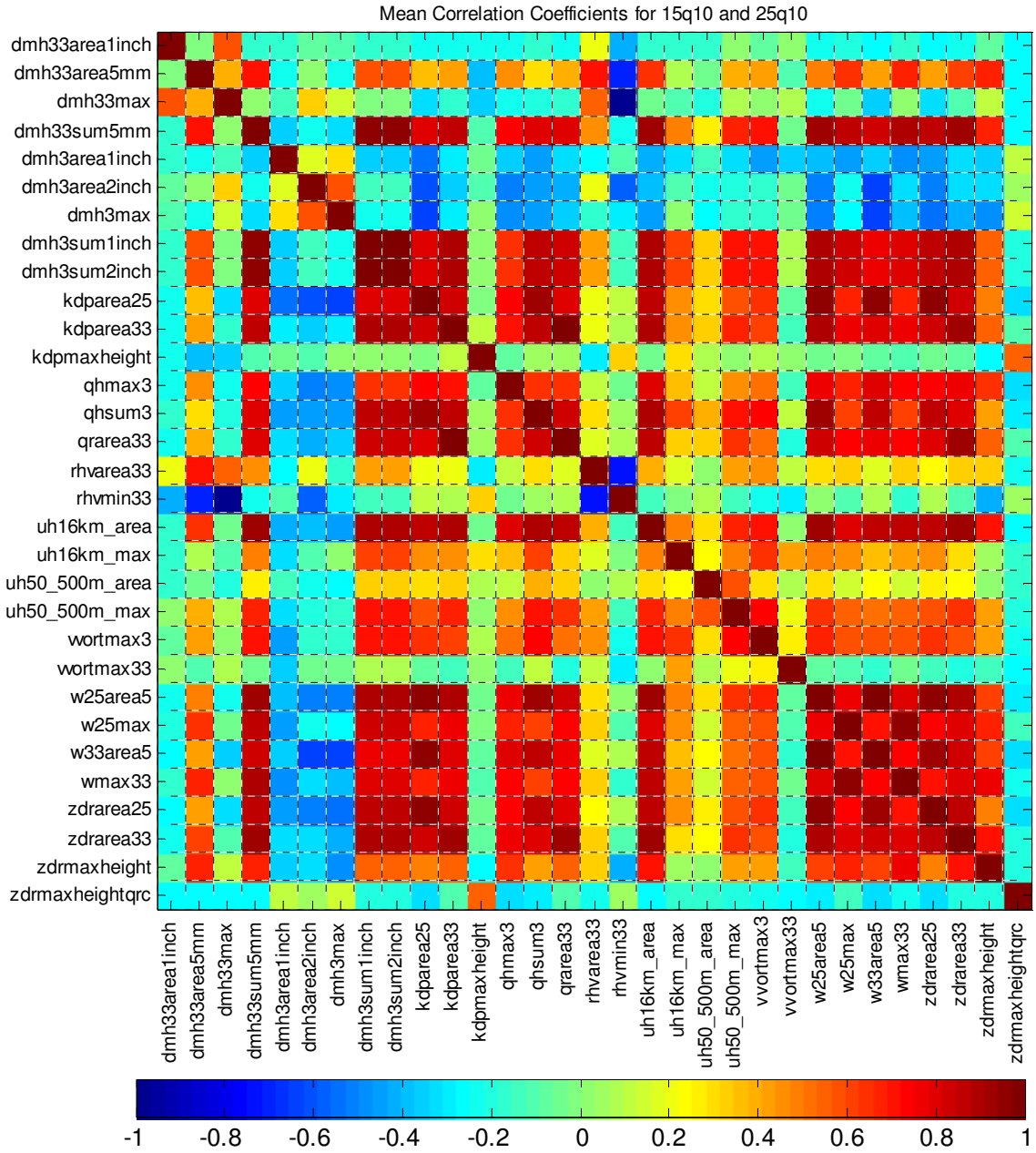

Figure 72. As in Figure 67 but for the *15q10* and *25q10* simulations.

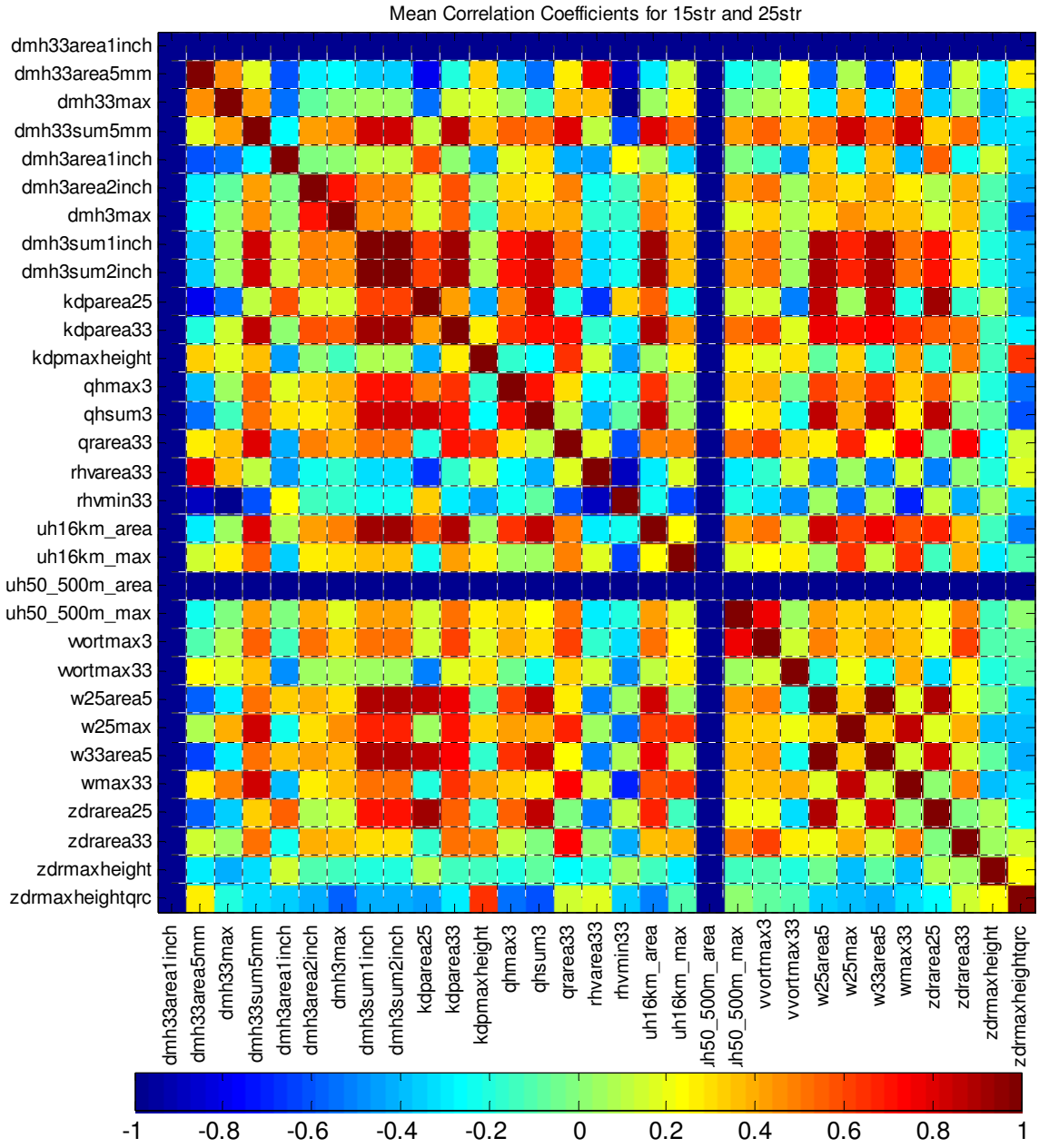

Figure 73. As in Figure 64 but for the *15str* and *25str* simulations.

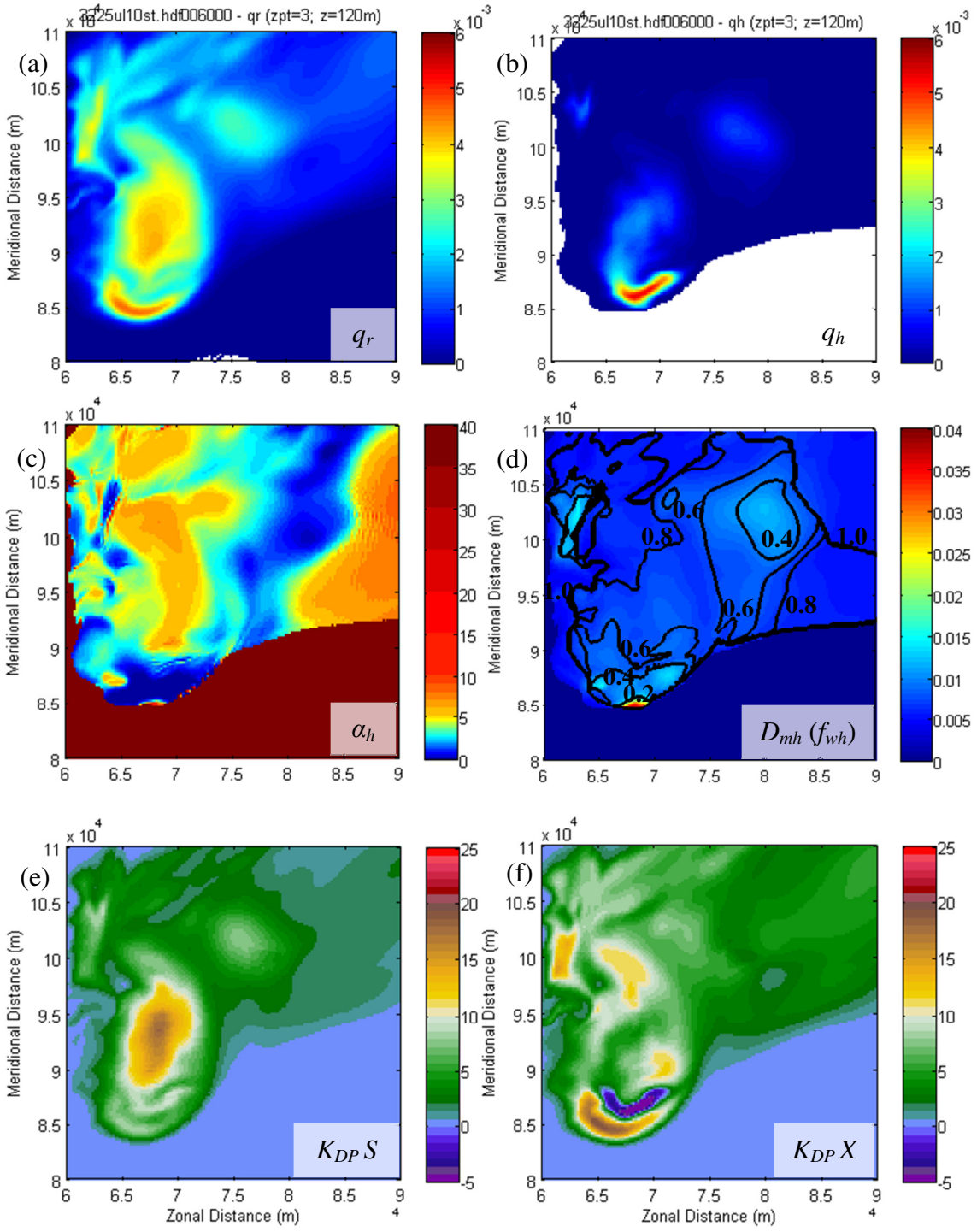

Figure 74. (a) q_r, (b) q_h, (c) α_h, (d) D_{mh} (m) and f_{wh} (contoured every 0.2), and K_{DP} (deg. km^{-1}) from (e) S and (f) X bands from 6000 s in the *25q10* simulation at ~120 m AGL.

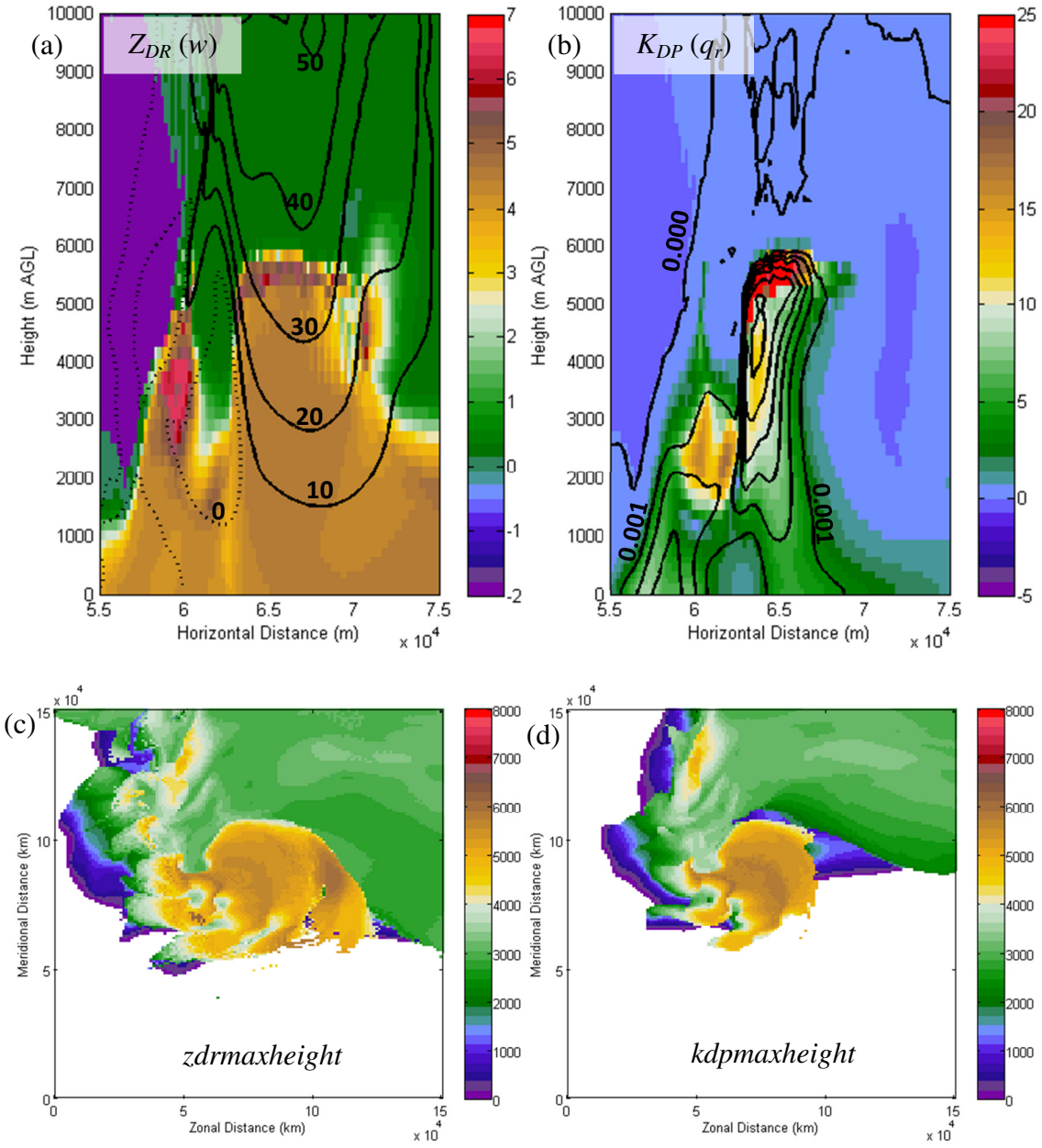

Figure 75. East-west vertical cross-sections of (a) Z_{DR} (color; dB) and w (contoured every 10 m s^{-1} with the dotted curves representing $w \leq 0$ m s^{-1}) and (b) K_{DP} (color; deg. km^{-1}) and q_r (contoured every 0.001) valid at 6000 s from the *25r10* simulation across the updraft. The highest occurrence of (c) $Z_{DR} > 1$ dB and (d) $K_{DP} > 1°$ km^{-1} are plotted to show the areal extent of the Z_{DR} and K_{DP} column.

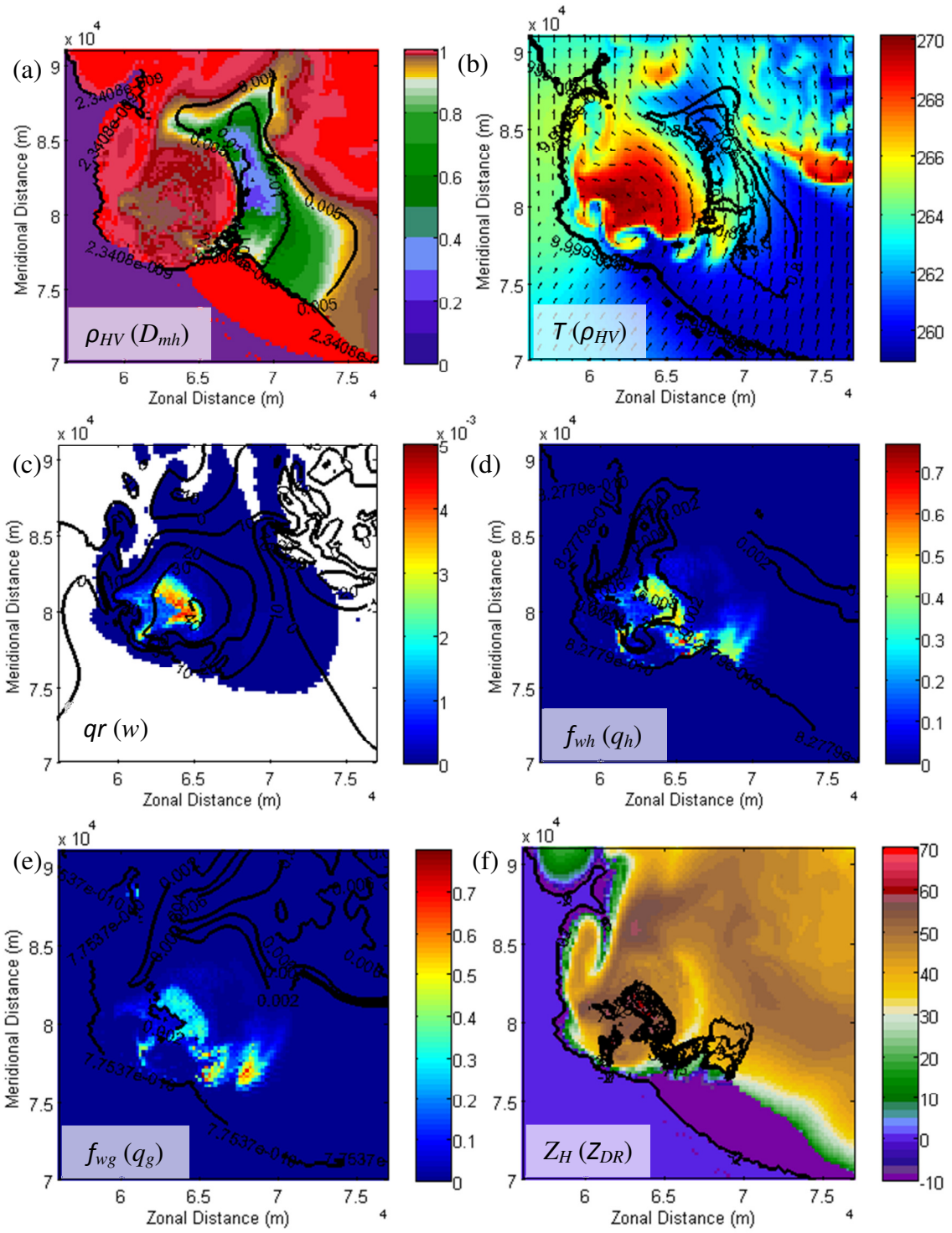

Figure 76. A ρ_{hv} half ring in the *25r10* simulation at t = 4800 s and ~5600 m AGL. (a) ρ_{hv} (color) and D_{mh} (contoured every 0.005 m), (b) T (color; K) and ρ_{hv}, (c) q_r (color) and w (contoured every 10 m s^{-1}), (d) f_{wh} (color) and q_h (contoured every 0.002), (e) f_{wg} (color) and q_g (contoured every 0.002), and (f) Z_H (color; dBZ) and Z_{DR} (contoured every 1 dB).

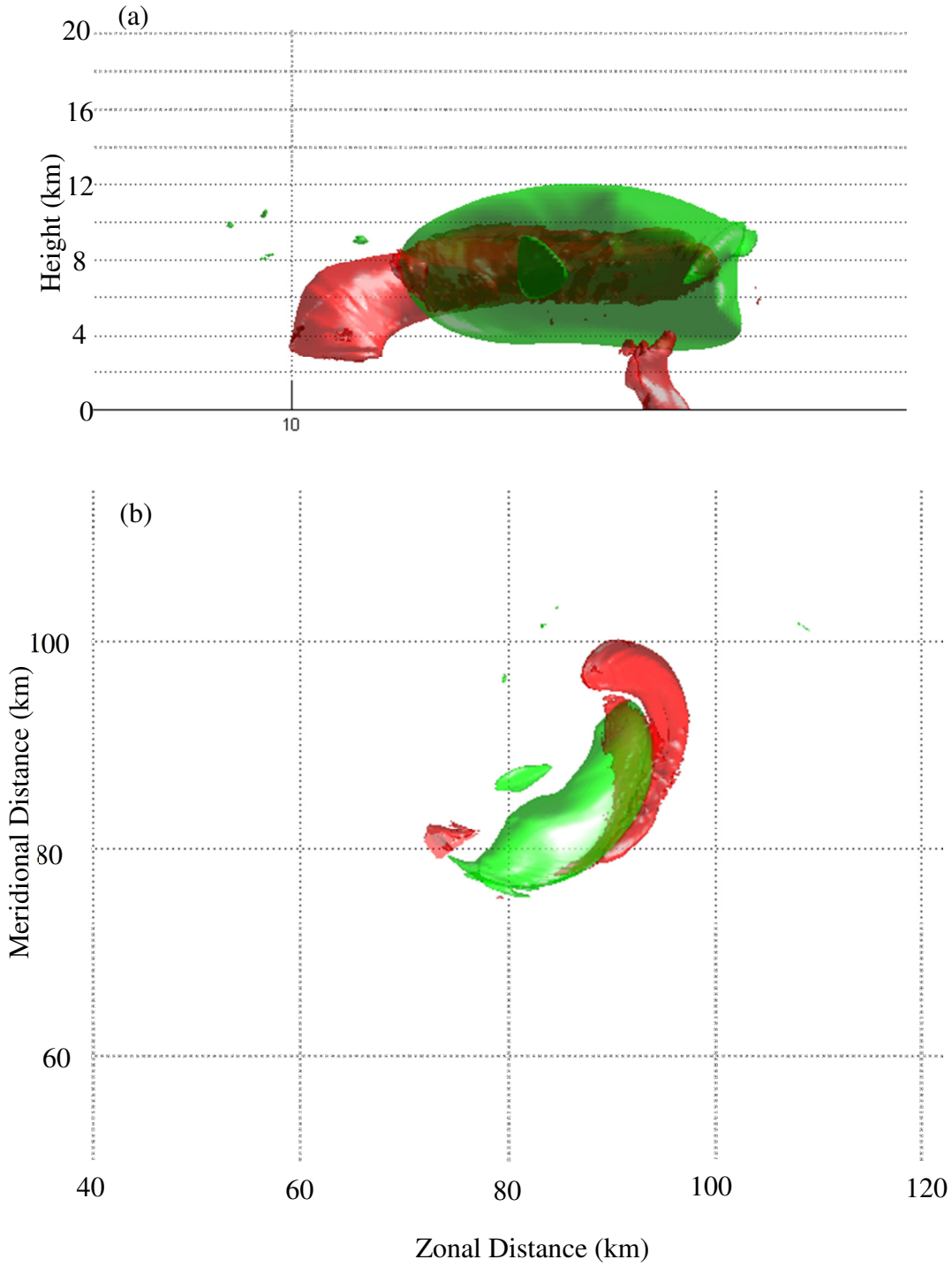

Figure 77. Isosurfaces of ρ_{hv} = 0.8 (red) and w = 30 m s^{-1} (green) valid 7320 s from the *25q10* simulation looking (a) horizontally to the east and (b) downward from the top of the domain. The gridlines in (a) mark the height AGL every 4 km; the gridlines in (b) represent horizontal extent and are marked every 20 km.

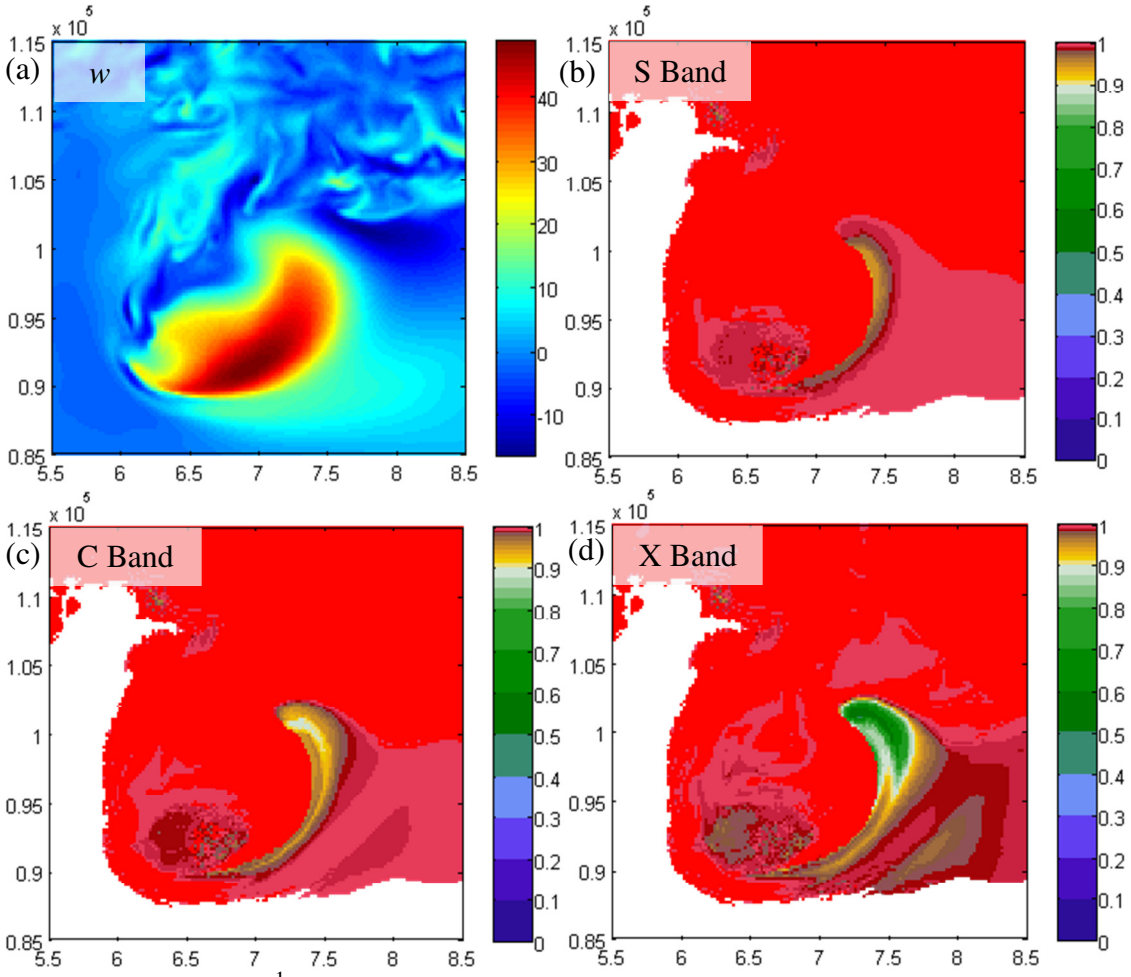

Figure 78. (a) w (m s^{-1}) and ρ_{hv} at (b) S, (c) C, and (d) X bands from the *25q10* simulation at t = 4220 s and 5600 m AGL. The ρ_{hv} half ring is more prominent and is larger at increasing radar frequency. In all cases, the half ring is located along the eastern edge of the convective updraft.

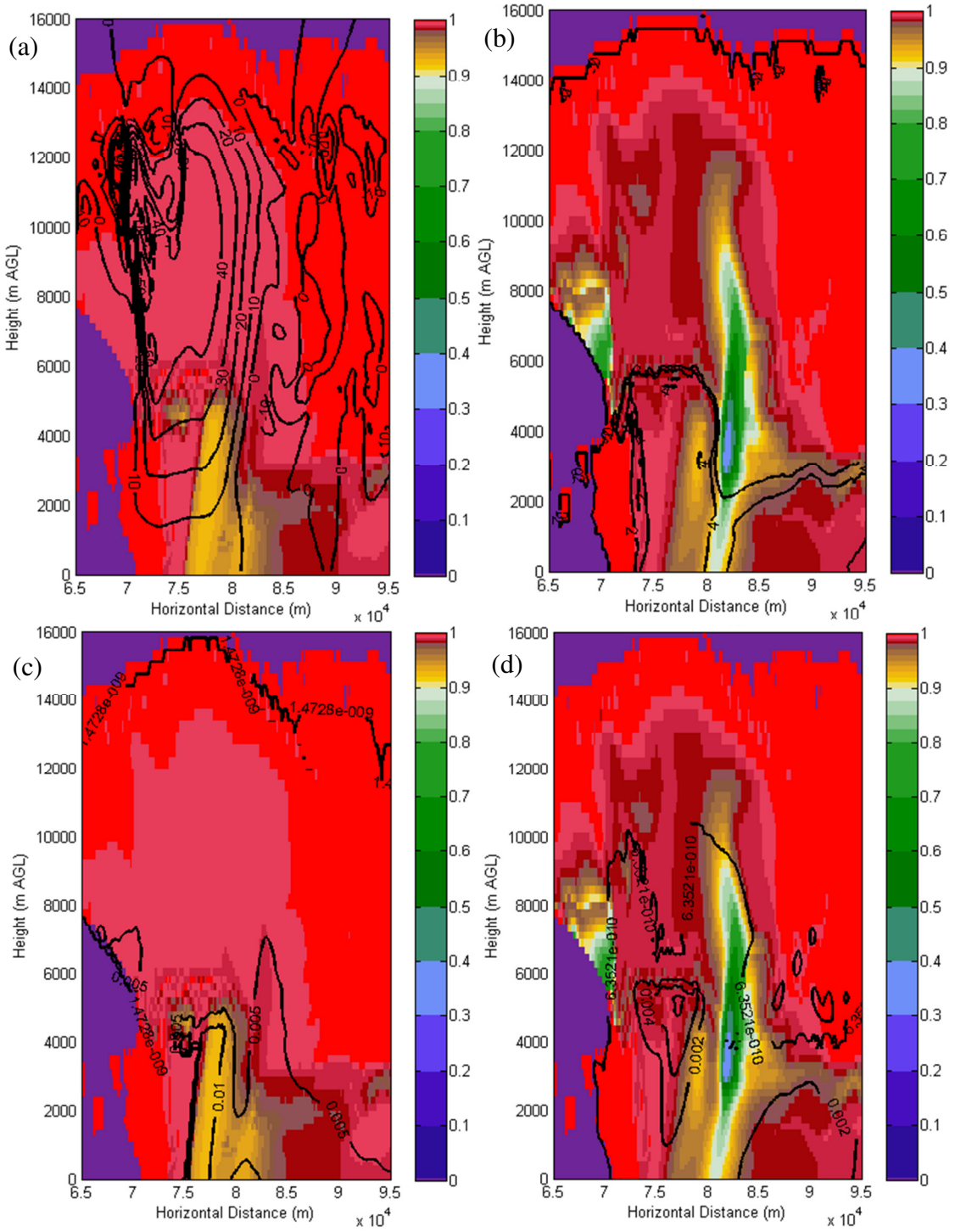

Figure 79. A north-south vertical cross-section of (a) ρ_{hv} (color) at S band and w (contoured every 10 m s^{-1}), (b) ρ_{hv} (color) at X band and Z_{DR} (contoured every 2 dB), (c) ρ_{hv} (color) at S band and D_{mh} (m), and (d) ρ_{hv} (color) at X band with q_r (contoured). Data are from the *25r10* simulation.

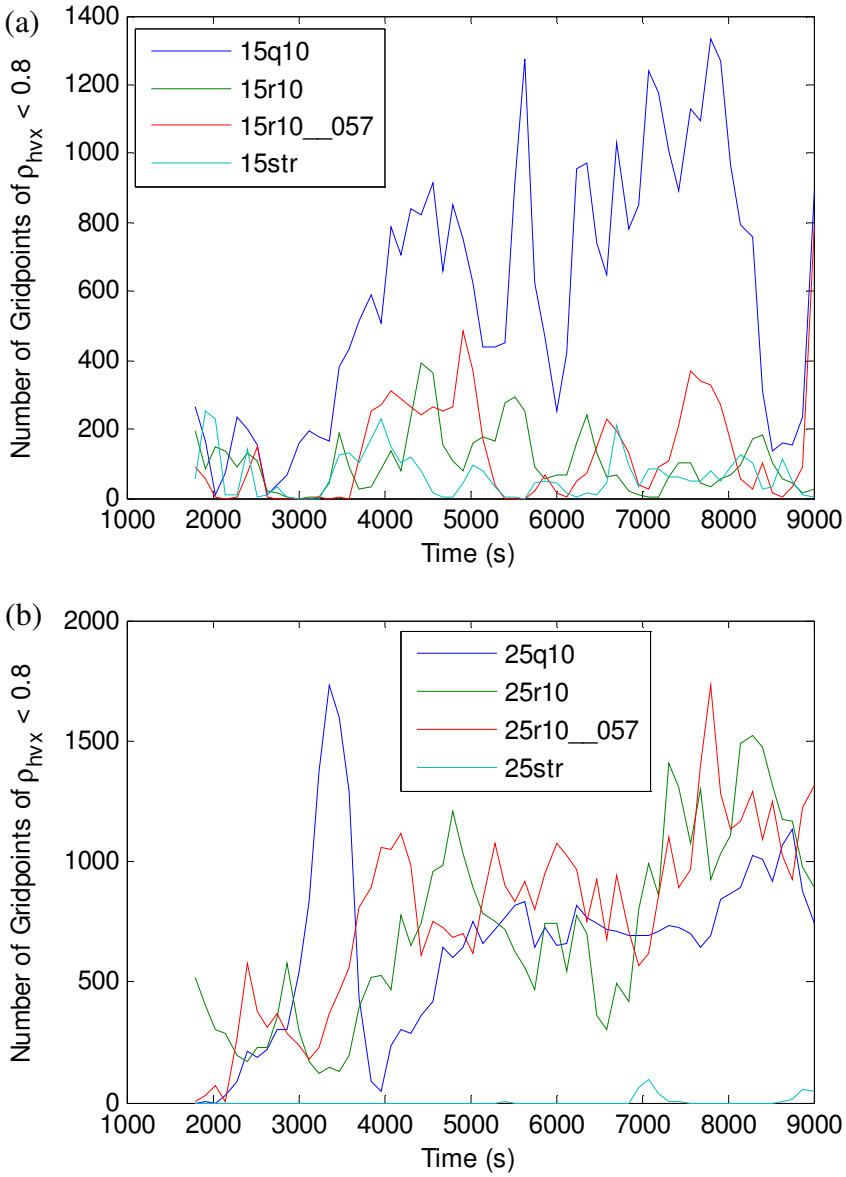

Figure 80. Time series of the number of gridpoints of $\rho_{hv} < 0.8$ at X band from the (a) "weak" shear and (b) "strong" shear simulations.

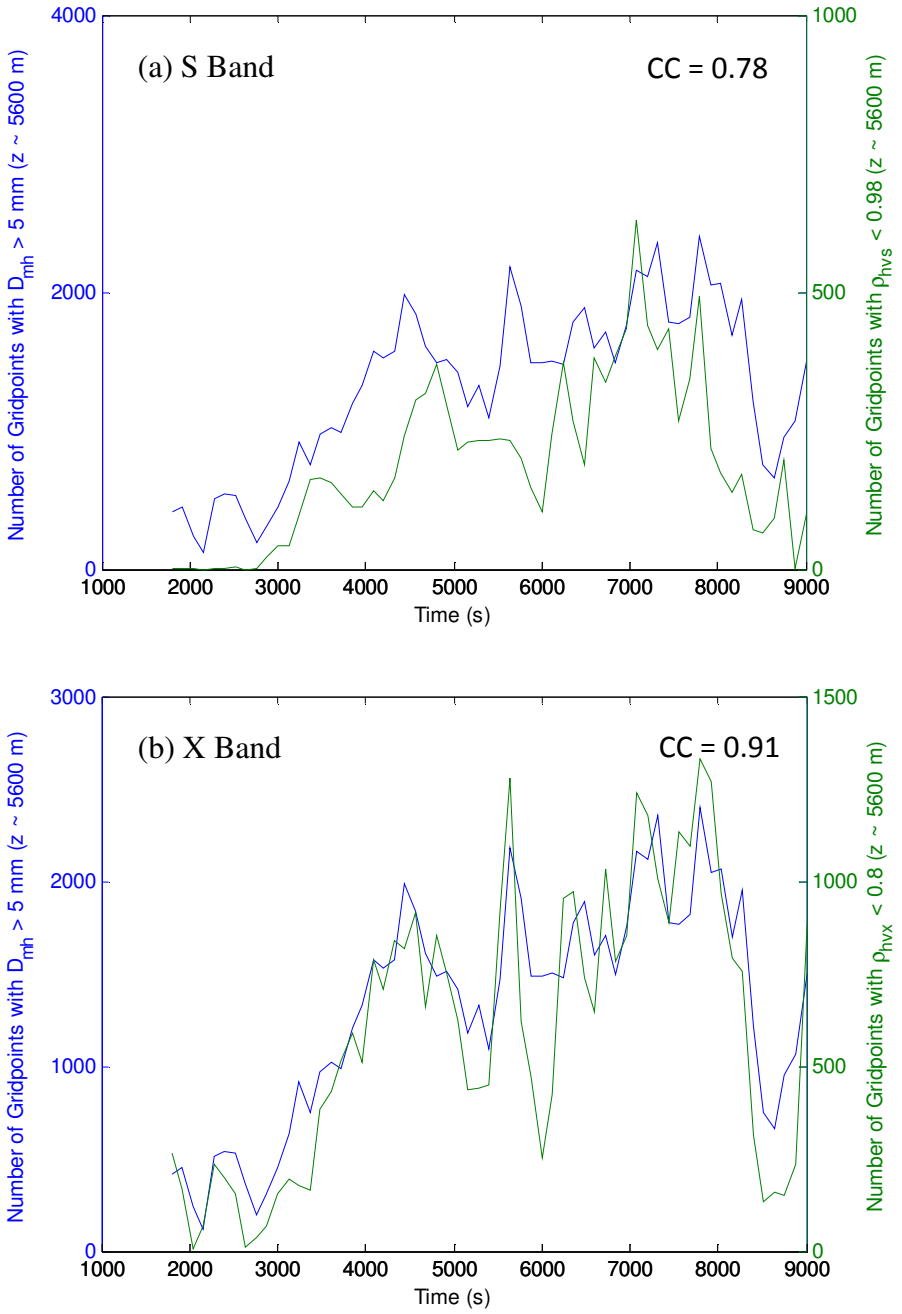

Figure 81. Time series of the number of gridpoints with $D_{mh} > 0.5$ cm (green line) and the number of gridpoints with low ρ_{hv} (blue line) at (a) S band and (b) X band. All data taken from the vertical grid-level at ~5600 m AGL from the *15r10* simulation.

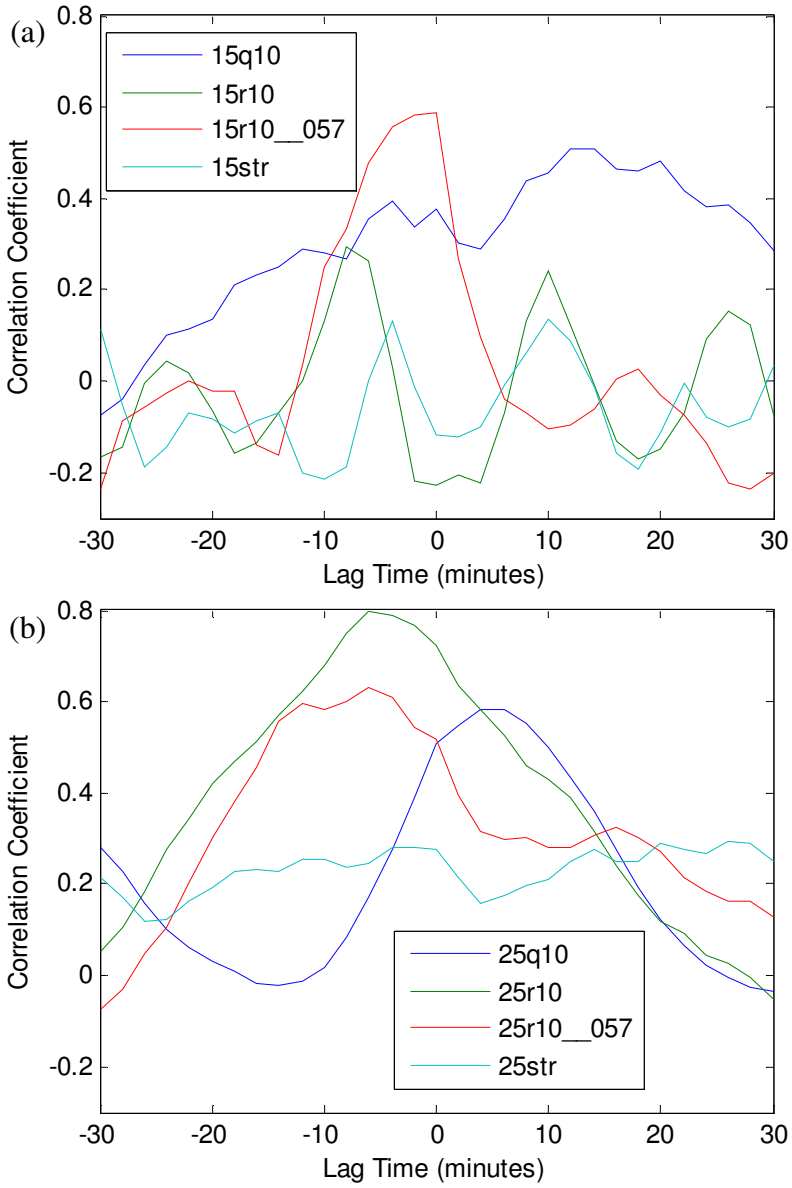

Figure 82. Correlation coefficient between *wmax33* and *rhv33area* as a function of lag time for the (a) "weak" and (b) "strong" shear simulations.

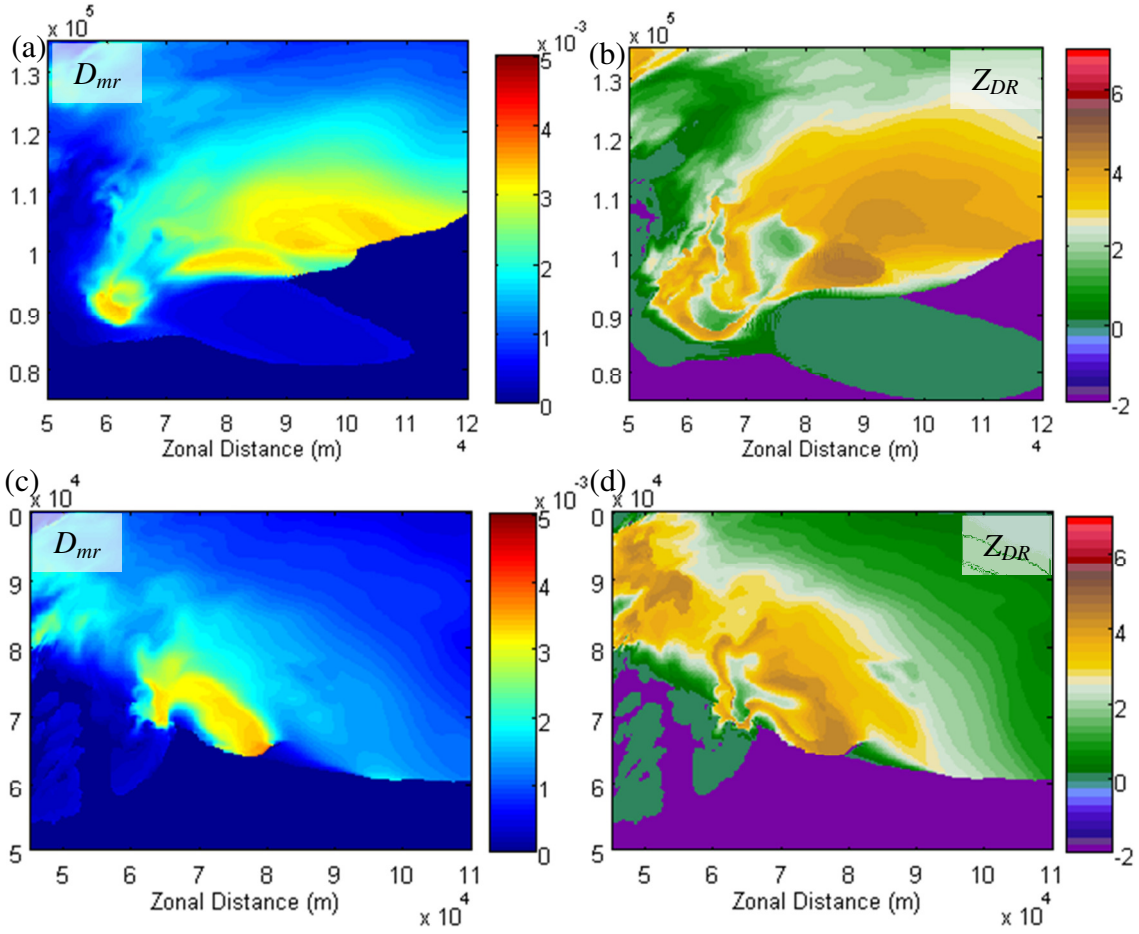

Figure 83. (a, c) D_{mr} (m) and (b, d) S-band Z_{DR} (dB) from the *25q10* (a,b) and *15r10* (c,d) simulations valid at 120 m AGL.

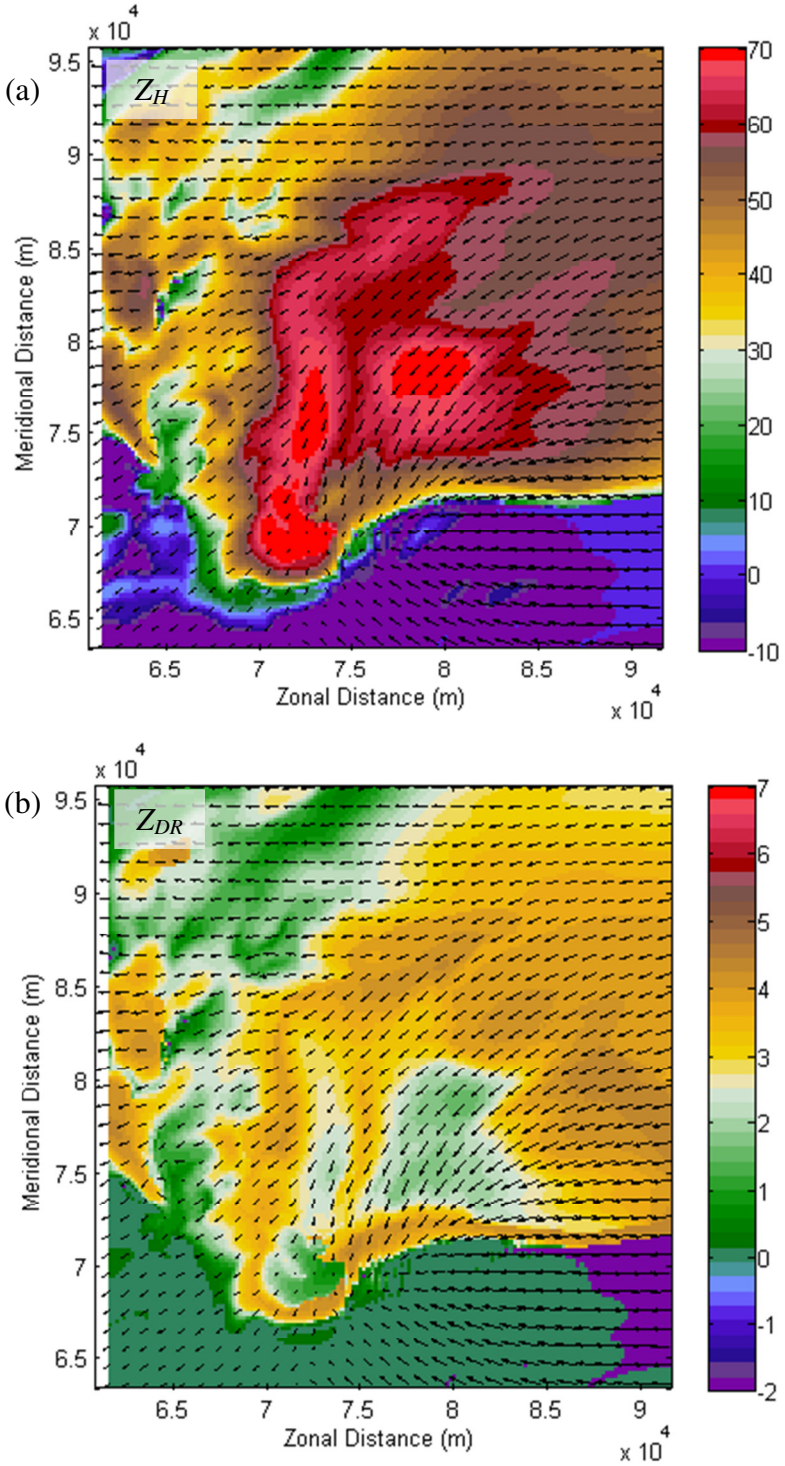

Figure 84. S-band (a) Z_H (dBZ) and (b) Z_{DR} (dB) at a height of 37.5 m AGL valid 4800 s in the *15q10* simulation. A feature that looks similar to an LRR is evident in (a), but the LRR-like feature is characterized by a local maximum in Z_{DR}. In this case, large hail is occurring on either side of the LRR-like feature, which does not seem consistent with observations of the LRR presented in this paper. Every fifth wind vector is plotted (i.e., wind vectors are plotted every 1 km).

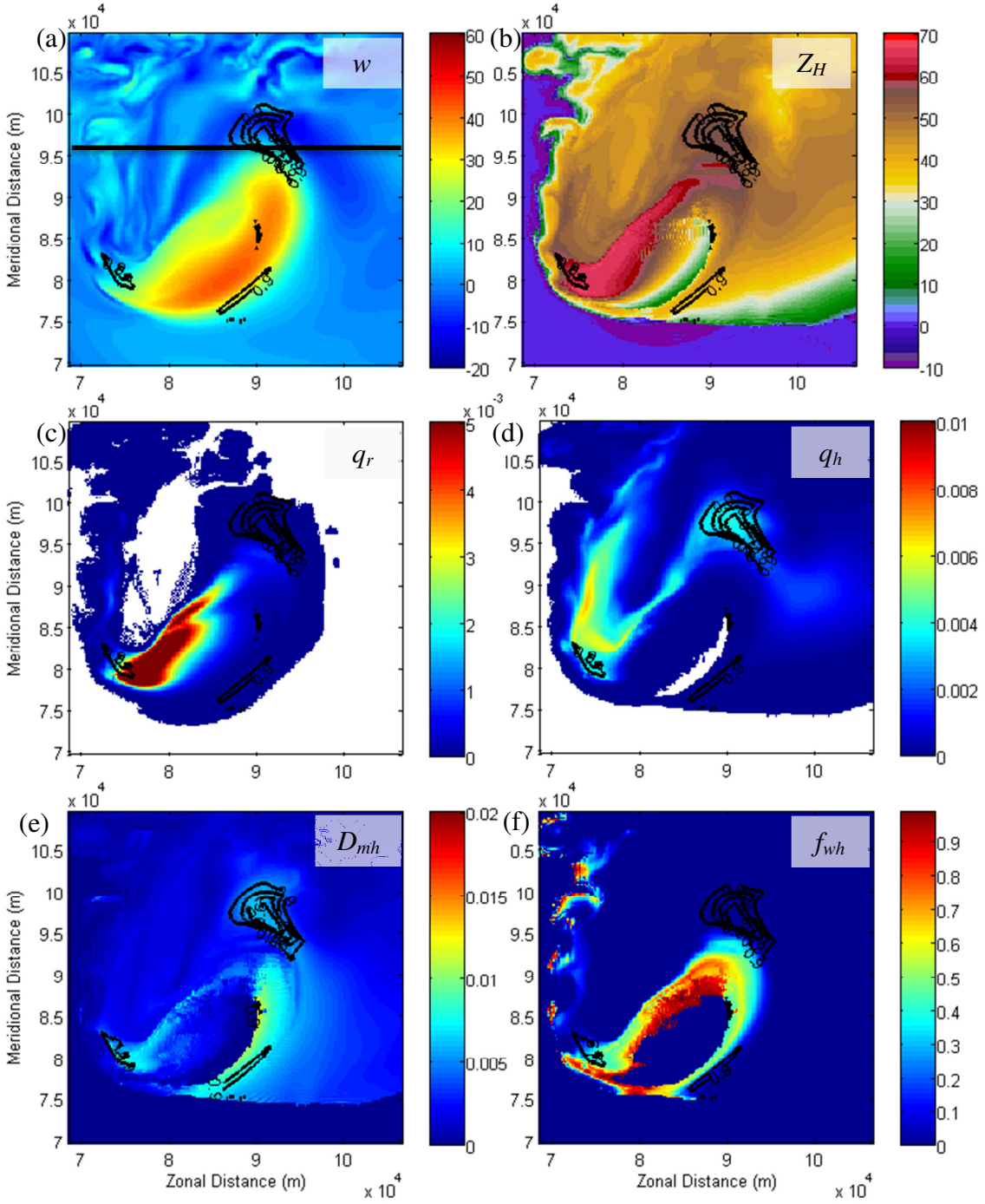

Figure 85. (a) w (m s^{-1}), (b) Z_H (dBZ), (c) q_r, (d) q_h, (e) D_{mh}, and (f) f_{wh} from the *25q10* simulation at 7320 s and ~4600 m AGL. In all panels, ρ_{hv} is contoured every 0.1 decreasing from 0.9. The black line in (a) marks the approximate location of the vertical cross-section shown in Figure 86.

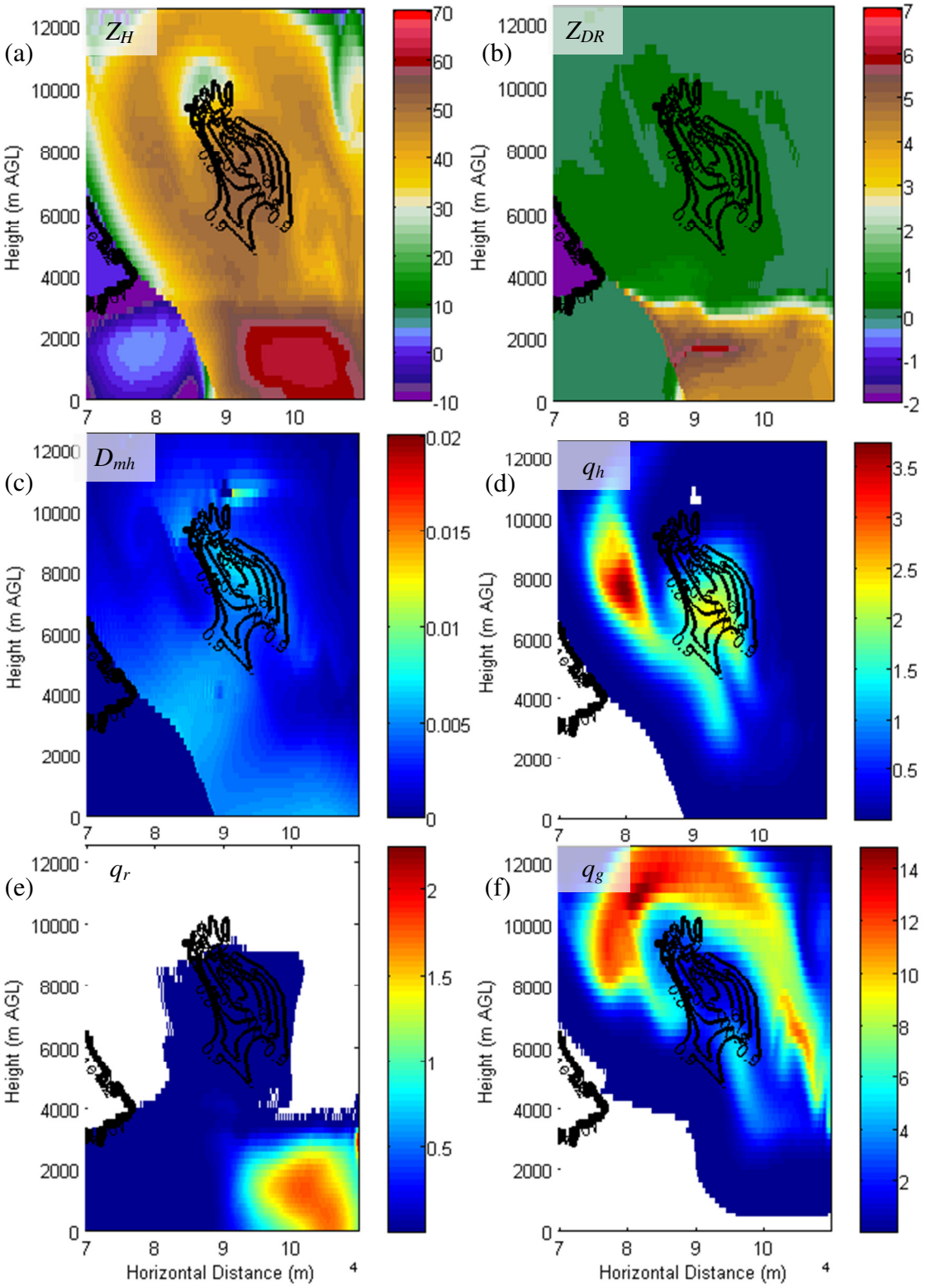

Figure 86. An east-west vertical cross-section along the black line in Figure 85a showing (a) Z_H (dBZ), (b) Z_{DR} (dB), (c) D_{mh} (m), (d) q_hx10^3 (e) q_rx10^3, and (f) q_gx10^3 from the *25q10* simulation at 7320 s. In all panels, ρ_{hv} is contoured every 0.1.

References

Browning, K. A., 1964: Airflow and precipitation trajectories within severe local storms which travel to the right of the winds. *J. Atmos. Sci.*, **21**, 634–639.

Browning, K. A., and R. J. Donaldson, 1963: Airflow and structure of a tornadic storm. *J. Atmos. Sci.*, **20**, 533–545.

Adlerman, E. J., and K. K. Droegemeier, 2002: The sensitivity of numerically simulated mesocyclogenesis to variations in model physics and computational parameters. *Mon. Wea. Rev.,* **130,** 2671–2691.

Adlerman, E. J., and K. K. Droegemeier, 2005: The dependence of numerically simulated cyclic mesocyclogenesis upon environmental vertical wind shear. *Mon. Wea. Rev.,* **133,** 3595–3623.

Aydin, K., Y. Zhao, and T. A. Seliga, 1990: A differential reflectivity radar hall measurement technique: Observations during the Denver hailstorm of 13 June 1984. *J. Atmos. Oceanic Technol.*, **7,** 104–113.

Balakrishnan, N., and D. S. Zrnic, 1990: Use of polarization to characterize precipitation and discriminate large hail. *J. Atmos. Sci.*, **47,** 1525–1540.

Biggerstaff, M. I., and Coauthors, 2005: The Shared Mobile Atmospheric Research and Teaching Radar: A collaboration to enhance research and teaching. *Bull. Amer. Meteor. Soc.*, **86,** 1263–1274.

Bluestein, H. B., and W. P. Unruh, 1989: Observations of the wind fields in tornadoes, funnel clouds, and wall clouds with a portable Doppler radar. *Bull. Amer. Meteor. Soc.,* **70,** 1514–1525.

Bluestein, H. B., and A. L. Pazmany, 2000: Observations of tornadoes and other convective phenomena with a mobile, 3-mm wavelength, Doppler radar: The spring 1999 field experiment. *Bull. Amer. Meteor. Soc.*, **81,** 2939–2951.

Bluestein, H. B., and S. G. Gaddy, 2001: Airborne pseudo-dual-Doppler analysis of a rear-inflow jet and deep convergence zone within a supercell. *Mon. Wea. Rev.,* **129,** 2270–2289.

Bluestein, H. B., A. L. Pazmany, J. C. Galloway, and R. E. McIntosh, 1995: Studies of the substructure of severe convective storms using a mobile 3-mm-wavelength Doppler radar. *Bull. Amer. Meteor. Soc.*, **76**, 2155–2169.

Bluestein, H. B., M. M. French, R. L. Tanamachi, S. Frasier, K. Hardwick, F. Junyent, and A. L. Pazmany, 2007a: Close-range observations of tornadoes in supercells made with a dual-polarization, X-band, mobile Doppler radar. *Mon. Wea. Rev.*, **135,** 1522–1543.

Bluestein, H. B., C. C. Weiss, M. M. French, E. M. Holthaus, R. L. Tanamachi, S. Frasier, and A. L. Pazmany, 2007b: The structure of tornadoes near Attica, Kansas, on 12 May 2004: High-resolution, mobile, Doppler radar observations. *Mon. Wea. Rev.*, **135,** 475–506.

Bluestein, H. B., M. M. French, I. PopStefanija, R. T. Bluth, and J. B. Knorr, 2010: A mobile, phased-array Doppler radar for the study of severe convective storms. *Bull. Amer. Meteor. Soc*., **91**, 579–600.

Borowska et al., 2011: Attenuation and differential attenuation of 5-cm-wavelength radiation in melting hail. *J. Appl. Meteor. Climatol.,* **50,** 59–76.

Brandes, E. A., 1978: Mesocyclone evolution and tornadogenesis: Some observations. *Mon. Wea. Rev.*, **106,** 995–1011.

Brandes, E. A., 1984: Vertical vorticity generation and mesocyclone sustenance in tornadic thunderstorms: The observational evidence. *Mon. Wea. Rev.,* **112,** 2253–2269.

Brandes, E. A., 1993: Tornado thunderstorm characteristics determined with Doppler radar. *The Tornado: Its Structure, Dynamics, Prediction and Hazards, Geophys. Monog.,* Vol. 79, Amer. Geophys. Union, 143–159.

Brandes, E. A., and K. Ikeda, 2004: Freezing-level estimation with polarimetric radar. *J. Appl. Meteor.*, **43,** 1541–1553.

Brandes, E. A., J. Vivekanandan, J. D. Tuttle, and C. J. Kessinger, 1995: A study of thunderstorm microphysics with multiparameter radar and aircraft observations. *Mon. Wea. Rev.,* **123,** 3129–3143.

Brandes, E. A., A. V. Ryzhkov, and D. S. Zrnic, 2001: An evaluation of radar rainfall estimates from specific differential phase. *J. Atmos. Oceanic Technol.,* **18,** 363–375.

Brandes, E. A., G. Zhang, and J. Vivekanandan, 2002: Experiments in rainfall estimation with polarimetric radar in a subtropical environment. *J. Appl. Meteor.,* **41,** 674–685.

Brandes, E. A., G. Zhang, and J. Vivekanandan, 2004a: Comparison of polarimetric radar drop size distribution retrieval algorithms. *J. Atmos. Oceanic Technol.*, **21,** 584–598.

Brandes, E. A., G. Zhang, and J. Vivekanandan, 2004b: Drop size distribution retrieval with polarimetric radar: Model and application. *J. Appl. Meteor.*, **43,** 461–475.

Bringi, V. N., and V. Chandrasekar, 2001: *Polarimetric Doppler Weather Radar: Principle and Applications.* Cambridge University Press, 636 pp.

Bringi, V. N., V. Chandrasekar, N. Balakrishnan, and D. S. Zrnic, 1990: An examination of propagation effects in rainfall on radar measurements at microwave

frequencies. *J. Atmos. Oceanic Technol.*, **7,** 829–840.

Bringi, V. N., D. A. Burrows, and S. M. Menon, 1991: Multiparameter radar and aircraft study of raindrop spectral evolution in warm-based clouds. *J. Appl. Meteor.*, **30**, 853–880.

Bringi, V. N., T. D. Keenan, and V. Chandrasekar, 2001: Correcting C-band radar reflectivity and differential reflectivity data for rain attenuation: A self-consistent method with constraints. *IEEE Trans. Geosci. Remote Sens.*, **39,** 1906–1915.

Bringi, V. N., G.-J. Huang, V. Chandrasekar, and E. Gorgucci, 2002: A methodology for estimating the parameters of a gamma raindrop size distribution model from polarimetric radar data: application to a squall-line event from the TRMM/Brazil campaign. *J. Atmos. Oceanic Technol.,***19,** 633–645.

Browning, K. A., 1964: Airflow and precipitation trajectories within severe local storms which travel to the right of the winds. *J. Atmos. Sci.*, **21**, 634–639.

Browning, K. A., and R. J. Donaldson, 1963: Airflow and structure of a tornadic storm. *J. Atmos. Sci.*, **20**, 533–545.

Bryan, G. H., J. C. Wyngaard, and J. M. Fritsch, 2003: Resolution requirements for the simulation of deep moist convection. *Mon. Wea. Rev.,* **131,** 2394–2416.

Burgess, D. W., E. R. Mansell, C. M. Schwarz, and B. J. Allen, 2010: Tornado and tornadogenesis events seen by the NOXP x-band, dual-polarization radar during VORTEX2 2010. Preprints, *25th Conf. on Severe Local Storms,* Denver, CO, Amer. Meteor. Soc., 5.2.

Cao, Q., G. Zhang, E. Brandes, T. Schuur, A. V. Ryzhkov, and K. Ikeda, 2008: Analysis of video disdrometer and polarimetric radar data to characterize rain microphysics in Oklahoma. *J. Appl. Meteor. Climatol.*, **47**, 2238–2255.

Carey, L. D., S. A. Rutledge, D. A. Ahijevych, and T. D. Keenan, 2000: Correcting propagation effects in C-band polarimetric radar observations of tropical convection using differential propagation phase. *J. Appl. Meteor.*, **39,** 1405–1433.

Chandrasekar, V., W. A. Cooper, and V. N. Bringi, 1988: Axis ratios and oscillations of raindrops. *J. Atmos. Sci.*, **45**, 1323–1333.

Chisholm, A. J., 1973: Alberta hailstorms. Part I: Radar case studies and airflow models. *Meteor. Monogr.*, **14**, Boston, Amer. Meteor. Soc., 1–36.

Conway, J. W. and D. S. Zrnic, 1993: A study of embryo production and hail growth using dual-Doppler and multiparameter radars. *Mon. Wea. Rev.,* **121,** 2511–2528.

Craven, J. P., and H. E. Brooks, 2004: Baseline climatology of sounding derived parameters associated with deep moist convection. *Natl. Wea. Dig.,* **28,** 13–24.

Davies-Jones, R. P., D. W. Burgess, and M. Foster, 1990: Test of helicity as a tornado forecast parameter. Preprints, *16th Conf. on Severe Local Storms,* Kananaskis Park, AB, Canada, Amer. Meteor. Soc., 588–592.

Dawson, D. T., and G. Romine, 2010: A preliminary survey of DSD measurements collected during VORTEX2. Preprints, *25th Conf. of Severe Local Storms,* Denver, CO, Amer. Meteor. Soc., 8A.4. [Available online at http://ams.confex.com/ams/pdfpapers/176115.pdf]

Dawson, D.T., M. Xue, J.A. Milbrandt, and M.K. Yau, 2010: Comparison of evaporation and cold pool development between single-moment and multi-moment bulk microphysics schemes in idealized simulations of tornadic thunderstorms. *Mon. Wea. Rev.*, **138**, 1152–1171.

Dawson, D. T., E. R. Mansell, Y. Jung, L. J. Wicker, M. R. Kumjian, and M. Xue, 2013: Low-level Z_{DR} signatures in supercell forward flanks: the role of size sorting and melting of hail. *J. Atmos. Sci*, **in press**.

Dolan, B., and S. A. Rutledge, 2009: A theory-based hydrometeor identification algorithm for X-band polarimetric radars. *J. Atmos. Oceanic Technol.,* **26,** 2071–2088.

Doswell, C., and E. Rasmussen, 1994: The effect of neglecting the virtual temperature correction on CAPE calculations. *Wea. Forecasting*, **9,** 625–629.

Doviak, R. J., V. Bringi, A. V. Ryzhkov, A. Zahrai, and D. S. Zrnic, 2000: Considerations for polarimetric upgrades to operational WSR-88D radars. *J. Atmos. Oceanic Technol.,* **17,** 257–278.

Ferrier, B.S., W.-K. Tao, and J. Simpson, 1995: A double-moment multiple-phase four-class bulk ice scheme. Part II: Simulations of convective storms in different large-scale environments and comparisons with other bulk parameterizations. *J. Atmos. Sci.*, **52**, 1001–1033. Preprints, *35th Conf. on Radar Meteorology*, Pittsburgh, PA, Amer. Meteor. Soc., 8B.6.

Giangrande, S. E., J. M. Krause, and A. V. Ryzhkov, 2008: Automatic designation of the melting layer with a polarimetric prototype of the WSR-88D radar. *J. Appl. Meteor. Climatol.*, **47**, 1354–1364.

Giangrande, S. E., and A. V. Ryzhkov, 2008: Estimation of rainfall based on the result of polarimetric echo classification. *J. Appl. Meteor. Climatol.,* **47,** 2445–2462.

Gilmore, M. S., J. M. Straka, and E. N. Rasmussen, 2004: Precipitation uncertainty due to variations in precipitation particle parameters within a simple microphysics scheme. *Mon. Wea. Rev.,* **132,** 2610–2627.

Green, A. W., 1975: An approximation for the shape of large raindrops. *J Appl. Meteor.,* **14,** 1578–1583.

Gorgucci, E., V. Chandrasekar, V. N. Bringi, and G. Scarchilli, 2002: Estimation of raindrop size distribution parameters from polarimetric radar measurements. *J. Atmos. Sci.,* **59,** 2373–2384.

Gu, J-Y, A. Ryzhkov, P. Zhang, P. Neilley, M. Knight, B. Wolf, and D-I Lee, 2011: Polarimetric attenuation correction in heavy rain at C band. *J. Appl. Meteor. Climatol.*, **50,** 39-58.

Gunn, K. L. S., and T. W. R. East, 1954: The microwave properties of precipitation particles. *Quart. J. Roy. Meteor. Soc.*, **80,** 522–545.

Hall, M. P. M., J. W. F. Goddard, and S. M. Curry, 1984: Identification of hydrometeors and other targets by dual-polarization radar. *Radio Sci.,* **19,** 132–140.

Herzegh, P. H. and A. R. Jameson, 1992: Observing precipitation through dual-polarization radar measurements. *Bull. Amer. Meteor. Soc.,* **73,** 1365–1374.

Hitschfeld, W., and J. Bordan, 1954: Errors inherent in the radar measurement of rainfall at attenuating wavelengths. *J. Meteor.*, **11**, 58–67.

Holler, H., V. N. Bringi, J. Hubbert, M. Hagen, and P. F. Meischner, 1994: Life cycle and precipitation formation in a hybrid-type hailstorm revealed by polarimetric and Doppler radar measurements. *J. Atmos. Sci.*, **51,** 2500–2522.

Hubbert, J., and V. N. Bringi, 1995: An iterative filtering technique for the analysis of copolar differential phase and dual-frequency radar measurements. *J. Atmos. Oceanic Technol.*, **12,** 643–648.

Hubbert, J. C., and V. N. Bringi, 2000: The effects of three-body scattering on differential reflectivity signatures. *J. Atmos. Oceanic Technol.*, **17**, 51–61.

Hubbert, J., V. N. Bringi, L. D. Carey, and S. Bolen, 1998: CSU-CHILL polarimetric radar measurements from a severe hail storm in eastern Colorado. *J. Appl. Meteor.,* **37,** 749–775.

Istok, M. J., and Coauthors, 2009: WSR-88D Dual Polarization Initial Operational Capabilities. Preprints, *25th Conf. on International Information and Processing Systems for Meteorol., Oceanography, and Hydrology*, Phoenix, AZ, Amer. Meteor. Soc., 15.5.

Iwanami, K., K. Kusunoki, N. Orikasa, M. Maki, R. Misumi, and M. Murakami, 2007: Hydrometeor type classification in winter clouds using X-band polarimetric radar measurements -- comparison of X-band polarimetric radar data with in-situ measurements by HYVIS. Preprints, *33rd Conf. on Radar Meteorology*, Cairns, Queensland, Amer. Meteor. Soc., P10.11.

James, R. P., and P. M. Markowski, 2010: A numerical investigation of the effects of dry air aloft on deep convection. *Mon. Wea. Rev.*, **138**, 140–161.

Jameson, A. R., 1983: Microphysical interpretation of multi-parameter radar measurements in rain. Part I: Interpretation of polarization measurements and estimation of raindrop shapes. *J. Atmos. Sci.,* **40,** 1792–1802.

Jameson, A. R., 1992: The effect of temperature on attenuation-correction schemes in rain using polarization propagation differential phase shift. *J. Appl. Meteor.*, **31,** 1106–1118.

Jameson, A. R., M. J. Murphy, and E. P. Krider, 1996: Multiple-parameter radar observations of isolated Florida thunderstorms during the onset of electrification. *J. Appl. Meteor.*, **35**, 343–354.

Jung, Y., G. Zhang, and M. Xue, 2008: Assimilation of simulated polarimetric radar data for a convective storm using the ensemble Kalman filter. Part I: Observation operators for reflectivity and polarimetric variables. *Mon. Wea. Rev.,* **136,** 2228–2245.

Jung, Y., M. Xue, and G. Zhang, 2010: Simulations of polarimetric radar signatures of a supercell storm using a two-moment bulk microphysics scheme. *J. Appl. Meteor. Climatol.*, **49**, 146–163.

Junyent-Lopez, F. J., 2003: The design, development, and initial field deployment of an X-band polarimetric Doppler weather radar. M. S. thesis, Electrical and Computer Engineering, University of Massachusetts Amherst, 120 pp.

Keenan, T., 2003: Hydrometeor classification with C-band polarimetric radar. *Aust. Meteor. Mag.*, **51,** 23–31.

Kennedy, P. C., S. A. Rutledge, W. A. Petersen, and V. N. Bringi, 2001: Polarimetric radar observations of hail formation. *J. Appl. Meteor.*, **40**, 1347–1366.

Kessler, E., 1969: *On the Distribution and Continuity of Water Substance in Atmospheric Circulations*. Meteor. Monogr. No. 32, Amer. Meteor. Soc., 84 pp.

Khain, A., and B. Lynn, 2009: Simulations of a supercell storm in clean and dirty atmosphere using Weather Research and Forecast model with spectral bin microphysics. *J. Geophys. Res.,* **114,** D19209, doi:10.1029/2009JD011827.

Klemp, J. B., and R. B. Wilhelmson, 1978: The simulation of three-dimensional convective storm dynamics. *J. Atmos. Sci.,* **35,** 1070–1096.

Klemp, J. B., and R. Rotunno, 1983: A study of the tornadic region within a supercell thunderstorm. *J. Atmos. Sci.*, **40**, 359–377.

Klemp, J. B., R. B. Wilhelmson, and P. S. Ray, 1981: Observed and numerically simulated structure of a mature supercell thunderstorm. *J. Atmos. Sci.,* **38,** 1558–1580.

Knight, C. A., and N. C. Knight, 1970: The falling behavior of hailstones. *J. Atmos. Sci.*, **27**, 672–681.

Kumjian, M. R., 2011: Precipitation properties of supercell hook echoes. *Electr. J. Severe Storms Meteor.,* **6 (5)**.

Kumjian, M. R., and A. V. Ryzhkov, 2007: Polarimetric characteristics of tornadic and nontornadic supercell thunderstorms. Preprints, *33rd Conf. on Radar Meteorology*, Cairns, Queensland, Amer. Meteor. Soc., P10.11.

Kumjian, M. R., and A. V. Ryzhkov, 2008a: Polarimetric signatures in supercell thunderstorms. *J. Appl. Meteor. Climatol.,* **47,** 1940-1961.

Kumjian, M. R., and A. V. Ryzhkov, 2008b: Microphysical size sorting revealed by dual-polarization Doppler radar. Preprints, *88th Annual AMS Meeting*, New Orleans, Amer. Meteor. Soc., P2.13.

Kumjian, M. R., and A. V. Ryzhkov, 2009: Storm-relative helicity revealed from polarimetric radar measurements. *J. Atmos. Sci.*, **66**, 667–685.

Kumjian, M. R., A. V. Ryzhkov, V. M. Melnikov, and T. J. Schuur, 2010a: Rapid-scan super-resolution observations of a cyclic supercell with a dual-polarization WSR-88D. *Mon. Wea. Rev.,* **138,** 3762–3786.

Kumjian, M. R., J. C. Picca, S. M. Ganson, A. V. Ryzhkov, J. Krause, D. S. Zrnic, and A. Khain, 2010b: Polarimetric radar characteristics of large hail. *25th Conf. on Severe Local Storms,* Denver, CO, Amer. Meteor. Soc., 11.2.

Kumjian, M. R., S. Ganson, and A. V. Ryzhkov, 2012: Raindrop freezing in deep convective updrafts: polarimetric and microphysical model. *J. Atmos. Sci.*, **69**, 3471–3490.

Le Bouar, E., J. Testud, and S. Y. Matrosov, 2002: Rainfall rate estimate from the rain profiling algorithm ZPHI applied to X-band polarimetric radar data. *Proc. Second European Conf. on Radar Meteorology*, Delft, Netherlands, European Meteorological Society, 238–242.

Lemon, L. R., and C. A. Doswell, 1979: Severe thunderstorm evolution and mesocyclone structure as related to tornadogenesis. *Mon. Wea. Rev.*, **107,** 1184–1197.

Lim, S., V. Chandrasekar, and V. N. Bringi, 2005: Hydrometeor classification system using dual-polarization radar measurements: Model improvements and in situ verification. *IEEE Trans. Geosci. Remote Sens.*, **43,** 792–801.

Lin, Y.-L., R.D. Farley, and H.D. Orville, 1983: Bulk parameterization of the snow field in a cloud model. *J. Climate Appl. Meteor.*, **22**, 1065–1092.

Liu, H., and V. Chandrasekar, 2000: Classification of hydrometeors based on polarimetric radar measurements: Development of fuzzy logic and neuro-fuzzy systems, and in situ verification. *J. Atmos. Oceanic Technol.*, **17,** 140–164.

Loney, M.L., D.S. Zrnic, J.M. Straka, and A.V. Ryzhkov, 2002: Enhanced polarimetric radar signatures above the melting level in a supercell storm. *J. Appl. Meteor.*, **41**, 1179–1194.

Mahale, V. N., G. Zhang, and M. Xue, 2013: Fuzzy logic classification of three-body scattering from S-band polarimetric radar measurements. Preprints, *36th Conf. on Radar Meteorology*, Breckenridge, CO, Amer. Meteor. Soc., 261.

Mallet, C., and L. Barthes, 2009: Estimation of gamma raindrop size distribution parameters: statistical fluctuations and estimation errors. *J. Atmos. Oceanic Technol.*, **26**, 1572–1584.

Marshall, J.S., and W. Mc K. Palmer, 1948: The distribution of raindrops with size. *J. Meteor.*, **5**, 165–166.

Marwitz, J.D., 1972: The structure and motion of severe hailstorms. Part I: Supercell storms. *J. Appl. Meteor.*, **11**, 166–179.

Marzano, F. S., D. Scaranari, M. Celano, P. P. Alberoni, G. Vulpiani, and M. Montopoli, 2006: Hydrometeor classification from dual-polarized weather radar: Extending fuzzy logic from S-band to C-band data. *Advances in Geosciences*, **7,** 109–114.

Matrosov, S. Y., R. A. Kropfli, R. F. Reinking, and B. E. Martner, 1999: Prospects for measuring rainfall using propagation differential phase in X- and Ka-radar bands. *J. Appl. Meteor.*, **38,** 766–776.

Matrosov, S. Y., K. A. Clark, B. E. Martner, and A. Tokay, 2002: X-band polarimetric radar measurements of rainfall. *J. Appl. Meteor.*, **41,** 941–952.

Maxwell Garnett, J. C., 1904: Colours in metal glasses and metal films. *Philos. Trans. R. Soc. London, Sect. A*, **3**, 385–420.

Meyers, M. P., R. L. Walko, J. R. Harrintong, and W. R. Cotton, 1997: New RAMS cloud microphysics parameterization. Part II: The two-moment scheme. *Atmos. Res.,* **45,** 3–39.

McCaul, E. W., and C. Cohen, 2002: The impact on simulated storm structure and intensity of variations in the mixed layer and moist layer depths. *Mon. Wea. Rev.*, **130**, 1722–1748.

McLaughlin, D., and Coauthors, 2009: Short-wavelength technology and the potential for distributed networks of small radar systems. *Bull. Amer. Meteor. Soc.,* **90,** 1797–1817.

Meischner, P. F., V. N. Bringi, D. Heimann, and H. Holler, 1991: A squall line in southern Germany: kinematics and precipitation formation as deduced by advanced polarimetric and Doppler radar measurements. *Mon. Wea. Rev.,* **119,** 678–701.

Melnikov, V., D. Zrnic, A. Ryzhkov, A. Zahrai, and J. Carter, 2009: Validation of attenuation correction at X band performed with collocated S-band polarimetric radar. Preprints, *34th Conf. on Radar Meteorology*, Williamsburg, VA, Amer. Meteor. Soc., 11A.5.

Milbrandt, J. A. and M. K. Yau, 2005a: A multimoment bulk microphysics parameterization. Part I: Analysis of the role of the spectral shape parameter. *J. Atmos. Sci.*, **62**, 3051–3064.

Milbrandt, J. A., and M. K. Yau, 2005b: A multimoment bulk microphysics parameterization. Part II: A proposed three-moment closure and scheme description. *J. Atmos. Sci.*, **62**, 3065–3081.

Milbrandt, J. A. and R. McTaggart-Cowan, 2010: Sedimentation-induced errors in bulk microphysics schemes. *J. Atmos. Sci.*, **67**, 3931–3948.

Morrison, H., J. A. Curry, and V. I. Khvorostyanov, 2005: A new double-moment microphysics parameterization for application in cloud and climate models. Part I: Description. *J. Atmos. Sci.,* **62,** 1665–1677.

Munchak, S. J., and A. Tokay, 2008: Retrieval of raindrop size distribution from simulated dual-frequency radar measurements. *J. Appl. Meteor. Climatol.*, **47**, 223–239.

Naylor, J., and M. S. Gilmore, 2012: Convective initiation in an idealized cloud model using an updraft nudging technique. *Mon. Wea. Rev.*, **140**, 3699-3705.

Palmer, R. D., D. Bodine, M. Kumjian, B. Cheong, G. Zhang, Q. Cao, H. B. Bluestein, A. V. Ryzhkov, T.-Y. Yu, and Y. Wang, 2011: Observations of the 10 May 2010 tornado outbreak using OU-PRIME: potential for new science with high-resolution polarimetric radar. *Bull. Amer. Meteor. Soc.,* **92,** 871–891.

Park, H., A. V. Ryzhkov, D. S. Zrnic, and K. Kim, 2009: The Hydrometeor Classification Algorithm for the Polarimetric WSR-88D: Description and Application to an MCS. *Wea. Forecasting*, **24,** 730–748.

Park, S. G., V. N. Bringi, V. Chandrasekar, M. Maki, and K. Iwanami, 2005a: Correction of radar reflectivity and differential reflectivity for rain attenuation at X band. Part I: Theoretical and empirical basis. *J. Atmos. Oceanic Technol.*, **22,** 1621–1632.

Park, S. G., M. Maki, K. Iwanami, V. N. Bringi, and V. Chandrasekar, 2005b: Correction of radar reflectivity and differential reflectivity for rain attenuation at X band. Part II: Evaluation and application. *J. Atmos. Oceanic Technol.*, **22,** 1633–1655.

Payne, C. D., T. J. Schuur, D. R. MacGorman, M. I. Biggerstaff, K. M. Kuhlman, and W. D. Rust, 2010: Polarimetric and electrical characteristics of a lightning ring in a supercell storm. *Mon. Wea. Rev.*, **138**, 2405–2425.

Pazmany, A. L., F. J. Lopez, H. B. Bluestein, and M. Kramar, 2003: Quantitative rain measurements with a mobile, X-band, polarimetric Doppler radar. Preprints, *31st Conf. on Radar Meteorology*, Seattle, WA, American Meteorological Society, 858–859.

Pazmany, A. L., J. B. Mead, H. B. Bluestein, J. C. Snyder, and J. B. Houser, 2013: A mobile rapid-scanning polarimetric (RaXPol) Doppler radar system. *J. Atmos. Oceanic Technol.*, **30**, 1398–1413.

Petch, J. C., 2006: Sensitivity studies of developing convection in a cloud-resolving model. *Quart. J. Roy. Meteor. Soc.*, **132**, 345–358.

Petersen, W. A. and Coauthors, 2005: The UAH-NSSTC/WHNT ARMOR dual-polarimetric radar: a unique collaboration in research, education, and technology transfer. Preprints, *32nd Conf. on Radar Meteorology,* Albuquerque, NM, Amer. Meteor. Soc., 12R.4.

Picca, J. C., and A. V. Ryzhkov, 2012: A Dual-Wavelength Polarimetric Analysis of the 16 May 2010 Oklahoma City Extreme Hailstorm. *Mon. Wea. Rev.*, **140**, 1385–1403.

Pfeifer, M., G.C. Craig, M. Hagan, and C. Keil, 2008: A polarimetric radar forward operator for model evaluation. *J. Appl. Meteor. Clim.*, **47**, 3202–3220.

Pruppacher, H. R., and K. V. Beard, 1970: A wind tunnel investigation of the internal circulation and shape of water drops falling at terminal velocity in air. *Quart. J. Roy. Meteor. Soc.*, **96,** 247–256.

Rasmussen, E. N., 2003: Refined supercell and tornado forecast parameters. *Wea. Forecasting,* **18,** 530–535.

Rasmussen, E. N., and D. O. Blanchard, 1998: A baseline climatology of sounding-derived supercell and tornado forecast parameters. *Wea. Forecasting,* **13,** 1148–1164.

Rasmussen, R. M., and A. J. Heymsfield, 1987: Melting and shedding of graupel and hail. Part I: Model physics. *J. Atmos. Sci.*, **44,** 2754–2763.

Rasmussen, R. M., V. Levizzani, and H. R. Pruppacher, 1984: A wind tunnel and theoretical study on the melting behavior of atmospheric ice particles: III. Experiment and theory for spherical ice particles of radius > 500 μm. *J. Atmos. Sci.*, **41,** 381–388.

Reisner, J., R. M. Rasmussen, and R. T. Bruintjes, 1998: Explicit forecasting of supercooled liquid water in winter storms using the MM5 mesoscale model. *Quart. J. Roy. Meteor. Soc.,* **124,** 1071–1107.

Romine, G. S., D. W. Burgess, and R. B. Wilhelmson, 2008: A dual polarization-radar-based assessment of the 8 May 2003 Oklahoma City area tornadic supercell. *Mon. Wea. Rev.,* **136,** 2849–2870.

Rotunno, R., 1981: On the evolution of thunderstorm rotation. *Mon. Wea. Rev.,* **109,**

171–180.

Ryzhkov, A. V., 2001: Interpretation of polarimetric radar covariance matrix for meteorological scatterers: theoretical analysis. *J. Atmos. Oceanic Technol.*, **18**, 315–328.

Ryzhkov, A. V., and D. S. Zrnic, 1995: Precipitation and attenuation measurements at a 10-cm wavelength. *J. Appl. Meteor.*, **34,** 2121–2134.

Ryzhkov, A. V., and D. S. Zrnic, 1996: Assessment of rainfall measurement that uses specific differential phase. *J. Appl. Meteor.*, **35,** 2080–2090.

Ryzhkov, A. V., and D. Zrnic, 2005: Radar polarimetry at S, C, and X bands: Comparative analysis and operational implications. Preprints, *32nd Conf. on Radar Meteorology*, Albuquerque, NM, American Meteorological Society, 9R.3.

Ryzhkov, A. V., D. W. Burgess, D. S. Zrnic, T. Smith, and S. E. Giangrande, 2002: Polarimetric analysis of a 3 May 1999 tornado. Preprints, *21st Conf. on Severe Local Storms*, San Antonio, TX, Amer. Meteor. Soc., 515–518.

Ryzhkov, A. V., S. E. Giagrande, and T. J. Schuur, 2005a: Rainfall estimation with a polarimetric prototype of WSR-88D. *J. Appl. Meteor.,* **44,** 502–515.

Ryzhkov, A. V., T. J. Schuur, D. W. Burgess, and D. S. Zrnic, 2005b: Polarimetric tornado detection. *J. Appl. Meteor.*, **44,** 557-570.

Ryzhkov, A. V., T. J. Schuur, D. W. Burgess, P. L. Heinselman, S. E. Giagrande, and D. S. Zrnic, 2005c: The Joint Polarization Experiments: Polarimetric measurements and hydrometeor classification. *Bull. Amer. Meteor. Soc.,* **86,** 809–824.

Ryzhkov, A. V., S. M. Ganson, A. Khain, M. Pinsky, and A. Pokrovsky, 2009: Polarimetric characteristics of melting hail at S and C bands. Preprints, *34th Conf. on Radar Meteorology*, Williamsburg, VA, Amer. Meteor. Soc., 4A.6.

Ryzhkov, A. V., M. Pinsky, A. Pokrovsky, and A. Khain, 2011: Polarimetric radar observation operator for a cloud model with spectral microphysics. *J. Appl. Meteor. Climatol.*, **50,** 873–894.

Scarchilli, G., E. Goroucci, V. Chandrasekar, and T. A. Seliga, 1993: Rainfall estimation using polarimetric techniques at C-band frequencies. *J. Appl. Meteor.*, **32,** 1150–1160.

Schlatter, P. T., 2003: Polarimetric radar and in-situ measurements of a nontornadic supercell. M.S. thesis, School of Meteorology, University of Oklahoma, 97 pp.

Schultz, C. J., and Coauthors, 2012: Dual-polarimetric radar-based tornado debris signatures and paths associated with tornadoes over northern Alabama during the historic outbreak of 27 April 2011. *92nd Annual Meeting,* New Orleans, LA, Amer.

Meteor. Soc., J2.2.

Schwarz, C. M., 2011: Supercell observations obtained during VORTEX2 from the NOAA (NSSL) X-band polarized mobile weather radar. M.S. thesis, School of Meteorology, University of Oklahoma, 184 pp.

Seifert, A., and K. D. Beheng, 2006: A two-moment cloud microphysical parameterization for mixed phase clouds. Part 1: Model description. *Meteor. Atmos. Phys.*, **92**, 45–66.

Seliga, T. A., and V. N. Bringi, 1976: Potential use of radar differential reflectivity measurements at orthogonal polarizations for measuring precipitation. *J. Appl. Meteor.,* **15,** 69–76.

Snook, N., and M. Xue, 2008: Effects of microphysical drop size distribution on tornadogenesis in supercell thunderstorms. *Geophys. Res. Lett.,* **35,** L24803, doi:10.21029/22008GL035866.

Snyder, J. C., H. B. Bluestein, Y.-S. Jung, S. J. Frasier, and V. Venkatesh, 2010a: The structure and time evolution of polarimetric signatures in severe convection storms: high-resolution numerical simulations and data from a mobile, X-band Doppler radar. *25th Conf. on Severe Local Storms,* Denver, CO, Amer. Meteor. Soc., P8.8.

Snyder, J. C., H. B. Bluestein, G. Zhang, and S. F. Frasier, 2010b: Attenuation correction and hydrometeor classification of high-resolution, X-band, dual-polarized mobile radar measurements in severe convective storms. *J. Atmos. Oceanic Technol.,* **27,** 1979–2001.

Snyder, J. C., H. B. Bluestein, V. Venkatesh, and S. J. Frasier, 2013: Observations of polarimetric signatures in supercells by an X-band mobile Doppler radar. *Mon. Wea. Rev.*, **141**, 3–29.

Straka, J. M., 2009: *Cloud and Precipitation Microphysics: Principles and Parameterizations*. Cambridge University Press, 392 pp.

Straka, J. M., and E. N. Rasmussen, 1997: Toward improving microphysical parameterizations of conversion processes. *J. Appl. Meteor.*, **36**, 896–902.

Straka, J. M., Zrnic, D. S., and A. V. Ryzhkov, 2000: Bulk hydrometeor classification and quantification using polarimetric radar data: Synthesis of relations. *J. Appl. Meteor.*, **39,** 1341–1372.

Testud, J., E. Le Bouar, E. Obligis, and M. Ali-Mehenni, 2000: The rain profiling algorithm applied to polarimetric weather radar. *J. Atmos. Oceanic Technol.*, **17,** 332–356.

Thompson, G., R. M. Rasmussen, and K. Manning, 2004: Explicit forecasts of winter precipitation using an improved bulk microphysics scheme. Part I: Description and sensitivity analysis. *Mon. Weather Rev.,* **132,** 519–542.

Thompson, R. L., R. Edwards, J. A. Hart, K. L. Elmore, and P. Markowski, 2003: Close proximity soundings within supercell environments obtained from the Rapid Update Cycle. *Wea. Forecasting,* **18,** 1243–1261.

Tripoli, G. J. and W. R. Cotton, 1980: A numerical investigation of several factors contributing to the observed variable intensity of deep convection over south Florida. *J. Appl. Meteor.*, **19**, 1037–1063.

Tuttle, J. D., V. N. Bringi, H. D. Orville, and F. J. Kopp, 1989: Multiparameter radar study of a microburst: comparison with model results. *J. Atmos. Sci.,* **46,** 601–620.

Ulbrich, C. W., 1983: Natural variations in the analytical form of the raindrop size distribution. *J. Climate Appl. Meteor.,* **22,** 1204–1215.

Van den Broeke, M. S., J. M. Straka, and E. N. Rasmussen, 2008: Polarimetric radar observations at low levels during tornado life cycles in a small sample of classic southern Plains supercells. *J. Appl. Meteor. Climatol.,* **47,** 1232–1247.

Van den Broeke, M.S., J.M. Straka, and E. Rasmussen, 2010, Mesocyclone and RFD evolution in simulated supercell storms with varying wind profiles. *25th Conf. on Severe Local Storms*, Denver, CO, Amer. Meteor. Soc., 8A.6.

Van Vleck, J. H., 1947a: The absorption of microwaves by uncondensed water vapor. *Phys. Rev.*, **71,** 425–433.

Van Vleck, J. H., 1947b: Absorption of microwaves by oxygen. *Phys. Rev.*, **71,** 413–424.

Vivekanandan, J., W. M. Adams, and V. N. Bringi, 1991: Rigorous approach to polarimetric radar modeling of hydrometeor orientation distributions. *J. Appl. Meteor.*, **30**, 1053–1063.

Vivekanandan, J., S. M. Ellis, R. Oye, D. S. Zrnic, A. V. Ryzhkov, and J. Straka, 1999: Cloud microphysics retrieval using S-band dual-polarization radar measurements. *Bull. Amer. Meteor. Soc.*, **80,** 381–388.

Vivekanandan, J., G. Zhang, and E. Brandes, 2004: Polarimetric radar estimators based on a constrained gamma drop size distribution model. *J. Appl. Meteor.*, **43,** 217–230.

Wakimoto, R. M., W.-C. Lee, H. B. Bluestein, C.-H. Liu, and P. H. Hildebrand, 1996: ELDORA observations during VORTEX 95. *Bull. Amer. Metoro. Soc.,* **77,** 2949–2950.

Waldvogel, A., 1974: The N0-jump of raindrop spectra. *J. Atmos. Sci.,* **31,** 1067–1078.

Weisman, M. L., and J. B. Klemp, 1982: The dependence of numerically simulated convective storms on vertical wind shear and buoyancy. *Mon. Wea. Rev.,* **110,** 504–520.

Weisman, M. L., and J. B. Klemp, 1984: The structure and classification of numerically simulated convective storms in directionally varying wind shears. *Mon. Wea. Rev.*, **112**, 2479-2498.

Wicker, L. J., and R. B. Wilhelmson, 1995: Simulation and analysis of tornado development and decay within a three-dimensional supercell thunderstorm. *J. Atmos. Sci.*, **52,** 2675–2703.

Wicker, L. J., M. P. Kay, and M. P. Foster, 1997: STORMTIPE-95: results from a convective storm forecast experiment. *Wea. Forecasting*, **12**, 388–398.

Wurman, J., J. M. Straka, E. Rasmussen, M. Randall, and A. Zahrai, 1997: Design and deployment of a portable, pencil-beam, pulsed, 3-cm Doppler radar. *J. Atmos. Oceanic Technol.*, **14,** 1502–1512.

Wurman, J., D. Dowell, Y. Richardson, P. Markowski, E. Rasmussen, D. Burgess, L. Wicker, and H. B. Bluestein, 2012: The Second Verification of the Origins of Rotation in Tornadoes Experiment: VORTEX2. *Bull. Amer. Meteor. Soc.*, **93,** 1147–1170.

Xue, M., 2000: High-order monotonic numerical diffusion and smoothing. *Mon. Wea. Rev.,* **128,** 2853–2864.

Xue, M., K. K. Droegemeier, and V. Wong, 2000: The Advanced Regional Prediction System (ARPS) - A multiscale nonhydrostatic atmospheric simulation and prediction tool. Part I: Model dynamics and verification. *Meteor. Atmos. Phys.,***75,** 161–193.

Xue, M., and Coauthors, 2001: The Advanced Regional Prediction System (ARPS) - A multiscale nonhydrostatic atmospheric simulation and prediction tool. Part II: Model physics and applications. *Meteor. Atmos. Phys.,* **76,** 143–165.

Xue, M., D.-H. Wang, J.-D. Gao, K. Brewster, and K. K. Droegemeier, 2003: The Advanced Regional Prediction System (ARPS), storm-scale numerical weather prediction and data assimilation. *Meteor. Atmos. Phys.,* **82,** 139–170.

Zhang, G., J. Vivekanandan, and E. Brandes, 2001: A method for estimating rain rate and drop size distribution from polarimetric radar measurements. *IEEE Trans. Geosci. Remote Sens.*, **39,** 830–841.

Ziegler, C.L., 1985: Retrieval of thermal and microphysical variables in observed convective storms. Part I: Model development and preliminary testing. *J. Atmos. Sci.*, **42**, 14871509.

Zrnic, D. S., and A. V. Ryzhkov, 1995: Advantages of rain measurements using specific differential phase. *J. Atmos. Oceanic Technol.,* **13,** 454–464.

Zrnic, D. S. and A. V. Ryzhkov, 1999: Polarimetry for weather surveillance radars. *Bull. Amer. Meteor. Soc.,* **80,** 389–406.

Zrnic, D. S., A. V. Ryzhkov, J. Straka, Y. Liu, and J. Vivekanandan, 2001: Testing a procedure for automatic classification of hydrometeor types. *J. Atmos. Oceanic Technol.*, **18,** 892–913.